J. Astrophys. Astr. (2002) **23,** 1–2

Preface

X-ray astronomy has seen many revolutionary trends since the discovery of the first X-ray source in 1962. Starting as a part of cosmic ray research with the early experiments using rockets and balloons, it has acquired a leading place in the mainstream Astronomy and Astrophysics. The first path breaking event took place in 1970 with the launch of the UHURU satellite. The first technological breakthrough came with the launch of the Einstein satellite in 1978, which for the first time employed the principle of focusing optics in the low energy X-ray region. The X-ray sky today is dotted with sources, which are 17 magnitudes fainter than Sco X-1, the first discovered source. A wealth of observational data has been produced since then, on the entire ensemble of visible and invisible universe. But still by no means is one close to a complete understanding of the complexities of temporal and spectral properties of the large variety of X-ray sources. Due to limitations of the available technology of detecting high energy photons, the energy band above 20 keV is still poorly explored. The most recent trend in the efforts to unlock the mysteries of our universe is the 'multi-wavelength' approach which can give a more complete picture of the X-ray sources and emission mechanisms.

Experimental work in X-ray astronomy at the Tata Institute of Fundamental Research (TIFR) started in 1966, using balloon borne instruments in the energy band of $20 - 100$ keV region. Rocket-borne soft X-ray surveys ($0.15 - 2$ keV) were conducted by the group during $1972 - 1982$. An all sky monitor to detect transient sources and study the time variability of steady X-ray sources in the energy range $2 - 20$ keV was fabricated by the group and launched on board the second Indian satellite, Bhaskara, in 1979. Our next opportunity for a space borne payload arose in 1996 by the launch of the Indian X-ray Astronomy Experiment (IXAE) on board IRS-P3 satellite carried by an Indian Rocket. In view of the success of IXAE, a dedicated astronomy satellite named 'ASTROSAT' has been approved by the Indian Space Research Organization. Keeping with the present day trend and capabilities of the Indian launcher, the new satellite will be configured for multiwavelength observations of X-ray sources.

It seemed to several of us in the group that it would be the most appropriate time to hold an international symposium to take stock of the recent developments in the X-ray astronomy with a particular emphasis on multi-wavelength observations. A four day symposium entitled 'Multi-colour Universe' was thus held during September $11 - 14$, 2001 at Tata Institute of Fundamental Research, Mumbai with the main aim of educating ourselves about the enormity of the discipline and the emerging priorities for coming decades. The programme consisted of invited reviews, contributed talks and poster sessions.

Another motivation to host this symposium was to felicitate our esteemed colleague Prof. P. C. Agrawal on attaining the age of sixty. Prof. P. C. Agrawal, commonly known as 'Prahlad ji' to his close friends had a leading role in the X-ray astronomy group at TIFR since its inception. Energetic as ever, he has provided a strong leadership and motivation to the group members for the last 40 years and the recent approval of ‘ASTROSAT’ is entirely due to his efforts. We look forward to his dedicated and guiding role in the future. The special ‘ASTROSAT’ session held on day 3 of the symposium, was specifically arranged as a tribute to the contribution of Professor P. C. Agrawal to X-ray astronomy in India.

The proceedings of this Symposium are clearly representative of present day understanding of the X-ray universe. The large number of invited talks and the contributory papers illustrate the depth and breadth of the entire field. Various suggestions from the members of the scientific organizing committee made this programme possible. The presentations were divided into three broad categories, the Galactic sources (Black hole and neutron star X-ray binaries, CVs, SNRs and stars), the extragalactic X-ray sources (Galaxies, AGNs, Quasar, X-ray background and clusters of galaxies and third, new technologies and future missions. The symposium was attended by 140 participants with a total of 40 invited talks, 6 contributed talks and 60 poster papers. A selection of these papers, after suitable refereeing, are published in this issue of JAA. We wish to thank the Indian Academy of Sciences for agreeing to publish these papers in JAA and Hema Wesley of the Academy staff for editorial help.

R. K. Manchanda, TIFR
B. Paul, TIFR
(Guest Editors)

J. Astrophys. Astr. (2002) **23,** 3–8

Seismic View of the Solar Interior

H. M. Antia *Tata Institute of Fundamental Research, Homi Bhabha Road, Mumbai 400 005, India*

Abstract. The interior of the Sun is not directly observable to us. Nevertheless, it is possible to infer the physical conditions prevailing in the solar interior with the help of theoretical models coupled with observational input provided by measured frequencies of solar oscillations. The frequencies of these solar oscillations depend on the internal structure and dynamics of the Sun and from the knowledge of these frequencies it is possible to infer the internal structure as well as the large scale flows inside the Sun, in the same way as the observations of seismic waves on the surface of Earth help us in the study of its interior. With the accumulation of seismic data over the last six years it has also become possible to study temporal variations in the solar interior. Some of these seismic inferences would be described.

Key words. Sun: oscillations, interior, rotation.

1. Introduction

Until recently the only source of information about the solar interior were the so-called theoretical solar models constructed using the equations of stellar structure and evolution (cf., Christensen-Dalsgaard *et al.* 1996). These equations have been derived using a number of simplifying assumptions and it is not obvious if these are indeed valid. It is, therefore, necessary to verify the correctness of these models through observational constraints. Historically, the first probe of physical conditions in the solar core was supplied by the measurement of neutrinos generated in the thermonuclear reaction network operating in the central regions of the Sun. A complementary probe was provided by the detection of solar oscillations which have been identified to be superposition of global modes of oscillations of the Sun (cf., Deubner & Gough 1984). Just like a musical instrument, the Sun oscillates in a sequence of well-defined modes which are determined by its internal structure. These modes are characterised by three quantum numbers, n, ℓ, m, where n is the radial order which is the number of nodes along the radius in the corresponding eigenfunction, while ℓ, m are the degree and azimuthal order determined by the horizontal variations defined by the spherical harmonics $Y_\ell^m(\theta, \phi)$. These oscillations are studied using the Doppler shift caused by the motion of fluid elements at the solar surface. The measured Doppler shift at a grid of points on the solar surface is decomposed in terms of spherical harmonics to get the contribution to each spherical harmonic. The resulting time-series is then Fourier transformed to calculate the power spectra for each ℓ, m, which in turn determine the frequencies of oscillations.

Early study of solar oscillations (cf., Gough & Toomre 1991) established the importance of accurate measurement of oscillation frequencies. For this purpose we need to observe the Sun continuously for a long duration. From most sites on the surface of the Earth it is not possible to observe the Sun continuously for more than 15 hrs. Thus for longer duration there are mainly two alternatives, the first is to observe the Sun using a network of identical instruments located around the world. A number of such networks have been operating and most successful of these is the Global Oscillation Network Group (GONG) project (Harvey *et al.* 1996) with six instruments, which have been observing the Sun since May 1995. The second alternative is to observe from a suitably located satellite and most successful of these satellites is the Solar and Heliospheric Observatory (SOHO) which was launched in December 1995. The Michelson Doppler Imager (MDI) instrument on board SOHO (Scherrer *et al.* 1995) has been observing the Sun since then, except for some breaks during 1998–99. With the availability of high quality seismic data from GONG and MDI instruments it has become possible to study the solar interior with unprecedented precision.

Most of the observed modes of oscillations have been identified as the acoustic or p-modes, where pressure gradient is the dominant restoring force. These are essentially sound waves trapped in the solar interior. As these waves travel inwards they get refracted away from the radial direction due to increasing sound speed and at some depth they suffer a total internal reflection and turn back to the surface where they are reflected by the steeply falling density profile. Thus these modes are trapped in a layer below the solar surface. The lower turning point of the modes is determined by its horizontal wavelength and frequency. Thus different modes are trapped in different regions of solar interior and sample the properties of this region. Consequently, by examining a variety of modes it is possible to study the variation of solar structure and rotation rate in the interior. GONG has measured frequencies of some half a million modes which strongly constrain theories of stellar structure and evolution as well as those of angular momentum transport in stellar interior.

2. Seismic inference of solar structure

If the Sun were strictly spherically symmetric the frequencies of oscillations would be independent of azimuthal order m, and the frequencies $\nu_{n\ell}$ would depend on the internal structure. But the Sun is rotating and hence, the frequencies $\nu_{n\ell m}$ can be expressed in terms of the mean frequency $\nu_{n\ell}$ of the multiplet and a series of splitting coefficients. The mean frequency is determined by the horizontally averaged structure of the Sun, while the splitting coefficients depend on the aspherical perturbations to solar structure as well as rotation rate and magnetic field in the solar interior. In this section, we will consider the spherically symmetric solar structure which controls the mean frequencies of a n, ℓ multiplet. These frequencies have been determined to an accuracy of 10^{-5}. Since the frequencies of p-modes depend on the sound speed and density profile in the solar interior, these profiles can be determined from the observed frequencies. A number of inversion techniques have been developed for this purpose (Gough & Thompson 1991). An outstanding achievement of these inversion techniques is determination of sound speed profile in most of the solar interior to an accuracy of better than 0.1%, which provides a strong constraint on solar models.

From early inversion for sound speed it was demonstrated that there is a significant diffusion of helium and heavy elements from the convection zone into the radiative interior (Christensen-Dalsgaard *et al.* 1993). These elements being heavier than hydrogen slowly diffuse towards the centre, thus reducing the helium abundance in the solar

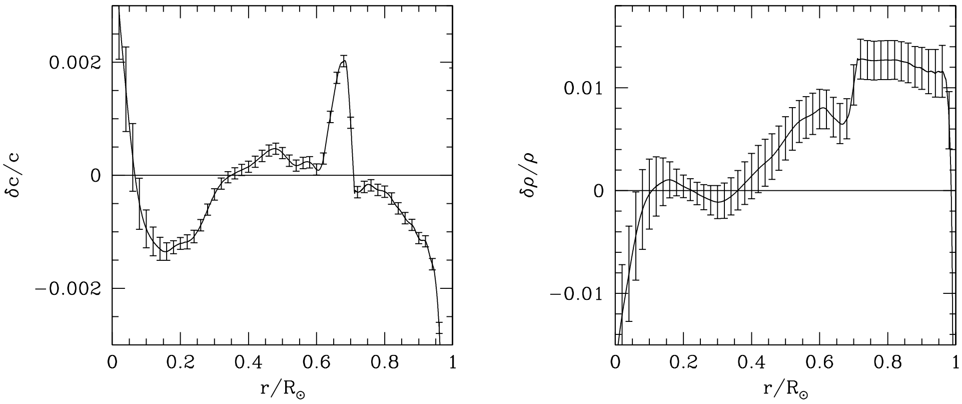

Figure 1. Relative difference in sound speed and density profiles between the Sun (as inferred by seismic inversions) and the standard solar model from Christensen-Dalsgaard *et al.* (1996).

envelope. Such a diffusion of helium and heavier elements should occur in interior of other stars as well. During the main sequence phase of stellar evolution hydrogen burning supplies the required energy to sustain the stellar luminosity; the diffusion of helium in the interior decreases the hydrogen abundance in the core, which in turn will reduce the main sequence life-time of stars. The ages of globular clusters are determined by calibrating against theoretical calculations of stellar evolution. The inclusion of the diffusion of helium would naturally reduce the estimated age of globular clusters. This should help in resolving the age problem in standard big bang model of cosmology.

Apart from diffusion it was also demonstrated that the opacity of solar material near the base of the convection zone needs to be revised upwards. This was later confirmed by revised OPAL opacities (Rogers & Iglesias 1992). The incorporation of revised opacity tables and diffusion of helium and heavy elements in solar interior improved the solar models significantly. Fig. 1 shows the plots of the relative difference in sound speed, and density between the Sun as inferred from helioseismic inversions and a standard solar model (Christensen-Dalsgaard *et al.* 1996). The agreement between the model and the Sun is fairly good except for a noticeable discrepancy near the base of the convection zone and a smaller discrepancy in the energy-generating core. The bump below $0.7R_\odot$ could be attributed to a sharp change in the gradient of helium abundance profile arising from diffusion in the reference model. This discrepancy occurs just below the base of the convection zone and a moderate amount of turbulent mixing (induced by say, a rotationally induced instability) in this region can alleviate this discrepant feature (Richard *et al.* 1996; Brun *et al.* 1999). This also happens to be the region where inversions for the rotation rate (cf., Schou *et al.* 1998) show the presence of a strong shear layer, which is referred to as the tachocline (Spiegel & Zahn 1992). The shearing motion in the tachocline is probably responsible for a certain amount of mixing in this region. This mixing also resolves the outstanding problem of low lithium abundance in the solar envelope, since the lithium can be destroyed by nuclear reactions near the base of the mixed layer.

With the knowledge of the sound speed and density profiles in the solar interior deduced through inversions, it is possible to employ the equations of thermal equilibrium to determine the temperature and chemical composition profiles inside the Sun (Gough & Kosovichev 1990; Takata & Shibahashi 1998; Antia & Chitre 1998) provided input physics like the opacity, equation of state and nuclear energy generation rates are known. In general, the computed luminosity resulting from these inferred profiles would not necessarily match the observed solar luminosity. The discrepancy between the computed and measured solar luminosity can, in fact, provide a test of input physics, and using these constraints it has been demonstrated that the nuclear reaction cross-section for the proton-proton reaction needs to be increased slightly (Antia & Chitre 1998; Degl'Innocenti *et al.* 1998; Schlattl *et al.* 1999). This cross-section has a controlling influence on the rate of nuclear energy generation and neutrino fluxes, but it has never been measured in the laboratory and all estimates are based on theoretical computations.

Using the inverted profiles for temperature, density and chemical composition it is possible to calculate the neutrino fluxes in the seismic model, which turn out to be close to those in the standard solar model. This suggests that the known discrepancy between the observed and predicted neutrino fluxes is likely to be due to non-standard neutrino physics. It can be shown that even if we allow for arbitrary variations in opacity or heavy element abundance in solar interior, it is not possible to construct any solar model satisfying the seismic constraint, which also matches the observed neutrino fluxes (Antia & Chitre 1997). Thus helioseismology has turned the Sun into a precision laboratory to study neutrino properties. Recent results from the Sudbury Neutrino Observatory (SNO) have confirmed (Ahmad *et al.* 2001) that the observed deficit in solar neutrinos is, indeed, due to oscillations between different neutrino species. A reliable estimate of neutrino fluxes from the Sun is required to distinguish between different possible mechanisms for oscillations between different species of neutrinos and seismic constraints have played a central role in improving these theoretical estimates of neutrino fluxes.

3. Rotation rate in the solar interior

Since the Sun is rotating, the frequencies of solar oscillations depend on m and the frequency splittings between different modes of same n, ℓ multiplet depends on rotation rate in the region where the mode is trapped. Thus from the observed frequency splittings it is possible to infer the rotation rate as a function of radial distance and latitude using a suitable inversion technique (Schou *et al.* 1998). The most striking feature of inferred rotation rate is that the differential rotation observed at the solar surface continues through the convection zone, while near the base of the convection zone there is a sharp transition to almost solid body rotation in the radiative interior (cf., Fig. 2). This region of intense shear has been named as tachocline (Spiegel & Zahn 1992). The origin of tachocline is not understood and provides a strong challenge to the theory of angular momentum transport in stellar interior.

Further, contrary to early expectation, the solar core is found to be rotating slower than the equatorial region at the surface. If the solar core were rotating much faster it could distort the Sun thus increasing its quadrupole moment. This could cause conflict with the test of general relativity based on the precession of orbit of planet mercury, since distorted Sun could produce a part of the precession by purely Newtonian effects. From the inverted rotation rate in solar interior we can estimate the quadrupole moment

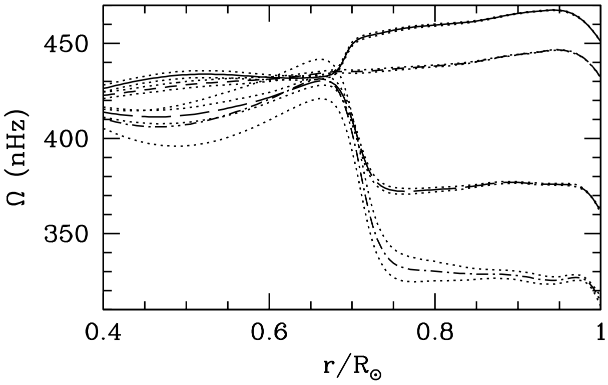

Figure 2. Rotation rate at various latitudes as a function of radial distance inferred from GONG data (Antia *et al.* 1998). The continuous, short-dashed, long-dashed and dot-dashed lines show the rotation rate at latitudes of 0°, 30°, 60°, 90° respectively. The dotted lines show the respective 1σ error limits.

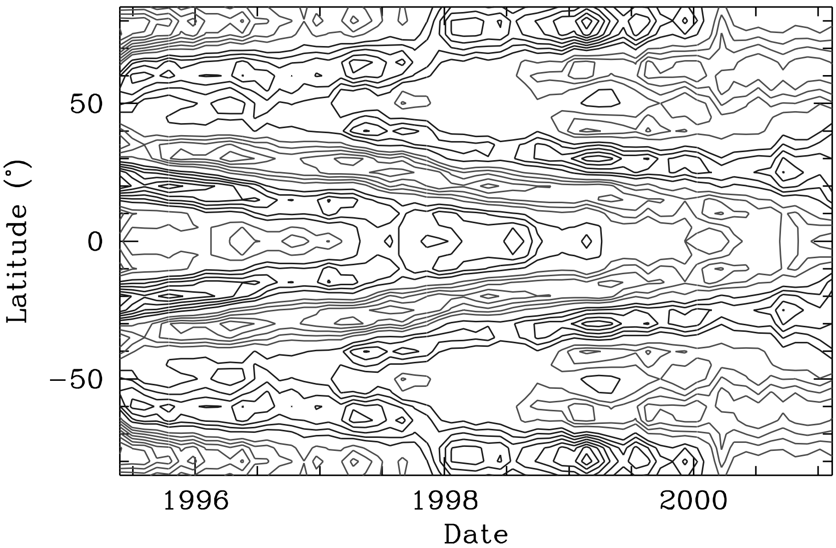

Figure 3. The contours of time varying component of rotation velocity, $v_{\rm zon} = \delta\Omega r \cos\theta$ (θ is the latitude) at a depth of $0.02 R_\odot$ below the solar surface obtained using the GONG data are shown as a function of latitude and time. The contours are drawn at interval of 1 m/s.

(Pijpers 1998) and it turns out that this results in negligible precession of orbit of mercury thus validating general relativity.

With the accumulation of seismic data over the last 6 years it is possible to study the temporal variations in the solar interior associated with the well-known 11 year solar cycle. From the measured variation in p-mode frequencies it should be possible to infer temporal variations in solar structure. But all the observed variation can be accounted for by variations in the outer surface layers (Basu & Antia 2000). In contrast the rotation rate shows significant variation in outer 10% of solar radius (Howe *et al.* 2000; Antia & Basu 2000). In order to study the temporal variation in rotation rate we subtract the temporal average of rotation rate at each latitude and radial distance from that determined at each epoch to obtain the residual. Fig. 3 shows the contours of constant residual of rotation velocity as a function of latitude and time at $r = 0.98R_\odot$. This shows a characteristic pattern with bands of faster and slower than average rotation velocity moving towards the equator at low latitude and towards the pole at higher latitude (Antia & Basu 2001). Similar pattern has been observed at the solar surface also (Howard and LaBonte 1980) and is referred to as torsional oscillations. These temporal variations in rotation rate would play a crucial role in the operation of solar dynamo, which is still not understood. The dynamo is generally believed to operate in the region near the base of the convection zone, but so far there is no evidence of any temporal variation in this region from seismic data.

References

Ahmad, Q. R. *et al.* 2001, *Phys. Rev. Lett.*, **87,** 071301.
Antia, H. M., Basu, S. 2000, *Ap. J.*, **541,** 442.
Antia, H. M., Basu, S. 2001, *Ap. J.*, **559,** L67.
Antia, H. M., Chitre, S. M. 1997, *MNRAS*, **289,** L1.
Antia, H. M., Chitre, S. M. 1998, *A&A*, **339,** 239.
Antia, H. M., Basu, S., Chitre, S. M. 1998, *MNRAS*, **298,** 543.
Basu, S., Antia, H. M. 2000, *Sol. Phy.*, **192,** 449.
Brun, A. S., Turck-Chièze, S., Zahn, J. P. 1999, *Ap. J.*, **525**, 1032.
Christensen-Dalsgaard, J., Proffitt, C. R., Thompson, M. J. 1993, *Ap. J.*, **403,** L75.
Christensen-Dalsgaard, J. *et al.* 1996, *Science*, **272,** 1286.
Degl'Innocenti, S., Fiorentini, G., Ricci, B. 1998, *Phys. Lett.*, **B416,** 365.
Deubner, F.-L., Gough, D. O. 1984, *ARA&A*, **22,** 593.
Gough, D. O., Kosovichev, A. G. 1990, in *Proc. IAU Colloquium No 121, Inside the Sun*, p. 327, (eds) G. Berthomieu & M. Cribier, (Dordrecht: Kluwer)
Gough, D. O., Thompson, M. J. 1991, in *Solar interior & atmosphere*, (eds) A. N. Cox, W. C. Livingston, & M. Matthews, p. 519, Space Science Series, University of Arizona Press.
Gough, D. O., Toomre, J. 1991, *ARA&A*, **29,** 627.
Harvey, J. W. *et al.* 1996, *Science*, **272,** 1284.
Howard, R., LaBonte, B. J. 1980, *Ap. J.*, **239,** L33.
Howe, R. *et al.* 2000, *Ap. J.*, **533,** L163.
Pijpers, F. P. 1998, *MNRAS*, **297,** L76.
Richard, O., Vauclair, S., Charbonnel, C., Dziembowski, W. A. 1996, *A&A*, **312,** 1000.
Rogers, F. J., Iglesias, C. A. 1992, *ApJS*, **79,** 507.
Schlattl, H., Bonanno, A., Paternó, L. 1999, *Phys. Rev.*, **D60,** 113002.
Scherrer, P. H. *et al.* 1995, *Solar Phys.*, **162,** 129.
Schou, J. *et al.* 1998, *Ap. J.*, **505,** 390.
Spiegel, E. A., Zahn, J. -P. 1992, *A&A*, **265,** 106.
Takata, M., Shibahashi, H. 1998, *Ap. J.*, **504,** 1035.

J. Astrophys. Astr. (2002) **23,** 9–14

Photometric Variability of Four Coronally Active Stars

J. C. Pandey[1], K. P. Singh[2], R. Sagar[1,3] & S. A. Drake[4]

[1]*State Observatory, Naini Tal 263 129, India.*
[2]*Tata Institute of Fundamental Research, Mumbai, India.*
[3]*Indian Institute of Astrophysics, Bangalore, India.*
[4]*Code 668, LHEA, NASA/Goddard Space Flight Center, Greenbelt, MD 20771, USA.*

Abstract. We present photometric observations of four stars that are optical counterparts of soft X-ray/EUV sources, namely 1ES 0829+15.9, 1ES0920-13.6, 2RE J110159+223509 and 1ES 1737+61.2. We have discovered periodic variability in two of the stars, viz., MCC 527 (1ES 0829+15.9; Period = $0^d.828 \pm 0.0047$) and HD 81032 (1ES 0920-13.6; Period = $\sim$ 57.02 $\pm$ 0.560 days). HD 95559 (2RE J110159+223509) is found to show a period of 3^d. HD 160934 (1ES1737+61.2) also shows photometric variability but needs to be monitored further for finding its period. These stars most likely belong to the class of chromospherically active stars.

Key words. Stars—variable, optical photometry, X-rays—source.

1. Introduction

A number of soft X-ray sources have recently been discovered in X-ray surveys with the Einstein and the ROSAT observatories and found to be associated with bright late-type stars. Many of these stars have not been studied in detail for their chromospheric and coronal activity, and their nature is not fully understood. As a result these are also not properly classified. We have carried out photometric observations of four such stars. Three of these: MCC 527, HD 81032, and HD 160934, were identified as likely optical counterparts of X-ray sources 1ES 0829+15.9, 1ES 0920-13.6, 1ES 1737+61.2 seen in the Einstien's IPC slew survey (Elvis *et al.* 1992). Another star, HD 95559, has been detected as an extreme ultraviolet (EUV) source named 2RE J110159+223509 by Mason *et al.* (1995). Optical spectra of these stars show chromospheric activities based on H_α and/or CaII, H and K emission lines. Table 1 lists the general information about these stars. Their X-ray, optical and radio properties, suggest that these may belong to various classes of coronally active stars.

2. Observations and data reductions

The BVR photometric observations were carried out using a CCD camera at f/13 Cassegrain focus of the 104-cm Sampurnanand Telescope at the State Observatory, Naini Tal. The CCD system consists of $24 \times 24\,\mu^2$ size pixel, having 2048×2048 pixels. To improve the signal-to-noise ratio the observations have been taken in a binning

Table 1. General information on the program stars. Δm is difference in magnitude between the maximum and minimum of light curve in a filter and σ is the standard deviation of the difference in magnitude of comparison stars.

X-ray source	Optical counterpart	V (mag)	Co-ordinate (2000)	Filter	Δm (mag)	σ (mag)	$\Delta m/\sigma$
1ES 0829+15.9	MCC 527	10.41	$\alpha = 08^h32^m30^s$	B	0.111	0.007	14.1
			$\delta = 15^0 49'26''$	V	0.114	0.006	17.9
				R	0.103	0.007	14.7
1ES 0920-13.6	HD 81032	9.02	$\alpha = 09^h22^m53^s$	B	0.300	0.025	12
			$\delta = -13^0 49'43''$	V	0.284	0.014	19.7
				R	0.261	0.014	18.4
WFC J1102.0+2235	HD 95559	8.96	$\alpha = 11^h02^m02^s$	B	0.080	0.012	6.7
			$\delta = 22^0 35'45''$	V	0.076	0.012	6.3
				R	0.060	0.009	6.7
1ES 1737+61.2	HD 160934	10.29	$\alpha = 17^h38^m30^s$	B	0.116	0.012	9.7
			$\delta = 61^0 15'09''$	V	0.111	0.014	8.0
				R	0.080	0.009	8.9

mode of 2×2 pixel^2, where each super pixel corresponds to 0.72×0.72 arcsec^2. The CCD covers a field of view $\sim 13 \times 13$ arcminute^2.

Multiple CCD frames were taken with the exposure time ranging from 2 to 120 secs depending on the seeing conditions and the filters used. A number of bias and twilight flat field frames were also taken during the observing run. The frames were cleaned employing the IRAF/MIDAS software. The differential magnitude of the stars were determined by aperture photometry.

3. Analysis and light curve

Three comparison stars for each program star (2 for HD 95559), having magnitude and colour similar to the program star and in the same CCD frame, were used to check for the variability in the program stars. Pair wise differential magnitudes of the comparison stars were computed and the standard deviations (σ) examined. In each case, the standard deviations were found to be nearly equal. Further analysis was carried out with only one of the comparison stars, closest to the program star. The ratio $\Delta m/\sigma$ indicates that all the program stars show statistically significant variability. In each filter, Δm, the difference between the maxima and the minima of the light curves was also determined. The light curves were analysed for periodicity using the Lomb-Scragle periodigram method in Starlink's Period software, and by fitting a sinusoidal function using the least square deviation method. Results from this analysis for each variable star are given below.

3.1 *1ES 0829+15.9 (MCC 527)*

Light curves obtained for MCC 527 in the B,V and R filters are shown in Fig. 1 (left panel). MCC 527 is a K8 spectral type star (A. V. Kazarovets *et al.* 1999), and is also listed as an unsolved variable (FR Cnc) in the Hipparcos catalogue (Perryman *et al.* 1997). Measurements with the Hipparcos satellite (Perryman *et al.* 1997) provide

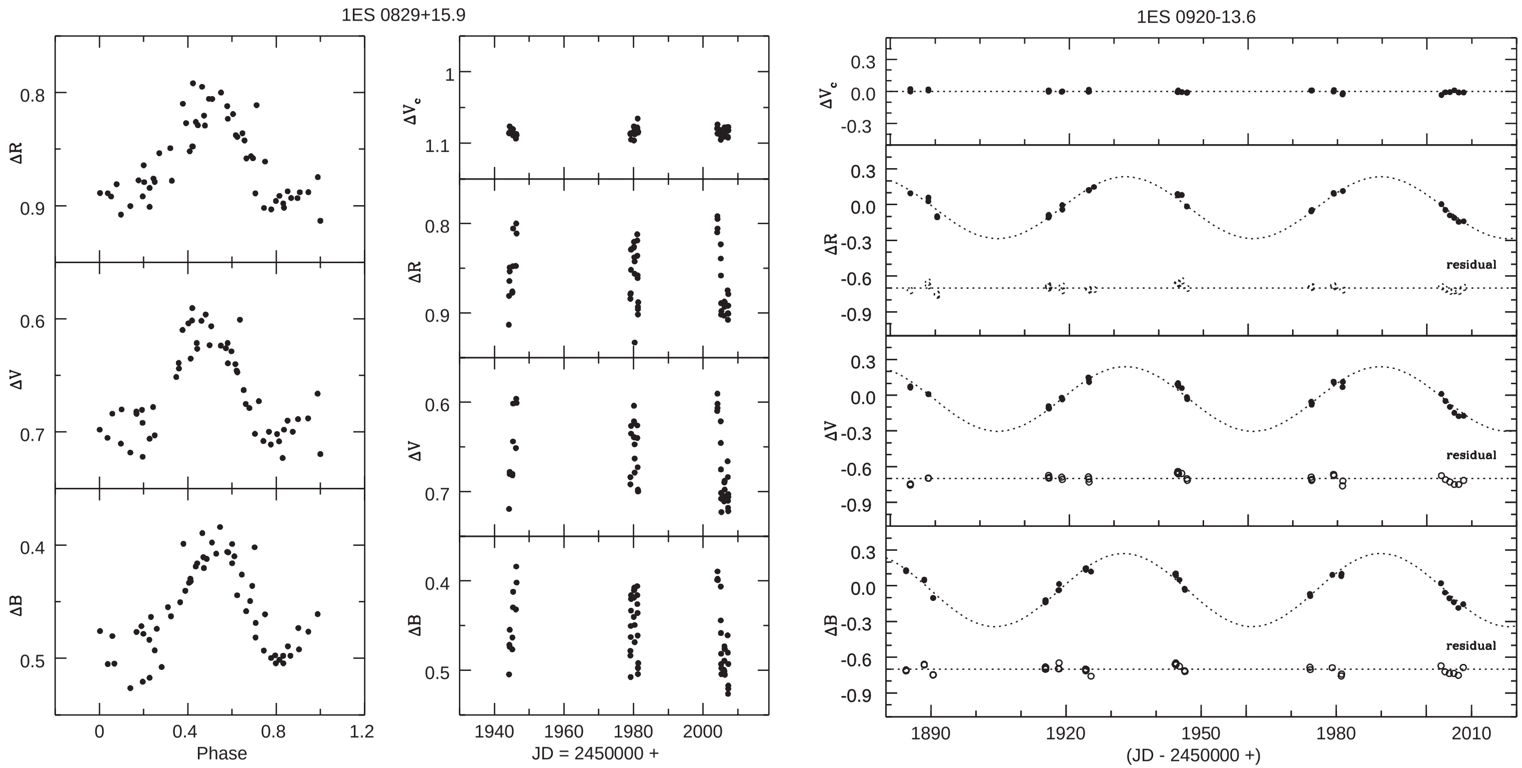

Figure 1. **Left panel**: Differential B, V, R magnitudes of MCC 527(1ES 0829+15.9) from February – April 2001 observing season against phase, and against Julian date. **Right panel**: Differential B, V and R light curve of the star HD 81032 (1ES 0920-13.6), observed during 2000–2001.

the basic parameters of this star: $V = 10.41$ mag, $(B - V) = 1.16 \pm 0.997$ mag, $(V - I) = 2.64 \pm 0.49$ mag, $V_{\rm max} = 10.276$ mag, $V_{\rm min} = 10.47$ mag, variability magnitude $(\Delta V) = 0.172 \pm 0.043$ mag and a parallax of 30.24 ± 2.03 milliarcsec which implies a distance of 33^{+2}_{-2} pc and a visual absolute magnitude of ~ 7.8 mag. We have discovered a period of $\sim 0.8281 \pm 0.0027$ days in the star. Fig. 1 (left panel) shows the light curves folded with this period.

3.2 *1ES 0920-13.6 (HD 81032)*

B, V and R light curves of HD 81032, optical counterpart of 1ES 0920-13.6, are shown in the right panel of Fig. 1. The basic parameters of HD 81032 are: $V = 9.019 \pm 0.023$ mag, $(B - V) = 1.033 \pm 0.023$ mag and a parallax of 6.6 milliarcsec (Hog *et al.* 1997). Our period search finds that the best periods in the B, V and R light curves 57.100 ± 0.280, 57.035 ± 0.371 and 57.061 ± 0.313 days respectively and the corresponding amplitude are 0.300 ± 0.034, 0.272 ± 0.037 and 0.260 ± 0.031 respectively. The mean period thus found is 57.065 ± 0.560 days. If confirmed, this will be a new periodic variable. The best fit sinusoidal curves, using the least square deviation, are shown in the right panel of Fig. 1.

3.3 *HD 95559*

B, V and R light curves of HD 95559 observed by us are shown in the left panel of Fig. 2. HD 95559 = BD 23^0 2297 has recently been shown to be a double-lined spectroscopic binary with an orbital period of 1.5260, and with a photometric period of 1.5264 days indicating that the rotation in HD 95559 is tightly synchronised to the orbital motion (Fekel & Henry 2000). Previous reports that this system has a 2.9 day photometric period (Jeffries *et al.* 1994; Strassmeier *et al.* 2000) appear to have been detections of the 1-day alias of the 1.526 day orbital period. According to the Hipparacos catalogue (Perryman *et al.* 1997) the basic parameters of this star are: $V = 8.96$ mag, $(B-V) = 0.87 \pm 0.026$ mag, $(V-I) = 0.88 \pm 0.02$ mag, $V_{\rm max} = 9.040$ mag, $V_{\rm min} = 9.158$, mag variability magnitude $(\Delta V) = 0.095 \pm 0.025$ and parallax = 18.43 ± 1.19 milliarcsec which gives a distance of 54^{+4}_{-3} pc and absolute magnitude of ~ 5.3. Its spectral class is K1V (Fekel & Henry 2000). A combination of the sinusoidals $(f(x) = a_0 + a_1 \cos(2\pi f(x+l_1)) + a_2 \cos(2\pi f(x+l_2)) + a_3 \sin(2\pi f(x+l_3)) + a_4 \sin(2\pi f(x+l_4)))$ was fitted using the least square deviation method in each of the B, V and R light curves (left panel of Fig. 2) which show primary and secondary minima. The period was determined by fitting a parabola to the two consecutive primary minimas and is found to be $3^d.03 \pm 0.02$, consistent with the 1-day alias of the orbital period.

3.4 *1ES 1737+61.2 (HD 160934)*

Light curves obtained for HD 160934 in the B, V and R filters are shown in Fig. 2 (right panel). HD 160934 is a flare star (Gershberg *et al.* 1999) of spectral type K8V. Its basic parameters are as follows: $V = 10.29$ mag, $(B - V) = 1.591 \pm 0.4$ mag, $(V - I) = 2.58 \pm 0.91$ mag, $V_{\rm max} = 10.21$ mag, $V_{\rm min} = 10.36$ mag (Hipparcos catalogue). The parallax of 40.75 ± 12.06 milliarcsec provides a distance of 25^{+10}_{-6} pc and absolute visual magnitude of 8.4. The observed points shown in Fig. 2 are not

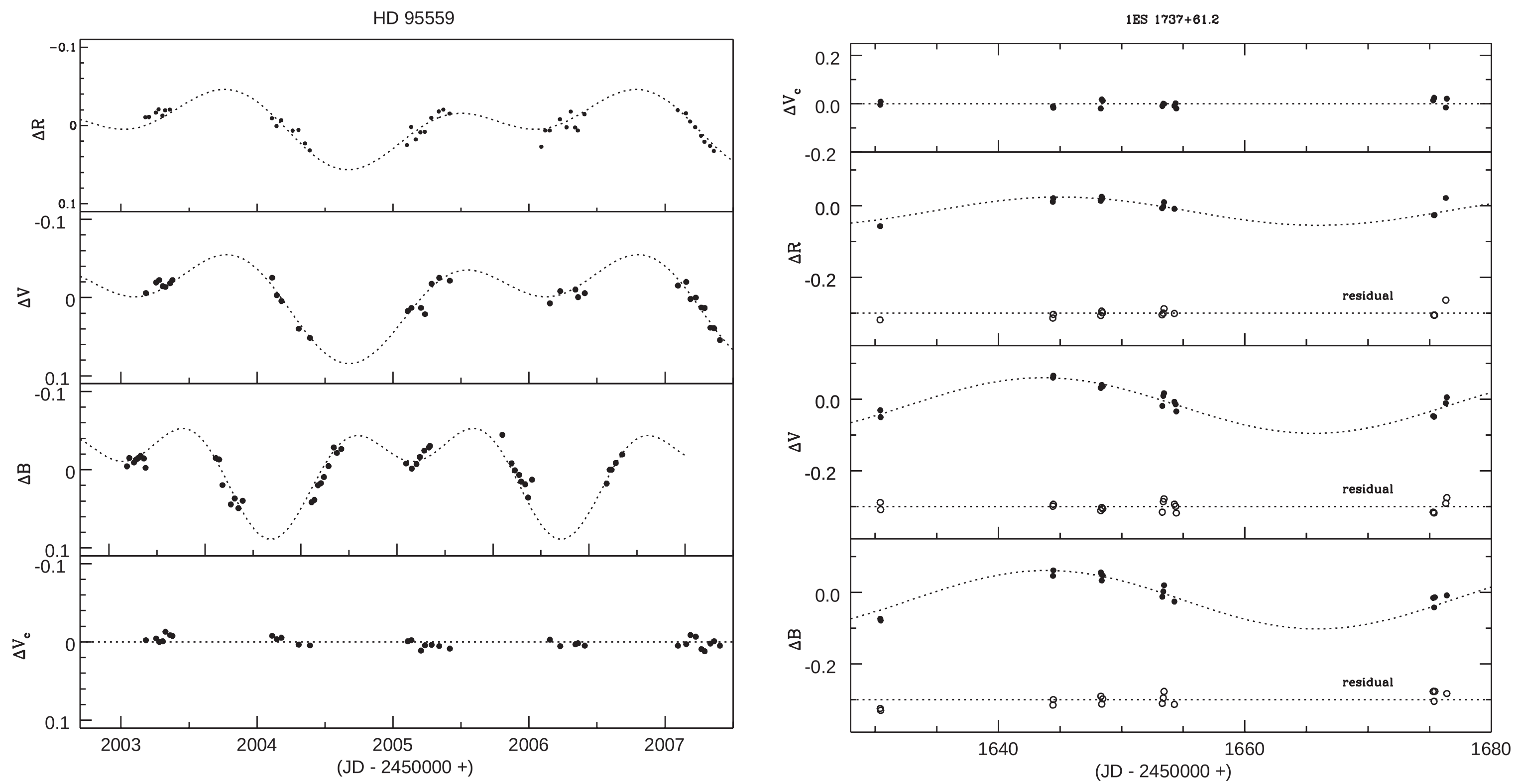

Figure 2. **Left panel**: B, V and R light curves of HD 95559 as observed in April 3–8, 2001. **Right panel**: B, V and R light curves of HD 160934 (1ES 1737+61.2) as observed during the year 2000.

sufficient for finding a reliable period, however, a sinusoidal curve is fitted using the method of the least square deviations for each of the B, V and R light curves. The best period found in B, V and R light curves is 43.918 ± 0.0154, 43.931 ± 0.012 and 41.719 ± 0.0035 respectively, giving a mean value of $43.182 \pm .040$ days. The inferred period seems rather long for an active late K dwarf considering that $v \sin\ i = 16.4$km/s for this star (Fekel 1997), and assuming that R = 0.6$R_{/odot}$, the maximum period (for $\sin\ i = 1.0$) is 1.85 days. More extensive observations are required for this star.

4. Summary

Optical photometry of the counterparts of four soft X-ray sources has led to the discovery of periods in two of them, viz., MCC 527 (P = $0^d.828 \pm 0.0047$) and HD 81032 (P = $\sim 57.065 \pm 0.560$ days). The observed variability appears to be of a different type in each source. We have also found the stars HD 95559 and HD 160934 to be variable. We plan to monitor these objects for longer time periods in three different filters, and to carry out spectroscopic observations, to understand the nature of variability in these stars. Stars MCC 527 and HD 81032 could belong to the short-period and long-period RSCVn class of objects, respectively.

References

Elvis, M. *et al.* 1992, *ApJS*, **80,** 257.
Fekel, F. C. 1997, *PASP*, **109,** 514.
Fekel, F. C., Henry, G. W. 2000, *AJ*, **120,** 3265.
Gershberg, R. E. *et al.* 1999, *A&AS*, **193,** 555.
Hog, E. *et al.* 1997, *A & A*, **323,** L57.
Jeffries, R. D. *et al.* 1994, *IBVS* Number 4091.
Kazarovets, A. V. *et al.* 1999, *IBVS* No. 4659.
Mason, K. O. *et al.* 1995, *MNRAS*, **274,** 1194.
Perryman, M. A. *et al.* 1997, *A & A*, **323,** L49.
Strassmeier, K. G. *et al.* 2000, *A & AS*, **142,** 247.

J. Astrophys. Astr. (2002) **23,** 15–18

The Investigation of Nova-like Variable MV Lyr during the 1999–2001 Years

N. A. Katysheva & S. Yu. Shugarov[1], E. P. Pavlenko[2] & P. V. Abolmasov[3]

[1]*Sternberg Astronomical Institute, Moscow, Russia.*
[2]*Crimean Astrophysical Observatory, p. Nauchny, Crimea.*
[3]*Physical Department, Moscow State University, Moscow, Russia.*

Abstract. A peculiar nova-like MV Lyr was investigated. The CCD-observations of MV Lyr were continued in Crimea during the outbursts and quiescent states. Last year its behavior became non-typical for "anti-dwarf novae". The length of its first deep minimum was 10 years. A modern state is characterized by very strong outbursts and very often changes of the stages. The periods $0.^{d}128$ and $0.^{d}136$ were obtained for 1998 and 1999 years accordingly. Possibly, a relation between the photometric period and the brightness exists.

Key words. Cataclysmic variables—"anti-dwarf novae".

1. Introduction

MV Lyr is one of the brightest cataclysmic variables of the northern sky. It was discovered by Parenago (1946) in 1946 as a star with an irregular variability. Later it was classified as nova-like subtype star – the VY Scl-star, or "anti-dwarf nova". In the years 1979–1989 this star similar to other "anti-dwarf novae" spent its time in a high brightness state ("on" stage, $B \simeq 12.^{m}5$), getting weaker by 2^{m}–8^{m} sometimes ("off" stage, $B \simeq 18^{m}$) and returning to the "on" stage. But later its behaviour became non-typical for indicated stars. The length of its first deep minimum was 10 years. In this state the outburst amplitude was 1^{m}–4^{m}. The main characteristic of its variability is the relatively stable sets in the high and low states with the amplitude about 5 magnitudes. The detailed description of the long-term photometric behaviour during 1951–1996 is presented in review by Pavlenko & Shugarov (1998) and some parameters of the system are in Highly Evolved Close Binary Systems Catalog (Cherepashchuk *et al.* 1996). The outbursts in 1997 were described in Pavlenko & Shugarov (1999) and some 1998–1999 ones in Katysheva *et al*. (2001).

The appearance of nova-like stars and particularly, MV Lyr in the high brightness state is an unpredictable event: our experience has shown that the brightness of "ordinary" outbursts never reaches the brightness of the real "high" state in MV Lyr. Even the most powerful outbursts are fainter than high state on 0.5 mag. Since 1994 MV Lyr changed its style of behaviour into a controversial one and we had already started to hunt for the real "prolonged high" state. So when in 1998 the brightness of MV Lyr had jumped above the level, which distinguishes the outburst from the "real" high state, we started the multilongitude photometric campaign. Its results (1998–1999 observations) are present in Katysheva *et al.* (2001). Last two years we continued to study the behaviour of MV Lyr in B, V, R, I-bands.

2. Observations

Observations of the years 2000–2001 have been carried out at the Zeiss-600 and ZTE 1.25-m telescopes of the Crimean Laboratory of the Sternberg Astronomical Institute, at the 38-cm telescope of the Crimean Astrophysical Observatory and at the Newton 30-cm telescope of the SAI Student Observatory (Moscow). The light detectors were CCD-cameras: ST-6, ST-7 and ST-8. Observations were in R-band of the Johnson system with time resolutions 1.5–3 minutes. The dead times between exposures were 15sec and in total we obtained several hundred measurements over 30 nights in Moscow and in Crimea (1999–2001: JD 2451522–52230). The comparison stars were used from Pavlenko & Shugarov (1999).

The light curve of MV Lyr over the last 25 years was shown in Katysheva *et al.* (2001). The light curve of the last four years is present in Fig. 1 (1998–2001), it is plotted (R-band) according to our data.

Over the first "low" state (1979–1989) MV Lyr has shown the sequence of relatively short dwarf-like outbursts of different amplitudes and durations (see Pavlenko & Shugarov 1998), that are superposed on the level of quiet state ($B \sim 17.^m5$). In 1989 this state rapidly changed on the high one ($B \sim 12.^m5$), that lasted till 1995. Then MV Lyr entered into the state that is different from the previous states: it displayed a sequence of strong outbursts of near equal amplitudes ($4^m - 5^m$), that were larger then those of the most strong outbursts of the first low state. Over our campaign (1999–2001) MV Lyr displayed possibly three or four bright outbursts.

The question of the light variations in the vicinity of the orbital period is still puzzling. The spectral observations by Schneider *et al.* (1981) and Skillman *et al.* (1995) gave the $P_{\rm orb} = 0.^d133$. The photometric behaviour has been studied by several

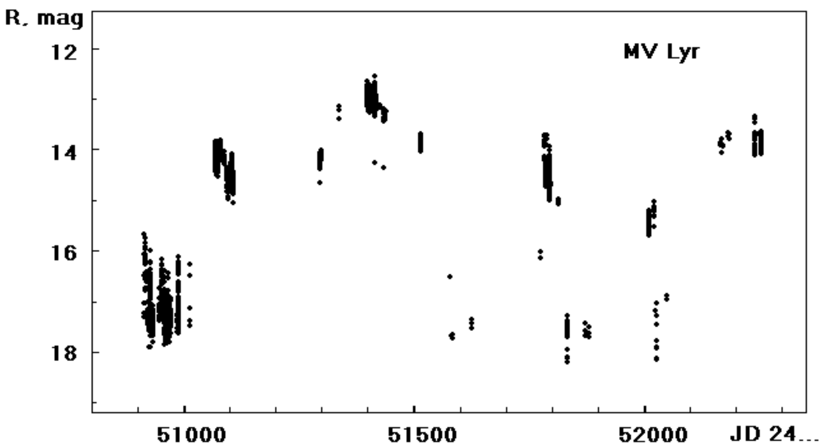

Figure 1. The overall light curve of MV Lyr during 1998–2001. The magnitudes R are plotted versus Julian date.

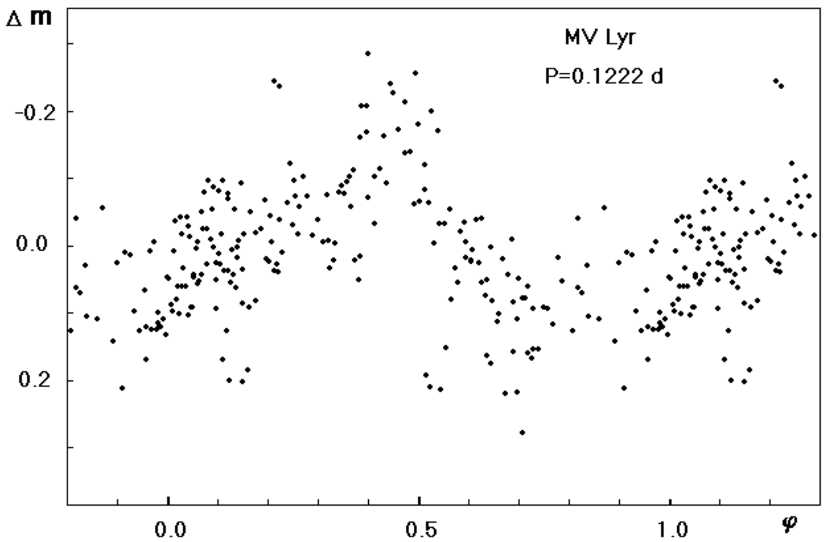

Figure 2. The data folded on the period 0.1222d (2001).

authors, but there was no simple result. Borisov (1992) and Skillman *et al.* (1995) observed this star at a high level of brightness and found the period $0.^{d}138$. This value is somewhat larger than the spectroscopic period and was interpreted as possible positive superhumps. Pavlenko & Shugarov (1998) found the most likely light variations of $0.^{d}1294$ (or $0.^{d}1487$). The first one seemed to be more preferable as it was close to that for known negative superhumpers. The second period was less likely because it was placed far above the known empirical relation between the fractional period excess (P_{sh}–P_{orb}), where P_{sh} and P_{orb} are the superhump and orbital periods respec-

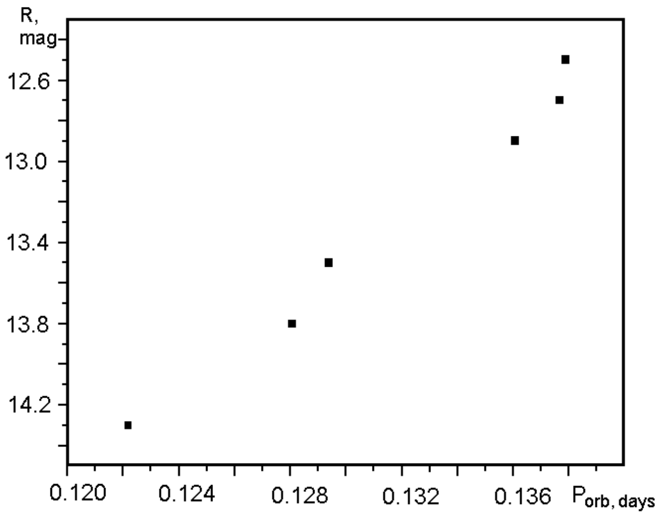

Figure 3. The magnitude versus period for MV Lyr.

tively (Stolz & Schoembs 1984). Our observations of 1998–1999 during two outbursts (Katysheva *et al.* 2001) give for 1999 the most likely period – $0.^{d}1361$ and for 1998 – $0.^{d}1281$.

We gathered all available data on the finding of the near-orbital light variations and plotted them against the brightness of MV Lyr. The result was given in Fig. 4 (Katysheva *et al.* (2001). It was seen that the photometric period decreases when the brightness decreases. Our conclusion was: a possible relation between the brightness state and the photometric period exists! Obviously it cannot be caused by the known decreasing of the superhump period for the SU UMa stars over the course of the superoutburst: the scale of the superhump period decrease is much smaller. We found the most likely light variations of $0.^{d}1222$ (or $0.^{d}139$). The first one seemed to be more preferable as it was close to that for known negative superhumpers. The relation "brightness–photometrical period" is present in Fig. 3. A point $0.^{d}1222$ lies on the indicated line.

The following observations of this peculiar nova-like star are strongly recommended for the study of this relation.

Acknowledgement

This work was supported by RFBR grants 00-15-96553, 00-02-16471, 01-02-27244 and "University of Russia". NK is grateful to SOC and LOC for the possibility to participate in this meeting.

References

Borisov, G. V. 1992, *A& Ap*, **261,** 154.
Cherepashchuk, A. M. *et al.* 1996, *Highly Evolved Close Binary Stars.* Catalog./ (ed) A. M. Cherepashchuk (Brussel: Gordon & Breach Science Publ.)
Katysheva N. A. *et al.* 2001, *Kinem. Physics Celect. Bodies, Suppl.* **3,** 393.
Parenago, P. P. 1946, *Perem. Zvezdy* (Variable Stars), **6,** 26.
Pavlenko, E. P., Shugarov, S. Yu. 1998, *As. Ap. Trans.* **15,** 89.
Pavlenko, E. P., Shugarov, S. Yu. 1999, *A & Ap*, **343,** 909.
Schneider, D. P. *et al.* 1981, *ApJ*, **245,** 644.
Skillman, D. R. *et al.* 1995, *PASP*, **107,** 545.
Stolz, B., Schoembs, R. 1984, *A& Ap*, **132,** 187.

J. Astrophys. Astr. (2002) **23,** 19–22

High Energy Phenomena in Eta Carinae

Roberto F. Viotti[1], Lucio Angelo Antonelli[2], Sonja Rebecchi[3] & Corinne Rossi[4]

[1]*Istituto di Astrofisica Spaziale, CNR, 00133 Roma, Italy.*
e-mail: uvspace@ias.rm.cnr.it
[2]*Osservatorio Astronomico di Roma, 00040 Monte Porzio, Italy.*
[3]*ASI Science Data Centre, ESA-ESRIN, 00044 Frascati, Italy.*
[4]*Dipartimento di Fisica, Università La Sapienza, 00185 Roma, Italy.*

Abstract. We have investigated with BeppoSAX the long term behaviour of the harder X-ray component of the supposed supermassive binary system η Car along its 5.52 year cycle. We have found that in March 1998 during egress from the last December 1997 eclipse, this component was the same as outside eclipse, but for a large ($\times$3.5) increase of NH_h, that can be attributed to the presence or formation of opaque matter in front of the source near periastron. Unexpectedly, at that time the iron 6.7 keV emission line was 40% stronger. BeppoSAX has for the first time found a *hard X-ray tail* extending to at least 50 keV, that cannot be adequately fitted with an additional hotter thermal component. The 2–100 keV spectrum of η Car is instead well fitted with an absorbed powerlaw spectrum with photon index 2.53, suggesting non-thermal emission as an alternative model for the core source.

Key words. Colliding winds model—non-thermal emission—stars: η Car—X-ray emission.

1. The η Car phenomenon

The X-ray spectrum of the superluminous star η Car and its time variability is providing a fundamental key for understanding the emission mechanisms in very massive stars, and for unveiling the physical nature of η Car itself. The star shows a complex X-ray spectrum consisting of at least two distinct components:

- a spatially extended softer ($\sim$0.5 keV) thermal source ηSX associated with the nebulosities surrounding the star, and
- a very bright point-like harder component ηHX with kT_h $\sim$4.7 keV centred on the stellar core, that dominates the spectrum in the 2–10 keV range (e.g., Tsuboi *et al.* 1997; Corcoran *et al.* 1998, Viotti *et al.* 1998, 2002).

The thermal ηHX component is commonly interpreted with colliding wind emission in a close binary system. The model is based on Damineli's (1996) discovery of a 5.52 year periodicity in the recurrent deep excitation minima of the optical emission line spectrum. Later, Damineli *et al.* (1997) attributed this variability to a highly eccentric orbital motion of two very massive stars, the primary being an S Doradus variable (or LBV) that has a 600–1200 km s^{-1} very massive wind. Its unseen companion should be a less evolved early-type star. It was found that the two last spectroscopic minima of June 1992 and December 1997 coincided with two X-ray eclipses detected by ROSAT, ASCA, and RossiXTE (Corcoran *et al.* 1995; Ishibashi *et al.* 1999: Corcoran *et al.* 2000). According to Augusto Damineli, the next spectroscopic event (and, consequently, the next X-ray eclipse) will occur in June 2003.

BeppoSAX observed η Car in four different phases of its 5.52 year spectroscopic cycle (Φ=0.828, 1.048, 1.371 and 1.457). We have found that the X-ray temperature (4.7 keV) and the unabsorbed luminosity ($\sim 1 \times 10^{-10}$ erg cm^{-2} s^{-1}) of the 2–10 keV component, supposed to be thermal, were nearly the same, but for a large ($\times 3.5$) increase of NH_h in March 1998 during egress from the last December 1997 eclipse (Fig. 1(a)). This effect was accompained by the presence in the optical spectrum of extended P Cygni absorptions (Viotti *et al.* 2002). We have also noted that after the December 1997 minimum, the recovering in the optical spectrum was slower than in X-rays.

2. The 6.7 keV iron line

A contrasting aspect of the BeppoSAX observations is the larger flux (and equivalent width) of the 6.7 keV emission line in March 1998 when the star was still in its low spectroscopic state, while in the other three epochs this line had the same strength within the errors (Rebecchi *et al.* 2001; Figure 1). At that time the nearby continuum flux was equal to that measured by BeppoSAX in December 1996, and in January and June 2000. This result seems to be pointing out to a formation region different from that of the continuum. If so, the iron abundances derived from the standard analysis procedure should be taken as upper limits.

3. The BeppoSAX high energy tail

BeppoSAX has for the first time detected η Car above 10 keV, a nd found that the flux is in excess with respect to the 4.7 keV thermal fit of the 2–10 keV intermediate energy spectrum (Rebecchi *et al.* 2001, Viotti *et al.* 2002). The last well exposed BeppoSAX observations of June 2000 not only confirmed the high energy tail in the X-ray spectrum of η Car, but also revealed that it extends to at least 50 keV (Fig. 1(b)). We were however unable to adequately fit the high energy excess with an additional hotter thermal component. The overall spectrum can instead be well described by an absorbed power law spectrum with photon index 2.53 ± 0.03, typical of a non thermal source. Alternatively, one might consider that the point source has a large temperature stratification. In this regard, we recall that the most recent CHANDRA observations have also suggested that the hot gas near η Car is not isothermal (Corcoran *et al.* 2001).

A further interesting feature is the possible weakening of the high energy tail in March 1998, when no PDS countrate above the background was detected (Rebecchi *et al.* 2001).

We remind that no present or planned future satellite will be able to observe η Car above 10 keV with the BeppoSAX sensitivity. In particular, η Car will be probably rather weak for INTEGRAL, though we expect a positive detection above 100 keV. Hence, BeppoSAX has been a unique opportunity to observe this source in this most crucial energy range.

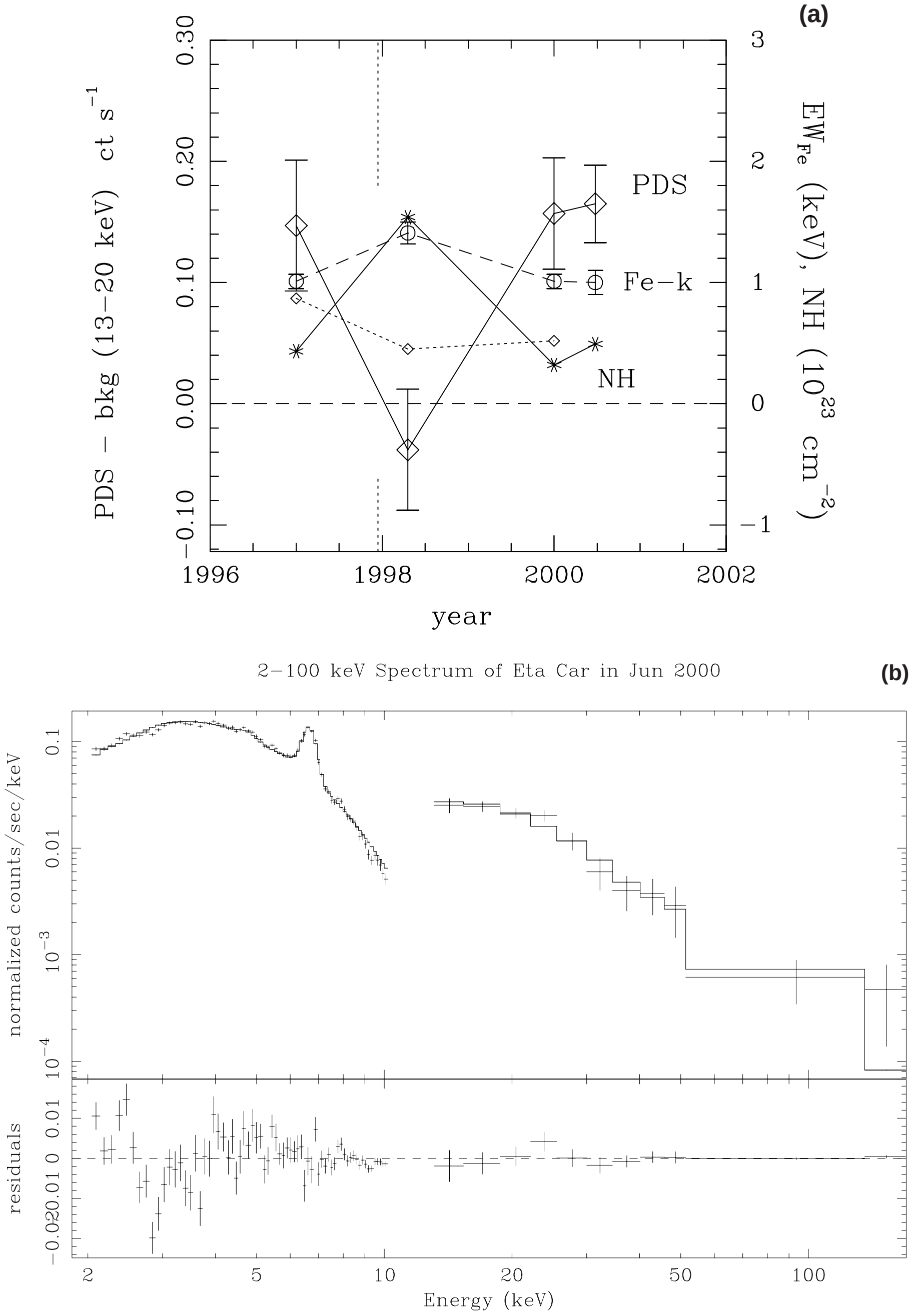

Figure 1. BeppoSAX observations of η Car. **(a)** Time variation of the 13–20 keV countrate (PDS, s^{-1}), the 6.7 keV–line equivalent width (in keV, dashed line), and the H I column density (in 10^{23} cm^{-2}) during the four BeppoSAX observations. The expected PDS countrate extrapolated from the 4.7 keV intermediate energy spectrum is shown for comparison (dotted line). The vertical lines mark the December 1997 minimum. **(b)** The 2–100 keV (MECS+PDS) countrates in June 2000 fitted with a powerlaw (ν=2.53).

4. A zero-order interpretation

In principle, the high temperature of the core X-ray emission of η Car can be explained by winds' collision from two gravitationally bounded stars – one being an early-type massive star with a high velocity wind, and the other one an S Doradus-type variable (or LBV) with a 600–1200 km s^{-1} very massive wind (Viotti *et al.* 1989). The model would imply a gradual increase of the X-ray flux when the stars approach periastron, which however is only marginally supported by the RossiXTE observations. One needs to introduce an additional process to explain the X-ray flux minimum, e.g., a large absorption by matter present around the stars near periastron. The peculiar behaviour of the iron line observed by the ASCA and BeppoSAX observations near the 1997–1998 eclipse, and the future observations of the next June 2003 eclipse may solve the problem with the use of a more detailed model, also based on the observations in other frequency bands.

Even more intriguing are the results of the BeppoSAX 10–100 keV observations of η Car, that seem to disprove the thermal emission model currently proposed for the 2–10 keV spectrum (which actually is the hard energy band covered by most of the X-ray satellites that have pointed η Car). In this regard, a crucial test should be provided by the future INTEGRAL observations, which will be, or will not be able to trace the spectrum of η Car beyond 100 keV, and to look whether the power spectrum extends to higher energies. At any rate, the constancy of the 10–20 keV flux during three different phases of the 5.52 years cycle is difficult to reconcile with current colliding-wind models. Multifrequency observations of the next event of June 2003 will be of the highest scientific interest.

References

Corcoran, M. F. *et al.* 1995, *Ap. J.*, **445,** L121.
Corcoran, M. F. *et al.* 1998, *Ap. J.*, **494,** 381.
Corcoran, M. F. *et al.* 2000, *Ap. J.*, **545,** 420.
Corcoran, M. F. *et al.* 2001, *Ap. J.*, **562,** 1031.
Damineli, A., 1996, *Ap. J.*, **460,** L49.
Damineli, A. *et al.* 1997, *New Astronomy*, **2,** 107.
Ishibashi, K. *et al.* 1999, *Ap. J.*, **524,** 983.
Rebecchi, S. *et al.* 2001, in *X-Ray Astronomy 2000, ASP Conf. Ser.*, Vol. **234,** (in press).
Tsuboi, Y. *et al.* 1979, *PASJ*, **49,** 85.
Viotti, R. *et al.* 1989, *Ap. J. S.* **71,** 983.
Viotti, R. *et al.* 1998, *Nucl. Phys. B* (Proc. Suppl.), 69/1-3, 36.
Viotti, R. F. *et al.* 2002, *A & A* **385,** 874.

J. Astrophys. Astr. (2002) **23,** 23–26

Upper Limits on O VI Emission from *Voyager* Observations

Jayant Murthy *Indian Institute of Astrophysics, Koramangala, Bangalore 560 034, India*

Abstract. We have examined 426 *Voyager* fields distributed across the sky for O VI ($\lambda\lambda$ 1032/1038 Å) emission from the Galactic diffuse interstellar medium. No such emission was detected in any of our observed fields. Our most constraining limit was a 90% confidence upper limit of 2600 photons cm^{-2} sr^{-1} s^{-1} on the doublet emission in the direction (l, b) = (117.3, 50.6). Combining this with an absorption line measurement in nearly the same direction allows us to place an upper limit of 0.01 cm^{-3} on the electron density of the hot gas in this direction. We have placed 90% confidence upper limits of less than or equal to 10,000 photons cm^{-2} sr^{-1} s^{-1} on the O VI emission in 16 of our 426 observations.

Key words. Galaxy: halo ISM: general.

1. Introduction

There have been many detections of ultraviolet resonance line absorption by highly ionized, presumably hot, gas in the Galactic halo (e.g., Sembach & Savage 1992; Hurwitz & Bowyer 1996), but only three claimed detections of ultraviolet resonance line emission from this gas (see Murthy *et al.* 2001 for a full discussion and references). In this work, we will discuss limits, from the *Voyager* data set described by Murthy *et al.* 2001, on O VI (1032/1038 Å) line emission from the ISM. Although new instruments are now providing important results, the *Voyager* data are still the only source of information on the O VI emission over many different lines of sight.

2. Observations and data analysis

The two *Voyager* spacecrafts were launched in 1977 and have taken FUV (500–1700 Å) spectra of astronomical objects ever since. Each spacecraft includes a Wadsworth-mounted objective grating spectrometer (UVS) with a field of view of $0^{\circ}\!.1 \times 0^{\circ}\!.87$ and a spectral resolution of 38 Å for aperture filling diffuse sources. A full description of the UVS instruments and the *Voyager* mission is given by Holberg & Watkins (1992).

The data processing is described in Murthy *et al.* (1999) and resulted in 426 observations of the diffuse background which we have now examined for the presence of O VI emission. The O VI doublet ($\lambda\lambda$ 1032/1038 Å) is clearly visible in the *Voyager* spectra of bright sources such as supernovae remnants (Blair *et al.* 1995) and the Eridanus superbubble (Murthy *et al.* 1993), where the doublet is much brighter than the heliospheric hydrogen Ly β (λ 1026 Å) emission on whose wings it lies. However, the O VI emission from the diffuse halo gas is much less than the Ly β emission and we were forced to model the heliospheric emission.

Fortunately, because the Lyman lines are optically thick, the Ly β/Ly α ratio is constant throughout the heliosphere and we can use the Ly α line to scale the Ly β line. We determined the ratio between the two lines using UVS observations in which only the heliospheric lines were present and then used this empirical ratio to scale the Ly β line in each observation (see Murthy *et al.* 1999) for a full description of this procedure). We subtracted this scaled Ly β intensity from the observed spectrum and determined the O VI upper limit from the remainder.

3. Results and discussion

We detect no O VI emission in any of 426 UVS observations of the diffuse radiation field but do set upper limits on such emission in each direction. The best of these limits is 2600 photons cm^{-2} sr^{-1} s^{-1} (5.0×10^{-8} ergs cm^{-2} sr^{-1} s^{-1}) in the O VI resonance line doublet in the direction (l, b) = (117.3, 50.6). This direction is quite close to HD 121800 (l, b = 113.0, 49.8 , spectral type B1.5 V, distance = 2.2 kpc) towards which Hurwitz & Bowyer (1996) obtained a O VI column density of 1.1×10^{14} cm^{-2} using ORFEUS. Using these values and equation (5) of Shull & Slavin (1994), and confining the temperature range to that for which the fraction of oxygen atoms in the O VI state is within 10% of its maximum value in collisional ionization equilibrium plasma (T = $2.2 - 6.4 \times 10^5$ K—Shapiro & Moore 1977), we find an upper limit on the electron density of less than 0.010 cm^{-3}. Assuming that the emitting gas has a solar abundance of helium atoms and that the hydrogen and helium are fully ionized, there will be 1.9 particles per electron and thus the thermal pressure will be less than 12,000 K cm^{-3}, close to the thermal pressure of 15,000 K cm^{-3} in the Local Bubble derived by Snowden *et al.* (1998) from observations of the 1/4 keV soft X-ray flux seen by ROSAT.

The 94 locations in which we set 90% confidence upper limits of better than 5×10^{-7} ergs cm^{-2} sr^{-1} s^{-1} (25,000 photons cm^{-2} sr^{-1} s^{-1}) are plotted in Fig. 1 and those in which we set limits of better than 2×10^{-7} ergs cm^{-2} sr^{-1} s^{-1} ($\approx$ 10,000 photons cm^{-2} sr^{-1} s^{-1}) are listed in Table 1. Several of our observations are near the locations observed by Dixon *et al.* (1996) using HUT and we both set similar upper limits in those (with our *Voyager* limits in general being more constraining). Only in their Target 3 (UGC 5675; l = 218.2, b = 56.4) do we obtain inconsistent results, with Dixon *et al.* (1996) quoting a flux of 23,000 $\pm$ 6000 photons cm^{-2} sr^{-1} s^{-1} while we place a 90% upper limit of 10^4 photons cm^{-2} sr^{-1} s^{-1}at (l, b) = (216.8, 55.3) — about 1° away. Of course, it is entirely possible that there are truly spatial variations of this scale in the ISM.

We also have several observations near the four high latitude locations where Martin & Bowyer (1990) detected C IV emission but in none can we do more than say that the O VI/C IV ratio is not inconsistent with the theoretical ratios reported in the literature (eg. Shelton *et al.* 2001 and references therein).

4. Conclusion

Very recent results concerning galactic diffuse O VI emission include the *FUSE* detections by Shelton *et al.* (2001) and Dixon *et al.* (2001) at a level of 5000 photons cm^{-2} sr^{-1} s^{-1} and the *MINISAT-01* all-sky upper limit of 1200 photons cm^{-2} sr^{-1} s^{-1} by Edelstein *et al.* (1999). Combined with the present *Voyager* upper limits, it appears

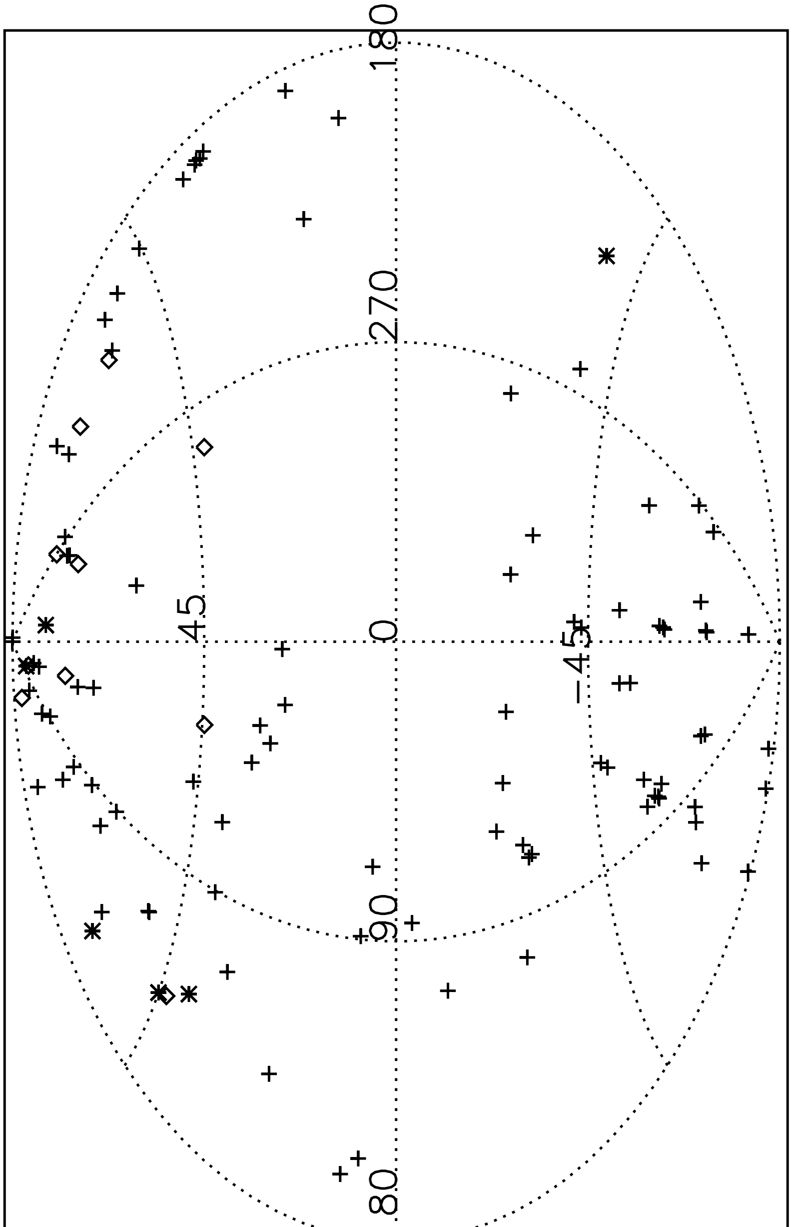

Figure 1. All of the *Voyager* observations in which we were able to set upper limits of less than 5×10^{-7} ergs cm^{-2} sr^{-1} s^{-1} (25,000 photons cm^{-2} sr^{-1} s^{-1}) are plotted as plus signs on an Aitoff map of the sky with the origin at the center and 180° at the left. The Dixon *et al.* (1996) targets are plotted as diamonds and the C IV detections of Martin & Bowyer (1990) are plotted as asterisks. In one direction in common (see text), we place a 90% confidence limit that is about half the claimed detection by Dixon *et al.*; however, given both sets of uncertainties and the different locations, we cannot rule out their claimed value.

Table 1. Best *Voyager* O VI Upper Limits: 90% Confidence Upper Limit on O VI Emission.

l degrees	b degrees	Flux photons cm^{-2} sr^{-1} s^{-1}
117.3	50.6	2,600
272.5	−67.4	4,100
67.8	5.2	5,700
60.3	−22.5	6,500
117.3	50.8	6,700
200.7	9.6	7,000
71.6	−59.6	7,400
189.6	32.3	8,600
91.1	61.4	8,700
115.7	72.6	9,000
32	70.5	9,100
331.7	60.5	9,200
99.3	80.3	9,500
225.7	68.3	9,900
190	33.3	10,000
216.8	55.3	10,000
346.6	−52.3	11,000

that much of the sky has an O VI emission of significantly less than 10,000 photons cm^{-2} sr^{-1} s^{-1}. Only the 4 HUT detections of Dixon *et al.* (1996) show higher fluxes. A mission dedicated to the observation and mapping of faint line emission from the Galactic halo would surely yield bountiful results.

References

Blair, W. P., Vancura, O., Knox, K. S. 1995, *A. J.*, **110,** 312.
Dixon, W. V., Davidsen, A. F., Ferguson, H. C. 1996, *Ap. J.*, **465,** 288.
Dixon, W. V., Sallmen, S., Hurwitz, M., Lieu, R. 2001, *Ap. J.*, **552,** L69.
Edelstein, J., Bowyer, C. S., Korpela, E., Lampton, M., Trapero, J., Gomez, J. F., Morales, C., Orozco, V. 1999, *American Astronomical Society Meeting*, **195,** 5302.
Holberg, J. B., Watkins, R. 1992, *Voyager Ultraviolet Spectrometer Guest Observer and Data Analysis Handbook*, Version 1.1
Hurwitz, M., Bowyer, S. 1996, *Ap. J.*, **465,** 296.
Martin, C., Bowyer, S. 1990, *Ap. J.*, **350,** 242.
Murthy, J., Im, M., Henry, R. C., Holberg, J. B. 1993, *Ap. J.*, **419,** 739.
Murthy, J., Hall, D. T., Earl, M., Henry, R. C., Holberg, J. B. 1999, *Ap. J.*, **522,** 904.
Murthy, J., Henry, R. C., Shelton, R. L., Holberg, J. B. 2001, *Ap. J. L.*, **557,** 47L.
Sembach, K. R., Savage, B. D. 1992, *Ap. J. S.*, **83,** 147.
Shapiro, P. R., Moore, R. T. 1977, *Ap. J.*, **217,** 621.
Shelton, R. L. *et al.* 2001, *Ap. J.*, **560,** 730.
Shull, J. M., Slavin, J. 1994, *Ap. J.*, **427,** 784.
Snowden, S. L., Egger, R., Finkbeiner, D. P., Freyberg, M. J., Plucinsky, P. P. 1998, *Ap. J.*, **493,** 715.

J. Astrophys. Astr. (2002) **23,** 27–31

Spectral Properties of the X-ray Binary Pulsar LMC X-4 during Different Intensity States

S. Naik & B. Paul *Tata Institute of Fundamental Research, Mumbai, 400 005, India.*

Abstract. We present spectral variations of the binary X-ray pulsar LMC X-4 observed with the RXTE/PCA during different phases of its 30.5 day long third period. Only out-of-eclipse data were used for this study. The 3–25 keV spectrum, modeled with high energy cut-off power-law and iron line emission is found to show strong dependence on the intensity state. Correlations between the Fe line emission flux and different parameters of the continuum are presented here.

Key words. Stars: individual: LMC X-4—stars: neutron—X-rays: stars.

1. Introduction

LMC X-4 is an eclipsing high-mass disk-fed accretion-powered binary X-ray pulsar in the Large Magellanic Cloud. A spin period of 13.5 s was discovered in LMC X-4 by Kelley *et al.* (1983) and X-ray eclipses with a 1.4 day recurring period was discovered by Li *et al.* (1978) and White (1978). The X-ray intensity varies by a factor of ~ 60 between high and low states with a periodic cycle time of 30.5 day (Lang *et al.* 1981; Paul & Kitamoto 2002). Flux modulation at super-orbital period in LMC X-4 is believed to be due to blockage of the direct X-ray beam by its precessing tilted accretion disk, as in the archetypal system Her X-1. Flaring events of duration ranging from $\sim$ 20s to 45 minutes (Levine *et al.* 1991 and references therein) are seen about once in a day during which the source intensity increases by factors up to ~ 20.

Broad band spectroscopy using GINGA and ROSAT data shows that the continuum can be modeled with a high energy cut-off power-law (Woo *et al.* 1996). The spectrum also shows a soft excess and a broad iron emission line. The soft excess detected with ROSAT was modeled as a combination of thermal bremsstrahlung and very soft black-body by Woo *et al.* (1996), while the same observed with Beppo-SAX (La Barbera *et al.* 2001) was modeled as black-body emission from accretion disk at magnetospheric radius Comptonized by moderately hot electrons. La Barbera *et al.* (2001) also reported the presence of a cyclotron absorption line at $\sim$ 100 keV.

In this paper we present the spectral variations of LMC X-4 during the 30.5 day long period using the archival data from RXTE observations.

2. Observation, analysis and results

To study the super-orbital phase dependence of various spectral parameters, we have analyzed 43 RXTE/PCA observations of LMC X-4 at different phases of the 30.5 day third period. The data used for analysis are out-of-eclipse and free from the flaring state. Energy spectra in 129 channels were generated from the Standard 2 mode PCA data. The standard procedures for data selection, and response matrix generation were followed. Background estimation was done using both bright and faint models of RXTE/PCA according to different intensity states of the source at different phases. We restricted our analysis to 3–25 keV energy range. Data from all five PCUs are added together. We have fitted the energy spectrum of the source using a model consisting of blackbody, power law and a high energy cutoff as model components. We have included a Gaussian line near the expected K_α emission from iron and absorption edge due to iron. The value of equivalent hydrogen column density N_H was set to have a lower threshold of $0.055 \times 10^{22} \mathrm{cm}^{-2}$ which is the Galactic column density towards this source. The blackbody temperature was kept fixed at $kT = 0.2$ keV, while the center and width of the iron emission line was fixed at 6.4 keV and 0.65 keV respectively with free normalization. The variation in 3–25 keV source flux during the RXTE/PCA observations are shown in the left panel of Fig. 1 whereas the right panel of Fig. 1 shows the energy spectrum for one of the observations at high intensity state. The variation of iron line flux and iron equivalent width with the source flux in 7–25 keV energy range are shown in the left and right panels of Fig. 2 respectively.

The results obtained from this work are summarized as follows.

- The iron emission line flux is found to be directly correlated with the source flux in 7–25 keV energy range.
- The source spectrum is found to be flat with power-law photon index in the range 0.5–0.7 during low intensity state (source flux $\leq 3 \times 10^{-10}$ ergs cm^{-2} s^{-1} at 3–25 keV energy range) whereas during high intensity state, the spectrum is steep with power-law photon index in the range 0.7–0.9.
- Equivalent width of the iron emission line is found to be highly variable in the range 0.25–1.1 keV during low intensity state (source flux $\leq 2 \times 10^{-10}$ ergs cm^{-2} s^{-1} in 7–25 keV energy range), whereas it remains almost constant (0.2–0.35 keV)

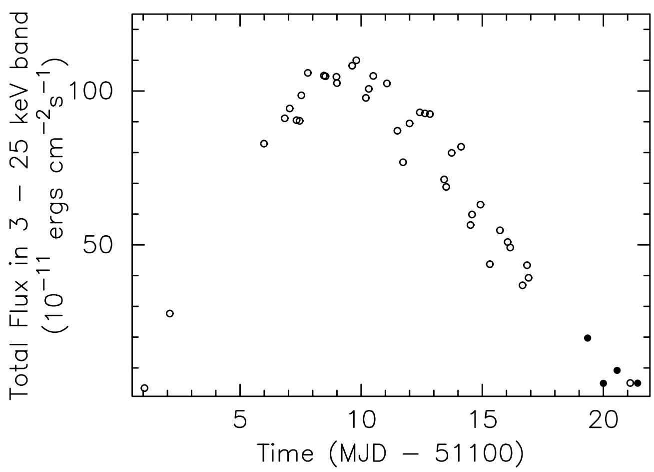

Figure 1(a). Average background-subtracted X-ray flux in 3 - 25 keV energy range obtained from the RXTE/PCA observations of LMC X-4 in 1998. The points marked by "•" are for the observations which were made outside the selected time range and have been included here based on the phase of the super-orbital period. These observations are used to get a better coverage of low intensity state.

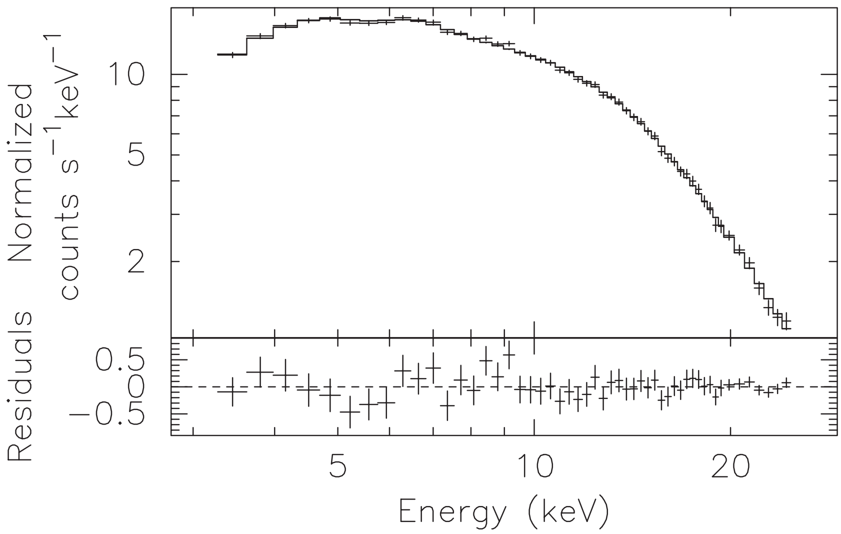

Figure 1(b). The figure shows the observed count rate spectrum of LMC X-4 on 1998 October 22nd. The best fit model consists of a blackbody (kT = 0.2 keV), a power law and a high energy cutoff. The iron emission line was kept fixed at 6.4 keV with width of 0.65 keV.

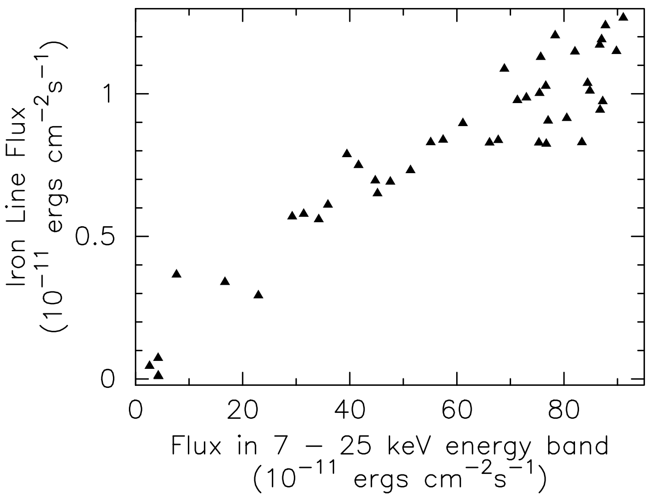

Figure 2(a). The figure shows the variation in iron line flux with the source flux in $7-25$ keV energy band.

during the high intensity state with source flux $\geq 2 \times 10^{-10}$ ergs cm^{-2} s^{-1} in 7–25 keV energy range.

3. Discussion

According to the results of the present work, it is observed that iron intensity correlates very well with the continuum intensity in 7–25 keV energy range. The equivalent width

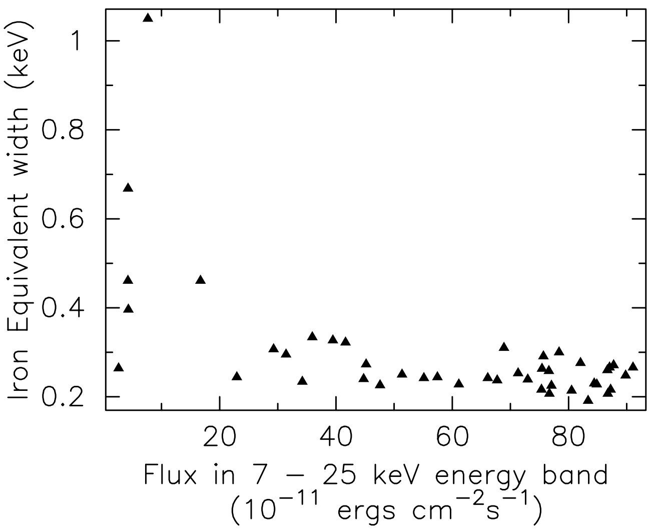

Figure 2(b). The variation in equivalent width of the iron emission line with the source flux in 7–25 keV energy range is shown. It is observed that the iron equivalent width is high when the source flux is low.

of the iron emission line is very high at low luminosity. Similar thing was found in Vela X-1 (Becker *et al.* 1979; White *et al.* 1983). In Vela X-1, it can be due to increase in absorption caused by the stellar wind of the primary.

Nagase *et al.* (1986) studied the change in equivalent widths of iron emission line against the column density of matter in the line of sight for Vela X-1. Similar studies were done for GX 301-2 by Makino *et al.* (1985) and for Her X-1 by Makishima (1986). These results suggest that the column density averaged over the whole direction does not change appreciably, whereas the absorption column density along the line of sight changes drastically with time and orbital phase. Inoue (1985) and Makishima (1986) estimated the equivalent widths of the fluorescence iron line emission from neutral matter in a sphere surrounding the X-ray source using a power law type incident spectrum. They found that, if the matter is located between the X-ray source and the observer, the continuum spectrum is absorbed by the matter resulting in increasing the equivalent width monotonically with the column density as observed in GX 301-2 (Makino *et al.* 1985). However, when the X-ray source is hidden by some thick material, the equivalent width remains almost constant ($\sim$ 1 keV) (as observed from Vela X-1 during the eclipse; Nagase *et al.* 1984). In case of accretion powered X-ray pulsars, if the compact object is hidden from direct view by the accretion disk and only X-rays scattered into the line of sight by an accretion disk corona or wind are visible, the iron equivalent width can be higher. This may explain the higher value of iron equivalent width during the low intensity states of LMC X-4.

4. Acknowledgement

The work of SN is partially supported by the Kanwal Rekhi Scholarship of the TIFR Endowment Fund. This research has made use of data obtained through the High

Energy Astrophysics Science Archive Research Center Online Service, provided by the NASA/Goddard Space Flight Center.

References

La Barbera, A., Burderi, L., Di Salvo, T., *et al.* 2001, *ApJ*, **553,** 375.
Becker, R. H., Boldt, E. A., Holt, S. S., *et al.* 1979, *ApJ*, **227,** L21.
Inoue, H. 1985, *Space Sci. Rev.*, **40,** 317.
Kelley, R. L., Jernigan, J. G., Levine, A., *et al.* 1983, *ApJ*, **264,** 568.
Lang, F. L., *et al.* 1981, *ApJ*, **246,** L21.
Levine, A., Rappaport, S., Putney, A., *et al.* 1991, *ApJ*, **381,** 101.
Li, F., Rappaport, S., Epstein, A. 1978, *Nature*, **271,** 37.
Makino, F., Leahy, D. A., Kawai, N. 1985, *Space Sci. Rev.*, **40,** 421.
Makishima, K. 1986, in *The Physics of Accretion onto Compact Objects*, (ed.) K. O. Mason, M. G. Watson & N. E. White, p. 249.
Nagase, F., Hayakawa, S., Tsuneo, S., *et al.* 1984, *PASJ*, **36,** 667.
Nagase, F., Hayakawa, S., Sato, N., *et al.* 1986, *PASJ*, **38,** 547.
Paul, B., Kitamoto, S. 2002, (this issue).
White, N. E. 1978, *Nature*, **271,** 38.
White, N. E., Swank, J. H., Holt, S. S. 1983, *ApJ*, **270,** 711.
Woo, J. W., Clark, G. W., Levine, A. M., *et al.* 1996, *ApJ*, **467,** 811.

J. Astrophys. Astr. (2002) **23,** 33–38

Superorbital Period Variations in the X-ray Pulsar LMC X-4

B. Paul[1] & S. Kitamoto[2]

[1]*Tata Institute of Fundamental Research, Homi Bhabha Road, Colaba, Mumbai, 400 005, India.*
[2]*Department of Physics, Rikkyo University, Nishii-Ikebukuro, 3-34-1, Toshima-ku, Tokyo, 171-8501, Japan.*

Abstract. We report the discovery of a decay in the superorbital period of the binary X-ray pulsar LMC X-4. Combining archival data and published long term X-ray light curves, we have found a decay in the third period in this system ($P \sim 30.3$ day, $\dot{P} \sim -2 \times 10^{-5}$ s s^{-1}). Along with this result, a comparison of the superorbital intensity variations in LMC X-4, Her X-1 and SMC X-1 is also presented.

Key words. Accretion, accretion disks—stars: individual (LMC X-4)—stars: neutron—X-rays: stars, binaries.

1. Introduction

Apart from the binary period, long-term periodic intensity variations are known to be present in many X-ray binaries. There are four X-ray binaries in which the presence of long periods is very well established. These are

(1) Her X-1 (a 1.7 d binary with a 35 d long third period, Giacconi *et al.* 1973),
(2) LMC X-4, (1.4 d and 30.5 d, Lang *et al.* 1981),
(3) SMC X-1, (3.9 d and 60 d, Wojdowski *et al.* 1998) and
(4) SS433, (13.1 d and 164 d, Margon 1984).

The first three of these, Her X-1, LMC X-4 and SMC X-1 are also accreting X-ray pulsars with pulse periods of 1.24, 13.5 and 0.75 s respectively. Superorbital periods in Her X-1, LMC X-4, and SS 433 are most stable and are believed to be produced by the precession of the accretion disks. The mechanisms proposed to cause the precession of the disks are

(1) forced precession of a tilted disk by the gravitational field of the companion star (Katz 1973) and
(2) precession of a disk that is slaved to a misaligned companion star (Roberts 1974).

Some excursions in the superorbital periods are known to be present in Her X-1 (Ögelman 1985) and SS 433 (Margon 1984). We report here detection of the same in LMC X-4.

2. Analysis and results

2.1 *Period analysis*

The superorbital period of LMC X-4 was discovered by Lang *et al.* (1981) using the HEAO-A1 scanning modulation colimator. They reported a period of 30.48 ± 0.06 day and the time of arrival of the rising edge was 2443371.0 ± 1.0 (JD). We have used the long term light curves of LMC X-4 obtained with the All Sky Monitors (ASM) of the GINGA and RXTE satellites and applied the Lomb and Scargle method to search for periodicities. The GINGA-ASM light curve resulted in a superorbital period of 30.17 $\pm$ 0.08 day with the time of arrival of the rising edge 2446836.0 ± 2.0 (JD) while the same obtained with the RXTE-ASM are 30.296 ± 0.014 day and 2450070.0 ± 1.0 (JD) respectively. The superorbital intensity variation profiles obtained by folding the light curves at the respective long periods are shown in Fig. 1.

The superorbital period of LMC X-4 obtained with GINGA-ASM and RXTE-ASM light curves is smaller than that obtained from the HEAO-A1 observations. The decrease in superorbital period over this time span corresponds to a period derivative of $-1.8 \pm 0.8 \times 10^{-5}$ s s^{-1} or a decoherence time scale of $\sim$ 20 years. The RXTE-ASM observations span about five years, which may cause considerable decoherence in the superorbital phase. We have, therefore, carried out a more detailed pulsation analysis allowing for a period derivative. The pulse folding and χ^2 maximising method was applied with a period derivative, and the same was done for 400 different period derivatives. From each trial, the maximum χ^2 and the corresponding long period was selected. The resulting distribution of maximum χ^2 against the respective period derivatives is shown in the left panel of Fig. 2. The maximum of this χ^2 distribution occurs corresponding to a period derivative of $-2.1 \pm 0.1 \times 10^{-5}$ s s^{-1}, obtained by fitting a gaussian profile near the maximum (shown in the inset). This is similar to the long term derivative of the superorbital period obtained by fitting a straight line to the three periods described above.

2.2 *Arrival time analysis*

Arrival time of the rising edge of the superorbital intensity variation is available for HEAO-A1 (Lang *et al.* 1981). We therefore determined the same from the GINGA-ASM and RXTE-ASM light curves. LMC X-4 was observed many times with the Medium Energy (ME) detectors of EXOSAT. Though the combined EXOSAT-ME light curves cannot be used for an independent determination of the superorbital period, we have determined the arrival time (2445620.0 ± 3.0 JD) by folding the light curve. The superorbital periods obtained from the HEAO-A1, GINGA-ASM and RXTE-ASM at the respective epochs were fitted with a straight line and an approximate value for the same during the EXOSAT-ME observations was calculated by interpolation. The EXOSAT-ME light curve has poor coverage in the rising part of the light curve (see right panel of Fig. 1), and therefore we associate a larger error with this arrival time. There is some ambiguity in the number of cycles between the GINGA and RXTE observations. Two superorbital phase connected solutions are obtained with different number of cycles between the GINGA and RXTE data. Residuals of the arrival times after fitting a straight line to these solutions are shown in Fig. 2(b) with data points marked as squares and circles respectively. The first solution has small residuals, but

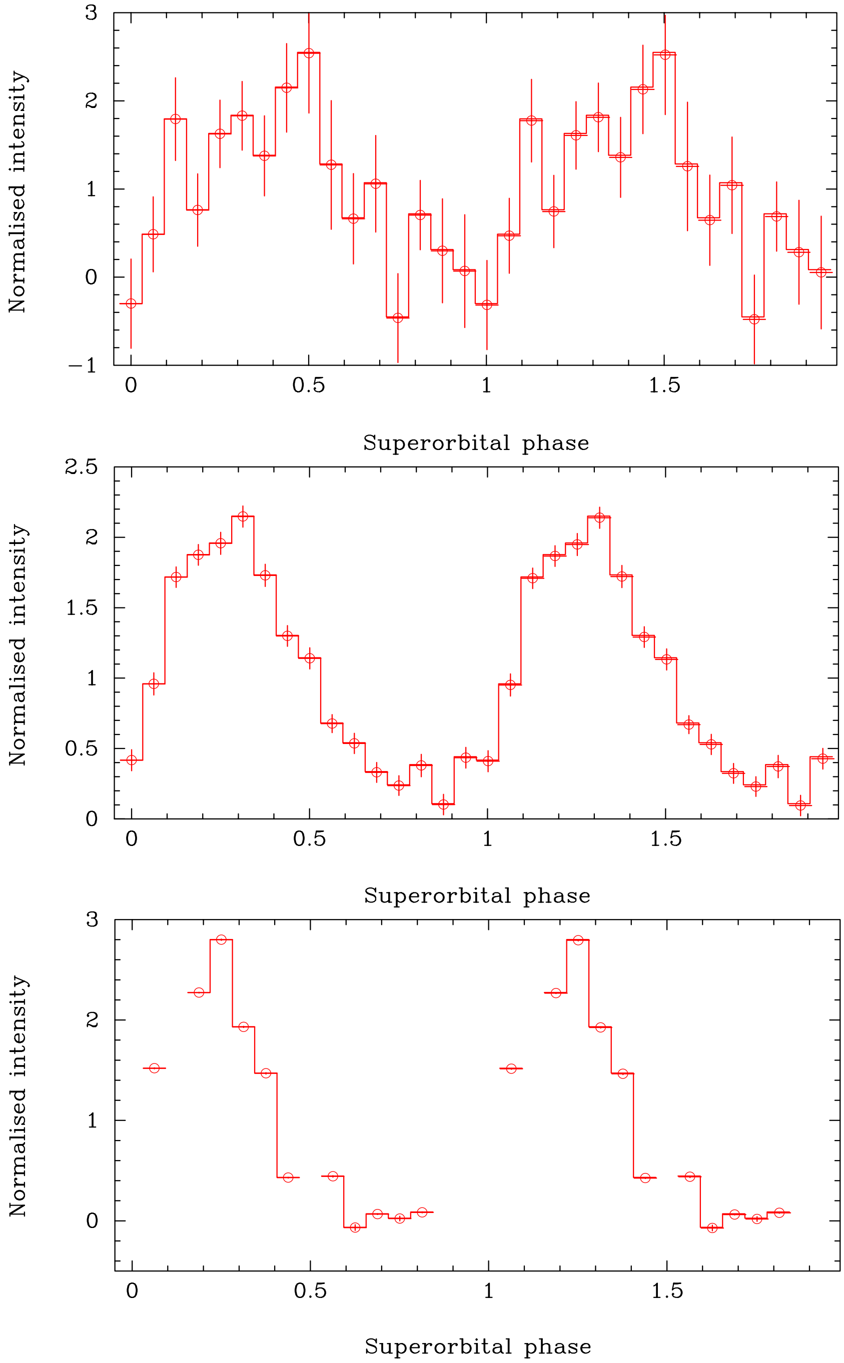

Figure 1. The profiles of superorbital intensity variations of LMC X-4 obtained from GINGA-ASM, RXTE-ASM and EXOSAT-ME light curves are shown from top to bottom. See text for details about the superorbital periods obtained/adopted for each data set.

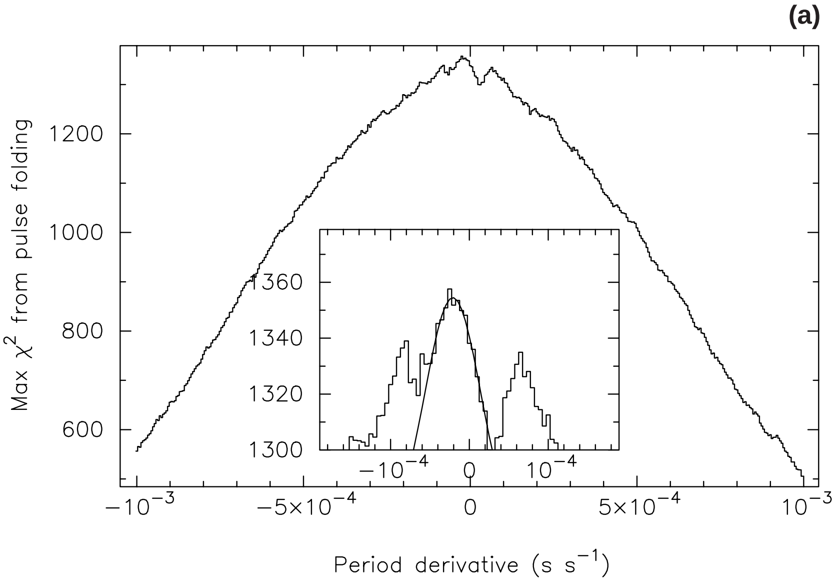

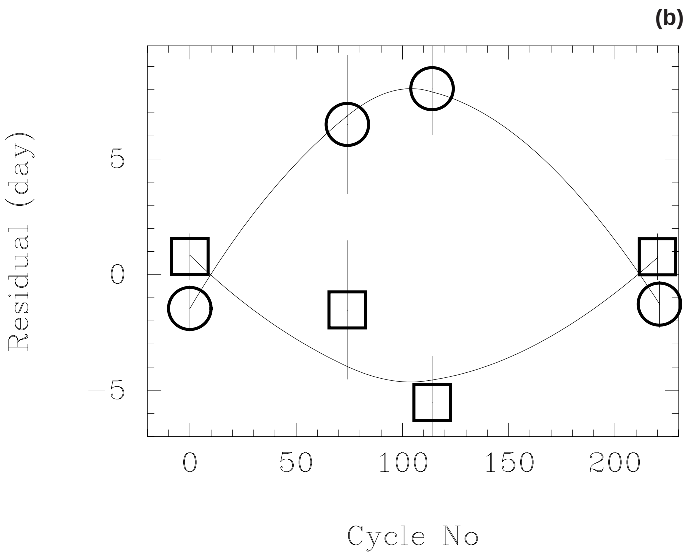

Figure 2. **(a)** The distribution of maximum χ^2 against the respective period derivatives obtained from the RXTE-ASM light curve is shown here. See text for details. The best fit gaussian profile near the maximum is shown in the inset. **(b)** Residuals of the arrival times after fitting a straight line to the arrival time data. An ambiguity in the number of cycles between the GINGA and RXTE observations results in two solutions presented with circles and stars in this figure. The lines represent the best fit quadratic solutions to the arrival time data.

the present superorbital period is required to be 30.45 day, which can be ruled out from RXTE-ASM data alone. The second solution requires a period of 30.31 d, close to the value obtained with the RXTE-ASM light curve. The second solution gives large residuals for the GINGA and EXOSAT arrival times. To account for the residuals, we introduced a period derivative and fitted a quadratic function to the arrival times.

With this, the two solutions require initial periods of 30.35 day and 30.48 day and period derivatives of $(3 \pm 2) \times 10^{-5}$ s s^{-1} and $(-5 \pm 2) \times 10^{-5}$ s s^{-1} respectively. The second solution is in rough agreement with the superorbital period and period derivative obtained from the RXTE-ASM light curve alone. We take this to be the correct representation of the long term evolution of LMC X-4 superorbital period.

3. Discussion

In the present work, we report detection of superorbital intensity variations in LMC X-4 with EXOSAT-ME, GINGA-ASM and RXTE-ASM detectors. These measurements, when combined with the first detection of long period with HEAO A-1 (Lang *et al.* 1981), indicates a decay in the superorbital period of LMC X-4. We have applied three different techniques,

(1) period measurements from individual data sets,
(2) χ^2 maximisation by varying $\dot{P}$ with the RXTE-ASM data and
(3) arrival time analysis.

The results obtained from these analyses are consistent and indicate a long period derivative of about -2×10^{-5} s s^{-1}.

As mentioned earlier, superorbital periodic intensity variations have been observed in many X-ray binaries. However, there is strong difference in the way these intensity variations take place even in the subclass of accreting binary X-ray pulsars. While the superorbital intensity variations in LMC X-4 is coherent, in Her X-1 it has short term variations because it is synchronized with the binary cycle and switch-over to the high state takes place at specific orbital phases (Boynton *et al.* 1980, Scott and Leahy 1999). During anomalous low states in Her X-1, which can last for a few months, a change in the length or phase of the superorbital period is noticed (Oosterbroek *et al.* 2001). On the other hand, the superorbital intensity variations in SMC X-1 is quasi-periodic with recurrence times that wander between 50 and 60 days (Wojdowski *et al.* 1998).

In either case of forced precession or a slaved disk model, the period of precession is linked with the orbital period of the binary. Recently, Levine *et al.* (2000) reported a firm detection of orbital period decay in LMC X-4. In the precessing accretion disk model, it is therefore possible that the changing binary parameters cause the decay in the superorbital period in LMC X-4.

Acknowledgement

This research has made use of data obtained through the HEASARC Online Service, provided by the NASA/GSFC. We also thank the RXTE-ASM and GINGA-ASM teams for providing the valuable data.

References

Boynton, P. E. *et al.* 1980, *Ap. J.*, **237,** 169.
Giacconi, R. *et al.* 1973, *Ap. J.*, **184,** 227.
Katz, J. I. 1973, *Nature*, **246,** 87.
Lang, F. L. *et al.* 1981, *Ap. J.*, **246,** L21.

Levine, A. M. *et al.* 2000, *Ap. J.*, **541,** L194.
Margon, B. 1984, *ARA&A*, **22,** 507.
Ögelman, H. 1985, *Space Sci. Rev.*, **40,** 3470.
Scott, D. M., Leahy, D. A. 1999, *Ap. J.*, **510,** 974.
Oosterbroek, T. *et al.* 2001, *A&A*, **375,** 922.
Roberts, W. J. 1974, *Ap. J.*, **187,** 575.
Wojdowski, P. *et al.* 1998, *Ap. J.*, **502,** 253.

J. Astrophys. Astr. (2002) **23,** 39–43

X-ray Spectroscopy of Cygnus X-3

M. Choudhury & A. R. Rao *Tata Institute of Fundamental Research, Mumbai 400 005, India.*

Abstract. We have analysed the X-ray spectra of the highly variable X-ray source Cygnus X-3 over a wide energy range from 5 keV to 150 keV using data selected from the RXTE archives. Separate analysis of the low and hard states show the presence of a hard powerlaw tail in both the states. Here we present the result of the wide band spectral study of the source.

Key words. Binaries: close—stars: individual: Cygnus X-3—X-rays: binaries.

1. Introduction

Cygnus X-3 is a high mass X-ray binary star system, comprising a compact object and a Wolf-Rayet type of star as the companion (vanKerkwijk *et al.* 1992). It is located at a distance of 9 kpc (Prehedl *et al.* 2000) in one of the Galactic arms. It is also very bright in the radio and the infra-red region of the electromagnetic spectrum. The soft X-ray, as well as the infra-red emission, exhibits a periodicity of 4.8 hours which is attributed to the orbital period of the binary system. In the radio band it shows flaring activity and exhibits radio jets analogous to the powerful radio galaxies and quasars during the burst phase.

The X-ray luminosity is highly variable with the source exhibiting two states, viz. low/hard and high/soft states. The X-ray high state is correlated with the major radio flares (with flux $>$ 1Jy) (Watanabe *et al.* 1994). The prominent features of the X-ray spectra are the three Fe lines at 6.37, 6.67, & 6.96 keV, respectively (resolved by ASCA observation (Kitamoto *et al.* 1994), and two absorption edges at $\sim$ 7.1keV (Rajeev *et al.* 1994) and at $\sim$9.1keV (Nakamura *et al.* 1993; Rajeev *et al.* 1994). Several models, comprising mostly of thermal (disc) blackbody, Comptonization of seed photons from a thermal multi-coloured accretion disk by a thermal Comptonizing plasma cloud (Sunyaev *et al.* 1980) and cutoff-powerlaw components, have been proposed to explain the continuum spectra of the source (Nakamura *et al.* 1993; Rajeev *et al.* 1994). The absorption of the soft X-ray due to the effective H column for this source is reported to be very high (Nakamura *et al.* 1993).

2. Data and analysis

To get a broad-band (5–150 keV) spectral picture we used 22 sets of the pointed observations of both the narrow field of view instruments aboard the RXTE: viz., PCA and the HEXTE. A systematic error of 2% was added to the PCA Standard 2 data (all

Table 1. The MJD of the pointed observations of RXTE along with the average flux obtained by ASM (2–10 keV), BATSE (20–600 keV) and GBI (radio–2.2 & 8.3 GHz.)

MJD	ASM^1	BATSE^2	GBI^3(2.2GHZ)	GBI^3(8.3GHZ)	Spectral state
50319	7.495	0.039	-	-	low/hard
50321	8.160	0.028	-	-	low/hard
50322	10.298	0.009	-	-	low/hard
50324	10.291	0.035	-	-	low/hard
50325	15.279	0.034	-	-	low/hard
50500	21.141	0.018	0.101	0.098	high/soft
50501	21.29	0.041	0.095	0.090	high/soft
50604	28.722		0.130	0.197	high/soft
50609	22.137	0.001	0.111	0.316	high/soft
50612	17.675	0.042	3.511	2.478	high/soft
50616	26.746	0.005	0.729	0.964	high/soft
50618	20.635	0.034	0.737	0.966	high/soft
50624	32.351	0.056	0.115	0.550	high/soft
50652	7.636	0.055	0.071	0.081	high/soft
50661	8.150	0.051	0.071	0.083	high/soft
50717	10.778	0.038	0.118	0.205	low/hard
50950	5.573	0.043	0.061	0.083	low/hard
50951	6.715	0.052	0.071	0.082	low/hard
50952	5.453	0.046	0.087	0.098	low/hard
50953	5.551	0.051	0.065	0.067	low/hard
50954	5.384	0.058	0.049	0.080	low/hard

Units: ^{1}counts s^{-1}; ^{2}photons cm^{-2} s^{-1}; ^{3}mJy.

PCUs added), which included all the 129 channel PHA data, and it was simultaneously fit with 64 channel data from only the cluster 0 of the HEXTE, to get a proper fit (Vadawale *et al.* 2001). Of these 22 sets of observation 13 are in the low/hard state and 9 are in the high/soft state, the details of which are given in Table 1. To get a proper idea of the spectral state during the pointed observations, in Table 1 we give the flux as observed by three more instruments: viz.,

(1) ASM aboard the RXTE, in the soft X-ray energy region (2–10 keV),
(2) BATSE aboard the CGRO, in the hard X-ray energy region (20–600 keV), and
(3) the Green Bank Interferometer (GBI) in the radio region, of the electromagnetic spectrum.

The background noise was removed from the source PHA file during the fit, and the background PHA file was generated from the model of background noise for the corresponding epoch of RXTE observation, as provided.

The resolution of the three Fe lines (Kitamoto *et al.* 1994) and the two absorption edges (Rajeev *et al.* 1994) are beyond the capability of the PCA, hence we fix the relative separation of line and edge energies as reported earlier (Nakamura *et al.* 1993; Rajeev *et al.* 1994; Kitamoto *et al.* 1994), and treat the edge energy at 7.1 keV and the normalization of all the lines and edges as the variable parameters in the fit. Throughout we fix the line width at 80 ev (reasonably accepted value as obtained from ASCA observations (Kitamoto *et al.* 1994). This mode of tying the line energies with one edge energy doesn't affect the continuum fitting, but brings the χ^2 value corrsponding to the best fit parameters within the acceptable limit. The spectra is fit separately for the

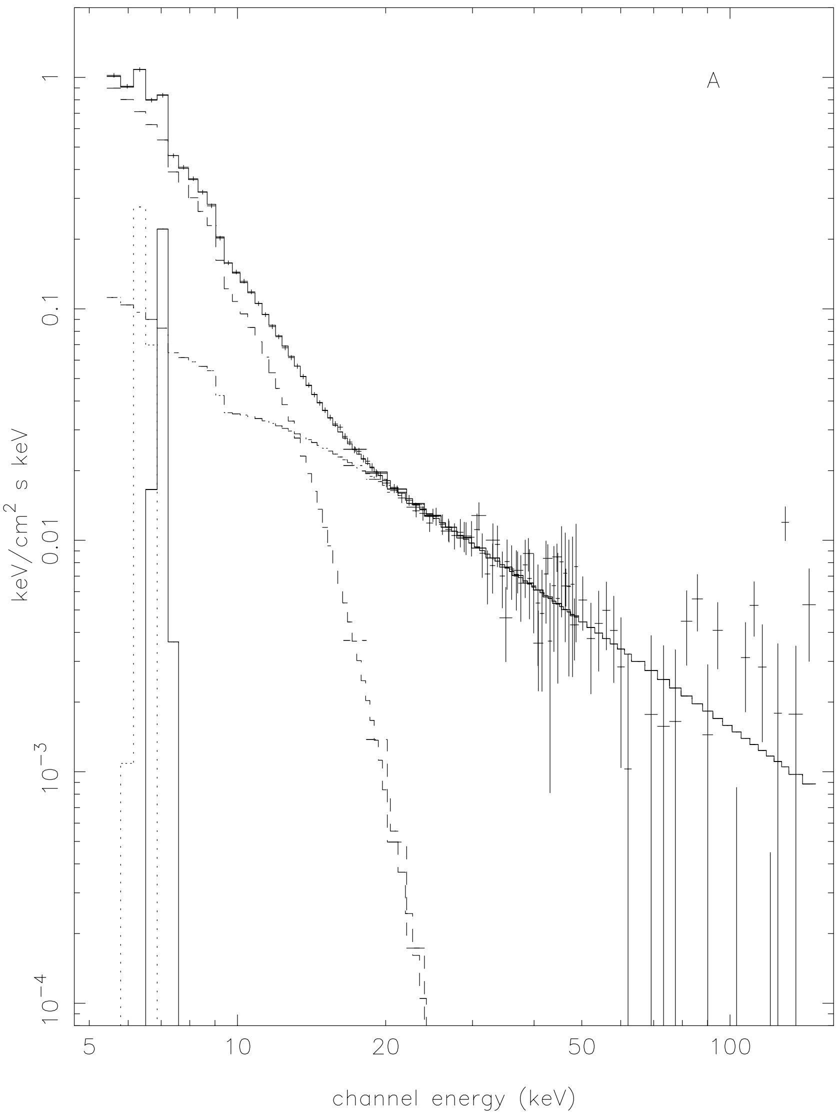

Figure 1(A). The spectra of observation on MJD 50616 showing all the components, viz., three Fe lines, two absorption edges, multicoloured disk blackbody and the powerlaw continuum.

high/soft and low/hard states. The unfolded spectra of an observation in high/soft state (MJD 50616) is shown in Fig. 1(A), and that of one of the low/hard states (MJD 50954) is shown in Fig. 1(B). The criteria of choosing these two as the representative of their respective states are: 1) exposure time, 2) quality of data, i.e., better background subtraction. Since the resolution of the PCA is poor in the lower energies and the absorption due to effective H column is a very sensitive parameter in this region, we neglect data below 5 keV and fix the height of H column to 1.6×10^{22} cm (low/hard state) and 5×10^{22} cm (high/soft state), as reported by Rajeev *et al.* (1994). The details of the best fit parameter values of the continuum components of the spectral modelling

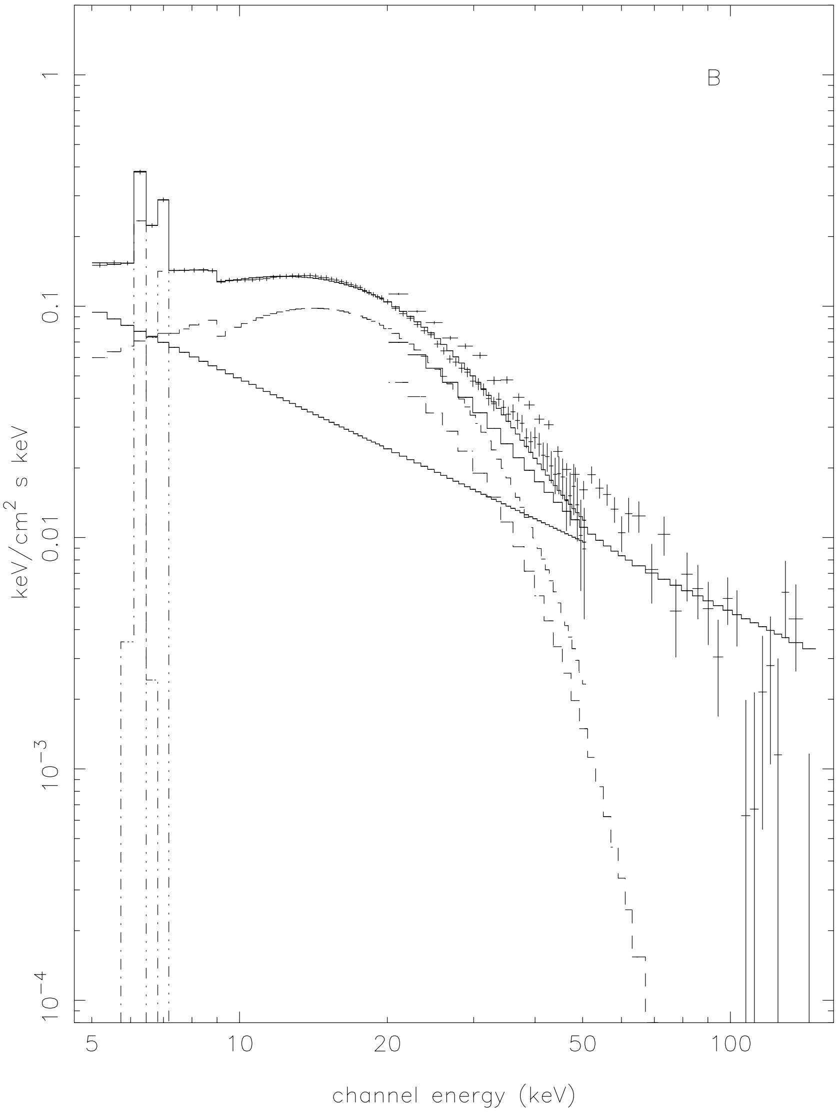

Figure 1(B). The spectra of observation on MJD 50954 showing all the components, viz., three Fe lines, two absorption edges, compST (Sunyaev & Titarchuk 1980) and the powerlaw continuum.

in the low/hard state is given in Table 2(A), and those in the high/soft state is given in Table 2(B).

3. Discussion

The high/soft state continuum emission spectra is fit by the combination of multi-coloured disk blackbody and powerlaw components. Powerlaw is needed to fit hard X-ray continuum and incorporation of any extra component viz., compST doesn't improve the quality of the fit. The low hard state continuum emission spectra is best fit

Table 2. Best fit X-ray spectral parameters of Cygnus X-3

MJD	kT_e (keV)	Γ_X	χ^2_ν(d.o f.)	MJD	kT_e (keV)	Γ_X	χ^2_ν(d.o.f.)
A. Low/hard state. Best fit parameters for CompST + power law							
50319	4.45	2.47	1.26(86)	50321	4.39	2.51	0.90(108)
50321*	4.47	2.61	1.18(108)	50322	4.91	2.51	1.08(108)
50322*	4.36	2.70	0.92(108)	50324	4.17	2.67	0.77(108)
50325	5.58	2.45	0.60(108)	50717	5.09	2.55	0.74(86)
50950	4.97	2.10	1.26(88)	50951	4.74	2.08	1.34(89)
50952	5.02	2.03	1.43(86)	50953	5.06	2.02	1.45(91)
50954	4.87	2.01	1.42(108)				
B. High/soft state. Best fit parameters for diskbb + power law							
MJD	kT_B (keV)	Γ_X	χ^2_ν(d.o f.)	MJD	kT_B (keV)	Γ_X	χ^2_ν(d.o.f.)
50604	1.49	2.55	0.53(109)	50609	1.59	2.21	1.19(109)
50612	1.62	2.25	1.22(109)	50616	1.55	2.53	0.65(109)
50618	1.53	2.34	0.83(109)	50624	1.52	2.63	0.60(109)
50500	1.74	2.98	0.55(109)	50501	2.91	3.06	0.54(109)
50501*	2.56	2.98	0.59(109)				

*Extended observation.

by a combination of compST (Sunyaev *et al.* 1980) and a powerlaw. Incorporation of multicoloured blackbody doesn't improve the fit. Fe line features, although significant in both states, are more prominent in the low/hard state. Absorption edges also form very important spectral features in both the states.

Hard powerlaw tail is present in both the states. This tail extends beyond 150 keV. The presence of this tail suggests thermal/non-thermal Comptonization (Zdziarski *et al.* 2001; Gierlinski *et al.* 1999) occurring in the source. Hard powerlaw tail in the high/soft state is being reported for the first time in this source, which might suggest that the compact object might be a blackhole candidate.

Cygnus X-3 is an unusually compact binary with a Wolf-Rayet companion, the wind obscuring the disc blackbody component of the soft X-ray, especially in the low/hard state, when the 10–30 keV bump (Fig. 1B), due to Comptonization, is more prominent. The high/soft state is characterised by enhanced thermal emission from the disc, changing the shape of the spectra. Therefore two different fits for the two different states are needed.

References

Gierlinski, M., Zdziarski, A. A., Poutanen, J., *et al.* 1999, *MNRAS*, **309,** 496.
Kitamoto. S., Kawashima, K., Negoro, H., *et al.* 1994, *PASJ*, **46,** L105.
Nakamura H., Matsuoka, M., Kawai, N. *et al.* 1993, *MNRAS*, **261,**. 353.
Prehedl, P., Burwitz, V., Paerels, F. *et al.* 2000, *A&A*, **357,** L25.
Rajeev, M. R., Chitnis, V. R., Rao, A. R. *et al.* 1994, *Ap. J.*, **424,** 376.
Sunyaev, R. A., Titarchuk, L. G. 1980, *A&A*, **86,** 121.
Vadawale, S. V., Rao, A. R., Chakrabarti, S. K. 2001, *A&A*, **370,** L17.
vanKerkwijk, M. H., Charles, P. A., Gebale, T. R., *et al.* 1992, *Nat*, **355,** 703.
Watanabe, H., Kitamoto, S., Miyamoto, S., *et al.* 1994, *Ap. J.*, **433,** 350.
Zdziarski, A. A., Grove, E., Poutanen, J., *et al.* 2001, *Ap. J.*, **554,** L45.

J. Astrophys. Astr. (2002) **23,** 45–51

Very High Energy γ- rays from Galactic Sources

P. R. Vishwanath *Tata Institute of Fundamental Research, Colaba, Mumbai 400 005, India.*

Abstract. The field of Very High Energy (VHE) gamma ray astronomy using the Atmospheric Cerenkov Technique has entered an interesting phase with detection of various galactic and extragalactic sources. Among galactic sources, only the Crab nebula has been established as a standard candle. Most observations on pulsars are in agreement as to the necessity for the GeV spectra to steepen at $<$200 GeV. While the Imaging method for increase of sensitivity has been successful with many results, an alternate technique – *Wavefront Sampling Technique* – is also being used by an increasing number of experiments. The recently commissioned experiment at Pachmarhi (PACT) in India is presented as an example of this technique. Preliminary results from this experiment show detection of VHE γ-ray emission from **(a)** the Crab nebula at a high significance and **(b)** Crab and Geminga pulsars at $>$ 1.5 TeV which could be the second component of the Outer Gap pulsar models.

Key words. Galactic sources—γ-ray astronomy—PACT.

1. Introduction

While the field of Very High Energy gamma ray astronomy using the Atmospheric Cerenkov technique began as an offshoot of Cosmic ray studies, it has rightly earned its place in recent years as an important electromagnetic band for study of all astronomical sources. The detection of VHE gamma rays from the Crab nebula in the late ’80s by the WHIPPLE Imaging telescope (Weekes *et al.* 1989) established the field of VHE gamma ray astronomy on a firm basis. While most of the results in the past decade have come from imaging telescopes, several groups have started using alternate techniques like *wave front sampling* (WFS) to increase the sensitivity of detections. This technique uses both the temporal and spatial distribution of Cerenkov photons for distinguishing between proton and gamma ray showers. In this paper, we at first review observational results on VHE gamma ray emission from galactic sources. Later we discuss an experiment in India using the WFS technique as an example of an alternate technique in the field and present some of the preliminary results from the experiment.

2. Earlier results

Since Cosmic ray origin has been an important aspect of the VHE γ-ray studies from the very beginning, it is quite natural to look for objects like Supernova remnants (SNR) which are expected to be sources of Cosmic rays of energy 100 TeV – 1000 TeV. Thus, searches for emission from SNRs is an important part of the observation programs of VHE gamma ray telescopes.

The Crab nebula has been the most intensively studied object in all High Energy Astrophysics and VHE gamma ray astronomy is no exception. In the past decade the energy range from 100 GeV – 7000 GeV has been covered by the Atmospheric Cerenkov telescopes. The lower energy results are from the solar farm arrays, while results at $>$400 GeV are mostly from imaging telescopes and EAS experiments (see Ong 1998). The VHE gamma ray flux at $>$ 1 TeV is $(2.1 \pm 0.45) \times 10^{-11}$ per sq cm per sec according to the fit given by the WHIPPLE experiment (Hillas *et al.* 1998) with the slope of the differential spectrum given as $-1.49 \pm .07$

While Crab (and Vela) belong to a subclass of SNRs having a pulsar, the more common SNRs are the ones without the pulsar but only with the shell. Since even these shell SNRs are well established as radio and X-ray emitters, the particles could be accelerated to high energies here also and it is important to look for gamma rays from these objects. The positive results are of (a) CAS-A by HEGRA: $> 5\sigma$ at $>$1 TeV - flux levels are 3 % of Crab at similar energies (Puehlhofer *et al*, 2001) (b) SN 1006 by CANGAROO $> 5\sigma$ and $>7\sigma$ in 2 observation periods (Kifune *et al.* 1997). The DURHAM group working in Australia has not seen any evidence for emission from SN1006.

Pulsar studies played a very important role in VHE gamma ray astronomy in the earlier years. In spite of many conflicting results, it was becoming clear from experiments in the ’80s that time averaged pulsar spectra have to steepen at the energies where atmospheric Cerenkov technique starts becoming viable. These earlier tentative conclusions from the VHE experiments (for reviews, see Fegan 1996; Kifune 1996; Vishwanath 2002) have been borne out in general by the exhaustive studies in the ’90s on pulsars by the EGRET (Thompson 2000) results.

The Vela Pulsar is the brightest gamma ray pulsar. Earlier observations were of a modest peak at $>$ 4 TeV coincident with the optical Main pulse (Grindlay *et al.* 1975) and a $> 4\sigma$ signal, again at the optical Main pulse, by the three year observations of the TATA group (at differing thresholds - 5 to 12 TeV) (Bhat *et al.* 1987) . However, there are several upper limits: from the Adelaide group (Edwards *et al.* 1994) at $>$800 GeV, from the Potchefstroom group (Nel *et al.* 1993) at $>$2.3 TeV. In the recent years, CANGAROO group using the imaging technique reported only unpulsed emission above 2.5 TeV from the Vela region (Yoshikoshi *et al.* 1997). Later, the Durham group did not see either the pulsed or the unpulsed emission at lower energy thresholds (300 GeV). When one considers all these results together, the picture emerging is of no emission from Vela pulsar at lower energies, but emission (pulsed or unpulsed) at higher energies. As for another southern pulsar PSR 1706-44, the CANGAROO group (Kifune *et al.* 1995) and the Durham group (Chadwick *et al.* 1997) have detected only unpulsed emission from the object.

PSR 0355+54 is a pulsar with low timing noise indicating high internal temperatures and has the largest glitch ever found. The TATA group, working at Pachmarhi, observed the source in 1987 soon after the glitch and found a peak of significance 4.3σ (Bhat *et al.* 1990) at $>$ 2 TeV with a fairly constant signal level throughout the data period. The next two observation seasons did not yield any time averaged signal. The EGRET has termed it a ‘a prime candidate for future observations’.

The Crab pulsar was the object of many studies in the past. The Durham group, (Dowthwaite *et al.* 1984) working at the Dugway site in USA, detected a 4.3σ signal at the main pulse phase position from 103 hours of observation at an energy threshold of 1 TeV. While the TATA group found several bursts at the main pulse position, the Durham experiment was the only experiment of the '80s to see a time averaged signal from the Crab pulsar. It should be noted that the detected flux is quite small, about 3 per hour ! Recently, a thorough search for pulsed emission has been done with the WHIPPLE imaging telescope (Burdett *et al.* 1999). Using the data collected between 1995 and 1997, for an exposure of about 73 hours above 250 GeV, they give an upper limit for pulsed emission at several energies from 250–4000 GeV. The CELESTE experiment and the STACEE experiment, both with solar arrays and at thresholds $<$250 GeV, also do not see evidence for pulsed emission in their respective energy regions.

Geminga remained a mystery for almost a decade till the discovery of 237 msec periodicity by ROSAT and later by EGRET. After the discovery by EGRET, two VHE gamma ray groups (Durham and Ooty – Bowden *et al.* 1993; Vishwanath *et al.* 1993) reanalyzed their archival data and found modest level pulsar signatures at $>$ 1 TeV with VHE gamma ray peaks coinciding with the peaks in Cos-B data. Later, in the '90s, an upper limit for pulsed emission was given by the WHIPPLE group (Akerlof *et al.* 1993) . The HEGRA (Aharonian *et al.* 1999) group in their recent analysis has also not found pulsed emission of VHE gamma rays from either the Crab or the Geminga pulsar

During 1992–1994, the Tata group working at Pachmarhi ran an interim array for testing some of the hypothesis concerning lateral distribution of VHE gamma rays (Vishwanath 1997). It was shown that the events at phases at which GeV emission was found (main pulse region for Crab and around 0.6 for Geminga) displayed features expected from gamma ray events.

3. Recent PACT observations on galactic sources

A new atmospheric Cerenkov array to study cosmic sources of Very High Energy (VHE) Gamma rays has been set up in Pachmarhi in central India. The aim of the new Pachmarhi Atmospheric Cerenkov Telescope (PACT) array has been to use the temporal and spatial distribution of Cerenkov photons in distinguishing between proton and gamma ray showers for increase of sensitivity. The array consists of 25 telescopes, each consisting of 7 parabolic mirrors, deployed in a field of 80 m $\times$ 100 m area (Bhat *et al.* 2000). The total physical area of the mirrors is $\sim$105 sq.meters. Each mirror is looked at by a fast PMT behind a 3 degree circular mask. While a single sector (with only 6 telescopes) trigger event rate was about 3 to 4 HZ for most atmospheric conditions, the overall event rate with all the 4 sectors was about 9 HZ. Both the timing and pulse height information for each mirror were recorded. Monte Carlo estimates of the energy threshold for one sector is 700 – 800 GeV. The angular resolution of the entire array was found to be $0^\circ.23$ when all the royal sum (addition of mirrors in each telescope) pulses were used; the same improved to $0^\circ.04$ when arrival times of the shower at individual mirrors were used.

Many simulations, including the recent extensive calculations by Chitnis and Bhat (Chitnis & Bhat 1998, 1999) have shown that the gamma ray lateral distribution (LD) is very different from that of protons. They have also shown that pulse shape parameters like the decay times, the FWHM etc. could help increase the sensitivity in atmospheric

Cerenkov experiments. The PACT experiment with pulse height and timing information from 175 mirrors is thus dealt for exploiting the various capabilities of the WFS technique.

A total of 49 hours of data was taken with the newly commissioned PACT experiment on the Crab nebula and about 16 hours on several background regions, but with the same declination as Crab. The Crab data (Nov 1999–Nov 2000) was taken when only 2 sectors (12 telescopes) were operational. Arrival direction for each event which triggered both sectors and thus, the space angle difference between the directions of the source and the event was determined. The source and the background space angle difference distributions were compared. The excess number of events from the source direction corresponded to 2.71$\pm$ 0.15 gamma ray events per minute. This amounts to a significance of $>$18 σ. The integral flux at 900 GeV from this preliminary analysis which amounts to (3.6$\pm$1.0) $\times$ 10^{-11} photons per sqcm per sec is shown in the left hand panel of Fig. 1 along with earlier measurements of other groups.

A total of 28 hours of data on Crab pulsar and 10 hours was taken on Geminga pulsar. Standard epoch folding method was used to get the phase for each event. Fig. 1(a)

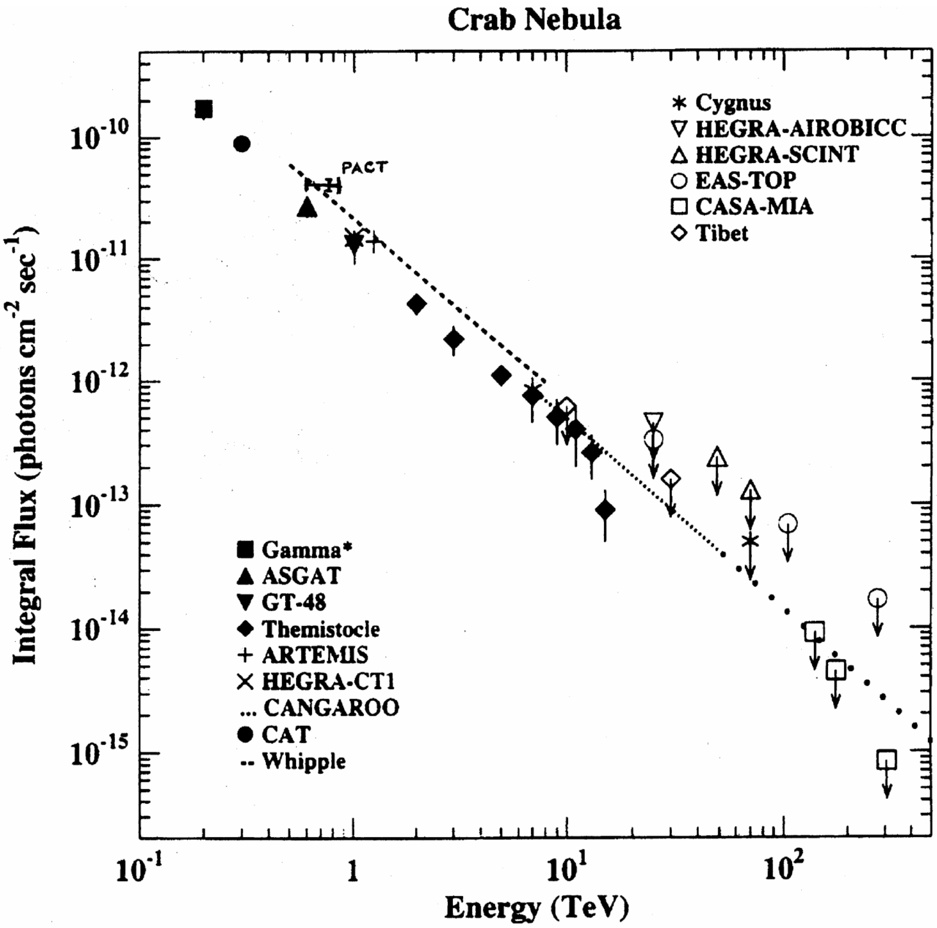

Figure 1(a). The Energy Spectrum of Crab nebula.

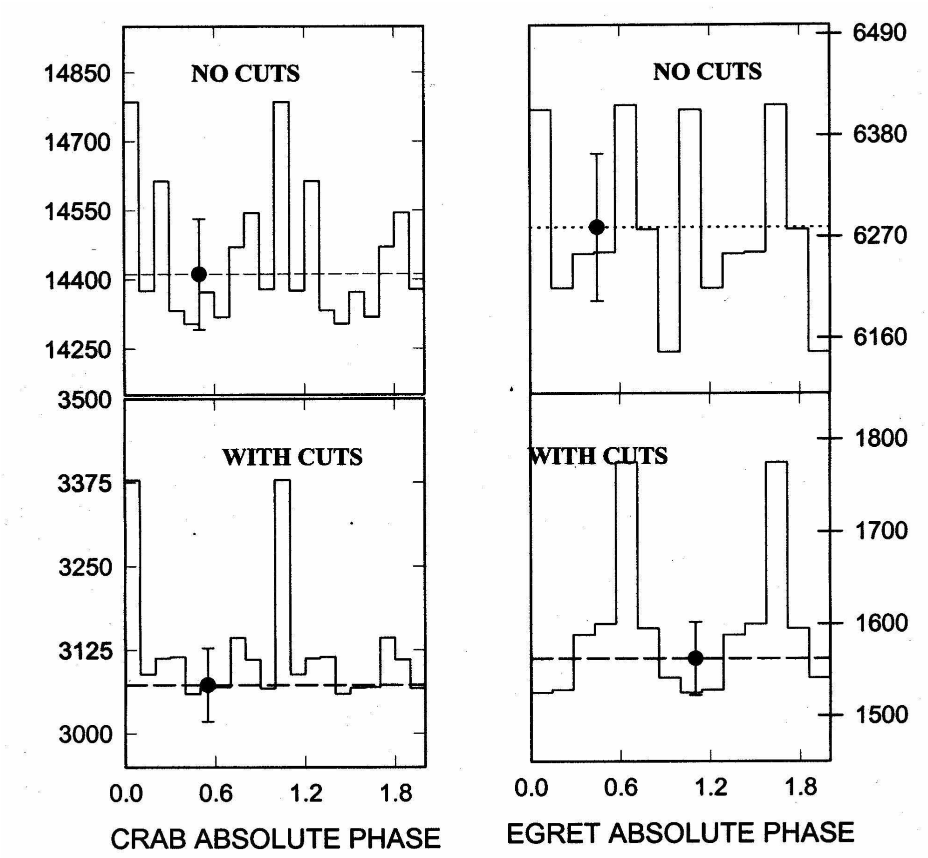

Figure 1(b). The phasograms for Crab and Geminga pulsars with and without cuts from the recent PACT experiment. The LHS and RHS figures refer to Crab and Geminga respectively. The peaks in the phasograms with cuts are at the Main Pulse position for Crab and the EGRET second pulse for Geminga.

shows the Crab and Geminga pulsar phasograms without any cut and with the cuts. It can be seen that the phasograms without any cuts do not show any significant emission at any phase. The cuts retained **(a)** events within 1 degree of the source and **(b)** larger pulse height events With these cuts, only about 25% of the events are retained. The resulting phasograms show very clearly peaks with $> 5\ \sigma$ at **(a)** Main pulse position for Crab and **(b)** EGRET pulse P1 position for Geminga. The pulse height cuts place these selected events at $>$1500–2000 GeV. The preliminary fluxes derived from these peaks, while much lower than that of the Crab nebula at these energies, are much higher than the upper limits set by the groups using the imaging technique. It should be noted that the collection area for the supercut events with the imaging technique shows a steady decrease from 1 TeV onwards (Punch 1994). Further, as Bhat *et al.* (Bhat *et al.* 1994) pointed out, the gamma ray images at high energies, especially for flatter spectrum sources, look more and more like proton images. However, the reasons for these discrepancies have to be explored further.

4. Discussion

The importance of the Crab nebula is that it has provided a standard candle for VHE gamma rays as in other bands of the electromagnetic spectrum. The VHE gamma ray emission from Crab has been explained as inverse Compton scattering of relativistic electrons off soft neighbouring photons (see Ong 1998 and references therein). By comparing the measured energy spectrum with predictions for different values of the magnetic field in the nebula, the WHIPPLE group showed that a value of 16 nanoTesla gives a good agreement with the flux at different energies. This shows the potential of a very new field like VHE gamma ray astronomy to probe the interior of the nebula. There is still no single SNR source (apart from Crab) which has been seen by more than one experiment. While it is highly likely that some of the positive detections will be proved correct with time, the most common explanation for these detections is inverse Compton scattering of electrons with ambient photons. Further detections and measurements are needed to really resolve the source of VHE gamma rays in shell type SNRs.

It is certain that most of the pulsar energy spectra have to steepen in the energy range of the atmospheric Cerenkov experiments. The precise energy of the steepening will be clear when some of the lower energy threshold experiments become fully functional. Different sites for the acceleration of charged particles provide the basic difference between theoretical models for pulsars (Harding 2000). Polar Cap/Outer Gap models predict steep/gradual cut-offs. The outer gap models also predict an inverse Compton component due to the interaction of gap accelerated particles with IR photons with a peak around 1 TeV. The preliminary results from PACT indicate the possibility of a second component at TeV energies

5. Acknowledgements

It is a pleasure to thank Profs. B. S. Acharya, P. N. Bhat and Dr. V. Chitnis for discussions and Sri Pratik Majumdar for discussions and help with the manuscript. It is a pleasure to thank Sarvashri A. I. D'Souza, J. Francis, A. V. John, K. S. Gothe, B. K. Nagesh, M. S. Pose, P. N. Purohit, M. A. Rahman, K. K. Rao, S. K. Rao, S. K. Sharma, B. B. Singh, A. J. Stanislaus, P. V. Sudershanan, S. S. Upadhya, and B. L. Venkatesha Murthy for their participation in various aspects of the PACT experiment.

References

Akerlof C. W. *et al.* 1993, *A&A*, **274,** L17.
Aharonian F. A. *et al.* 1999, *A&A*, **346,** 913.
Bhat P. N. *et al.* 1987, ibid, **242,** 178
Bhat P. N. *et al.* 1990, ibid, **236,** L1.
Bhat P. N. *et al.* 2000, *Bull. Astr. Soc. India*, **28,** 455.
Bhat C. L. *et al.* 1994, *Towards a major atmospheric cerenkov detector III* (ed.) T. Kifune, (Universal Academy Press, Tokyo), **207**.
Bowden C. G. G. *et al.* 1993, *J. Phys. G.*, **19,** L29.
Burdett A. M. *et al.* 1999, *Proc. 26th ICRC.*
Chadwick P. M. *et al.* 1997, *Proc. 25th ICRC,* **3,** 189.
Chitnis V. R., Bhat. P. N., 1998, *Astroparticle Physics,* **9,** 45.
Chitnis V. R., Bhat. P. N., 1999, ibid, **12,** 45.

Dowthwaite. T. C. *et al.* 1989, *Ap. J.*, **286,** L35.
Edwards P. G. *et al.* 1994, *A&A*, **291,** 468.
Fegan D. J., 1996, *Space Science Reviews*, **75,** 137.
Grindlay J. E. *et al.* 1975, *Ap. J.*, **201,** 82.
Harding A. K., 2000, *Proc. High energy gamma ray astronomy*, Heidelberg.
Hillas A. M., *et al.* 1998, *Ap. J.*, **503,** 744.
Kifune T. *et al*, 1995, *Ap. J Letters*, **438,** L91.
Kifune T., 1996, *Pulsars (IAU colloquium 160)*.
Kifune T. *et al.* 1997, Proceedings of the Fourth Compton Symposium, (eds) C. D. Dermer, M. S. Strickman & J. D. Kurfess, *AIP Conference Proceedings*, **410,** p. 1507.
Nel H. I. *et al.* 1993, *Ap. J.*, **418,** 836.
Ong R., 1998, *Physics Reports*, **305,** 93.
Puehlhofer *et al.* 2001, *Proc. of 27th ICRC* (Hamburg).
Punch M., 1994, *Towards a major atmospheric cerenkov detector III* (ed.) T. Kifune, (Universal Academy Press, Tokyo), **163**.
Thompson D. J., 2000, *Proc. High energy gamma ray astronomy*, Heidelberg.
Vishwanath P. R. *et al.* 1993, *A&A*, **267,** L5.
Vishwanath P. R. 1997, *High energy astrophysics and astronomy* (eds) P. C. Agrawal & P. R. Vishwanath, (Universities Press), **204**.
Vishwanath P. R, 2002, to appear in *Bull. Astro. Soc. India*.
Weekes, T. C. *et al.* 1989, *Ap. J.*, **342,** 379.
Yoshikoshi T., *et al.* 1997, *Ap. J.*, **487,** L65.

J. Astrophys. Astr. (2002) **23,** 53–57

Arecibo Observations of Parkes Multibeam Pulsars

N. D. R. Bhat[1], F. Camilo[2], J. M. Cordes[3], D. J. Nice[4], D. R. Lorimer[5], S. Chatterjee[6]

[1]*National Astronomy and Ionosphere Center, Arecibo Observatory, U.S.A.*
[2]*Columbia Astrophysics Laboratory, Columbia University, U.S.A.*
[3]*National Astronomy and Ionosphere Center and Cornell University, U.S.A.*
[4]*Department of Physics, Princeton University, U.S.A.*
[5]*Jodrell Bank Observatory, University of Manchester, U.K.*
[6]*Department of Astronomy, Cornell University, U.S.A.*

Abstract. The on-going Parkes multibeam survey has been astoundingly successful (Manchester *et al.* 2001), and its discovery of over 600 pulsars has opened up new avenues for probing the Galaxy's electron content and magnetic field. Here we report on recent observations made with the Arecibo 305-m telescope, where 80 distant, high dispersion measure pulsars (of which 35 are from the multibeam survey) were studied at multiple frequency bands in the range 0.4–2.4 GHz, in order to determine their scattering properties, rotation measures and spectral indices. The results will be used to meet a variety of science goals; viz., creating an improved model of the electron density, mapping out the Galactic magnetic field, and modeling the pulsar population.

Key words. Pulsars—interstellar matter—scattering—polarization.

1. Introduction

Pulsars make excellent probes of the interstellar medium, and measurements of their dispersion measures (DMs) and scattering properties help us to infer the interstellar electron density (n_e) and its distribution in the Galaxy. Although the best present model of n_e in the Galaxy (Taylor & Cordes 1993) has proven useful for many applications, it is poorly constrained towards the inner Galaxy. The most newly discovered pulsars from the Parkes multibeam survey (Manchester *et al.* 2001) have high DMs, with a median DM of 400 pc cm^{-3}, making them excellent probes of the electron content in and around inner parts of the Galaxy. The scattering properties of such distant pulsars are best studied via their pulse-broadening times (the lengthening of the pulse profile due to scattering of rays between the pulsar and the Earth). This requires data from a high frequency to obtain the intrinsic, un-broadened profile and a low frequency to measure the broadened profile.

As is well known, most pulsars are polarized, and the observed angle of polarization at some wavelength, λ, is rotated from its intrinsic angle by an amount $\Delta\psi = RM\ \lambda^2$, where the rotation measure (RM) is the integral of $n_e B$ along the line of sight (where B is the magnetic field). By measuring the polarization position angle of a pulsar at several frequencies, we can determine the RM and therefore the average magnetic field, weighted by electron density.

Observations show magnetic field lines in spiral galaxies tend to follow the spiral arms, with fields arranged either in clockwise and counterclockwise directions within an overall spiral pattern (“bisymmetric spiral structure”) or with fields arranged in a more uniform direction (“axisymmetric spiral structure”) (e.g., Wielebinski & Krause 1993). The origin and evolution of field patterns remain controversial (Zweibel & Heiles 1997). Further, observations suggest that the local magnetic field in our Galaxy is largely in the azimuthal direction, but its inclination differs from that expected for a bisymmetric spiral structure (e.g., Han *et al.* 1999). Clearly, a further study of the shape of the Galactic field is required.

The Parkes survey was conducted at a substantially higher frequency (1.4 GHz) than those commonly used in most earlier pulsar surveys. The newly discovered pulsars pose a challenge for models of the pulsar content in the Galaxy. An intriguing question is to what extent are they a new population, whose discovery was missed by earlier surveys due to their low luminosities at low frequencies and/or heavy scattering? The spectral behaviour, together with the scattering properties, will enable us to address this question, and will also help optimize the future directions of pulsar searches.

2. Observations and results

We have undertaken a study of the multibeam pulsars visible from Arecibo, along with previously known pulsars in the same region of the sky, in order to meet the above science goals. In the first phase (May–July 2001), observations were made of 35 pulsars from the multibeam survey for which sufficiently accurate positions were available (Manchester *et al.* 2001), and 45 previously known ones (Taylor *et al.* 1995) at 0.4, 1.2, 1.5 and 2.4 GHz. Observations at frequencies above 1 GHz were made with the new pulsar backend, the Wideband Arecibo Pulsar Processor (WAPP), whereby all four stokes parameters are measured. Data at 0.4 GHz were recorded with the Penn State Pulsar Machine (PSPM). Observations are made over bandwidths of 100 MHz at 1.2 and 1.5 GHz, 50 MHz at 2.4 GHz and 10 MHz at 0.4 GHz, with integration times of 300 to 600 seconds. The data products are made available in the following formats:

(1) total intensity profiles at all four frequency bands (Fig. 1), and
(2) polarization data (i.e., the stokes I, L, V profiles and position angle vs pulse phase) at 1.2 and 1.5 GHz (Fig. 2).

Detailed analysis and interpretation are underway. Follow-ups of the current study will involve the use of the GBT (Green Bank Telescope) and the GMRT (Giant Metre-wave Radio Telescope), as well as the Parkes 64-m telescope, for the study of the objects south of the equator.

Preliminary results from our on-going analysis are briefly described below:

Pulse-broadening times: The observed pulse profile can be modeled as an intrinsic pulse shape convolved with a pulse-broadening function (i.e., the impulse response function characterizing the scatter broadening). Estimates (or upper limits) of pulse-broadening time (τ_p) have been obtained for about 40 objects, which marks as a substantial improvement upon the data available (for 170 of the $\sim$1500 pulsars known) for modeling the Galaxy’s electron content. For several objects, measurements of τ_p have been made at 2 to 3 frequencies, and in some cases, there is also clear evidence

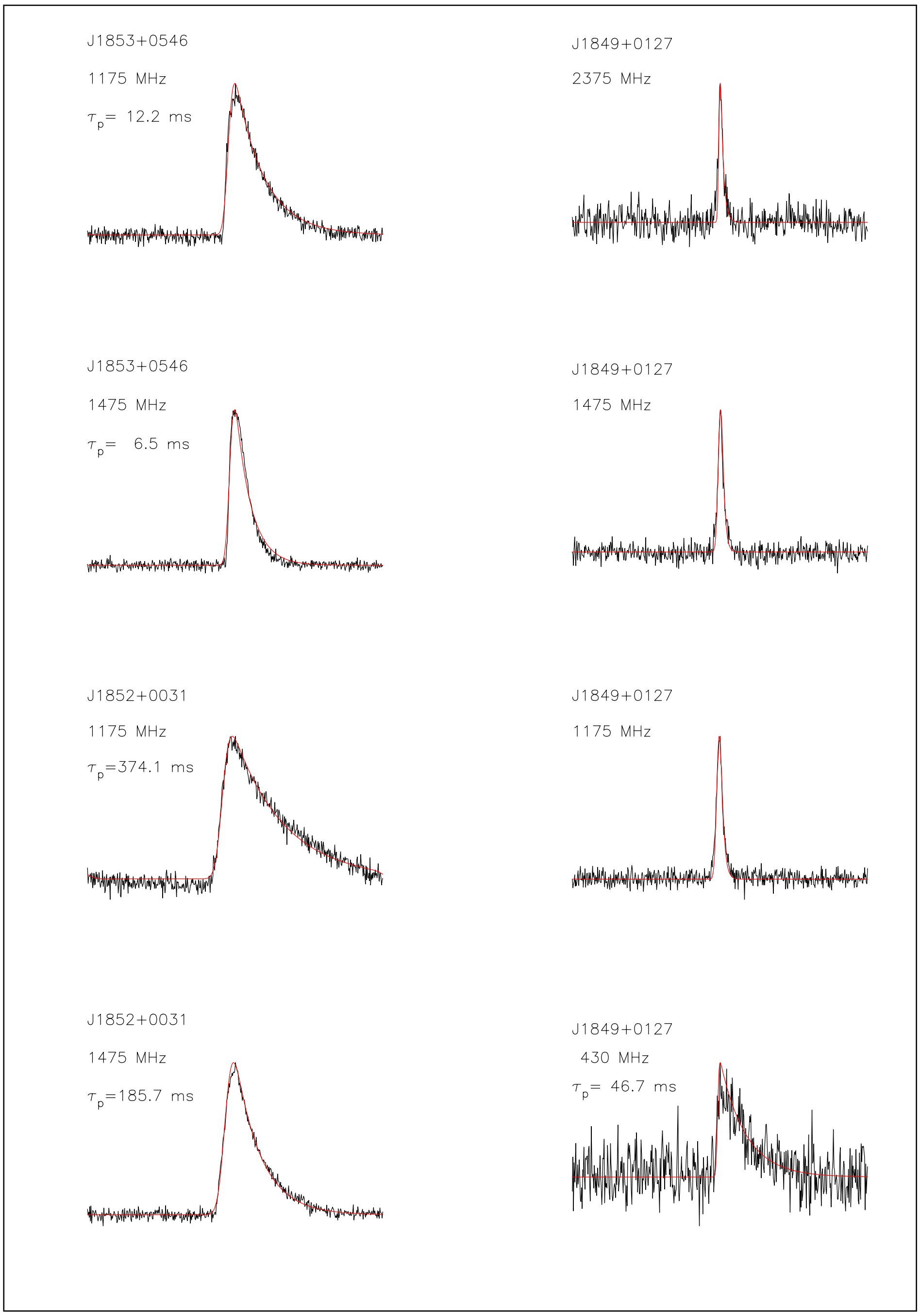

Figure 1. Examples of multi-frequency pulsar data. Scatter-broadened profiles are shown for a multibeam pulsar (J1853 + 0546) and a cataloged pulsar (J1852 + 0031) at two different frequencies (left panel). Profiles of another multibeam pulsar (J1849 + 0127) are shown at four frequencies (right panel); scattering is clearly visible at the lowest frequency, 430 MHz.

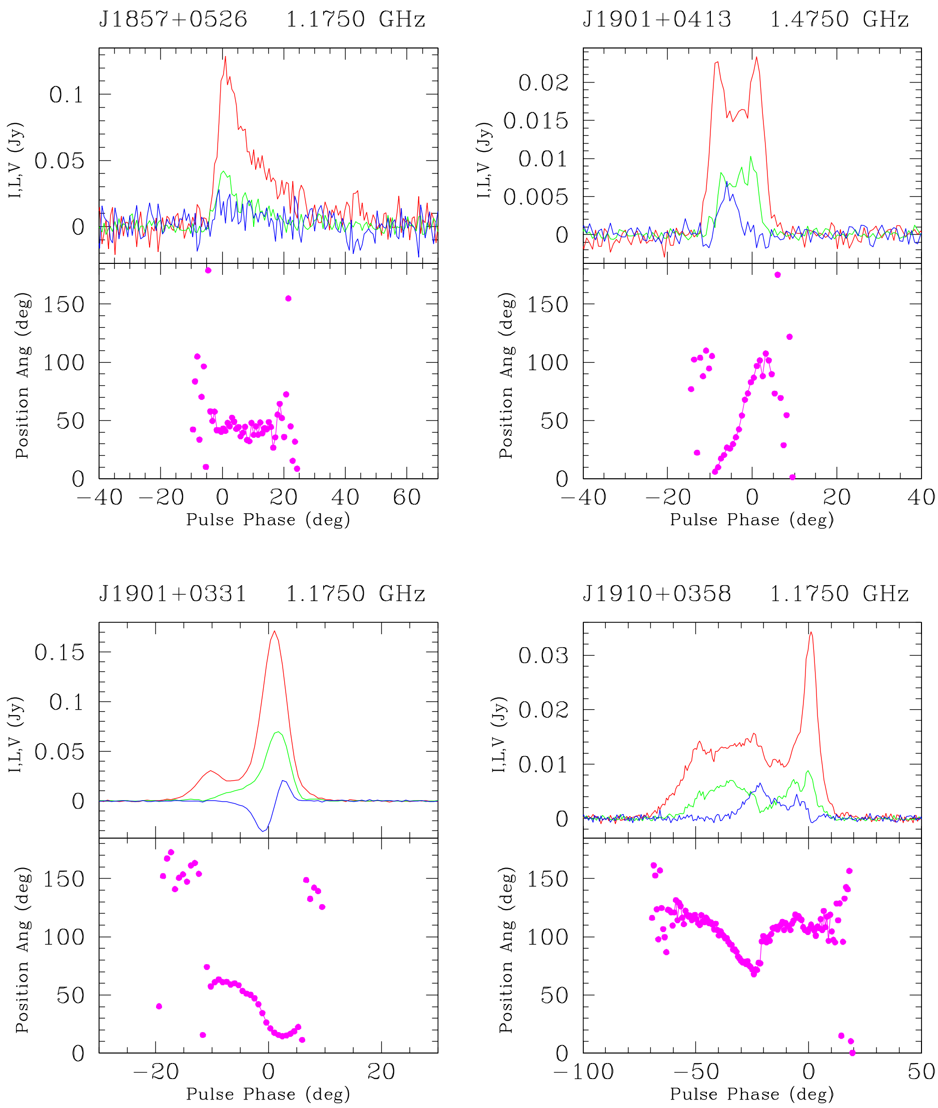

Figure 2. Polarization profiles for four distant pulsars observed with the WAPP: PSRs J1857 + 0526 and J1901 + 0413 are new discoveries from the multibeam survey. The upper panels show the total intensity, linearly polarized flux density and circular polarization, and the lower ones are the plots of position angle vs pulse phase within the on-pulse window.

that the scaling of τ_p with frequency is significantly weaker than that expected ($\sim \lambda^{4.4}$) from standard theories (Fig. 1). Such anomalous scattering has been predicted recently by Cordes & Lazio (2001).

Rotation measures: Although we derive full Stokes profiles from our data in multiple frequency bands, our current estimates of RM are obtained by measuring the rotation of position angle across the 100 MHz band near 1.2 GHz. This technique yields satisfactory results for data with sufficiently good signal-to-noise ratios. Our analysis so far has provided RMs for about 40% of the observed objects. The new estimates range from $\sim$100 to $\sim$1000 rad m^{-2}, and these measurements will significantly improve upon the data available for studying the structure of the Galactic magnetic field.

Spectral behaviour: The multi-frequency nature of our observations allow estimation of the spectral indices of these pulsars. Almost all multibeam objects have been detected at 2.4 GHz with signal-to-noise ratios quite comparable to those at 1.2 GHz, despite the fact that the observations were made with similar levels of sensitivity. This may indicate that the spectra of the new pulsars are somewhat flatter than those for the population known from earlier low-frequency searches.

References

Cordes, J. M., Lazio, T. J. W. 2001, *Ap. J.*, **549,** 997.
Han, J. L., Manchester, R. N., Qiao, G. J. 1999, *MNRAS*, **306,** 371.
Manchester, R. N., Lyne, A. G., Camilo, F., *et al.* 2001, *MNRAS*, **328,** 17.
Taylor, J. H., Cordes, J. M. 1993, *Ap. J.*, **411,** 674.
Taylor, J. H., *et al.* 1995, ftp://pulsar.princeton.edu/pub/catalog
Wielebinski, R., Krause, F. 1993, *A&A Reviews*, **4,** 449.
Zweibel, E. G., Heiles, C. 1997, *Nature*, **385,** 131.

J. Astrophys. Astr. (2002) **23,** 59–65

Spectroscopic Studies of X-Ray Binary Pulsars

F. Nagase *The Institute of Space and Astronautical Science, Japan.*

Abstract. Several new features of X-ray binary pulsars are revealed from recent observations with ASCA, RXTE, BeppoSAX and other X-ray observatories. Among these, I will review in this paper some recent progress in spectroscopic studies of accreting X-ray pulsars in binary systems (XBPs). First, I will discuss soft excess features observed in the energy spectra of XBPs and propose that it is a common feature for various subclasses of XBPs. Next I will present some recent results of high resolution spectroscopy with ASCA and Chandra.

Key words. X-ray binaries, pulsars, spectra.

1. Introduction

Accreting X-ray pulsars in binary systems have a unique type of energy spectra among various classes of X-ray sources (White *et al*. 1983; Nagase 1989). X-ray spectra of supernova remnants, stellar coronae and clusters of galaxies show signature of thermal emission. X-ray spectra of black hole binaries and active galactic nuclei show a non-thermal power law spectra extended over wide energy range toward hard X-rays to γ-rays. In contrast to these X-ray sources, XBPs fundamentally show a power law spectra with photon indices 1–2 with high-energy turnover at relatively low energies of 10–30 keV. This spectral turnover is considered to be related to the strong magnetic field of the neutron star in XBPs.

Since most XBPs are located in the Galactic plane, their spectra are usually subjected to strong soft X-ray absorption. Massive wind-fed XBPs often exhibit a strong iron emission line at 6.4 keV and the intensity of this fluorescent line provides estimates of the column density of accreting matter surrounding the neutron star in the binary system.

Neutron stars in XBPs are relatively young and theoretically estimated to have a strong magnetic field of the strength 10^{12}–10^{13} G at the neutron star surface. In fact, the magnetic field of those neutron stars can be measured directly by detection of absorption features in X-ray spectra due to electron cyclotron resonant scattering feature (CRSF). The absorption feature appears at an energy of $E = 11.6B_{12}$ keV where B_{12} is the magnetic field strength in units of 10^{12} G. Until late 1980s, this feature has been observed only from two pulsars, Her X-1 (Trümper *et al*. 1978), and 4U0115+63 (Wheaton *et al*. 1979). In early 1990s, the CRSF in the XBP spectrum has been systematically searched with large area proportional counters on board Ginga and detected from a dozen of XBPs (Mihara 1995; Makishima *et al*. 1999). The Ginga observations revealed that the surface magnetic field strengths of XBPs distribute over a narrow range of (1–4) $\times$ 10^{12} G as estimated from the CRSFs and the energy of CRSF is correlated with the turnover energy.

In addition to those features of XBP spectra, it was known that some low mass XBPs (LMXBPs), such as Her X-1 (McCray *et al*. 1982; Endo *et al*. 2000) and 4U1626−67 (Kii *et al*. 1986; Angelini *et al*. 1995), show a soft excess component at $\sim$ 1 keV in the spectra which can be fitted by an additional blackbody emission. Recent progress in observations with ASCA and BeppoSAX revealed that such soft-excess features are seen not only from LMXBPs but also from high mass XBPs (HMXBPs) and transient Be-star XBPs (BeXBPs) that constitute more than 70% among subclasses of XBPs. This soft excess feature in XBP spectra is discussed in the next section.

Spectroscopic studies with the CCD cameras on board ASCA revealed the existence of line-dominated component that is reprocessed by stellar wind surrounding the neutron star and has been highly photoionized due to irradiation by strong X-ray beam from the source. Strong emission lines due to radiative recombination followed by cascades are seen in the spectra of Vela X-1 (Nagase *et al*. 1994) and Cen X-3 (Ebisawa *et al*. 1996). The measurement of recombination lines from highly photoionized heavy elements provides a new tool to study densities, ionization structures, elemental abundances of these elements. Further detailed studies are expected to be carried out by observations with transmission gratings on board Chandra and reflection gratings on board XMM-Newton. Some early results with ASCA and Chandra will be presented in section 3.

2. Soft excess features in the spectra of XBPs

A soft-excess feature, a feature of excess intensities at energy below 1 keV in the spectrum over the extrapolation of a power low spectrum fitted to the higher energy, was first detected from a LMXBP, Her X-1 (McCray *et al*. 1982) and later from another LMXBP, 4U 1626−67 (Kii *et al*. 1986). The feature has been intensively investigated thereafter (e.g., Dal Fiume *et al*. 1998; Endo *et al*. 2000 for Her X-1 and Angelini *et al*. 1995; Orlandini *et al*. 1998 for 4U 1626–67). The excess over the power law component can be fitted by a blackbody emission of temperature $\sim$ 0.1 keV. Although it has been known that the pulses at low energies below 1 keV in Her X-1 show a broad sinusoidal shape, Endo *et al*. (2000) confirmed that this broad pulses at low energies correspond to the blackbody component. This fact supported the interpretation of the blackbody emission to be the result of reprocessing of the hard X-rays at the inner boundary of accretion disk (McCray *et al*. 1982).

Evidence of such a soft excess feature has also been reported from HMXBPs in the Magellanic clouds, LMC X-4 (Woo *et al*. 1996; La Barbera 2001) and SMC X-1 (Marshall *et al*. 1983, Wojdowski *et al*. 1998) owing to a small column density of soft X-ray absorption by intervening interstellar matter toward these directions. The soft component can also be fitted by a blackbody emission of temperatures $\sim$ 0.1 keV. Those soft excess features in spectra of LMC X-4 and SMC X-1 were also confirmed with the ASCA observations (Paul *et al*. 2001). The spectra observed with ASCA from SMC X-1 and LMC X-4 are basically fitted by a sum of a power law with a photon index $\Gamma = 0.8$–0.9 and a blackbody emission of a temperature $kT = 0.16$–0.19 keV and an iron fluorescent line at 6.4 keV, although the spectrum of LMC X-4 requires additional broad lines at $\sim$ 1 and $\sim$ 2 keV.

Such a clear soft excess feature, however, has not been reported from BeXBPs till the observations of pulsars in the Magellanic clouds with ASCA, because most of Galactic BeXBPs are subjected to a large soft X-ray absorption. Recently, clear examples of such a soft excess feature were obtained from ASCA observations of BeXBPs in SMC, such as RX J0059.2–7138 (Hughes 1994; Kohno *et al*. 2000) and XTE J0111.2–7317 (Yokogawa *et al*. 2000). The observed and unfolded energy spectra observed with ASCA from a BeXBP, XTE J0111.2−7317 is shown in Fig. 1 demonstrating clear existence of a soft excess component. A model of power law plus blackbody emission can fit the spectrum. The best fit parameters are given as $\Gamma = 0.8$, $kT = 0.15$ keV, and $N_{\rm H} = 2.7 \times 10^{21}$ cm^{-2} for XTE J0111.2−7317 and these values are quite similar with those of SMC X-1 and LMC X-4 mentioned above. Thus, the spectral model that involves a power law and a soft blackbody emission, which is widely adopted to fit the soft-excess spectra observed from LMXBPs and HMXBPs, can be adopted also to the soft-excess feature seen in the spectra of some BeXBPs. This suggests that the emission mechanism and site of the soft component, which can be fitted by a blackbody model, should be common for all subclasses of accreting X-ray pulsars. It should be noted that the fraction of luminosity of the blackbody component is about 10% of the power law component for all the cases of Her X-1, SMC X-1, LMC X-4, and XTE J0111.2−7317.

However, the total X-ray luminosity of XTE J0111.2–7317 is as large as $\sim 2 \times 10^{38}$ erg s^{-1}, which is about the same as SMC X-1 and LMC X-4. If the soft excess emission is really blackbody emission from spherical body, the luminosity fraction of about one tenth of the total luminosity implies that the blackbody radii becomes about two order of magnitudes larger than the neutron star radius, assuming spherical emission at the distances of Magellanic clouds. Hence, it is an issue to be investigated further if the interpretation applied to Her X-1 (McCray *et al*. 1982; Endo *et al*. 2000), where the blackbody emission is considered to be the result of reprocessing of the hard X-rays at the inner boundary of accretion disk, is applicable to these XBPs in Magellanic clouds.

To further investigate this problem, Paul *et al*. (2002) performed a pulse-phase resolved spectral analysis of SMC X-1 data obtained with ASCA. The pulse phase dependences of the power-law flux, blackbody flux, and total flux are plotted in the right panel of Fig. 2 together with the energy dependent pulse profiles (left panel). Although statistically limited, the blackbody flux is modulated with a broad sinusoidal shape, as seen in the top of right panel of Fig. 2, contrary to the sharp double peak feature of power-law flux, which is just the same as the pulse profiles at high energies. A phase lag in modulation between the peaks of the blackbody component and that of the power law component is also seen in the figure. Interestingly, these situations are quite similar with those of Her X-1. This fact may give some hints to understand the soft-excess features commonly seen from LMXBPs, HMXBPs and BeXBPs, although some crucial consideration of the binary system geometry is required to explain the large luminosity of pulsating blackbody emission at the distances of Magellanic clouds.

Soft excess features are also observed from X-ray spectra of active galactic nuclei and black hole candidates, and they are considered to be the result of reprocessing by an accretion disk of the original X-ray emission. Hence it is interesting to investigate if the soft excess features observed from XBP spectra are related with the reprocessing by an accretion disk and share common mechanism with those X-ray sources. A merit of investigating soft excess feature using XBP spectra is that it allows us to search pulse modulation of the soft component.

Anomalous X-ray pulsars (AXPs) are also known to have a two component spectra, a steep power law and blackbody emission model (e.g., Mereghetti & Stella 1995).

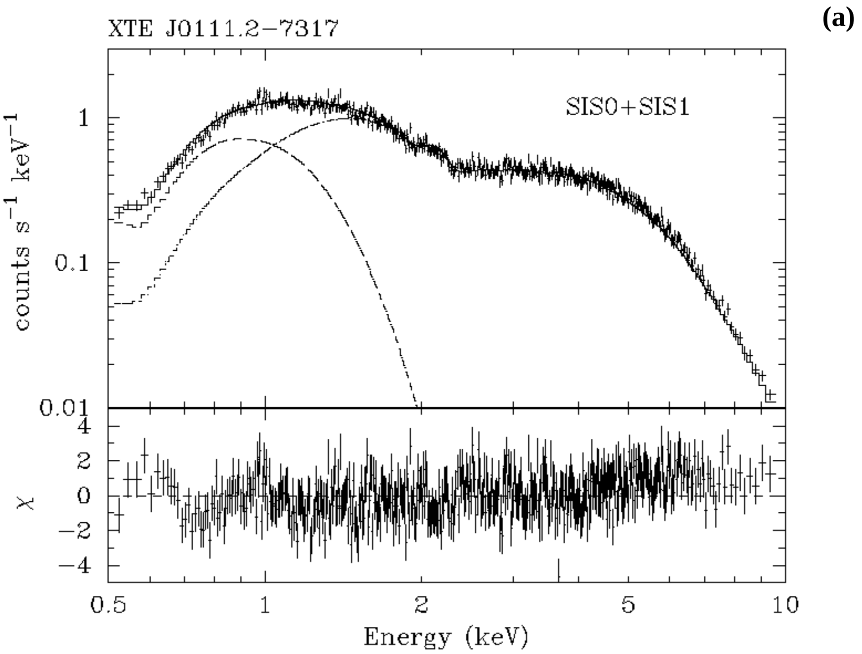

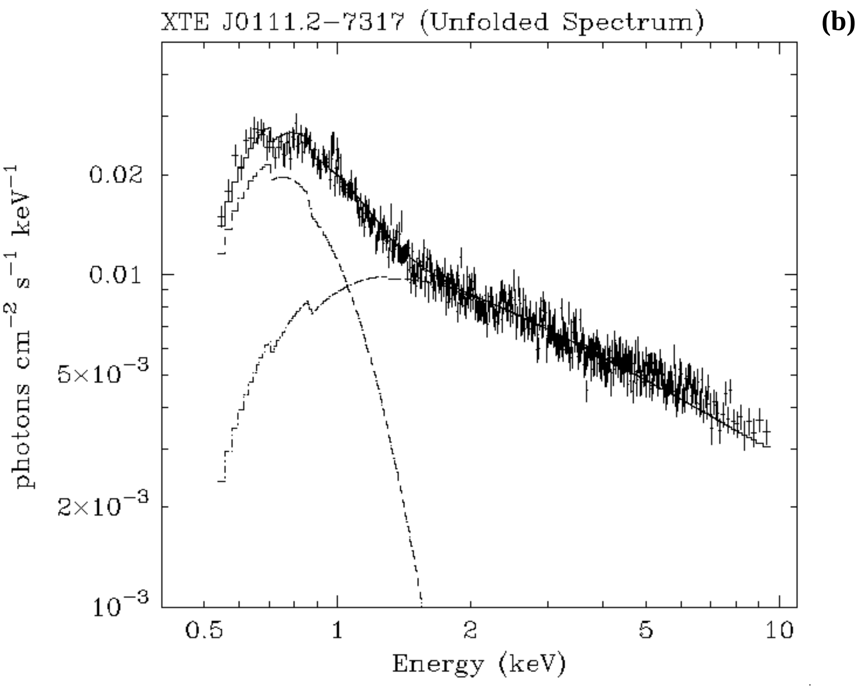

Figure 1. **(a)** Energy spectrum of XTE J0111.2–7317 observed with ASCA. The solid line indicates a summed best fit model, and the dotted and dashed lines represent the power law and blackbody components, respectively. **(b)** Unfolded incident spectrum of XTE J0111.2–7317.

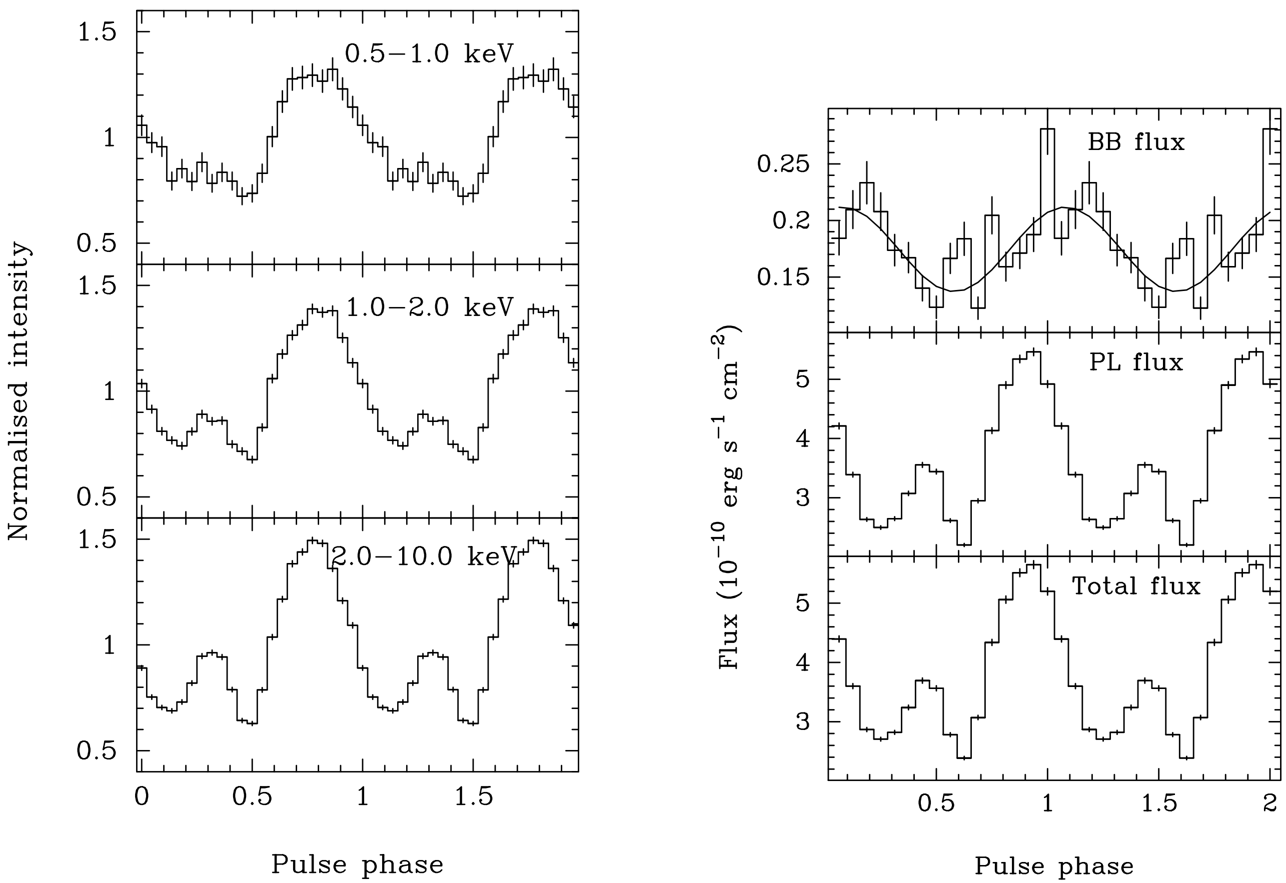

Figure 2. **Left panel**: Normalized pulse profiles of SMC X-1 in three energy bands observed with ASCA/GIS in 1993. **Right panel**: Modulation of the blackbody flux, power-law flux, and total flux in the 0.5–10 keV band of SMC X-1 obtained from pulse-phase resolved analysis of the ASCA/GIS spectrum.

However, the blackbody temperatures of AXPs are relatively high and the flux fraction of the blackbody emission to that of the power law component is significantly larger than that in the LMXBP, HMXBP, and BeXBP spectra. Thus the situation in AXPs is somehow different from the soft excess feature seen in other accreting X-ray pulsars. Recently AXPs are interpreted to be not in binary systems but consist of an isolated neutron star with extremely strong magnetic field (i.e., Magnetars) and X-ray emission is due to some different mechanisms (e.g., Thompson & Duncan 1996, Baring & Harding 1998).

3. High resolution spectroscopy of XBPs

Solid state imaging spectrometers (SIS, i.e., CCD cameras) on board ASCA had a good energy resolution, and it became possible to resolve Kα emission lines of highly ionized (H-like or He-like) atoms of heavy elements, such as Mg, Si, S, Ar, Ca, and Fe, from those of neutral or low-ionization atoms. A few new discoveries were made in the field of accreting X-ray pulsars by utilizing the good resolution spectroscopy with the SIS.

A prominent emission line was detected at 1 keV in the spectrum of 4U 1626–67 and the line was identified as the Kα line of He-like Ne (Angelini *et al*. 1995), giving an opportunity to study the nature of the companion star. Recombination lines of He-like and H-like ions of various heavy elements were detected in the spectra observed with ASCA from Vela X-1 (Nagase *et al*. 1994; Sako *et al*. 1999) and Cen X-3 (Ebisawa *et al*. 1996, Wojdowski *et al*. 2001) during their eclipse phase. These detections of recombination lines proved the existence of photoionized plasma spheres of stellar wind that were produced through the irradiation of stellar wind by the X-rays emitted from the neutron star. These observations made it possible to investigate in detail the photoionized structure of stellar wind surrounding the neutron star (Sako *et al*. 1999; Wojdowski *et al*. 2001).

Further detailed studies of plasma structure became possible with the high resolution grating spectrometers on board the recently launched X-ray astronomy observatories, Chandra and XMM-Newton. They have a power to resolve the triplet (resonance, intercombination, and forbidden) lines of He-like ions for various elements from oxygen to iron. Already, many early results of high resolution spectroscopy have been reported from observations of various X-ray sources including XBPs. An interesting example is the detection of blue and red shifted Doppler pair of lines from the LMXBP, 4U1626$-$67 with the Chandra/HETGS (Schulz *et al*. 2001). They resolved the O/Ne complex lines into blue shifted line of 1600–2600 km s^{-1} and red shifted lines of 770–1900 km s^{-1}.

High resolution spectroscopy of Vela X-1 with Chandra/HETGS at three different orbital phases revealed dramatic changes of spectra with orbital phase (Sako *et al.* 2001). Spectra at orbital phases 0.0 and 0.5 are dominated by a lot of emission lines (about 50 lines), whereas the spectrum at orbital phase 0.25 consists primarily of continuum radiation with several weak resonant absorption lines. From comparison of spectra observed at orbital phases 0.0 and 0.5, bulk velocity fields of $\sim$ 500 km s^{-1} are detected in the Ne X, Mg XII, and Si XIV Kα lines. These observations provide crucial clues to understand the structure and dynamics of circumstellar matter in the binary system. Emission-line dominated spectra similar to Vela X-1 were also observed from SMC X-1 during eclipse and during the X-ray low state, contrary to the continuum dominated spectrum observed during X-ray high, non-eclipse phase (Vrtilek *et al.* 2001). Thus, it is promising that the high resolution observations with Chandra and XMM-Newton will open a new window to diagnose plasma structure and stellar wind dynamics in X-ray binary systems.

References

Angelini, L. *et al*. 1995, *ApJ*, **449,** L41.
Baring M. G., Harding A. K. 1998, *ApJ*, **507,** L55.
Dal Fiume, D. *et al*. 1998, *A&A*, **329,** L41.
Ebisawa, K. *et al*. 1996, *PASJ*, **48,** 425.
Endo, T., Nagase, F., Mihara, T. 2000, *PASJ*, **52,** 223.
Hughes, J. P. 1994, *ApJ*, **427,** L25.
Kii, T. *et al*. 1986, *PASJ* **38,** 751.
Kohno, M. Yokogawa, J., Koyama, K., 2000, *PASJ*, **52,** 299.
La Barbera, A. *et al*. 2001, *ApJ*, **553,** 375.
Makishima, K., Mihara, T., Nagase, F., Tanaka, Y. 1999, *ApJ*, **525,** 978.
Marshall, F. E., White, N. E., Becker, R. H. 1983, *ApJ*, **266,** 814.
McCray, R. A. *et al*. 1982, *ApJ*, **262,** 301.
Mereghetti S., Stella L. 1995, *ApJ*, **442,** L17.
Mihara, T. 1995, PhD thesis, Dept. of Physics, Univ. of Tokyo.
McCray, R. A. *et al*. 1982, *ApJ*, **262,** 301.
Nagase, F. 1989, *PASJ*, **41,** 1.
Nagase, F. *et al*. 1994, *APJ*, **436,** L1.
Orlandini, M. *et al*. 1998, *ApJ*, **500,** L163.
Paul, B. *et al*. 2001, *AdSpR*, **21,** 399P.
Paul, B. *et al*. 2002, *ApJ* submitted.
Sako, M., Liedahl, D. A., Kahn, S. M., Paerels, F. 1999, *ApJ*, **525,** 921.
Sako, M. *et al*. 2001, *AAS*, **198,** 1202S
Schulz, N. S. *et al.* 2001, *ApJ*, **563,** 941.
Thompson C., Dancan R. C. 1996, *ApJ*, **473,** 322.
Trümper, J. *et al*. 1978, *ApJ*, **219,** L105.
Vrtilek, S. D. *et al*. 2001, *ApJ*, **563,** L139.
Wheaton, W. A. *et al*. 1979, *Nature*, **282,** 240.
White, N. E., Swank, J. H., Holt, S. S. 1983, *ApJ 270,* 711.
Wojdowski, P. *et al*. 1998, *ApJ*, **502,** 253.
Wojdowski, P. S., Liedahl, D. A., Sako, M. 2001, *ApJ*, **547,** 973.
Woo, J. W. *et al*. 1996, *ApJ*, **467,** 811.
Yokogawa, J. *et al*. 2000, *ApJ*, **539,** 191y.

J. Astrophys. Astr. (2002) **23,** 67–72

Evolution of Neutron Star Magnetic Fields

Dipankar Bhattacharya *Raman Research Institute, Bangalore 560 080, India.*

Abstract. This paper reviews the current status of the theoretical models of the evolution of the magnetic fields of neutron stars other than magnetars. It appears that the magnetic fields of neutron stars decay significantly only if they are in binary systems. Three major physical models for this, namely spindown-induced flux expulsion, ohmic evolution of crustal field and diamagnetic screening of the field by accreted plasma, are reviewed.

Key words. Neutron stars—Magnetic field.

1. Introduction

Neutron stars are strongly magnetised objects, with the surface field strength ranging from $\sim 10^8$ to 10^{13} G, as inferred from radio pulsars, accreting X-ray pulsars and low-mass X-ray binaries. There also exists another class of objects, consisting of anomalous X-ray pulsars and soft gamma repeaters, often referred to under the umbrella term "magnetars", in which the magnetic field of the underlying neutron stars probably approaches $\sim 10^{15}$ G. In this lecture I shall address the issue of the evolution of the magnetic fields of neutron stars of the first variety. At field strengths as high as those for magnetars, a different physics operates to determine field evolution (see Thompson 2000), which will be beyond the scope of this brief review.

It is now an established fact that among radio pulsars the isolated objects primarily have their magnetic field strengths clustered around 10^{12} G, and significantly lower field strengths are mainly associated with pulsars in binary systems. While it was once thought that pulsars in binary systems have lower field strengths simply by virtue of their larger age, detailed analyses of the radio pulsar population have failed to find evidence of spontaneous field decay in isolated objects (Bhattacharya *et al.* 1992; Mukherjee and Kembhavi 1997; Lorimer *et al.* 1997). The currently preferred view, therefore, is that processing of neutron stars in binary systems affect their magnetic field strength.

The magnetic field of a neutron star determines the evolution of its spin, its radiative properties and its interaction with the surrounding medium. The evolution of the magnetic field is therefore a key component in the evolution of the neutron star as a whole, but it remains to be clearly understood. In the following sections I shall review our current, relatively incomplete, understanding of the magnetic field evolution.

2. Location of the field

A neutron star has two distinct regions in its structure:

- A core, constituting the bulk of the star, where the density is above nuclear matter density. In this region the neutrons ($\sim$99%) and protons ($\sim$ 1%) are not bound in nuclei. The neutrons are expected to form a ^3P superfluid and the protons a ^1S superconductor (Sauls 1989).
- A crust overlying the core. Here the density gradient is sharp, rising from a few g/cm^3 at the surface to nuclear density (3×10^{14} g/cm^3) within $\sim$10% of the stellar radius. The protons in the crust are bound in nuclei that get progressively neutron rich as density rises. At densities above 4×10^{11} g/cm^3 free neutrons appear, and co-exist with nuclei until nuclear density is reached. The nuclei in the crust are expected to form a lattice; the electrons are free and highly degenerate, resulting in metal-like transport properties (electrical and heat conductivities) in this region (Yakovlev & Urpin 1980).

We have no *a priori* knowledge of the distribution of the magnetic field in the interior of the neutron star. This would be determined by the process that generated the magnetic field in the first place. In the simplest scenario, that of flux-freezing from the progenitor, the field would most likely be distributed throughout the interior. However, in some other scenarios, e.g., the thermo-magnetic battery effect (Blandford *et al.* 1983), most of the magnetic field will be confined to the crust.

The evolution of the magnetic field in these different cases is expected to be different. Observation of the long-term evolution of the magnetic field could therefore in principle be used to put constraints on the location of the field in the neutron star interior. However the subject is still too premature to realise this in practice.

In either model of the location of the magnetic field, changes in the field strength could be expected both due to spontaneous evolution and due to accretion. A physical model of field evolution should satisfy the observational constraints that relatively little magnetic field decay should take place in isolated radio pulsar population (dominated by neutron stars in the age range 10^5–10^7 years), while accretion should be able to reduce the surface field strength by several orders of magnitude.

3. Mechanisms of field evolution

The simplest possible cause for field decay would be ohmic dissipation. Conductivities low enough for this to be important are encountered only in the outer parts of the crust in an isolated, cooling neutron star. If the neutron star is accreting, however, the resulting increase in crustal temperature and the consequent reduction of conductivity could be important for most of the crust.

If the magnetic flux is originally located in the superconducting interior, it has to be first expelled to the crust before any decay can occur. A mechanism for this was suggested by Srinivasan *et al.* (1990): In the core of the neutron star the protons are expected to form a Type II superconductor, which can carry magnetic flux in quantized fluxoids. Although the magnetic field here is probably less than the lower critical field, estimated to be of order 10^{15} G, the flux is nevertheless thought to be trapped in fluxoids in a metastable state. The reason for this is that the electrons, which also permeate this region, form an extremely highly conducting normal fluid, making it impossible to expel the flux from this region in the time scale of nucleation of superconductivity in the initial few months after the formation of the neutron star (see Sauls 1989 for a review). The rotation of the neutron star causes vortices in the neutron superfluid co-existing with the proton superconductor. Pinning and electromagnetic interaction are expected to exist between the neutron vortices and proton fluxoids, causing the fluxoids to be dragged out to the crust as the star spins down and vortices are expelled (Srinivasan *et al.* 1990, Bhattacharya & Srinivasan 1995).

Just the expulsion of the magnetic flux from the core still does not imply a change in the field strength of the star as experienced by an external observer. The expelled field must then decay due to ohmic processes for this to happen. If the crust is made of pure cold catalysed matter annealed into a perfect crystalline state, the conductivity of the inner crust is much too high for the flux deposited at the bottom of the crust to evolve appreciably in a Hubble time. A significant impurity concentration in the crust and/or a turbulent Hall cascade (creating small scale current loops) must be invoked to bring the effective ohmic time scale down to interesting values (Goldreich & Reisenegger 1992; Bhattacharya & Datta 1996).

Yet another possible way to reduce the magnetic field strength felt outside the star is to screen the field away by accreting matter (e.g., Bisnovatyi-Kogan & Komberg 1974). As the highly conducting accreting plasma settles and spreads onto the surface of the neutron star, it could produce a diamagnetic screening effect, burying the stellar field underneath it. This mechanism would not depend on the location of the field in the stellar interior.

4. Recent results

4.1 *Core field*

The vortex-fluxoid coupling model has been developed considerably since its first suggestion, and application to various classes of neutron stars has been explored in some detail. The most comprehensive work to date is by Jahan-Miri (2000), who finds that it is possible to reproduce the long-lived low magnetic field strengths of most binary pulsars, assuming a decay time of $\sim 10^7$ yr for the expelled field, and a rather efficient spin-down of the neutron star during the "propeller phase" of accretion, when the accreting plasma is expelled from the magnetosphere, extracting angular momentum from the spinning neutron star via magnetic coupling. The shorter the decay time scale of the expelled field, the quicker the propeller phase ends, limiting the total amount of flux expulsion from the interior. Decay time scales as short as 10^7 yr are, however, somewhat difficult to reconcile with some of the accreting X-ray pulsars in massive binary systems where fields of order 10^{12} G appear to survive, as well as with the population of isolated pulsars if most pulsars are born with spin periods much less than a second (Bhattacharya *et al.* 1992; Jahan Miri & Bhattacharya 1994). It appears difficult in this model to reproduce the high residual magnetic fields in some recycled pulsars arising from low-mass X-ray binaries (e.g., 3×10^{11} G in PSR B0820+02).

Of late, some attempts have been made to model the feedback of the expelled and accumulated flux at the crust bottom on further flux expulsion. Konenkov & Geppert (2000), within a simplified model, estimate this feedback to be very strong for magnetic field strengths above $\sim 10^{11}$ G, and suggest that the spindown-induced flux expulsion would be very ineffective for neutron stars with original core field strengths above this value.

4.2 *Crustal field*

The evolution of the magnetic flux originally confined to the crust depends on the depth at which the bulk of the current distribution is located. This is because conductivity rises steeply with depth, nearly proportional to density in a pure matter crust. In the outer crust, conductivity depends significantly on the local temperature, while in the inner crust (at densities above $\sim 10^{13}$ g/cm^3) impurity scattering may dominate the resistivity mechanism.

A neutron star is born hot, and cools with time (unless accretion occurs on the surface). The conductivity of the outer crust therefore increases with time. Cooling rates of neutron stars have been computed under various assumptions, a useful compendium is found in Page (1998). Using a typical "standard" cooling curve for a neutron star, one finds that the magnetic field of an isolated neutron star would decay by some amount in the first $\sim 10^5$ yr, when the star is still relatively hot, and thereafter remain constant (cf. Urpin & Van Riper 1993). This field reduction could be about a factor of ~ 30 if the initial confinement depth of the field corresponds to a density $\rho \sim 10^{11}$ g/cm^3, whereas it would be only a factor of ~ 2 for a confinement density of $\sim 10^{13}$ g/cm^3. However, since most observed radio pulsars are older than $\sim 10^5$ yr, it is at present not possible to determine the extent of this early decay from observations (Tauris & Konar 2001).

Accretion onto the neutron star affects the evolution of the crustal field in two ways. First, the accretion process raises the crustal temperature and maintains it at a high level through the duration of accretion. Second, the accreted mass compresses the original crustal matter, raising the density of the current carrying layers. After the accretion of about $\sim 10^{-2} M_\odot$ the original crust would be assimilated into the core. While the heating of the crust hastens the ohmic decay, the compression and the consequent rise in local conductivity retards it, so the final result depends on the competition between these two processes. Detailed computations show the general nature of the field evolution to be that of a rapid initial decay followed by a "freezing", at a "residual" field strength determined by the original confinement depth and the accretion rate. The lower the accretion rate, the longer the initial decay lasts, resulting in a correlation between the residual field strength and the accretion rate (Konar & Bhattacharya 1997), as appears to have been found in some low-mass X-ray binaries (White & Zhang 1997).

This scenario of field evolution is able to reproduce many of the broad features of the magnetic field distribution of neutron stars (Urpin, Geppert & Konenkov 1998; Konar & Bhattacharya 1999). More detailed work still remains to be done to model individual observed cases. Nevertheless, this remains one of the attractive models of field evolution.

4.3 *Diamagnetic screening*

The idea that the accreting stream of plasma could screen the magnetic field of a neutron star as it settles down has been in the literature for a long time (Bisnovatyi-Kogan & Komberg 1974; Taam & van den Heuvel 1986; Romani 1990). However this problem is only now beginning to be addressed with some of the necessary microphysics. It turns out that the accretion flow in the polar cap of a magnetised neutron star is acutely susceptible to various magnetohydrodynamic instabilities and it is difficult to make even a qualitative assessment of the effectiveness of screening without a full three-dimensional computation which is yet to be attempted. One-dimensional plane-parallel models by Cumming, Zweibel & Bildsten (2001) suggest that the diamagnetic screening is ineffective for field strengths above $\sim 10^{10}$ G as well as for accretion rates below ~ 1 per cent of the local Eddington rate. For higher field strengths, magnetic buoyancy prevents screening, and at lower accretion rates the field can diffuse through the accreting matter.

A two-dimensional (azimuthally symmetric) model explored recently by Rai Choudhuri & Konar (2001) uses a self-consistent velocity field of the accreted matter as it sinks and joins the rest of the crust. They find that the screening does operate in their model, but in the presence of magnetic buoyancy the net reduction in field strength does not exceed about an order of magnitude.

The real three-dimensional situation may be qualitatively different, however. Instabilities leading to bunching of magnetic field lines, leaving relatively low-field regions for the accreting matter to spread through are a real possibility. Such instabilities will further reduce the degree of diamagnetic screening that can be achieved. One needs to make realistic MHD simulations to address this possibility.

5. Conclusions

A successful model of the origin and evolution of the magnetic field of neutron stars should provide a natural explanation for the following basic observational facts:

- the range $\sim 10^{12}$ to $\sim 10^{15}$ G of the field strengths of young neutron stars,
- the relative stability of the field strength of isolated pulsars in the time scale of $\geq 10^8$ years, perhaps with a small reduction by less than an order of magnitude,
- the reduced magnetic fields in neutron stars processed in binaries,
- on an average, larger field reduction in products of low-mass X-ray binaries than those of high-mass X-ray binaries,
- evidence, from cyclotron lines, of strong ($\sim 10^{12}$ G) magnetic fields in several *accreting* X-ray binaries and
- apparent correlation between luminosity and magnetic field in low-mass X-ray binaries.

Clearly, none of the models presented above addresses all of these issues. On the whole, at present the ohmic evolution of crustal field appears to be somewhat more successful than the others. However several mechanisms, such as the diamagnetic screening by accreted matter as well as Hall effect-driven evolution are only now beginning to be explored in quantitative detail, and will hopefully be able to contribute to a better understanding of the field evolution.

References

Bhattacharya, D., Srinivasan, G. 1995, in: *X-ray Binaries*, (eds) W. H. G. Lewin, J. A. van Paradijs & E. P. J. van den Heuvel (Cambridge: Cambridge University Press), 495.

Bhattacharya, D., Datta, B. 1996, *MNRAS*, **282,** 1059.

Bhattacharya, D. *et al.* 1992, *A&A*, **254,** 198.

Bisnovatyi-Kogan, G. S., Komberg, B. V. 1974, *Sov. Astr.*, **18,** 217.

Blandford, R. D., Applegate, J. H., Hernquist, L. 1983, *MNRAS*, **204,** 1025.

Cumming, A., Zweibel, E., Bildsten, L. 2001, *Ap. J.*, **557,** 958.

Goldreich, P., Reisenegger, A. 1992, *Ap. J.*, **395,** 250.
Jahan-Miri, M. 2000, *Ap. J.*, **532,** 514.
Jahan Miri, M., Bhattacharya, D. 1994, *MNRAS*, **269,** 455.
Konar, S., Bhattacharya, D. 1997, *MNRAS*, **284,** 311.
Konar, S., Bhattacharya, D. 1999, *MNRAS*, **303,** 588.
Konenkov, D., Geppert, U. 2000, *MNRAS*, **313,** 66.
Lorimer, D. R., Bailes, M., Harrison, P. A. 1997, *MNRAS*, **289,** 592.
Mukherjee, S., Kembhavi, A. 1997, *Ap. J.*, **489,** 928.
Page, D. 1998, in: *The Many Faces of Neutron Stars*, (eds) R. Buccheri, J. A. van Paradijs & M. A. Alpar (Dordrecht: Kluwer), 539.
Rai Choudhuri, A. R., Konar, S. 2001, *MNRAS*, in press (astro-ph/0108229).
Romani, R. 1990, *Nature*, **347,** 741.
Sauls, J. A. 1989, in: *Timing Neutron Stars*, (ed.) H. Ögelman & E. P. J. van den Heuvel (NATO ASI C262: Dordrecht: Kluwer), 457.
Srinivasan, G. *et al.* 1990, *Curr Sci*, **59,** 31.
Taam, R. E., van den Heuvel, E. P. J. 1986, *Ap. J.*, **305,** 235.
Tauris, T. M., Konar, S. 2001, *A&A*, **376,** 543.
Thompson, C. 2000, in: *Pulsar Astronomy: 2000 and beyond*, (ed.) N. Wex & N. Wielebinski (San Francisco: ASP), 669.
Urpin, V., Geppert, U., Konenkov, D. 1998, *MNRAS*, **295,** 90.
Urpin, V., Van Riper, K. A. 1993, *Ap. J.*, **411,** 87.
White, N. E., Zhang, W. 1997, *Ap. J.*, **490,** L87.
Yakovlev, D. G., Urpin, V. A. 1980, *Soviet Astronomy*, **24,** 303.

J. Astrophys. Astr. (2002) **23,** 73–79

SROSS C-2 Detections of Gamma Ray Bursts and the SGR 1627-41

S. Sinha, P. Sreekumar & K. Kasturirangan *ISRO Satellite Center, Bangalore 560 017, India.*

Abstract. The GRB monitor (GRBM) on board the Indian SROSS C-2 satellite has detected 53 classical gamma ray bursts since its launch in May, 1994 till its re-entry in July, 2001. For a subset of 26 events, locations were obtained from simultaneous observations by other gamma-ray detectors in space. The sky distribution of these 26 SROSS C-2 bursts is consistent with isotropy. The distribution of event durations shows evidence for bimodality. There is an evidence for a moderate hardness ratio-intensity (HIC) correlation in the data. The SROSS C-2 GRBM has also detected three episodes of emission from the SGR 1627-41.

Key words. Gamma Ray Bursts—SGRs.

1. Introduction

The primary focus of gamma-ray burst research in the 80s and early 90s was to determine the sky distribution of the GRBs along with source localisations of sufficient accuracy (less than one arc minute) to permit observations at other frequencies. Given the poor angular resolutions of gamma-ray burst detectors and wide field-of-view, the objective was to obtain as many independent gamma-ray detections as possible, using many widely-spaced observing platforms in space. Such near-simultaneous observations of events with accurate arrival times permit event triangulation leading to a significantly smaller error box on the sky. After the discovery of X-ray afterglows from GRBs by the Italian-Dutch BeppoSax satellite in 1997 that provided accurate source positions and follow-up optical spectroscopy by large optical telescopes such as the 10-m KECK telescope, the extreme distances to these objects (billions of light years) and hence the enormous luminosity in gamma rays was convincingly demonstrated.

It is in the pre-1997 context that experiments to monitor gamma ray bursts were placed onboard the Stretched Rohini Series Satellites (SROSS). The most successful of these was onboard the SROSS C-2 satellite launched on May 4th, 1994 (Kasturirangan *et al.* 1997). The primary goals of this experiment included:

- detection of GRBs in the 20 keV to 3 MeV energy range,
- determination of intensity variation with high time-resolution (2 ms during the peak),
- providing arrival time information, and
- deriving the energy distribution of the GRB photons.

The GRB detector on SROSS C-2 has detected 56 events in total, the latest being GRB010611 at 79568.2 UT on June 11th, 2001 before the mission ended with an atmospheric re-entry in July, 2001.

2. Instrument capabilities

The details of the instrument are described elsewhere (Kasturirangan *et al.* 1997). The SROSS C-2 GRB monitor consists of a single CsI(Na) crystal (76 mm in diameter, 12.7 mm thick) viewed by a 76 mm diameter photomultiplier tube. The pulse height spectra (107 channels) are available between 20 keV and 3 MeV with varying energy resolution—the best being 4 keV per channel. The GRB time-histories are recorded between -65.536 sec and 204.8 sec of the GRB trigger, the integration time being 256 ms for the two broadband energy channels, viz., channel 1 (20–100 keV) and channel 2 (100–1024 keV). In addition, high resolution (2 ms) GRB time-history is available during T0-1.024 sec to T0+1.024 sec and with a slightly worse time resolution (16 ms) during T0+1.024 sec to T0+8 sec in the 20–1024 keV channel (channel 1 plus channel 2). The GRB time-history is also recorded in the 1.024-3 MeV channel (channel 3) during T0-2.048 sec to T0+204.8 sec. The integration time for the channel 3 data is 512 ms. The pre-trigger data are obtained using a circulating memory. A maximum of seven events may be stored on board before the next read-out. The SROSS C-2 GRB trigger is generated by the SROSS C-2 on board software if the detector counting rate exceeds either of two preset thresholds- the integration times for these being 256 ms and 1024 ms respectively. The detector has no anti-coincidence shield and hence has a relatively large background and large number of false (charged particle induced) triggers are recorded. Also, the duty cycle of the experiment is low due to earth occultation, passage through SAA and high latitude regions.

The GRB event trigger times are derived from the satellite house-keeping telemetry clock which is based on a 128 kHz crystal oscillator. This clock has a drift rate of 274 ± 44 ms (one sigma) per day. This on board clock is calibrated (usually once a day) using a ground-based atomic clock.

3. Data analysis

Candidate events were selected purely on the basis of their temporal characteristics, viz. their short durations, fast variability and the nature of the background before and after the trigger from a very large number ($\sim 10,000$) of triggers. After careful selection, the event parameters and their errors are determined using the temporal and spectral data.

Maximum amount of data have been used in order to calculate an accurate detector background. This is done by removing the BURST portion in the GRB time history, since quite often the real burst is of very short duration. The GRB duration (T_{90}) is calculated using an algorithm that detects the onset and disappearance of the burst precisely by successively higher time integration of the burst signal and when a consistent value for this parameter is achieved. For the peak hardness ratio calculation, a similar approach is used. The minimum S/N ratio in both channel 1 and channel 2 has to be equal to or greater than 5. The peak hardness ratio is defined as the hardness ratio when the signal peaks in the 2nd (triggering) channel (100–1024 keV). The GRB fluences in the three energy channels are calculated using successive spectral and temporal integration. Several systematic errors including the variable drift of the on board clock have been taken into account to arrive at accurate (few ms uncertainty) trigger times for several GRBs.

4. Results

4.1 *Timing accuracy*

The SROSS C-2 on board clock has a large drift rate which is also highly variable. However, for a few GRB events it has become possible to correct for all the systematic and random errors and finally arrive at accurate (a few ms uncertainty) absolute event trigger times. Cross-correlations of these SROSS C-2 GRB time-histories with their corresponding BATSE and BeppoSax time-histories (K. Hurley, pvt. comm.) have given the following results:

Table 1.

GRB Name	SROSS C-2 trigger time and its uncertainty (3σ)secs (UT)	Time lag (secs)
981226	38758.844 ± 0.014	0.037 ± 0.074
990323	62914.103 ± 0.008	-0.002 ± 0.044
990424	11489.819 ± 0.018	-0.034 ± 0.350
010427	67390.912 ± 0.012	0.059 ± 0.174

The first three event time-histories were cross-correlated with their corresponding BATSE time-histories and the last one with its corresponding BeppoSax time-history. The maximum expected time lag between a SROSS C-2 event and the corresponding BATSE event is $\sim$ 45 ms. The absolute time inaccuracy for the second and third events are respectively -4 ms and -36 ms. The large uncertainties in the time lag is due to the poor S/N ratio of these events.

4.2 *Sky distribution*

The locations of 26 classical GRBs (22 of these were obtained from the BATSE 4B and BATSE current catalogs for SROSS C-2 GRBs that have near simultaneous BATSE triggers, 2 were obtained from GCN 763 and GCN 853 (Hurley *et al.* 2000) and another 2 also determined by the 3rd IPN (K. Hurley, pvt. comm.)) are plotted in galactic coordinates (Fig. 1). The distribution is consistent with isotropy.

4.3 *The T_{90} (duration) distribution: The 'tip of the iceberg effect'*

T_{90} is a measure of the duration of a GRB (the time interval during which the burst integrated counts increases from 5 % to 95 % of the total counts). The T_{90} distribution for 49 GRBs is shown in Fig. 2(a). Our data are consistent with the bimodality reported earlier (Kouveliotou *et al.* 1993). Since the SROSS C-2 GRB monitor does not possess any anti-coincidence shield, the detector background is much higher compared to a GRB detector that has an anti-coincidence shield. This essentially implies that the S/N ratio of a detected burst is much smaller than what it would be for a detector having an anti-coincidence shield. Due to this reason, our T_{90} values are systematically lower than the corresponding BATSE T_{90} values. Hence the well known dip (Kouveliotou *et al.* 1993) near 2 secs is shifted in our case to 0.4 seconds in the T_{90} axis.

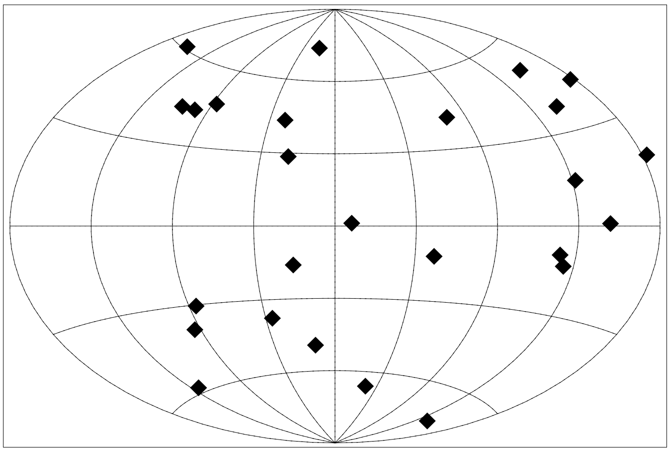

Figure 1. Sky distribution (Galactic coordinates) of 26 SROSS C-2 classical GRB events.

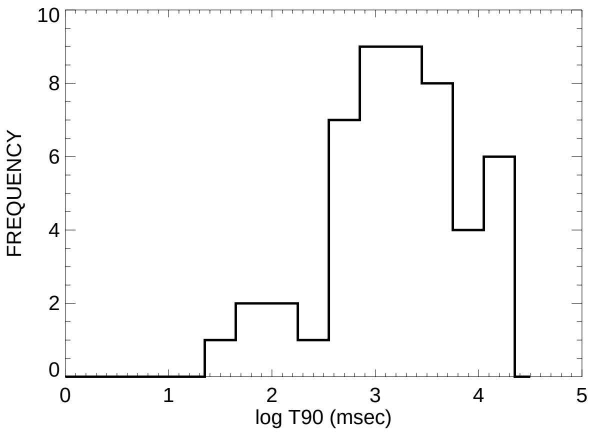

Figure 2(a). Duration distribution of 49 SROSS C-2 classical GRBs.

4.4 *The hardness ratio distribution*

The hardness ratio is defined as the ratio of detected counts in the 100–1024 keV energy band to that in the 20–100 keV energy band. The distribution of this parameter for 48 events observed by the SROSS C-2 GRBM is shown in Fig. 2(b). For the sake of comparison, the hardness ratio (similarly defined) distribution for the subset of 22 SROSS C-2 GRBs are shown (dotted histogram) that have near simultaneous BATSE events. The dotted histogram is normalised to have total number of events equal to 48. The hardness ratio distribution for the complete sample is essentially similar to that of the events that have common BATSE triggers. The calculated hardness ratios contain some systematic errors since for quite a few events the direction of arrival is not known.

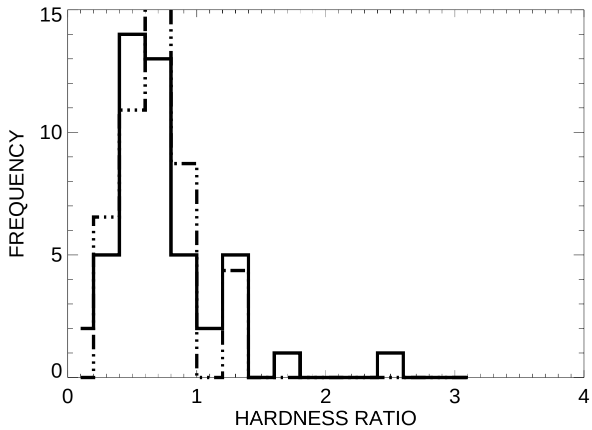

Figure 2(b). Hardness Ratio distribution of 48 SROSS C-2 GRBs (solid histogram). Hardness ratio distribution for 22 SROSS C-2 events having common BATSE triggers are also shown (dotted histogram, normalised to the same total number = 48).

4.5 *Correlations*

We have also studied correlations between different sets of parameters. The peak hardness ratio shows a moderate correlation (correlation coefficient 0.54, chance probability = 0.0028) with the peak counts in the channel two (100–1024 keV, triggering channel).

4.6 *SGR1627-41*

The SROSS C-2 GRBM has detected three episodes of emission from the SGR1627-41 on 18th June, 1998 at 6151.616 secs (UT) and at 14662.081 secs (UT) and also on 7th April, 2000 at 37496.804 secs (UT). These trigger times have small systematic errors. The durations of these outbursts from the SGR were respectively 970 ± 8 ms, 260 ± 8 ms and 1.6 ± 0.066 secs. Based on the known distance of SGR1627-41 (11 kpc) we derive the following values for the intrinsic luminosities of the source in gamma rays (assuming isotropic emission).

The peak luminosities (0.512 s) in the 20–150 keV band as observed by the SROSS C-2 GRBM for the three episodes are $6.3E39$, $2.2E40$ and $3.7E40$ ergs s^{-1} respectively. The peak luminosities (energy greater than 25 keV, $0.064s$) for 57 events observed by BATSE between 17th and 18th June, 2000 range between $1.0E39$ and $1.0E42$ ergs s^{-1} (Woods *et al.* 1999). Actually our luminosities are underestimated by factors that might be as large as twenty because of loss of signal due to the saturation of counters. Furthermore, the larger SROSS C-2 integration time ($0.512s$) compared to that of BATSE ($0.064s$) results in reduced estimates for the luminosities derived from our observations. Taking all these into consideration the luminosities derived by us agree very well with that derived by the BATSE experiment.

Based on the spectrum of the SGR derived by the BATSE group (Woods *et al.* 1999), we estimate a hardness ratio (as would be seen by the SROSS C-2 GRBM)

Table 2(a).

Episode	Peak flux (20-100) keV	(photons $cm^{-2}s^{-1}$) (100–150) keV	Fluence (20–100) keV	(ergs cm^{-2}) (100–150) keV
1	4.87	0.17	$0.36E-6$	$0.45E-7$
2	22.19	0.05	$0.20E-5$	$0.58E-7$
3	34.46	0.86	$0.33E-5$	$0.26E-6$

Table 2(b).

Episode	Peak luminosity (20–100) keV	(ergs s^{-1}) (100–150) keV	Integrated luminosity (20–100) keV	(ergs) (100–150) keV
1	$5.8E39$	$5.0E38$	$0.52E40$	$0.65E39$
2	$2.2E40$	$1.5E38$	$2.8E40$	$8.3E38$
3	$3.5E40$	$0.24E40$	$4.7E40$	$3.8E39$

to be 0.076 which also agrees well with the hardness ratios observed by the SROSS C-2 detector.

The 000407 event (episode 3 listed in Tables 2a and 2b) was not confirmed by any other spacecraft (K. Hurley, E. Mazets, pvt. comm.). The high time-resolution data resembles very much the flare from the SGR 1627-41 on 29th June, 1998 (BATSE trigger no. 6887) (Woods *et al.* 1999). The event time history has two peaks (T_{90} duration being 1.6 ± 0.066 sec). Also, during this trigger SGR 1627-41 makes the minimum space angle with the view axis of the GRBM (49.6 degrees) whereas the other known SGRs make much larger angles. From the data it is evident that the spectral hardness of the SGR emission decreases significantly (from 0.12 to 0.03) from the first episode to the second episode that has occurred only a few hours later. On the contrary, after nearly 22 months we notice that the photon spectrum has a spectral hardness that is intermediate (0.08) of the first two episodes. Fast Fourier Transforms of the high resolution (2 ms) data for the first two burst episodes of this SGR is consistent with the statistical noise in the data.

4.7 *Unconfirmed events*

The characteristics of five events are listed in Table 3. These were not confirmed by any other spacecrafts but their characteristics suggest that they are either GRBs or other high energy transients (e.g. hard X-ray transients).

Table 3.

Event name	Trigger time (TJD:sec)	Hardness ratio	Duration T_{90}(sec)
950106	9723:38397.586	0.86 ± 0.26	8.1 ± 0.11
980612	10976:74694.711	0.60 ± 0.12	0.97 ± 0.06
990119	11197:255.591	1.0 ± 0.28	0.011 ± 0.001
000131	11574:36286.907	0.73 ± 0.10	0.97 ± 0.02
010108	11917:10824.533	0.32 ± 0.05	1.6 ± 0.06

(TJD=JD-2440000.5).

5. Discussion and conclusion

Even though the clock used in our detector is not very accurate, it has become possible to arrive at accurate (few ms uncertainty) GRB trigger times for some events by applying corrections for several systematic errors including the highly variable drift of the clock. The accuracy of the derived trigger times have been established by cross-correlating SROSS C-2 event time histories with that of other spacecrafts.

The sky distribution of SROSS C-2 classical GRBs is consistent with isotropy.

Because of relatively larger detector background (absence of anti-coincidence shield), the SROSS C-2 T_{90} values for GRBs are systematically less than that of corresponding BATSE events. Hence the well-known dip in the 2 seconds region (Hurley *et al.* 2000) is shifted towards lower values (0.4 secs) in the T_{90} axis. The hardness ratio distribution of the SROSS C-2 global sample of GRBs agrees very well with that of those events having common BATSE triggers.

Also, we report detection of three flares from SGR 1627-41. The third flare has not been convincingly detected by any other spacecraft.

Finally, we may conclude that from this experiment many of the important results (derived from other satellites) on GRBs are verified using an independent sample of data though statistics are quite low because of limited sensitivity of the detector and limited duty cycle of this experiment.

Acknowledgements

We thank T. M. K. Marar, V. N. Padmini, S. Seetha, N. L. Prasad, M. Ramakrishna Sharma, N. Uphadhyay, C. N. Umapathy, N. SeetharamMurthy for developing the GRB detector, its electronics and first level data analysis. We thank Prof. U. R. Rao for his contributions to this experiment. We thank Mr. U. N. Das and others associated with the SROSS project team. We are very much indebted to Prof. Kevin Hurley for kindly providing confirmations of SROSS C-2 GRB events with satellites in the 3rd IPN. He has done the cross-correlations of SROSS C-2 events with corresponding BATSE and BeppoSax data. We thank Dr. M. Kippen for several clarifications and Dr. G. J. Fishman & Dr. F. Frontera for permitting us to use the BATSE and BeppoSax data.

References

Hurley *et al.* 2000, *GCN Observational Report* No. 763, 853.
Kasturirangan *et al.* 1997, *Astron. Astrophys.* **322,** 778–784.
Kouveliotou *et al.* 1993, *Ap. J.,* **413,** L101.
Woods *et al.* 1999, *Ap. J.,* **519:** L139-L142.

J. Astrophys. Astr. (2002) **23,** 81–87

Chandra Observations of Tycho's Supernova Remnant

U. Hwang[1], R. Petre[1], A. E. Szymkowiak[2] & S. S. Holt[3]

[1]*NASA GSFC ([1]University of Maryland), USA*
[2]*Yale University, USA*
[3]*Olin College of Engineering, USA*

Abstract. We present a new *Chandra* observation of Tycho's supernova remnant with the Advanced CCD Imaging Spectrometer. Multicolor X-ray imaging reveals new details of the outer shock and ejecta. At energies between 4 and 6 keV, the outline of the outer shock is clearly revealed in X-rays for the first time. The distribution of the emission from lines of Si and Fe are confirmed to have a different morphology from each other, and the Si ejecta are shown to extend to the blast shock at several locations. Characteristic spectra of the outer shock and ejecta are also presented.

Key words. X-rays—supernova remnants—interstellar medium—shocks—Tycho's SNR—SN 1572.

1. Imaging observations

The remnant of SN 1572 in our Galaxy, Tycho's supernova remnant (SNR) is considered to be the prototype for the remnants of Type Ia explosions that occur through runaway thermal instabilities in a white dwarf. It was observed for 50 ks with the superb 0.5″ resolution mirror on the *Chandra* X-ray Observatory and the moderate resolution Advanced CCD Imaging Spectrometer (ACIS). The linear array of 6 CCD chips comprising ACIS-S was used, with the remnant imaged mostly on the primary spectroscopic chip S3. The western edge falls on neighboring chip S2, and the southern edge is not imaged.

The 0.5–10 keV image obtained by *Chandra* is presented in the first panel of Fig. 1. It shows Tycho's familiar circular shape, but with important new details. First, the outer edge of the remnant is marked by a thin, smooth rim that is visible from the straight northeastern edge through most of the western half. This rim closely matches a similar feature seen at radio wavelengths (Dickel *et al.* 1991). The rim is readily identified with the forward shock of the remnant that is propagating into the interstellar medium. Because the broadband X-ray emission from Tycho's SNR comes mostly from the line-rich reverse-shocked ejecta, the image formed in the nearly line-free continuum energy band between 4 and 6 keV (shown after smoothing in the second panel of Fig. 1) highlights the location of the rim.

The *Chandra* image also reveals in exquisite detail the distribution of the ejecta. It has long been noted that the X-ray emission from Tycho's SNR is clumpy (Seward *et al.* 1983), and a recent, lower spatial resolution, image from the *XMM-Newton* observatory emphasizes this (Decourchelle *et al.* 2001), but the *Chandra* image has

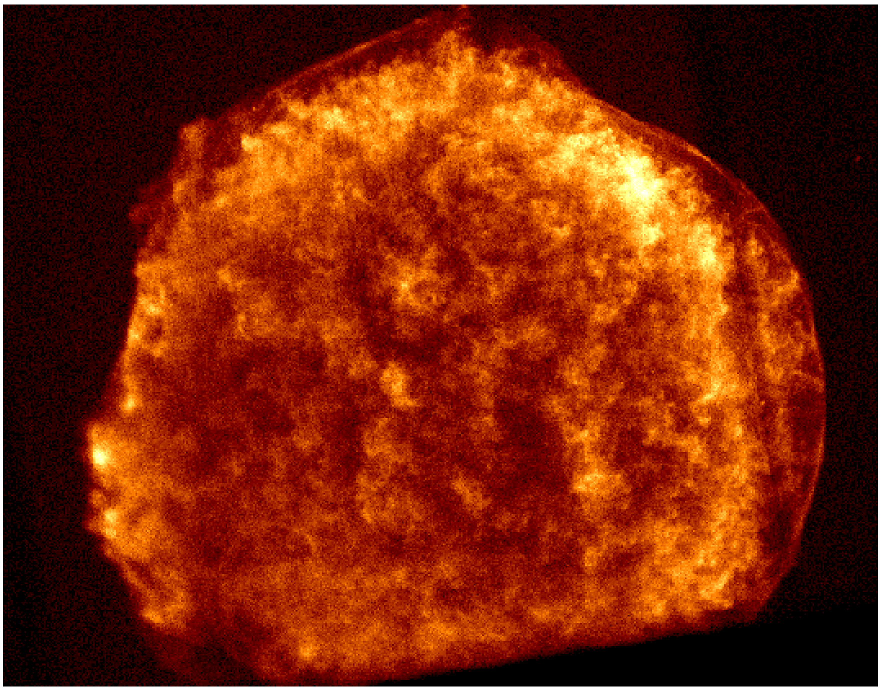

Figure 1(a). Broadband *Chandra* image of Tycho's SNR. The southernmost portion is not imaged.

the highest spatial resolution that has been obtained to date in X-rays. The third panel of Fig. 3 shows an "equivalent width" image of the Si He α blend near 1.86 keV, where the underlying continuum has been subtracted at each point in the Si image, and the ratio formed between the remaining line emission and the continuum. Such an image indicates where the Si element abundance (tracked by the relative strength of the Si line emission) is high. Most of the Si line emission is associated with ejecta because they require element abundances that are enhanced well above the solar values. This implies that the Si ejecta are distributed throughout the remnant, including at many positions near the edge of the remnant at the position of the forward shock.

2. Spectral observations

With *Chandra*'s superb spatial resolution, moderate resolution X-ray spectra can be obtained for any region of the remnant for which there are sufficient numbers of photons. Some spatially resolved spectra of compact regions obtained by *XMM-Newton* were presented by Decourchelle *et al.* (2001). Here we present a small sample of spectra on even smaller spatial scales from *Chandra*.

2.1 *Forward shock*

Chandra is able to obtain the spectrum of the thin rim and provide the first X-ray spectrum of the forward shock in this young, historical remnant. The spectrum shown on the left of Fig. 2 was taken from a portion of the northwest rim that is bright in

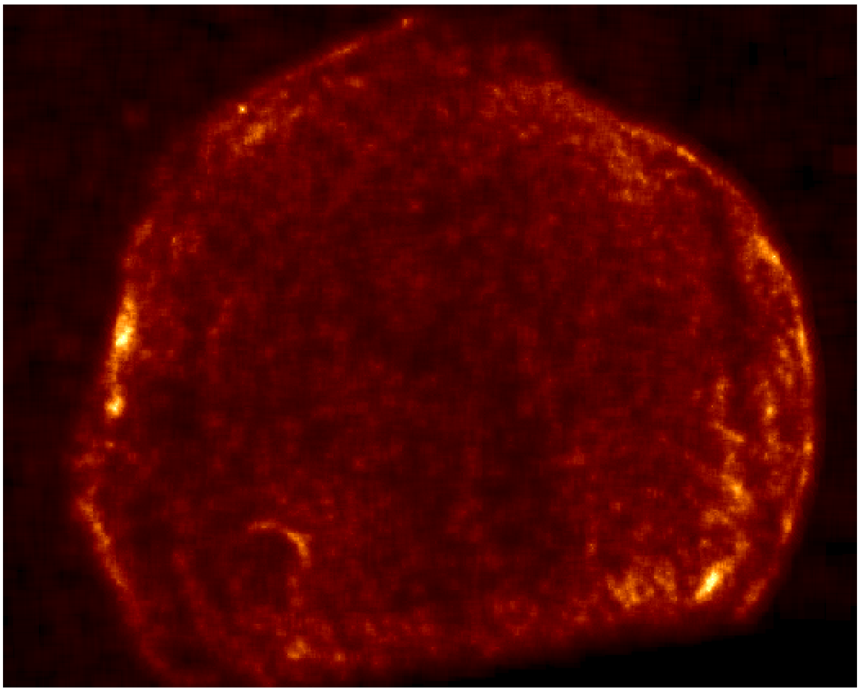

Figure 1(b). Image in the X-ray continuum at energies between 4 and 6 keV.

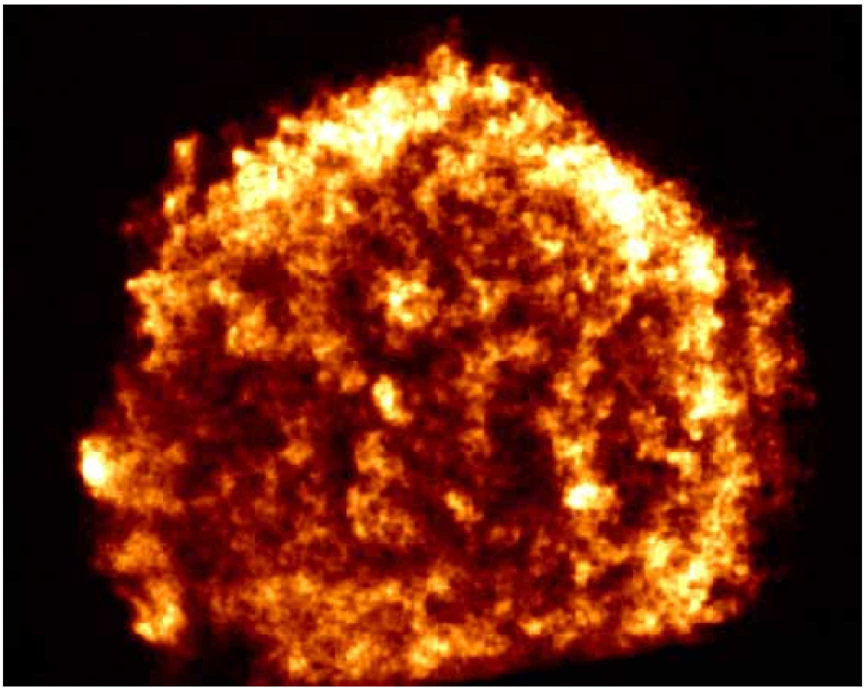

Figure 1(c). Equivalent width image (line to continuum ratio) of the Si He α blend near 1.86 keV.

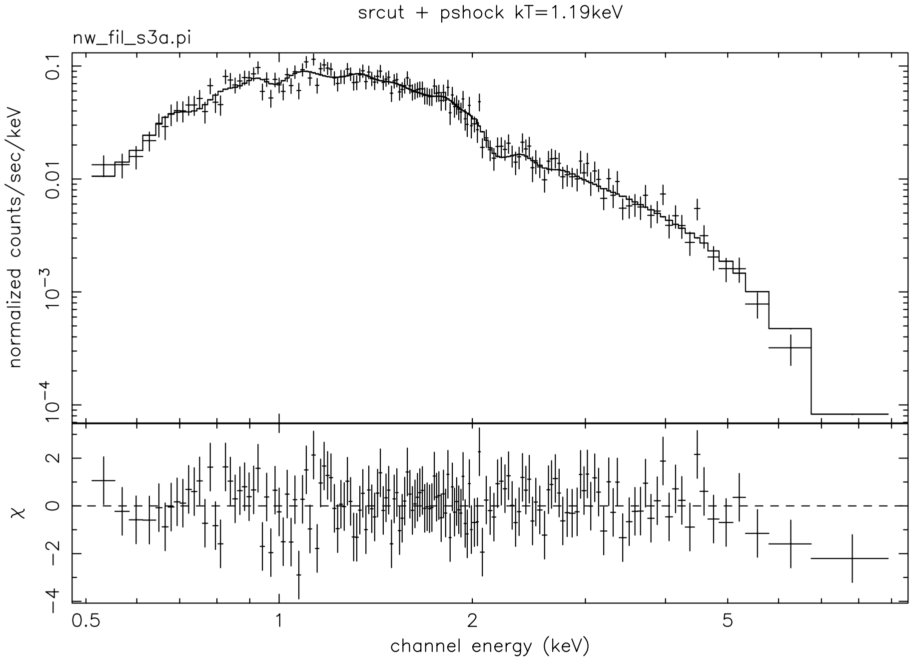

Figure 2(a). Spectrum of portion of rim in northwest. The model combines a cut-off synchrotron spectrum (srcut) and a plane parallel shock with a range of ionization ages (pshock).

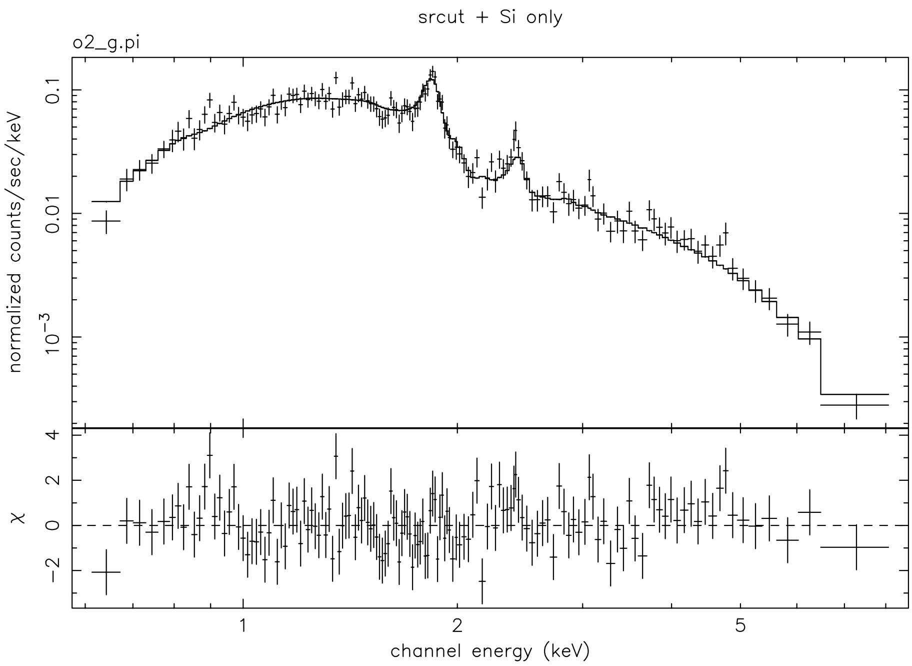

Figure 2(b). Spectrum of portion of rim in west, showing Si and S lines from ejecta.

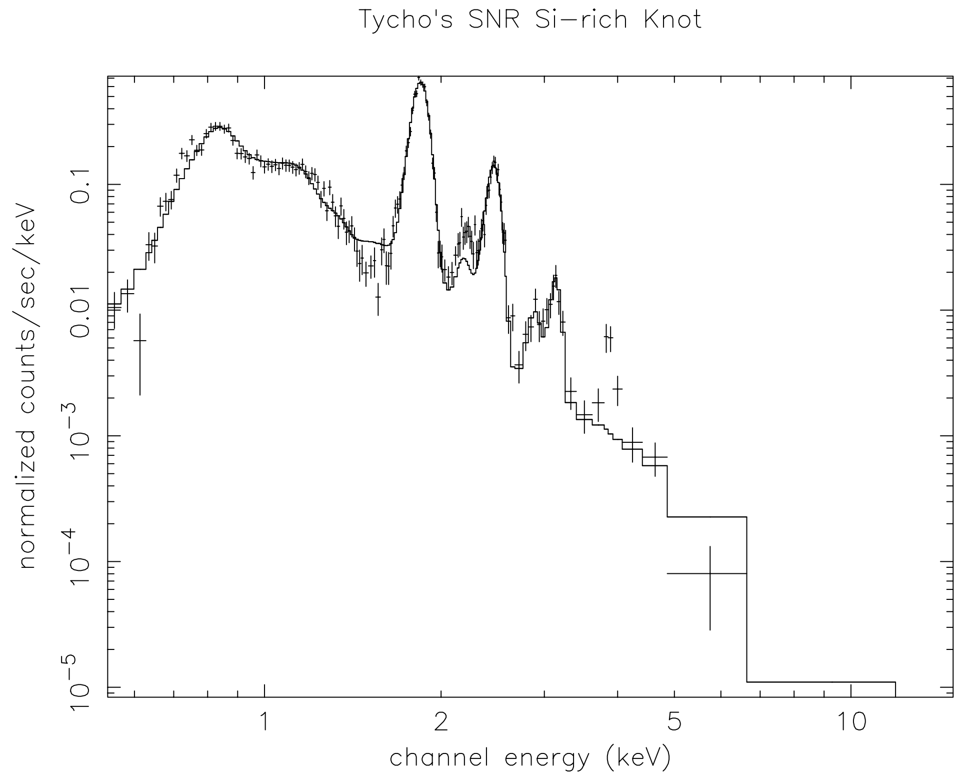

Figure 3(a). Spectrum of the Si-rich knot in the east.

the 4–6 keV continuum. It is nearly devoid of line features, and can be described either by a nonthermal synchrotron spectrum (we used one with an exponential cutoff in the electron distribution function, taking the cutoff frequency from Reynolds & Keohane (1999), and radio spectral indices from Katz-Stone *et al.* 2000), or by a thermal spectrum with very low ionization parameters and a temperature near 2 keV, or by a combination of these.

It is unfortunately not possible to distinguish between thermal and nonthermal scenarios on the basis of the *Chandra* spectra alone. Energy coverage is needed above 10 keV, where the curvatures in the spectra predicted by these models diverge more strongly. Nevertheless, it seems likely that some of the X-ray emission is nonthermal, as there is overall an excellent correspondence between the X-ray and radio outlines at the forward shock (Dickel *et al.* 1991). The nonthermal X-ray emission could come from a population of electrons accelerated to high energies at the shock in the same way as the electrons responsible for the radio emission. Moreover, the radio images show that this northwest arc is also bright in radio emission. Given that there is hard emission detected from the remnant as a whole at energies up to 25–30 keV, it is plausible that a nonthermal emission component coming from the forward shock could be associated with this hard emission.

If this emission is predominately thermal, it shows low electron temperatures compared to the roughly 4600 km/s expansion velocities measured for Tycho's SNR in X-rays (Hughes 2000). The spectra of other regions around the rim are qualitatively

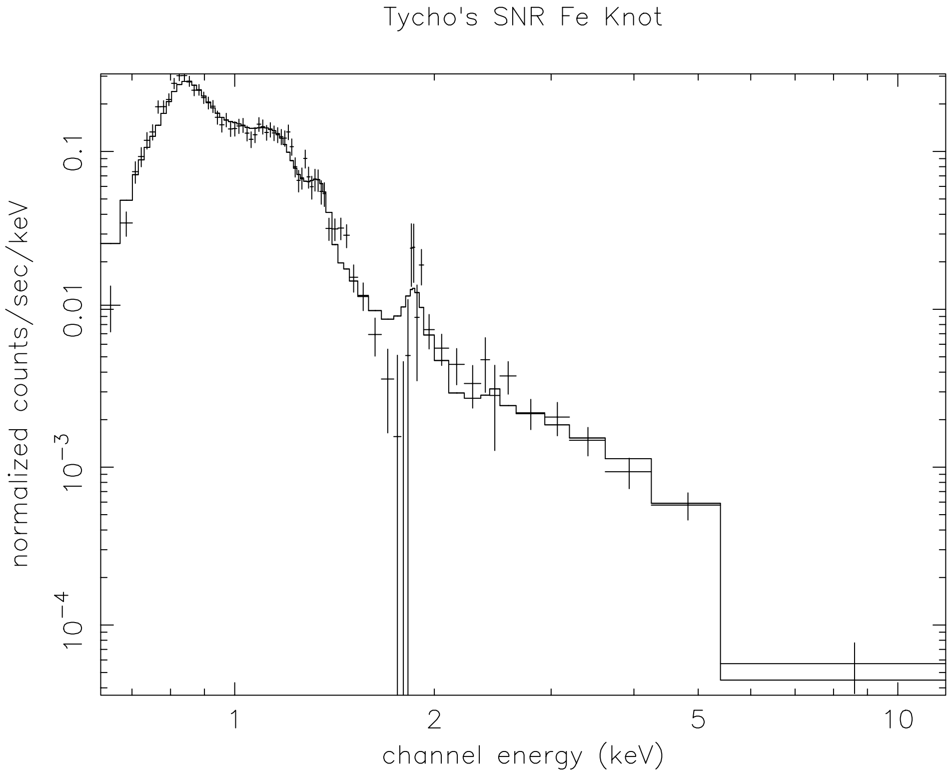

Figure 3(b). Spectrum of the Fe-rich knot in the east.

similar to that of the northwest arc, though they tend to show more Si and S line emission that comes from ejecta that have propagated to the forward shock. Such a spectrum, taken from a portion of the west rim of the remnant, is shown in the right panel of Fig. 2. The fitted model is for a nonthermal component with added thermal emission from Si and S ejecta.

2.2 *Ejecta*

Unlike in Cas A, a remnant with a massive progenitor that exploded via core-collapse, the ejecta in Tycho's SNR are relatively uniform on large scales. *Chandra* does not reveal new structures that were not previously known: the Fe ejecta traced by Fe K emission lies interior to the Si emission due to the thermal structure behind the reverse shock (Decourchelle *et al.* 2001; Hwang & Gotthelf 1997), and Si and Fe knots lie on the eastern edge of the remnant (Vancura *et al.* 1995). *Chandra* can now provide spectra for these regions, however. Fig. 3 shows spectra of the Si and Fe rich knots in the east, with the background taken from the surrounding emission. Clear qualitative differences in the spectra are immediately apparent. The spectrum of the Si-rich knot resembles the broadband spectrum of Tycho's SNR, with strong Si, S, Ar, and Ca emission lines, but shows relatively little Fe, either in the L transitions (to $n = 2$ levels) near 1 keV or in the K transitions (to $n = 1$ levels) near 6.5 keV. The Fe-rich knot shown in the right panel is the opposite. There is a residual Si feature (that is rather sensitive to the background subtraction), but the dominant spectral features are due to the Fe L emission. The spectra are fitted with nonequilibrium ionization thermal models.

3. Summary

Chandra and *XMM-Newton* have inaugurated the era of true spatially resolved X-ray spectroscopy. For supernova remnants like Tycho's SNR, this means the capability to measure, for the first time, the detailed distribution of the ejecta and the spectra of ejecta at different positions in the remnant. It also reveals the spectra at the forward shock, which most likely arise from both nonthermal and thermal emission processes.

References

Decourchelle, A., *et al.* 2001, *A&A*, **365,** L218.
Dickel, J. R., *et al.* 1991, *A. J.*, **101,** 2151.
Hughes, J. P. 2000, *Ap. J.*, **545,** L53.
Hwang, U., Gotthelf, E. V. 1997, *Ap. J.*, **475,** 665.
Katz-Stone, D. M., *et al.* 2000, *Ap. J.*, **529,** 453.
Reynolds, S. P., Keohane, J. W. 1999, *Ap. J.*, **525,** 368.
Seward, F., *et al.* 1983, *Ap. J.*, **266,** 287.
Vancura, O., Gorenstein, P., Hughes, J. P. 1995, *Ap. J.*, **441,** 680.

J. Astrophys. Astr. (2002) **23,** 89–93

The Multiwavelength Study of Two Unique Radio Galaxies

Nectaria A. B. Gizani[1], M. A. Garrett[2] & J. P. Leahy[3]

[1]*Centro de Astronomia e Astrofísica da Univ. de Lisboa, O.A.L., Portugal.*
[2]*Joint Institute for VLBI in Europe, Postbus 2, The Netherlands.*
[3]*Jodrell Bank Observatory, Univ. of Manchester, UK.*

Abstract. We present the usage of multi-frequency and multi-band radio, VLA, observations as well as X-ray observations in order to study the environment around two powerful radio galaxies, namely Hercules A and 3 C310. We study their environment both in pc- and kpc-scales. We have chosen these two radio galaxies as they present similar and unique characteristics, compared to the ones from our general knowledge about double radio galaxies associated with active galactic nuclei.

Key words. Galaxies: clusters: individual (Hercules A, 3 C310).

1. Introduction

Hercules A ($z = 0.154$, Gizani & Leahy 1999; Gizani & Leahy 2001a, b, c, in prep., Fig. 1) and 3C 310 ($z = 0.054$, van Breugel & Fomalont 1984, Fig. 2) are two radio galaxies with a similar and out of the ordinary behaviour: both sources appear with double optical nuclei (3C 310: Chiaberge *et al.* 1999; Hercules A: Baum *et al.* 1996). 3C 310 is smaller, less powerful than Hercules A.

They are classified as FR1.5 (Hercules A: Dreher & Feigelson 1984; 3C 310: Owen & Laing 1989). They have no compact hotspots and consist of sharply-bounded lobes. They are probably the only two radio galaxies that show large multiple circular radio features (ring-like structures) that are interior to the lobes and not just phenomena of the boundaries. A few of these rings are the largest material circles known anywhere. The projected magnetic field follows the edges of these features. They are steep spectrum sources of similar steepness. Their lobes present asymmetries with respect to brightness, depolarization and spectral index. Hercules A has a weaker radio core.

They are the hosts of clusters of galaxies (Hercules A: Feigelson & Berg 1983; 3C 310: Jenkins, Pooley & Riley 1977). 3C 310 has lower X-ray luminosity than Hercules A and for both sources the X-ray brightness profile can be described well if we assume contribution from a point source (Gizani & Leahy 1999; Hardcastle & Worrall 1999). While the intracluster medium in both the Hercules A and 3C 310 clusters (Abell and Zwicky respectively) has a similar temperature, it seems to be denser towards the center for the Hercules A cluster (see Leahy & Gizani 2002, for example).

The thermal pressure of the Hercules A cluster is larger than for the 3C 310 cluster and hence the confinement of its lobes by the intracluster medium is greater. The cluster thermal pressure at the distance of the radio lobes is typically an order of magnitude larger than the lobe minimum pressure for both radio galaxies (Leahy & Gizani 2001).

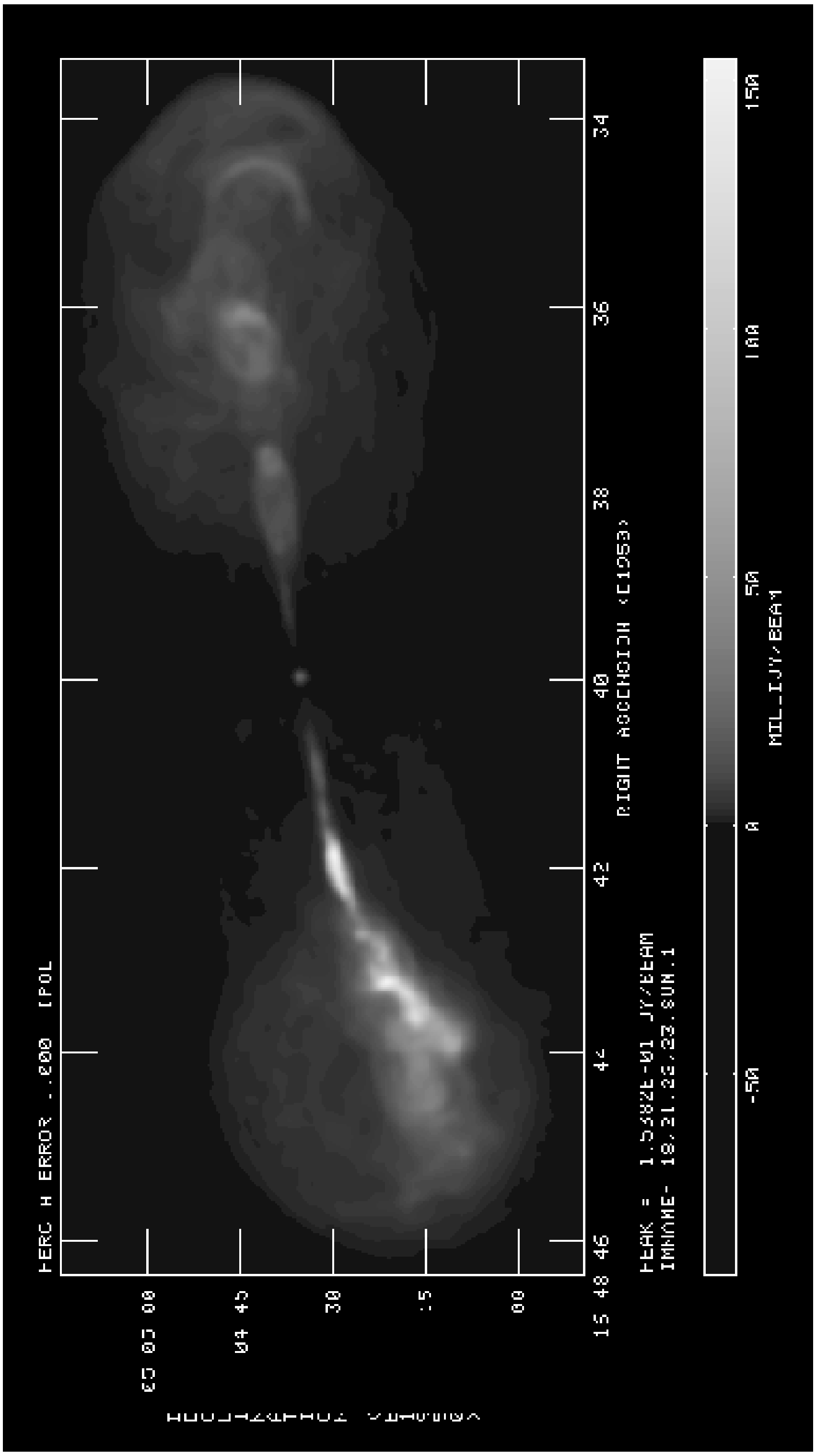

Figure 1. A grey scale VLA A+B+C map of the total intensity distribution of Hercules A at 20 cm created by combining the 4 frequency multiconfiguration data of the L-band at 1.4 arcsec. The presence of semi and/or full rings is apparent mostly in the western lobe.

2. The Environment

2.1 *Hercules A*

We have studied the **kpc-scale environment** of the powerful extragalactic radio source Hercules A in terms of the magnetic field of the intracluster gas in which the radio source is situated (Gizani & Leahy 1999; Gizani & Leahy 2002c, in prep). For this reason we have made VLA total intensity and polarization multiconfiguration observations at L- and X-bands. We have also retrieved and reprocessed the C-band data (Dreher & Feigelson 1984). In addition we have made ROSAT PSPC and HRI X-ray observations (Gizani & Leahy 2002a, in prep). The plan was to map the Faraday rotation field at high resolution (1.4 arcsec). We have found that Hercules A exhibits a strong Laing-Garrington effect (Garrington *et al.* 1988; Laing 1988). The X-ray observations have revealed an extended X-ray emission elongated along the radio galaxy axis and a weak nuclear component. The estimated temperature of the cluster is $kT = 2.45\,\mathrm{keV}$ and the central electron density is $n_\circ \simeq 7.8\cdot 10^{-3}$ cm^{-3} which reveals a hot, dense environment. By model fitting the Faraday dispersion profile from the radio data and the surface brightness profile from the X-ray data, we have found that the depolarization is mainly caused by a centrally condensed medium in which Hercules A is embedded at $\simeq 50^\circ$ to the line of sight. The western weak jet and associated lobe is behind the bulk of the depolarizing gas while the bright eastern jet and lobe are in front. We have estimated a central value of the magnetic field of $3 \lesssim B_\circ(\,\mu\mathrm{G}) \lesssim 9$ (Gizani & Leahy 1999).

We are also working on the **pc-scale environment** of the radio galaxy. We have observed the central region of Hercules A at 18 cm using the EVN-MERLIN array (Gizani, Garrett & Leahy 2001, 2002 in prep.). A faint but compact radio source, coincident with the optical centre of Hercules A was detected by the EVN with total flux density of 14.6 mJy, angular size 18×7 mas and position angle $\simeq 139^\circ$. There is also evidence for extended emission in the NW-SE direction, most probably from the eastern pc-scale jet. If this is true then there is a misalignment between the direction of the pc-eastern and the aligned kpc-scale jets of $\simeq 35^\circ$. The MERLIN data still need further reduction before we combine them with our existing VLA data at 18 cm.

2.2 *3C 310*

For the **kpc-scale environment** study, there are no high resolution radio and X-ray observations on 3C 310. We are going to use the existing observations (van Breugel & Fomalont 1984) combined with new radio observations which we are planning to make.

Total intensity and polarization VLA maps at 4 arcsec resolution at 6 and 21 cm (van Breugel & Formalont 1984), have shown that there is a fine-scale structure consisting of shells (rings) and filaments embedded in large, diffuse, low-brightness lobes. A small jet is also emanating from the core to the north (see Fig. 2). The ring-like features and the filaments have longitudinal magnetic fields.

ROSAT pointed observations have confirmed an extended X-ray emission. The HRI data have shown that this emission is centered on the radio galaxy (Hardcastle & Worrall 1999).

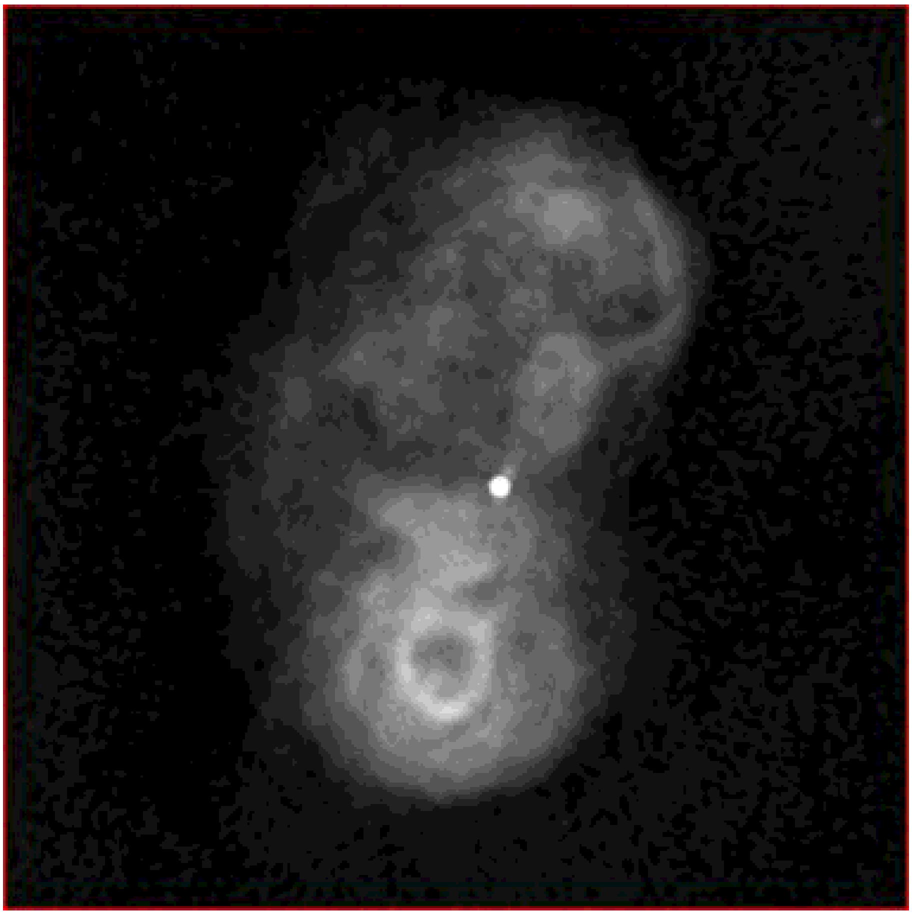

Figure 2. A grey scale VLA B+C map of the total intensity distribution of the radio galaxy 3C 310 at 1446 MHz at 4.0 arcsec (van Breugel & Fomalont 1984). The presence of ring-like features is apparent.

As can be seen from Fig. 2, the core is unresolved. The flux density of the core from the NRAO VLA Sky Survey (NVSS, Condon *et al.* 1998) at 21 cm is about 60 mJy at 45 arcsec (compared with 44 mJy at 20 cm, at 1.4 arcsec for Hercules A). To begin our study of the **pc-scale environment** we have already taken global VLBI as well as MERLIN data (Gizani & Garrett 2002 in prep) to resolve the core.

3. Conclusions

We are studying the two radio galaxies Hercules A and 3C310 as they are exceptional cases. Both radio sources have a similar behaviour and many differences from the usual morphology and characteristics of double radio sources associated with active galactic nuclei. In our case the determination of the unusual and similar structure and behaviour of these two radio galaxies, whether they originate in a similar fashion or not, will help to enrich our knowledge of the physical mechanisms dominating interior of the source and also in the medium in which the sources are situated. In other words we will try to find why these sources are different from the ones studied broadly. In addition this study will complement the Unified Theories.

For this reason we are planning observations in different wavelengths of the electromagnetic spectrum such as: HI observations of each radio galaxy with emphasis on their nuclear region; infrared observations of the ring-like and helical-structures of the radio emission of both radio sources; near IR polarimetric observations. X-ray follow-ups, where possible (Chandra Observations for 3C310, XMM observations of both sources); HST observations of 3C310; V, R, I-band observations to obtain a Hα map of the nuclear region; UV observations of the nuclear region as diagnostic of the ISM around the central region.

4. Acknowledgements

NG is grateful to the LOC for giving her most of the financial support to participate in this well organized and very interesting conference without which her participation would have been impossible. NG acknowledges her postdoc grant PRAXIS XXI/BPD/18860/98 from the Fundação para a Ciência e a Tecnologia, Portugal which also covered the rest of the expenses of her participation. The work on the pc-scale environment is supported by the European Community under its Access to Research Infrastructure action of the Improving Human Potential Programme, with contract number HPRI-CT-1999-00045. The European VLBI Network is a joint facility of European and Chinese radio astronomy institutes funded by their national research councils.

References

Baum *et al.* 1996, *ApJL.*, **465,** 5.
Chiaberge, M., Capetti, A., Celotti, A. 1999, *A&A*, **349,** 77.
Condon *et al.* 1998, *AJ*, **115,** 1693.
Dreher, J. W., Feigelson, E. D. 1984, *Nature*, **308,** 43.
Feigelson, E. D., Berg, C. J. 1983, *ApJ*, **269,** 400.
Garrington, S. T., Leahy, J. P., Conway, R. G., Laing, R. A. 1988 *Nat*, **331,** 147.
Gizani, N. A. B., Leahy, J. P. 1999, *NewAR*, vol. **99,** 639.
Gizani, N. A. B., Garrett, M. A., Leahy, J. P., 2001, *PASA*, in press (astro-ph / 0111607).
Hardcastle, M. J., Worrall. 1999, *MNRAS*, **309,** 969.
Jenkins, C. J., Pooley, G. G., Riley, J. M. 1977, *MemRAS*, **84,** 61.
Laing, R. A. 1988, *Nature*, **331,** 149.
Leahy, J. P., Gizani, N. A. B. 2002, *NewAR*, **46,** 117.
Owen F. N., Laing, R. A. 1989, *MNRAS*, **238,** 357.
van Breugel, W. J. M., Fomalont, E. B. 1984, *ApJL*, **282,** 55.

J. Astrophys. Astr. (2002) **23,** 95–99

Effect of Particle Acceleration Process on the Flare Characteristics of Blazars

S. Bhattacharyya, S. Sahayanathan & C. L. Kaul *Nuclear Research Laboratory, Bhabha Atomic Research Centre, Mumbai 400 085, India.*

Abstract. Following the kinetic equation approach, we study the flare processes in blazars in the optical-to-X-ray region, considering energy dependent acceleration time-scale of electrons and synchrotron and adiabatic cooling as their dominant energy loss processes.

1. Introduction

Blazars are characterised by a non-thermal photon spectrum ranging from radio-to-gamma-ray region and a high degree of optical polarisation (Maraschi 1992). Their spectral energy distribution shows two prominent peaks – a low energy peak in the optical/soft X-ray region, and the high energy peak in the GeV/Tev gamma-ray region (Kataoka *et al.* 1999). It is generally accepted that the radio-to-soft X-ray emission arises due to synchrotron cooling of relativistic electrons in the blazar jet, and that the hard X-ray to gamma-ray photons are produced by the inverse Compton scattering of low-energy photons (Kusunose *et al.*).

Blazar emissions also show large and rapid time-variability. Many models exist in the literature (Kirk *et al.* 1998) which attempt to understand the origin of some of the observed features of these flares, such as the rise and the decay times of fluxes, time-lag at different energies, etc., in the frame work of the kinetic equation approach. Following such a general approach and restricting our study to the optical to soft X-ray energy region of blazar spectra, we here study the effect of particle acceleration process on the variability features.

2. Model

It is necessary to first study the time-evolution of electron energy spectrum and in the model presented here we, therefore, consider two zones, namely, an acceleration zone (AR) around a shock front and a cooling zone (CR), the two being spatially separated within the blazar jet. Monoenergetic electrons of Lorentz factor γ_o are continously fed into AR at a rate $Q_o s^{-1}$ (consistent with the source bolometric luminosity) where they are accelerated at a rate $1/t_{\rm acc}$ in a diffusive shock acceleration process (Drury 1983), while simultaneously **(i)** losing energy due to synchrotron emission in the ambient magnetic field and **(ii)** escaping the AR at a rate $1/t_{\rm esc}$. The time-evolution of electron spectrum in AR is given by

$$\frac{\partial Q(\gamma,t)}{\partial t} + \frac{\partial}{\partial \gamma}[(\frac{\gamma}{t_{\rm acc}} - \beta\gamma^2)Q(\gamma,t)] + \frac{Q(\gamma,t)}{t_{\rm esc}} = Q_o\delta(\gamma-\gamma_o) \qquad (1)$$

where $t_{\rm acc} = \frac{20 m_e c^2 \xi \gamma}{3 v_s^2 e B_{\rm acc}}$, v_s is the velocity of the shock, $B_{\rm acc}$ is the ambient magnetic field in the AR and ξ is a parameter connected to Larmor radius. β is a function of $B_{\rm acc}$.

After leaving the AR at a rate $1/t_{\rm esc}$, particles enter into the CR which we consider here to be a spherical blob expanding adiabatically with expansion speed $v_{\rm exp}$, while moving down the jet relativistically with a Doppler factor δ. The relativistic electrons in the CR lose energy adiabatically and also emit electromagnetic radiation by synchrotron process in the *in situ* magnetic field B. The evolution of spectrum in CR is obtained by solving the kinetic equation

$$\frac{\partial N(\gamma,t)}{\partial t} + \frac{\partial}{\partial \gamma}[P(\gamma,t)N(\gamma,t)] + \frac{N(\gamma,t)}{\tau} = \frac{Q(\gamma,t)}{t_{\rm esc}} \qquad (2)$$

$$P(\gamma,t) = -\frac{v_{\rm exp}\gamma}{R} - \frac{4}{3}\frac{\sigma_T c}{m_e c^2}\frac{B^2}{8\pi}\gamma^2 \qquad (3)$$

where $R = R_o + v_{\rm exp} t$ and $B = B_o(\frac{R_o}{R})^m$ are the instantaneous radius and the magnetic field of the CR respectively and R_o, B_o their initial values. τ is the escape timescale of particles from the CR. The emitted synchrotron photon flux is next calculated by convoluting $N(\gamma,t)$ with the single particle emissivity $P(\nu,\gamma) = \frac{\sqrt{2}e^3 B}{m_e c^2} F(\nu/\nu_c)$, where $\nu_c = \frac{3eB}{4\pi mc}\sqrt{\frac{2}{3}}\gamma^2$ and $F(x) = x\int_x^\infty K_{\frac{5}{3}}(\xi)d\xi$. It is to be noted that the emission of radiation from energetic electrons in AR is not included in this study because of the smaller volume of AR compared to that of CR.

3. Results and discussion

Choosing the parameter space, with $\gamma_o = 2$, $\delta = 10$, $Q_o = 10^{46} s^{-1}$, $B_{\rm acc} = 0.1G$, $B_o = 0.2G$, $m = 1$, $R_o = 10^{13}$cm and $v_s = 0.4c$, together with the initial condition $Q(\gamma,0) = N(\gamma,0) = 0$ to reproduce the usually observed spectrum of blazars, we seek solutions of equations (1) and (2) for **(a)** energy-independent and **(b)** energy-dependent acceleration process cases. Using $t_{\rm esc} = t_{\rm acc}$, $\tau = 2R/c$ for both (a) and (b) cases, we replace γ (in the expression for $t_{\rm acc}$) by a constant value $\gamma_{\rm eff}(= 10^7)$ and obtain $t_{\rm acc} = 2 \times 10^4$s, $0.0418\gamma\ s$ in the source-frame in case (a) and case (b) respectively. For $t \geq 0$, the electron energy distribution and the photon spectrum evolve into a steady state when the flux values at different energies do not change with time. The maximum frequency of emitted radiation depends on the maximum value of the Lorentz factor of electrons, $\gamma_{\rm max}$ with the parameter values chosen here, for case (a), $\gamma_{\rm max} = \frac{1}{\beta t_{\rm acc}} = 8.89 \times 10^5$ and for case (b) $\gamma_{\rm max} = \frac{1}{\sqrt{t_{a,o}\beta}} = 2.98 \times 10^6$.

We represent a flare by a sudden increase in the injection rate, driven by source instability in the jet flow, into the AR for a small duration, once the system attains a steady state. In Fig. 1(a), we show the flare patterns at frequencies of 10^{17}, 10^{16} and 10^{15} for case (a) when Q_o increases from $10^{46}s^{-1}$ to $1.5 \times 10^{46}\ s^{-1}$ for 0.2 days (in observer's frame) after a steady state is already reached on the second day. It is seen that not only do low energy flares manifest themselves earlier in time than the higher energy flares but the time-lag between their respective peak positions also increases with increase in $t_{\rm acc}$ (not shown here). We also find that the hysterisis loop (a plot of X-ray flux vs spectral index) is traced anticlockwise (not shown here). These observations suggest the presence of the oft-quoted 'hard-lag' in the blazar spectra. In Fig. 1(b),

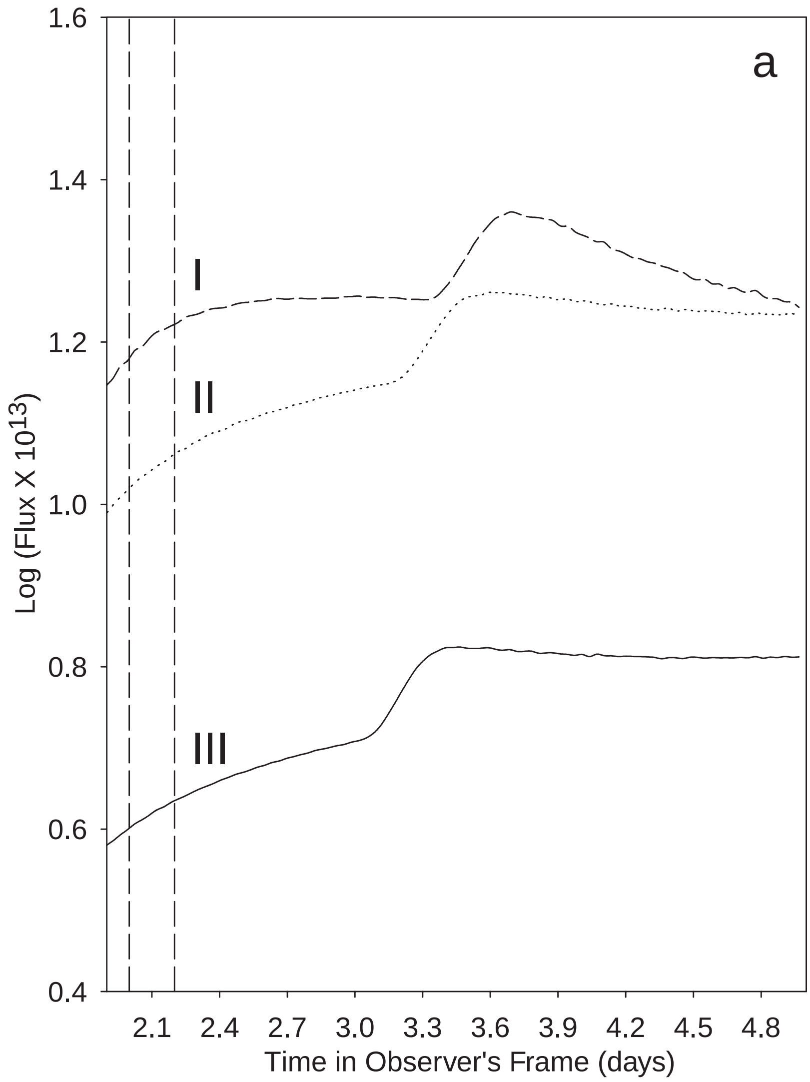

Figure 1. Flares at different frequencies **(I)** 10^{17} Hz, **(II)** 10^{16} Hz and **(III)** 10^{15} Hz: **(a)** energy-independent and **(b)** energy-dependent acceleration process. Vertical dashed lines show the duration of excess injection of particles in the AR.

we show the flare patterns for the same energies for case (b). We note that in this case the system attains a steady state much faster than in case (a) and the peak values at different frequencies are attained simultaneously. Contrary to case (a), the hysterisis loop is traced clockwise in this case (not shown here).

The light curves (Fig. 1a,b) are asymmetrical, with a shorter rise time and a longer decay time. It cannot obviously arise due to effects of light crossing time alone. Effects due to different acceleration and emission time-scales are folded in here. For one, the decay times depend upon energy loss time-scales which are known to be energy-dependent.

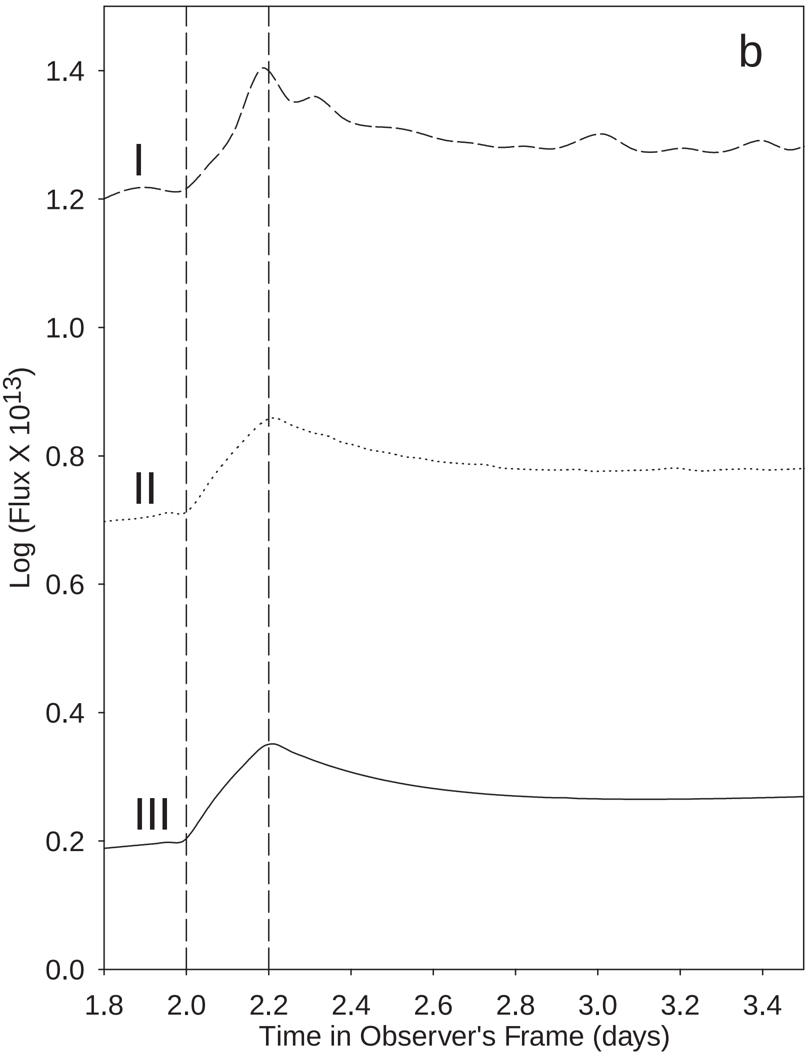

Figure 1. (*Continued*).

We also find that the inclusion of adiabatic cooling process merely stretches the decay part of the light curves slightly.

4. Conclusion

The model reproduces, though only qualitatively, the observed hard-lag in flare spectra from blazars in the optical-soft X-ray region. A detailed comparison of our model with observation is not warranted at this stage as correlated flux variations in the optical and X-ray remain as yet poorly established, although BeppoSax observations of Mrk421 do show flare spectra which have features somewhat similar to those presented here

(Fossati *et al.* 2000). Moreover, we are still in the process of fine-tuning our parameter space so as to be able to reproduce observations as closely as possible. The results will be presented elsewhere (Bhattacharyya *et al.*).

The absence of the hard-lag effect in case t_{acc} is energy-dependent suggesting that the hard-lag effect, if observed unequivocally may provide useful inputs in understanding the dynamics of particle acceleration in blazars.

References

Bhattacharyya, S., Sahayanathan, S. Kaul, C. L. *in preparation*
Drury, L. O. C. 1983, *Rep. Prog. Phys.*, **46**, 973.
Fossati, G. *et al.* 2000, *ApJ*, **541**, 153, 166.
Kataoka, J. *et al.* 1999, *ApJ*, **514**, 138.
Kirk, J. G., Riegler, F. M., Mastichiadis, A., 1998, *A&A*, **333**, 452.
Kusunose, M., Takahara, F., Li, H., astro-ph/0002137.
Maraschi, L. 1992, in *Variability of Blazars*, (ed.) E. Valtaoja & M. Valtonen (Cambridge: Cambridge Univ. Press), **447**

J. Astrophys. Astr. (2002) **23,** 101–105

Heating of the Intracluster Medium by Quasar Outflows

Suparna Roychowdhury & Biman B. Nath *Raman Research Institute, Bangalore 560 080, India*

Abstract. We study the possibility of quasar outflows in clusters and groups of galaxies heating the intracluster gas in order to explain the recent observation of excess entropy in this gas. We show that radio galaxies alone cannot provide the energy required to explain the observations but the inclusion of Broad Absorption Line (BAL) outflows can do so, and that in this scenario most of the heating takes place at $z \sim$ 1–4, the "preheating" epoch being at a lower redshift for lower mass clusters.

Key words. Cosmology: theory—Galaxies: intergalactic medium—X-rays: galaxies: clusters.

1. Introduction

Clusters and groups of galaxies contain a large amount of hot X-ray emitting gas called the intracluster medium, besides galaxies and the gravitationally dominant dark matter. Recent X-ray observations have provided evidences for non-gravitational heating of the ICM, in addition to the heating which occurs during the gravitational collapse. One of the first evidences was in the shape of the $L_x - T$ relation, which is steeper than the self-similar behaviour $L_x \propto T^2$ predicted in the case of only gravitational processes. Several authors like Kaiser (1991) and others have proposed that the missing element is the existence of a "preheated" high-entropy intergalactic gas prior to a cluster's collapse. Later, Ponman *et al.* (1999) and Lloyd-Davies *et al.* (2000) have found direct evidence of an entropy excess with respect to the level expected from gravitational heating in the centres of groups.

The candidate process which has been looked into as a source for this "preheating" are strong galactic winds driven by supernovae. However Valageas & Silk (1999) showed that the energy provided by supernovae cannot raise the entropy of intergalactic medium (IGM) up to the level required by current observations. The observed amount of required energy injection have been found to be in the range of 0.4 – 3 keV per gas particle (Wu *et al.* 2000; Lloyd-Davies *et al.* 2000 and others.)

An alternative source of heating, in the form AGN outflows in clusters, has been hypothesized by many authors to reconcile the observations. We have investigated the role of quasar outflows in this regard. We also try to constrain the epoch when this heating could have occurred.

2. Quasars inside clusters

For a proper evaluation of heat input from quasars inside clusters, one first needs to calculate their abundance and the dependence on the AGN mass, cluster mass, and the cluster formation redshift.

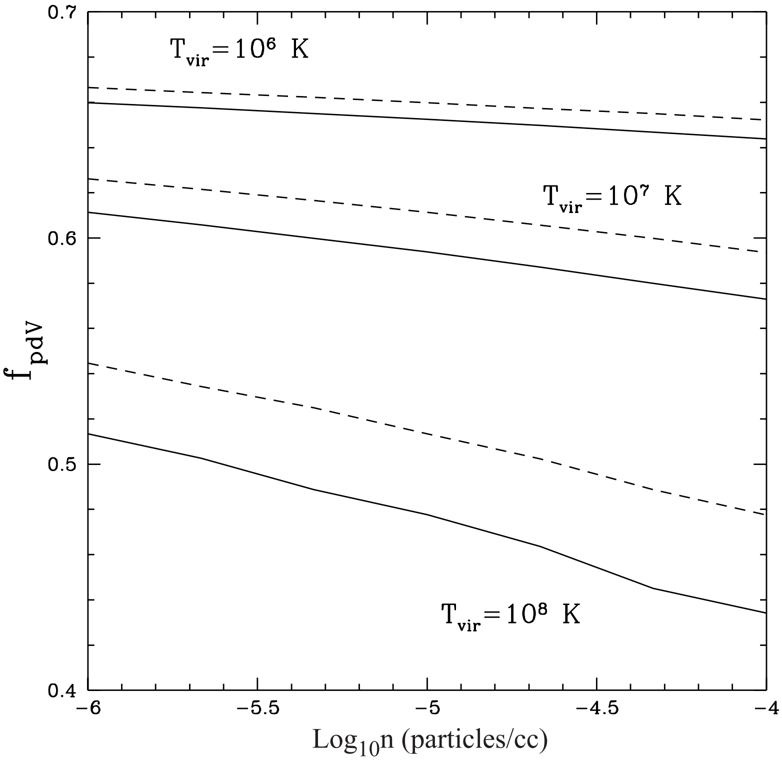

Figure 1(a). The dependence of f_{pdV} on the ambient density n is shown for various ambient temperatures T and kinetic luminosities of the jet, L_k (erg/s) . Solid and dashed lines are for $L_k = 10^{46}$ erg/s and 10^{47} erg/s respectively.

Following Yamada *et al.* (1999) (for $z = 0$), Haiman & Loeb (1998) and Furlanetto & Loeb (2001; FL01) at high redshift, we assume that the quasar abundance in clusters and low mass groups of galaxies is given by a fraction f_q of halos, where, $f_q \sim 0.1$ for $10^{13} \gtrsim M_h \gtrsim 10^{12}\, M_\odot$ and $f_q \sim 0$ for $M_h \gtrsim 10^{13}\, M_\odot$, & $M_h < 10^{12}\, M_\odot$. A life time of order 10^7 yr is assumed for the quasar (FL01).

To obtain the statistics of quasars *inside* clusters, that is, the rate of formation of quasars inside a future cluster of mass M_{cl}, one needs to have an extension of the Press-Schecter (PS) mass function which can predict the probability of a given halo merging into a bigger object later, or the probability of an object having had a projenitor of a given mass at an earlier epoch. Such extensions of the PS theory have been studied in detail by Bower (1991) and Lacey & Cole (1993)and others. The necessary growth factor in a cosmological constant dominated universe is taken from Kitayama & Suto (1996).

The above formalism leads to a *conservative* estimate of abundance of quasars in a cluster (and, therefore, the final heat input), because we ignore the increased pace of growth of perturbation and the merging rate inside a cluster. Our estimate of merging from the extended PS formalism is also conservative.

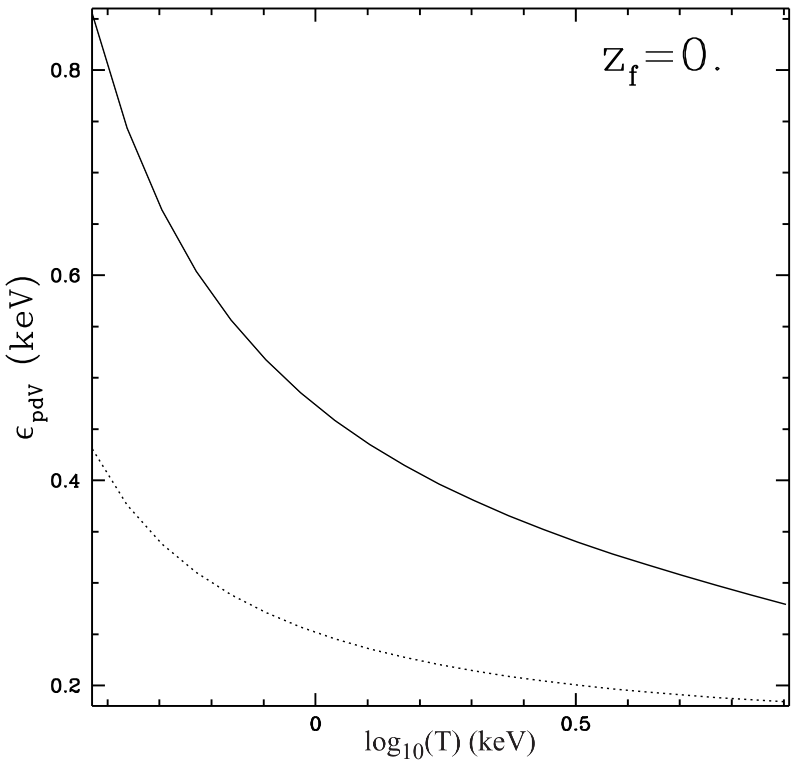

Figure 1(b). Excess energy (in keV) from BAL outflows is shown as a function of the cluster virial temperature (keV) for clusters with collapse redshift $z_f = 0$. The solid line shows the result of our calculation using the density and temperature dependent f_{pdV} and the dotted line shows the results when $f_{pdV} = 3/8$. (Bicknell *et al.* 1997)

3. Work done by quasar outflows

We then calculate the energy input from quasar outflows into the ambient medium. Two major types of outflows are considered: outflows from radio-loud quasars (RLQ) and broad absorption line (BAL) outflows. It has been assumed that during the active lifetime of the quasar, the energy output in the form of mechanical energy is given by the Eddington luminosity of the central black hole. We use the observed scaling between the central black hole mass and the halo mass (Magorrian *et al.* 1998; Gebhardt *et al.* 2000). Given the uncertainty in the geometry of the BAL outflows, we first calculate the work done by radio galaxy outflows and use similar values of the work done for BAL outflows. We also assume that all quasars go through the BAL outflow phase whereas the fraction of quasars being radio loud is of order ~ 0.1.

The standard scenario for outflows from radio loud quasars involves a ‘cocoon’ surrounding the core and the jet, and consisting of a shocked jet material (Scheuer 1974; Blandford & Rees 1974). We adopt the evolution of cocoons following the approach of Bicknell *et al.* (1997). Fig. 1(a) shows the dependence of the fraction of

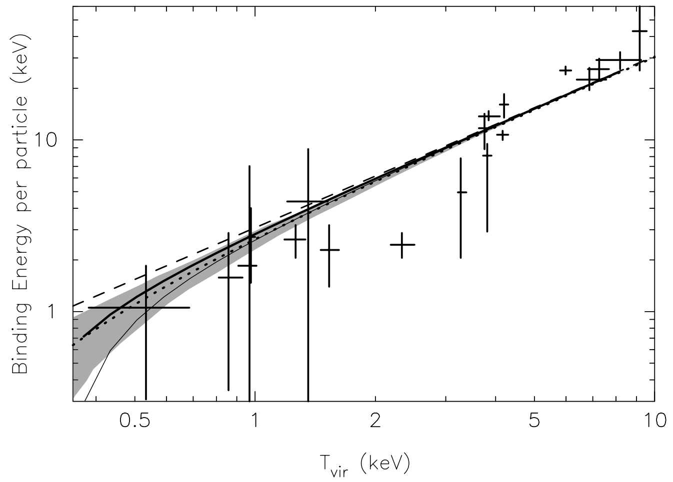

Figure 2. The prediction from our calculations is presented in the form of the final binding energy per particle of the central region of groups and clusters against the gas temperature. The data points are from the Figure 9 of Lloyd-Davies *et al.* (2000), and the dashed line refers to their fit $E \propto T$, derived from the data points for clusters with $T \geq 4$ keV. The dotted line refers to their second fit, with a constant excess energy of 0.44 keV per particle (subtracted from the binding energy) along with a formal 1 σ confidence interval shown by the shaded region. The darker and thicker solid line is the prediction of our calculation and the thinner and lighter solid line is the calculation using $f_{pdV} = 3/8$ (Bicknell *et al.* 1997).

energy of the jet lost through mechanical work f_{pdV} as a function of ambient density and ambient temperature.

4. Heating of the ICM

Equipped with the knowledge of the rate of formation of quasars in clusters and the fraction of total energy which is deposited as pdV work by the outflows from them, we now calculate the total amount on non-gravitational energy provided by quasar outflows in a cluster. Here we take the gas fraction of the total cluster mass, $f_{\rm gas} = 0.1$.

We present the results for the total non-gravitational energy input per gas particle as a function of cluster mass (or, equivalently, gas temperature) in the right panel of Fig. 1 (for a collapse redshift of $z_f = 0$). Recently, it has been shown by Lloyd-Davies *et al.* (2000) from observations of groups of clusters of galaxies that an excess energy of 0.44 ± 0.3 keV per particle suffices to explain the excess entropy in groups.

The solid curves in Fig. 1(b) and Fig. 2 show that the excess energy from pdV work done by the quasar outflows falls in this required range. Even if the fraction f_{pdV} is taken to be 3/8 (dotted line in Fig. 1(b) and thin solid line in Fig. 2), the excess energy still satisfies the requisite range. The excess energy from radio galaxies alone would be one tenth of the excess we have calculated, and will fall short of the requirement. We also find that the epoch of heating is in the range of $z \sim 1 - 4$, where this epoch is at lower redshifts for low mass clusters (Nath & Roychowdhury 2002).

References

Bicknell, G. V., Dopita, M. A., O'Dea, C. P. O. 1997, *Ap. J.*, **485,** 112.
Blandford, R. D., Rees, M. J. 1974, *MNRAS*, **169,** 395.
Bower, R. G. 1991, *MNRAS*, **248,** 332.
Furlanetto, S., Loeb, A. 2001, *Ap. J.*, **556,** 619 (FL01).
Gebhardt, K. *et al.* 2000, *Ap. J.*, **543,** 5.
Haiman, Z., Loeb, A. 1998, *Ap. J.*, **503,** 505.
Kaiser, N. 1991, *Ap. J.*, **383,** 104.
Kitayama, T., Suto, Y. 1996, *Ap. J.*, **469,** 480.
Lacey, C., Cole, S. 1993, *MNRAS*, **262,** 627.
Lloyd-Davies, E. J., Ponman, T. J., Cannon, D. B. 2000, *MNRAS*, **315,** 689.
Magorrian, J. *et al.* 1998, *A. J.*, **115,** 2285.
Nath, B. B., Roychowdhury, S. 2002, *MNRAS*, **333,** 145.
Ponman, T. J., Cannon, D, B., Navarro, J. F. 1999, *Nature*, **397,** 135.
Scheuer, P. A. G. 1974, *MNRAS*, **166,** 513.
Valageas, P., Silk, J. 1999, *A&A*, **350,** 725.
Wu, K. K. S., Fabian, A., Nulsen, P. E. J. 2000, *MNRAS*, **318,** 889.
Yamada, M., Sugiyama, N., Silk, J. 1999, *Ap. J.*, **622,** 66.

J. Astrophys. Astr. (2002) **23,** 107–113

Probes of Cosmic Star Formation History

Pranab Ghosh *Department of Astronomy & Astrophysics, Tata Institute of Fundamental Research, Bombay 400 005, India.*

Abstract. I summarize X-ray diagnostic studies of cosmic star formation history in terms of evolutionary schemes for X-ray binary evolution in normal galaxies with evolving star formation. Deep X-ray imaging studies by *Chandra* and *XMM-Newton* are now beginning to constrain both the X-ray luminosity evolution of galaxies and the log N–log S diagnostics of the X-ray background. I discuss these in the above context, summarizing current understanding and future prospects.

Key words. Galaxies: evolution—stars: formation—X-rays: galaxies, background—binaries: close.

1. Introduction

I describe here the current status and future potentials of X-ray diagnostics of the history of cosmic star-formation rate (SFR). Global SFR has undergone strong cosmological evolution: it was $\sim$ 10 times its present value at $z \approx 1$, had a peak value $\sim$ 10–100 times the present one in the redshift range $z \sim 1.5$–3.5, and declined again at high z (Madau, Pozzetti & Dickinson 1998, henceforth M98; Blain, Smail, Ivison & Kneib 1999, henceforth B99a; Blain *et al.* 1999, henceforth B99b, and references therein). Details of the SFR at high redshifts are still somewhat uncertain, because much of the star formation at $2 \lesssim z \lesssim 5$ may be dust-obscured and so missed by optical surveys, but detected readily through the copious submillimeter emission from the dust heated by star formation.

The X-ray emission of a normal galaxy (i.e., one without an active nucleus) is believed to be dominated by the integrated emission of the galaxy's X-ray binary population. I summarize here recent studies made in collaboration with N. White, A. Ptak, and R. Griffiths (White & Ghosh 1998, henceforth WG98; Ghosh & White 2001, henceforth GW01; Ptak *et al.* 2001, henceforth Ptak01) on the basic imprints of an evolving SFR on the evolution of X-ray binary populations of galaxies, on the general consequences of these studies for deep X-ray imaging of galaxy fields by *Chandra* and *XMM-Newton*, and on the first results that have emerged so far on the X-ray luminosity evolution in the Hubble Deep Field (HDF), and on the log N–log S diagnostics of the X-ray background. First results of Brandt *et al.* (2001, henceforth Bran01) from *Chandra* exposure of HDF North (HDF-N) indicate an evolution of the X-ray luminosities, L_X, from the Local Universe to $z \approx 0.5$, which I compare with the GW01 predictions. Fluctuation analyses of the $\sim$ 1 Ms *Chandra* exposure of (HDF-N) suggest (Miyaji & Griffiths 2002, henceforth MG02) that the log N–log S plot in the soft X-ray band continues to rise at very low fluxes, suggesting that the X-ray background at these fluxes is dominated by population different from the (usual) integrated AGN population (Gilli *et al.* 2001, henceforth GSH), which could be that of normal galaxies (Ptak01), bearing the signature of SFR history.

2. X-ray luminosity evolution

In the approach of WG98 and GW01, the total X-ray output of a normal galaxy is modeled as the sum of those of its high-mass X-ray binaries (HMXB) and low-mass X-ray binaries (LMXB), the evolution of each species "i" being described by a timescale τ_i. The evolution of the HMXB population in response to an evolving star-formation rate SFR(t) is given by

$$\frac{\partial n_{\rm HMXB}(t)}{\partial t} = \alpha_h {\rm SFR}(t) - \frac{n_{\rm HMXB}(t)}{\tau_{\rm HMXB}}, \tag{1}$$

where $n_{\rm HMXB}$ is the number density of HMXBs in the galaxy, and $\tau_{\rm HMXB}$ is the HMXB evolution timescale. α_h is the rate of formation of HMXBs per unit SFR, given approximately by $\alpha_h = \frac{1}{2} f_{\rm binary} f^h_{\rm prim} f^h_{\rm SN}$, where $f_{\rm binary}$ is the fraction of all stars in binaries, $f^h_{\rm prim}$ is that fraction of primordial binaries which has the correct range of stellar masses and orbital periods for producing HMXBs (van den Heuvel 1992, henceforth vdH92), and $f^h_{\rm SN} \approx 1$ is that fraction of massive binaries which survives the first supernova. In these calculations, a representative value $\tau_{\rm HMXB} \sim 5 \times 10^6$ yr is adopted according to current evolutionary models. Note that $\tau_{\rm HMXB}$ includes both **(a)** the time taken ($\sim 4 - 6 \times 10^6$ yr) by the massive companion of the neutron star to evolve from the instant of the neutron-star-producing supernova to the instant when the "standard" HMXB phase begins, and, **(b)** the (much shorter) duration ($\sim 2.5 \times 10^4$ yr) of this HMXB phase (vdH92 and references therein).

Of the two mechanisms of LMXB production generally envisaged, viz., **(a)** production in cores of globular clusters due to tidal capture, and, **(b)** general production by evolution of primordial binaries, I describe here only the latter one (which must be the dominant mechanism at least for spiral galaxies, since globular-cluster LMXB populations of such galaxies can account only for relatively small fractions of their total X-ray luminosities), deferring the former to section 4. LMXB evolution from primordial binaries has two stages (WG98) after the supernova produces a post-supernova binary (PSNB) containing the neutron star. First, the PSNB evolves on a timescale $\tau_{\rm PSNB}$ due to nuclear evolution of the neutron star's low-mass companion and/or decay of binary orbit due to gravitational radiation and magnetic braking, until the companion comes into Roche lobe contact and the LMXB turns on. Subsequently, the LMXB evolves on a timescale $\tau_{\rm LMXB}$. Since $\tau_{\rm PSNB}$ and $\tau_{\rm LMXB}$ are comparable in general, the two stages are described separately (WG98) by:

$$\frac{\partial n_{\rm PSNB}(t)}{\partial t} = \alpha_l {\rm SFR}(t) - \frac{n_{\rm PSNB}(t)}{\tau_{\rm PSNB}}, \tag{2}$$

$$\frac{\partial n_{\rm LMXB}(t)}{\partial t} = \frac{n_{\rm PSNB}(t)}{\tau_{\rm PSNB}} - \frac{n_{\rm LMXB}(t)}{\tau_{\rm LMXB}}. \tag{3}$$

Here, $n_{\rm PSNB}$ and $n_{\rm LMXB}$ are the respective number densities of PSNB and LMXB in the galaxy, and α_l is the rate of formation of LMXB per unit SFR, given approximately

Table 1. Star Formation Rate (SFR) profiles.

Model	z_{max}	p	Comments
Peak-M	0.39	4.6	Madau profile
Hierarchical	0.73	4.8	Hierarchical clustering
Anvil-10	1.49	3.8	Monolithic models
Peak-G	0.63	3.9	Peak part of composite "Gaussian" model
Gaussian	N/A	N/A	Gaussian starburst added at high z.

by $\alpha_l = \frac{1}{2} f_{\rm binary} f^l_{\rm prim} f^l_{\rm SN}$, the individual factors having meanings closely analogous to those for HMXBs (see GW01).

Evolution is displayed in terms of the redshift z, which is related to the cosmic time t by $t_9 = 13(z+1)^{-3/2}$, where t_9 is t in units of 10^9 yr, and a value of $H_0 = 50$km s^{-1} Mpc^{-1} has been used[1]. I consider the suite of current SFR models detailed in Table 1 to cover a plausible range, using the parameterization of B99a,b. Models of the "peak" class have the form:

$$\mathrm{SFR}_{\rm peak}(z) = 2\left(1 + \exp\frac{z}{z_{\rm max}}\right)^{-1}(1+z)^{p+\frac{1}{2z_{\rm max}}}, \tag{4}$$

while those of the "anvil" class have the form:

$$\mathrm{SFR}_{\rm anvil}(z) = \begin{cases} (1+z)^p, & z \le z_{\rm max}, \\ (1+z_{\rm max})^p, & z > z_{\rm max}. \end{cases} \tag{5}$$

These functional forms are convenient since they have a convenient low-z limit where all SFR profiles must agree with the optical/UV data (M98), and since the model parameters can be manipulated to mimic a wide range of star-formation histories (B99b). Peak-class profiles are useful for describing **(a)** SFRs determined from optical/UV observations, i.e., Madau-type (M98) profiles, called "Peak-M" in Table 1, and, **(b)** more general SFRs with enhanced star formation at high z, an example of which is the "hierarchical" model of B99b, wherein the submillimeter emission is associated with galaxy mergers in a hierarchical clustering model. Anvil-class profiles are useful for describing the results of "monolithic" models. The "Gaussian" model (B99a,b) is an attempt at giving a good account of the SFR at both low and high z by making a composite of the Peak-G model (see Table 1) and a Gaussian starburst at a high redshift z_p, i.e., a component

$$\mathrm{SFR}_{\rm Gauss}(z) = \Theta \exp\left\{-\frac{[t(z) - t(z_p)]^2}{2\sigma^2}\right\}. \tag{6}$$

Based on the *IRAS* luminosity function, this component is devised to account for the high-z data, particularly the submillimeter observations (B99a). For its parameters

[1]For ease of comparison with WG98, M98, and GW01, I use here a Friedman cosmology with $q_0 = 1/2$. Other values of the Hubble constant lead to a straightforward scaling: for $H_0 = 70$ km s^{-1} Mpc^{-1}, for example, $t_9 \approx 10(z+1)^{-3/2}$, so that the results remain unchanged if all timescales are shortened by a factor of 1.3.

(see Table 1), I have used the revised values given in B99b (see GW01). In all models described here, no galaxies exist for sufficiently large redshifts, $z > 10$. Fig. 1 shows the prompt evolution of HMXBs and the slow evolution of LMXBs, and the evolution of the total X-ray binary population, where the two components have been so weighted as to represent the total X-ray emission from the galaxy. The HMXB profile closely follows the SFR profile because $\tau_{\rm HMXB}$ is small compared to the SFR evolution timescale. By contrast, the LMXB profile has a significant lag behind the SFR profile because $\tau_{\rm PSNB}$ and $\tau_{\rm LMXB}$ are comparable to SFR evolution timescale: the LMXB profile generally peaks at redshifts $\sim$1–3 later than the HMXB profile—a characteristic signature of SFR evolution (WG98). Effects of both **(a)** varying the evolutionary timescales for fixed SFR profiles, and, **(b)** varying the SFR profile for fixed evolutionary timescales have been studied: see GW01 for details. I display the latter variation in Fig. 1 to emphasize that, since, for sufficiently *slow* LMXB evolution, the galaxy's X-ray emission is dominated by LMXBs at low redshifts ($0 \lesssim z \lesssim 1$), and by HMXBs at high redshifts, the total L_X-profile is strongly influenced at high redshifts by the SFR profile. Thus, determination of the L_X-profile even up to moderate redshifts may put interesting constraints on the SFR, making this an *independent* X-ray probe of cosmic star-formation history.

From their stacking analysis (see Bran01 and references therein for an exposition of the technique), Bran01 estimate that the average X-ray luminosity of the bright spiral galaxies at an average redshift $z \approx 0.5$ used in their study is about a factor of 3 higher than that in the local Universe. This observed evolution, $L_X(0.5)/L_X(0.0) \sim 3$, has been compared by GW01 with theoretical predictions from the above SFR profiles (see GW01 for details). The degree of evolution from $z = 0$ to $z = 0.5$–1.0 increases from Madau-type profiles to those with additional star formation at high redshifts, the numbers for the Peak-M profile being in best agreement with Bran01. Now, a most recent development in SFR research has been the study of star-formation histories of individual galaxies and various galaxy-types. SFR profiles of individual galaxies have been inferred using a variety of techniques. For various galaxy-types, models of spectrophotometric evolution, which use the synthesis code *Pégase* and are constrained by deep galaxy counts, have been developed (Rocca-Volmerange & Fioc 2000, henceforth RF00), leading to a model SFR profile for each type. In the light of these developments, I now suggest what may be the true significance of the Bran01 results just discussed.

Bran01 used bright spirals for their stacking analysis. RF00 have shown that the model SFR profile for such (Sa-Sbc) spirals rises roughly in a Madau fashion from $z = 0$ to $z \approx 1$ (which these authors ascribe to a bias in the original sample used to construct the Madau profile towards bright spirals), and thereafter flattens to a roughly constant value ~ 12 times that at $z = 0$, falling again at $z \gtrsim 7$. In the range $0 < z \lesssim 7$, this profile can be roughly represented by an anvil-type profile (see Sec. 2.), with the parameter $z_{\rm max}$ as given in Table 1, and the parameter $p \approx 2.7$. For such a profile with the timescales $\tau_{\rm PSNB}$ = 1.9 Gyr, $\tau_{\rm LMXB}$ = 1.0 Gyr, as in Fig. 1, the GW01 evolutionary scheme gives $L_X(0.5)/L_X(0.0) = 3.3$, and $L_X(1.0)/L_X(0.0) = 5.4$, in good agreement with both the Bran01 results and the Peak-M results. We now see why the Peak-M profile would appear to give a good account of the Bran01 results. In effect, the Bran01 analysis may be probing the SFR profile of *only* the bright spirals in HDF-N, and the fact that the Peak-M profile is consistent with the Bran01 results does *not* imply that the global SFR necessarily follows the Peak-M profile.

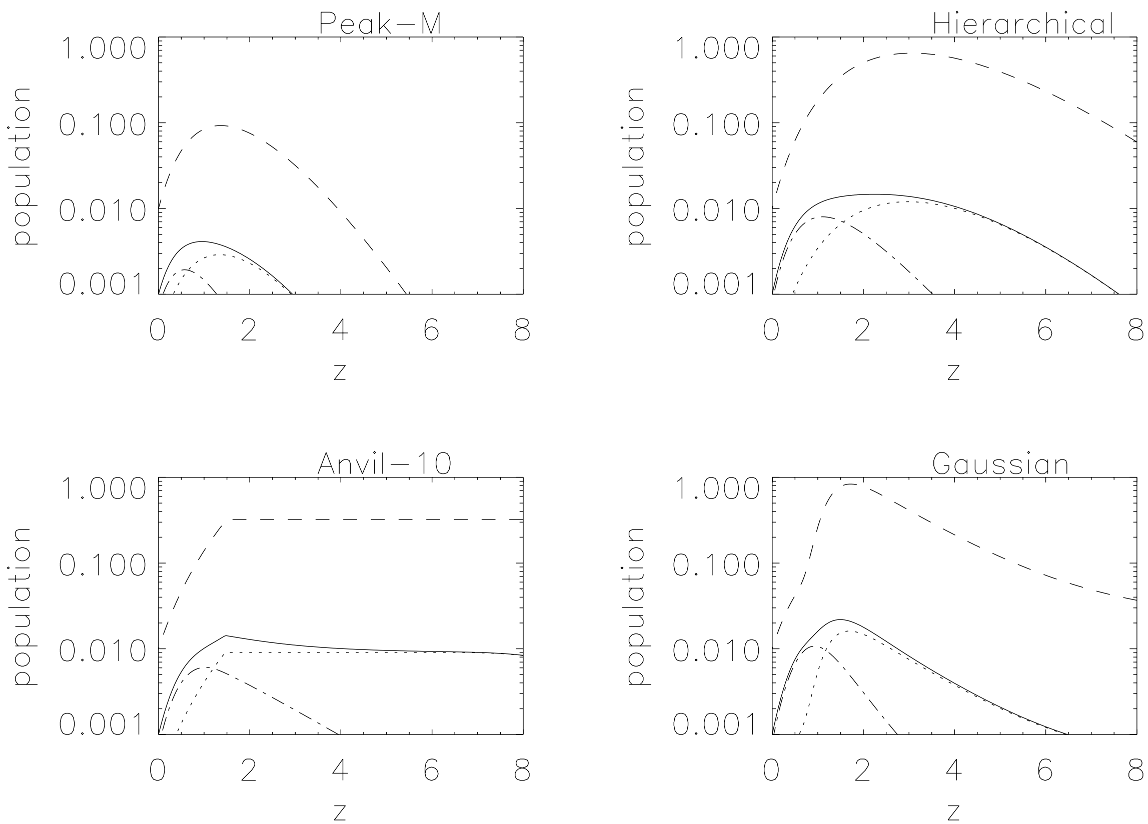

Figure 1. Evolution of HMXB population (dotted line), LMXB population (dash-dotted line), and the total X-ray luminosity L_X (solid line) of a galaxy with various SFR profiles (dashed line), from GW01. The effects of SFR variation are shown by keeping the evolutionary timescales fixed at $\tau_{\mathrm{PSNB}} = 1.9$ Gyr and $\tau_{\mathrm{LMXB}} = 1.0$ Gyr for all cases, and choosing various SFR profiles from Table 1. Each panel is labeled by the name of its SFR profile.

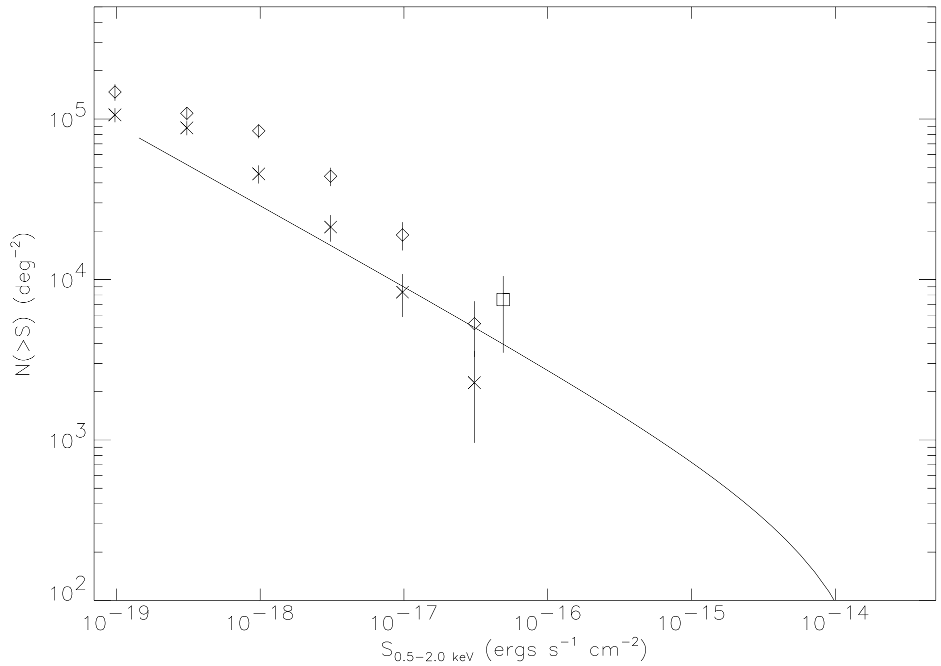

Figure 2. log N–log S plot in the soft (0.5 – 2.0 keV) band for HDF-N, from Ptak01. The diamonds correspond to the Gaussian SFR profile described in Sec. 2., and the crosses to the Peak-M profile. Note that an interpolation through the former points is represented by a dashed line in MG02 and that through the latter points by a dotted line. The solid line here is the double power law fit of Tozzi *et al.* to the *Chandra* observations of HDF South.

3. X-ray background: log *N*–log *S* diagnostics

Based on the results of Sec. 2., Ptak01 calculated the X-ray flux distributions and source count (log N–log S) plots expected for HDF-N. Figure 2 shows the Ptak01 plot in the soft (0.5–2.0 keV) X-ray band — a valuable diagnostic of current population synthesis models of the X-ray background. In this *Chandra* and *XMM-Newton* era of deep X-ray surveys, the cosmic X-ray background has been largely resolved into contributions from individual sources, the resolved fraction being $\gtrsim$ 90% in the soft (0.5–2.0 keV) band, and similar in the harder (2–10 keV) band. The long-standing belief that these sources are predominantly active galactic nuclei (AGN) was supported by the (now completed) optical identification programme which followed up the ROSAT deep survey, since it found the counterparts to be predominantly AGN. Ongoing optical identifications of the deepest *Chandra* and *XMM-Newton* fields are still far from complete. AGN population-synthesis models of the X-ray background are currently very useful and popular: these have been developed to a degree of detail (see GSH, which has references to earlier models) sufficient for extracting information about AGN population properties. The recent, ultradeep ($\sim$ 1 Ms) observations of both HDF-N and the Chandra Deep Field South (CDFS) have led to log N–log S plots in the soft (0.5–2.0 keV) X-ray band which go down to fluxes $S \sim 5 \times 10^{-17}$ erg cm^{-2} s^{-1}: these are fitted well by the GSH models, which show a clear cosmological flattening at fluxes below the above limit (MG02).

Fluctuation analysis, a powerful tool for constraining the source counts below source detection limit (see MG02 and references therein for an exposition of the method), has recently been applied by MG02 to the 1 Ms observation of HDF-N. MG02 have found the remarkable result that the constraints so obtained on the soft-band log N–log S plot suggest that the extension of the plot down to fluxes $S \sim 7 \times 10^{-18}$ erg cm^{-2} s^{-1} continues to rise as at higher fluxes, showing no signs of the cosmological flattening characteristic of the GSH models. The most obvious interpretation is that, while the AGN contribution, as modelled by GSH, begins to saturate at these fluxes, a new population of faint sources begins to dominate. The fact that the extension of the log N–log S plot, as inferred from the fluctuation-analysis constraints of MG02, agree well with that shown in the above Ptak01 plot (see MG02 for details) particularly for the Gaussian SFR profile, therefore leads to the exciting possibility that first signatures of cosmic star formation in the soft X-ray band log N–log S plots are revealing themselves.

4. Discussion

In this *Chandra* and *XMM-Newton* era, remarkable results on L_X-evolution and SFR signature have been possible so far by going below the source detection limit with stacking and fluctuation analysis. These suggestive indications must be confirmed with source detection at lower fluxes, first with longer exposures with *Chandra* and *XMM-Newton*, and then with the next generation of satellites like *Constellation-X* and *XEUS*. On the theoretical side, the evolutionary scheme must be generalized to include additional effects like **(a)** that, in the *soft* X-ray band, the output of a normal galaxy may have very significant contributions from supernova remnants, and, **(b)** that tidal capture creation of LMXBs in globular clusters may be the dominant production mechanism in certain galaxy-types. Inclusion of these effects presents no difficulties of principle: the results will be described elsewhere.

References

Blain, A. W., *et al.*1999, *MNRAS*, **302,** 632 (B99a).
Blain, A. W., *et al.*1999, *MNRAS*, **309,** 715 (B99b).
Brandt, W. N. *et al.*2001, *A. J.* **122,** 1 (Bran01).
Ghosh, P., White, N. 2001, *Ap. J.*, **559,** L97 (GW01).
Gilli, R., Salvati, M., Hasinger, G. 2001, *A&A* **366,** 407 (GSH).
Madau, P., Pozzetti, L., Dickinson, M. 1998, *MNRAS*, **498,** 106 (M98).
Miyaji, T., Griffiths, R. 2002, *Ap. J.*, **564,** L5 (MG02).
Ptak, A., Griffiths, R., White, N., Ghosh, P. 2001, *Ap. J.*, **559,** L91 (Ptak01).
Rocca-Volmerange, B., Fioc, M. 2000, in *Toward A New Millenium in Galaxy Morphology*, (ed.) D. L. Block, *et al.*, Kluwer: Dordrecht [astro-ph/0001398] (RF00).
White, N., Ghosh, P. 1998, *Ap. J.*, **504,** L31 (WG98).
van den Heuvel, E. P. J. 1992, in *X-ray Binaries and Recycled Pulsars*, (ed.) E. P. J. van den Heuvel and S. A. Rappaport, Kluwer: Dordrecht, p. 233 (vdH92).

J. Astrophys. Astr. (2002) **23,** 115–118

CLASS B $1359 + 154$: Modelling Lensing by a Group of Galaxies

Sunita Nair *Raman Research Institute, Bangalore 560 080, India*

Abstract. The recently discovered gravitationally lensed system CLASS B1359 + 154 appears to have six detectable images of a single background source at a redshift of 3.235. A group of galaxies acts as the lens, at a redshift of ~ 1. The present work identifies two distinct, physically plausible image configurations, a 7-image one and a 9-image one. Mass models are constructed corresponding to realizations of these two configurations. Both models call for, in addition to non-singular galaxy-type lenses, a larger scale mass component that resembles the extended dark matter distributions seen in relatively low-redshift galaxy groups. It is presently observationally impossible to study the extended X-ray emission from a group at such a high redshift, hence lensing studies are of some interest. A lensed system with a high image multiplicity does not necessarily admit of a unique lensing interpretation; discrimination is possible with additional observable details (e.g., the image parities, which are uncommon among even the simpler systems).

Key words. Gravitational lensing: multiple-imaging—individual systems: CLASS B1359 + 154—galaxy groups—dark matter.

1. Introduction

A find of the Cosmic Lens All-Sky Survey (CLASS; Myers *et al.* 1995), the radio lensed system B1359 + 154 was at first identified as a quadruply-imaged ('quad') system (Myers *et al.* 1999), although six compact radio features had been detected in a deep VLA observation at 8.46 GHz. The six radio components, denoted by letters A–F (starting from North, and labelled clockwise), have flat radio spectral indices ($\alpha_{1.7\,GHz}^{5\,GHz} \sim -0.23$ to -0.38, where $f_\nu \sim \alpha^\nu$; Rusin *et al.* 2001). Images A–D are arranged in what appears to be a typical quad configuration on a scale of $1''.7$, and E and F lie within this quad. The source that is multiply imaged has a spectroscopic redshift of $z = 3.235$ (Myers *et al.* 1999). The associated lens is a group of galaxies at an estimated redshift of 1 (Rusin *et al.* 2000), with three galaxies of similar luminosities within the circle of images and three more within $10''$ of the images, in a K-band observation.

2. The image configuration in B1359 + 154

Theoretically, it is possible to construct a variety of multiple image configurations. These are characterised by the form of the 'crossing contours', or those isochrones that self-intersect, among all the isochrones that describe the arrival time surface (written

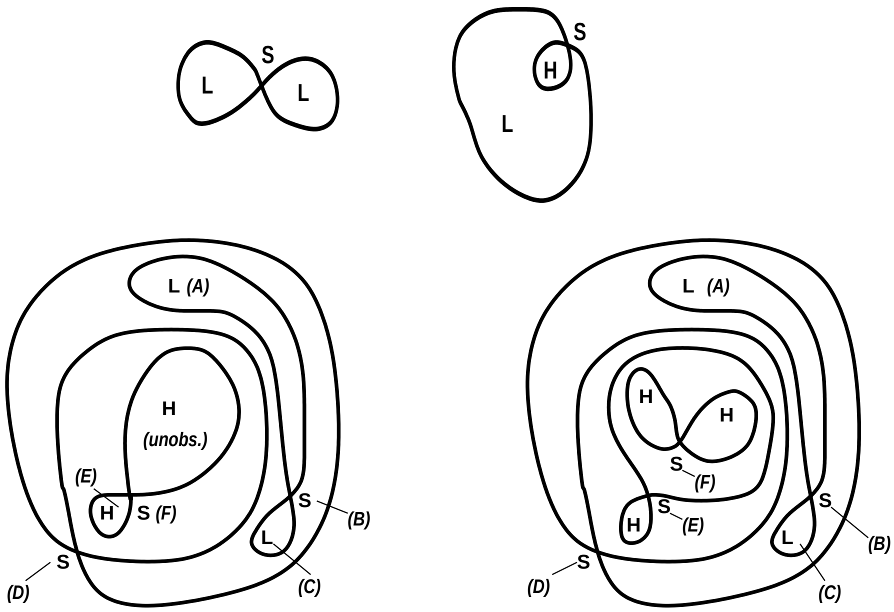

Figure 1. **(Top)**: Lemniscate (**left**) and limaçon (**right**), the three-image configuration building blocks of higher image multiplicity systems. **(Bottom)**: 7-image configuration for B1359 + 154, with one ‘core-captured’ demagnified H-type image (**left**), and 9-image configuration with three demagnified images (**right**).

Figure 2. Elementary 2-lens realization for the 6 images in B1359+154. (**Left**): Image plane critical curves with simulated images (contoured ellipses). Image magnification is proportional to the area enclosed by the ellipse. (**Right**): Source plane caustics, with source position marked by an asterisk.

as a function of possible image position, a two-dimensional vector in the plane of the sky) for light travelling from a distant source to the observer, and intercepted by a gravitational lens (Blandford & Narayan 1986). The crossing contours are either lemniscates or limaçons (for three-image configurations), or combinations of the two (for higher image multiplicities); see Fig. 1 (top). Applying Fermat’s Principle to the arrival time functional yields the number and location of the images in terms of image coordinates, and these appear at the mimima (L in Fig. 1 (top)), maxima (H) and saddle-points (S) of the arrival time surface.

The image configuration in B1359 + 154 is conceivably either a 7-image one (with one image demagnified) or a 9-image one (with three undetectable images), or, with lesser likelihood, one of even higher multiplicity and with more demagnified images. Realistic 7- and 9-image scenarios are illustrated in Fig. 1 – though it is possible to construct 25 and 111 distinct 7- and 9-image combinations out of limaçons and lemniscates, physical arguments can be employed in order to whittle down the candidates to these two. The 7-image one is a perturbation of the typical 5-image configuration obtained with an elliptical lensing potential. It can be readily obtained, for example (see Fig. 2), with the help of a non-singular elliptical lens combined with an off-centred non-singular circular (or favourably aligned elliptical) perturber lens; that such configurations are not observed oftener is perhaps because the central distinguishing images are faint and the observable images resemble a typical ‘quad’. This 7-image configuration can also be obtained with the three observed group-member galaxies proximal to the lensed images, plus some dark matter. The 9-image configuration is motivated by the presence of the three lens galaxies nearest to the images; if each lens galaxy’s mass distribution is sufficiently centrally condensed, each will harbour a demagnified ‘central’ image, so that there must be a total of 6 (visible) plus 3 (invisible) = 9 images. This too is realizable with a lens of three galaxies plus some dark matter. (Rusin *et al.* (2001) also chance upon this latter configuration, but use 3 singular lenses; the present models use non-singular lens mass distributions).

3. Realistic mass models

Realizations (Figs. 3 and 4) of the two image configurations discussed in the previous section are constructed by prescribing the lens centres for the galaxies, image positions

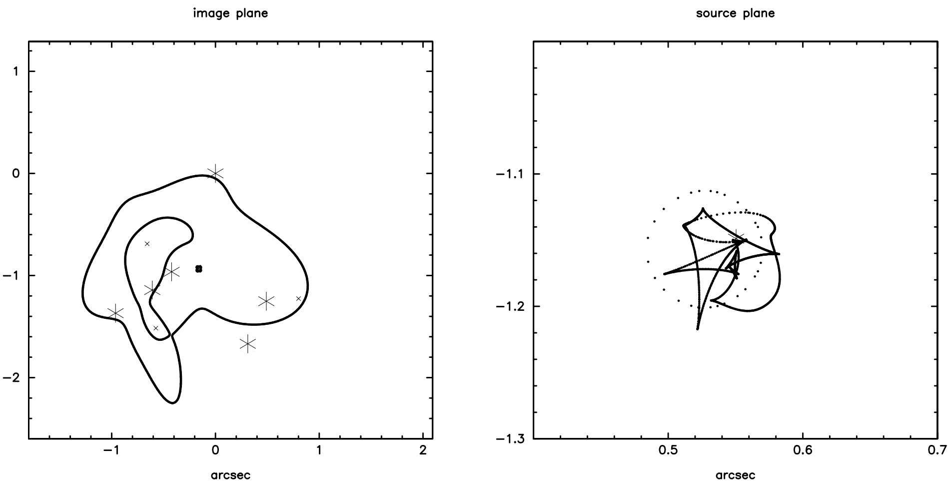

Figure 3. Model for the 7-image configuration (**Left**): Image plane critical curves; image locations are marked by asterisks, and lens centres by small crosses. The centre of the dark matter distribution is at (0.″80, −1.″23), to the west of the images. The demagnified image is near the centre of the westernmost lens galaxy at (−0.″14, −0″94). Note RA is reversed in the plots. Centre of coordinates is northernmost image A. (**Right**): The source plane caustics; the source is at the asterisk.

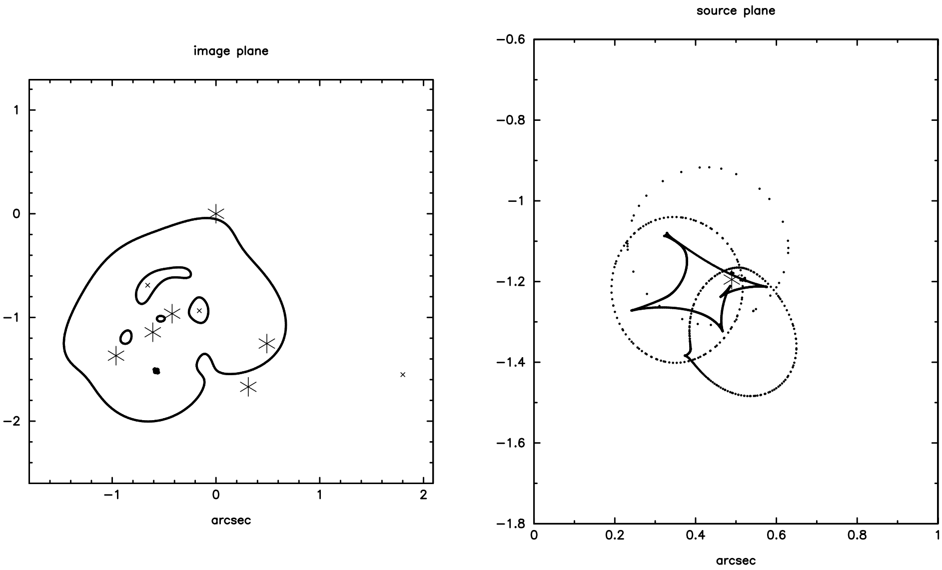

Figure 4. Model for the 9-image configuration. Details are as in previous figure, with 3 demagnified images, each proximal to one of the 3 galaxy lenses' centres. The centre of the dark matter distribution is at $(1.''80, -1.''55)$, again to the west of the image system.

and relative magnifications (from VLBA 1.7 GHz data of Rusin *et al.* 2001), and the desired image parities. The dark matter location, velocity dispersion and scale (non-singular isothermal sphere model) are determined by modelling. Scale lengths for the dark matter distribution are $2.''5$ and $1.''7$ for the 7- and 9-image configurations respectively, both centred within the region bounded by the six infrared lens galaxies of Rusin *et al.* (2000).

References

Blandford, R. D., Narayan, R. 1986, *Ap. J.*, **321,** 658.
Myers, S. T. *et al.* 1995, *Ap. J.*, **447,** L5.
Myers, S. T. *et al.* 1999, *A. J.*, **117,** 2565.
Rusin, D. *et al.* 2000, *Ap. J.*, **533,** L89.
Rusin, D. *et al.* 2001, *Ap. J.*, **557,** 594.

J. Astrophys. Astr. (2002) **23,** 119–122

Preliminary Results on VLT K-band Imaging Observations of GRB Host Galaxies

E. Le Floc'h, I. F. Mirabel & P.-A. Duc *Service d'Astrophysique, CEA-Saclay, France.*

Abstract. We have obtained K-band imaging observations of Gamma-Ray Burst (GRB) host galaxies with the near-infrared spectro-imager ISAAC installed on the Very Large Telescope at Paranal (Chile). The derived K magnitudes, combined with other photometric data taken from the literature, are used to investigate the R–K colors of GRB hosts. We do not find any extremely reddened starbursts in our sample, despite the capability of GRBs to trace star formation even in dusty regions. The observed R–K colors are on the contrary typical of irregular and spiral blue galaxies at high redshift.

Key words. Galaxies: evolution, high-redshift, dust—Gamma-ray Bursts.

1. Introduction

A major timely event in astrophysics has been the dramatic transformation in our understanding of gamma-ray bursts (GRBs). There is indeed increasing evidence that the most common GRBs, those with durations longer than a few seconds, are associated with sites of massive star formation at cosmological distances. The physical properties of the afterglows, their locations at a few kpc from the center of host galaxies (e.g., Djorgovski 1999), and the statistics from the several thousands of GRBs detected so far with BATSE (Fishman *et al.* 1998), give strong support to the idea that the majority of GRBs are linked to the cataclysmic collapse of massive stars into black holes (MacFayden & Woosley 1999). Thus they can be used to sample massive star formation sites in distant galaxies. One of the great advantages of this approach is that GRBs, because they are beamed in relativistic jets (Mészáros 1999), are bright enough to be detected at lookback times up to redshifts of 20 (Lamb & Reichart 2000). Moreover, they are not attenuated by intervening columns of dust and gas, thus making the selection of star forming regions less affected by the biases associated with optical and UV surveys (e.g., Lyman- and UV-dropout techniques).

Up to 25 GRB hosts have already been discovered. These sources are not over-luminous (Schaefer 2000), and high resolution images have shown that they exhibit morphologies typical of spiral, compact or irregular galaxies (e.g., Bloom *et al.* 2002). Spectra of northern targets obtained by the Keck telescopes had first provided evidence that these galaxies are actively forming stars, but not at a rate especially high (e.g., Bloom *et al.* 2001). Nevertheless, Sokolov *et al.* (2001) have shown that a significant internal extinction by dust in several GRB hosts has probably led to under-estimated star forming rates (SFR) based either on emission lines (Balmer lines, [OII],...) or the UV continuum. Using broad-band photometry obtained with the 6m telescope of SAO

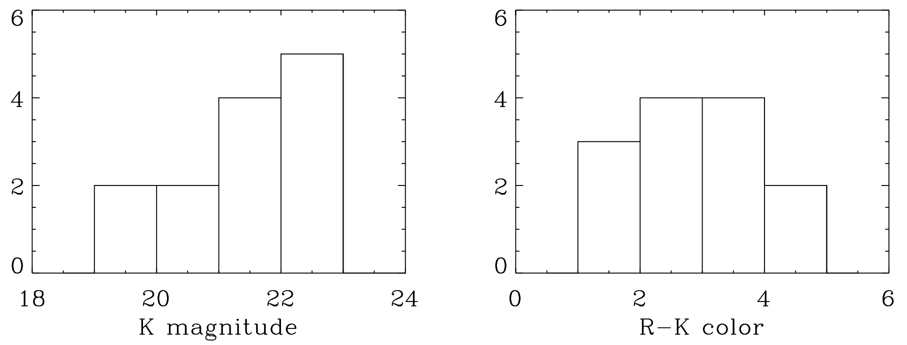

Figure 1. **Left:** *K* magnitude histogram of GRB host galaxies. Data were obtained as part of our on-going *K*-band imaging program on the VLT for 40%, the other photometric data points are quoted from Fruchter *et al.* (1999), Djorgovski *et al.* (2000), Vreeswijk *et al.* (1999), Bloom *et al.* (1999), Klose *et al.* (2000), Chary *et al.* (2002). **Right:** histogram of the observed *R*–*K* colors, for the similar sample of GRB hosts. The *R* magnitudes were taken from the literature, see Djorgovski *et al.* 2001 for references.

RAS, they measured the amount of dust absorption in a sub-sample of GRB hosts and revised their SFR to higher values, suggesting that some of them could harbor star formation rates greater than a few tens or even hundreds of solar masses per year. We finally note that the possibility to find powerful starbursts probed by Gamma-ray Bursts has been recently illustrated by the discovery of three Ultraluminous Infrared Galaxies among the GRB host sample (GRB 980703 host, Berger *et al.* 2001a – GRB 010222 host, Frail *et al.* 2002 – GRB 000418 host, Berger *et al.* 2001b) with SFR greater than 500 $M_\odot\,yr^{-1}$.

2. Observations and results

Here we report on K-band imaging of several GRB hosts obtained with the VLT. Near-infrared (NIR) observations, which are less affected by extinction than those performed at optical wavelengths, not only provide a better view on the evolved stellar populations of galaxies, but may also reveal whether an additional component from hot dust emission significantly contributes to the optical/near-infrared spectral energy distribution (SED). Reddened optical-to-NIR colors can indeed be used as a telltale indicator for dust enshrouded star formation (e.g. HR10, Dey *et al.* 1999), such as in the case of a high fraction of EROs (Extremely Red Objects, defined with e.g., $R - K \geq 5$). We have therefore compared the *K*-band photometry of the GRB hosts that we have observed, with their *R*-band magnitudes taken from the literature.

The histograms showing the distributions of the *K* photometry as well as the *R*-*K* colors are presented in Fig. 1. Since the current sample of sources probed by GRBs is rather small (less than 30 galaxies), we have also included the photometric data points of other GRB hosts obtained by various groups (see figure caption for references). This allowed us to gather a total of 13 sources, and derive a more representative statistical analysis of their NIR magnitudes and colors.

First, as it can be seen in the *K* magnitude histogram, it is yet naïve but important to note that GRB host galaxies are rather faint objects as expected for field sources at high redshifts. An important fraction of the sample has indeed *K* magnitudes greater than 22, showing that long exposure times on the largest 8-to-10 m diameter ground-based telescopes are required to detect those sources. Similarly, we note that numerous GRB hosts have R mag higher than 25 (see e.g., Djorgovski *et al.* 2001). Second, it is quite interesting to mention that we do not find any reddened objects among the current sample of GRB hosts. Rather, we have taken account of their redshift and their morphology as shown by the high resolution images obtained with the HST (e.g., Bloom *et al.* 2002) to calculate the k-corrections to their R and K magnitudes, and found that the R–K colors are simply typical of irregular and spiral galaxies at high redshift.

3. A brief discussion

It is now widely believed that the extremely reddened objects denote dusty starbursts reddened by dust as well as old stellar populations in distant elliptical galaxies whose dominant emission is redshifted to the near-infrared. Yet, the respective fractions of these two classes among the full ERO population still remain unclear, and the association of the embedded star forming activity pointed by the starburst-EROs with the dusty high-z galaxies luminous in the far-infrared and submillimeter (e.g., SCUBA galaxies, Hughes *et al.* 1998) is still a matter of debate. By no means GRB host observations alone will help in enlightening such key issues for our understanding of star formation and galaxy evolution in the distant universe. Yet, the fact that no ERO is currently detected among GRB hosts is rather puzzling, since GRBs are thought to trace star formation without being affected by dust extinction and could be used therefore to probe cosmic star forming sites even in dusty environments.

A rather natural explanation for such a non-detection of ERO could be simply due to the very poor statistics currently available regarding GRB hosts. Moreover, one must keep in mind that the GRBs for which host galaxies have been studied so far only represent a small fraction of the full sample of detected GRBs, mainly those which were localized with a position better than 1” thanks to their afterglows observed either at optical, near-infrared and/or radio wavelengths[1]. Even though gamma-rays are not attenuated by dust and gas, their optical transients could still be affected by extinction, meaning that a fraction of our sample would be biased toward unobscured star forming regions. On the other hand, one may note that Ultraluminous Infrared galaxies (ULIRGs) have already been detected among GRB hosts. Two of them are reported in our sample, and therefore do not harbor particularly red colors. Moreover, the optical transients of the GRBs discovered in some of these ULIRGs did not exhibit any signature of significant dust absorption. This may be linked to the fact that gamma and hard-X rays can sublimate the dust particules along the burst line of sight (Fruchter *et al.* 2001).

A better characterization of the properties of GRB transients from X-ray to radio wavelengths is therefore required, to allow a clear understanding of the biases affecting our current sample of GRB host galaxies. The recent and successful commissioning of the HETE-2 mission will help in detecting numerous new GRBs, and will likely lead to significant progress in this area.

[1]Note that arcsec positions may also be obtained in the X-rays with Chandra, which however has been successful in discovering X-ray GRB afterglows only in very few cases so far (e.g. GRB000210).

Acknowledgements

We acknowledge our referee for his/her comments which improved the quality of the manuscript. ELF wishes to warmly thank the Organizing Committee of the Conference "Multicolor Universe" for having organized such a fruitful and pleasant meeting in Mumbai, and partly granting his participation to that conference.

References

Berger E., Kulkarni S. R., Frail D. 2001a, *Ap. J.*, **560,** 652.
Berger E., *et al.* 2001b, *GCN*, 1182.
Bloom J. S., Odewahn S., Djorgovski S., *et al.* 1999, *Ap. J.*, **518,** L1.
Bloom J. S., Djorgovski S., Kularni S. 2001, *Ap. J.*, **554,** 678.
Bloom J. S., Kulkarni S., Djorgovski S. 2002, *AJ*, **123,** 1111.
Chary R., Becklin E., Armus L. 2002, *Ap. J.*, **566,** 229.
Dey A., Graham J., Ivison R., *et al.* 1999, *Ap. J.*, **519,** 610.
Djorgovski S. G., Odewahn S., Gal R., *et al.* 1999, *AAS*, **194,** 414.
Djorgovski S. G., Bloom J. S., Kularni S. 2000, *Ap. J. L.* submitted (astro-ph/0008029).
Djorgovski S. G., Frail D., Kulkarni S., *et al.* 2001, astro-ph/0106574.
Fishman G. J. 1998, in: *The Hot Universe*, (eds.) Koyama *et al.*, IAU S188, 159.
Frail D. A., Bertoldi F., Moriarty-Shieven G. H., *et al.* 2002, *Ap. J.*, **565,** 829.
Fruchter A., Pian E., Thorsett S., *et al.* 1999, *Ap. J.*, **516,** 683.
Fruchter A., Krolik J., Rhoads J. 2001, *Ap. J.*, **563,** 597.
Hughes D., Serjeant S., Dunlop J., *et al.* 1998, *Nature*, **394,** 241.
Klose S., Stecklum B., Masetti M., *et al.* 2000, *Ap. J.*, **545,** 271.
Lamb D. Q., Reichart D. E. 2000, *Ap. J.*, **536,** 1.
MacFayden A. I., Woosley S. E. 1999, *Ap. J.*, **524,** 262.
Mészáros P. 1999, *Nature*, **398,** 368.
Schaefer B. E. 2000, *Ap. J.*, **532,** L21.
Sokolov V. V., Fatkhullin T., Castro-Tirado A., *et al.* 2001, *A&A*, **372,** 438.
Vreeswijk P., Galama T., Owens A., *et al.* 1999, *Ap. J.*, **523,** 171.

J. Astrophys. Astr. (2002) **23,** 123–127

Multi-band Observations of Gamma Ray Bursts

S. G. Bhargavi *Indian Institute of Astrophysics, Bangalore 560 034, India*
email: bhargavi@iiap.ernet.in

Abstract. This talk focuses on the various aspects we learnt from multi-band observations of GRBs both, before and during the afterglow era. A statistical analysis to estimate the probable redshifts of host galaxies using the luminosity function of GRBs compatible with both the afterglow redshift data as well as the overall population of GRBs is discussed. We then address the question whether the observed fields of GRBs with precise localizations from third Inter-Planetary Network (IPN^3) contain suitable candidates for their host galaxies.

Key words. Gamma rays: bursts—CCD: observations—Methods: statistical.

1. Studies before the afterglow era

In 1994–95 we undertook a program to carry out an optical survey of a few GRB fields chosen from the IPN^3 catalog (Hurley 1995, private communication; Laros *et al.* 1998; Hurley *et al.* 2000). Deep CCD imaging of these fields was carried out at the 2.34 m and 1.02 m telescopes of Vainu Bappu Observatory (VBO), Kavalur until 1998. It was an attempt to identify the transient/quiescent counterparts of GRBs on the basis of photometric studies. For details on observations and photometric data analysis see Bhargavi (2001). In similar investigations the observers either looked for peculiar objects (Vrba *et al.* 1995) or an over-abundance of certain class of objects (Larson 1997) in their deep imaging surveys of IPN GRBs. None of our efforts led to an identification of a GRB counterpart.

Indeed, observational investigations were biased by the theoretical predictions (also vice versa), as it can be seen in the literature the earliest searches focussed on looking for Galactic objects where as those performed in 90s (after BATSE announced the first results) began to look for extra-galactic objects as possible sources of GRBs. In reality, the search strategies were rather vague due to our lack of knowledge of the nature of GRBs or their accompanying optical emission. Therefore it was not straight forward to associate an object to a GRB phenomenon.

Subsequent to the launch of the *BeppoSAX* satellite, which provided accurate sky co-ordinates within a few hours after the burst, the afterglow studies of GRBs have shown that fading Optical Transient (OT) is observable over a couple of months from ground-based optical telescopes (although with HST and in radio band the observations may be extended up to $\sim$year) and therefore one can safely rule out the possiblity of detecting any possible transient counterpart associated with IPN^3 GRBs in the CCD frames observed several years after the burst. Afterglow studies have also shown that

GRBs are hosted by faint galaxies at cosmological distances. In any given field of $\sim 10' \times 10'$ area one may find several faint galaxies and the number would increase as one observes deeper and deeper. However, it is difficult to pin down any of these objects as definite host of a GRB that occurred a few years ago. This is because the host galaxies neither show any evidence of burst in their quiescent state (i.e., OT does not leave behind any signature identifiable by optical observations after several years), nor exhibit any 'unusal' properties.

2. Luminosity function of GRBs

In an attempt to identify the potential candidates for the host galaxies of GRBs in our observed fields, we first ask what is the most probable redshift of the host galaxy of a GRB, given the γ-ray flux? This requires knowledge of the luminosity function of GRBs. Until recently one could detemine the luminosity function of GRBs from the number-count v/s flux ($\mathcal{N} - F$) relation. The optical afterglow observations have allowed redshift measurements for ~ 17 GRBs. In an analysis to detemine the luminosity function of GRBs Sethi & Bhargavi (2001) identified a luminosity function that is compatible with both the samples: **(a)** redshift distribution of GRBs with observed afterglows **(b)** number-count v/s flux ($\mathcal{N} - F$) relation of overall population of GRBs. While they considered Schechter, scale-free and log-normal luminosity distributions each with several evolutionary as well as no-evolution models using $\Omega_m = 0.3$, $\Omega_\Lambda = 0.7$ and $H_0 = 65\,\mathrm{km\,sec^{-1}\,Mpc^{-1}}$ cosmology, they found that only log-normal distribution is compatible with both (a) and (b) samples.

In the present analysis a few changes from the previous work of Sethi & Bhargavi (2001) have been incorporated: first, an additional factor of $(1+z)^{-1}$ has been introduced in their equation (3) which comes from cosmological time dilation of the rate of GRBs. Secondly, $p(z)$ in their equation (8), probability that burst of a given flux will occur in a redshift range of z to $z+dz$ here, is a joint redshift-flux probability $P(z, F)$.

Assuming a simple number density evolution the number of GRBs in the redshift range z and $z+dz$ and in the luminosity range L and $L+dL$ can be factorized as

$$N(z, L; a_i)dLdz = n(z)4\pi r^2 \frac{dr}{dz}\Phi(L; a_i)dLdz \tag{1}$$

a_i stands for the parameters of the luminosity function (e.g., σ and L_0 for the Log normal distribution). Here $n(z) = n_0(1+z)^\gamma$ is the comoving number density of GRBs up to a maximum redshift $Z_{\max}$ and $\Phi(L)$ is the non-evolving luminosity distribution. Using $L = 4\pi D_L^2 F$, we can get the number of GRBs in the redshifts range and the flux range F and $F+dF$:

$$N(z, F; a_i)dFdz = n_0(1+z)^\gamma 4\pi r^2 \frac{dr}{dz}\Phi(L; a_i)\frac{dL}{dF}dFdz. \tag{2}$$

Note that the Jacobian of transformation from $\{z, L\}$ to $\{z, F\}$ is simply $(dL/dF)_z$. For converting this into joint probability $P(z, F)$ of observing a source with flux in the range F and $F+dF$ and redshift range z and $z+dz$ one must divide $N(z, F)$ by the normalizing factor:

$$\mathcal{N} = \int_0^{z_{\max}} dz \int_{F_{\min}}^{\infty} dF N(z, F; a_i). \tag{3}$$

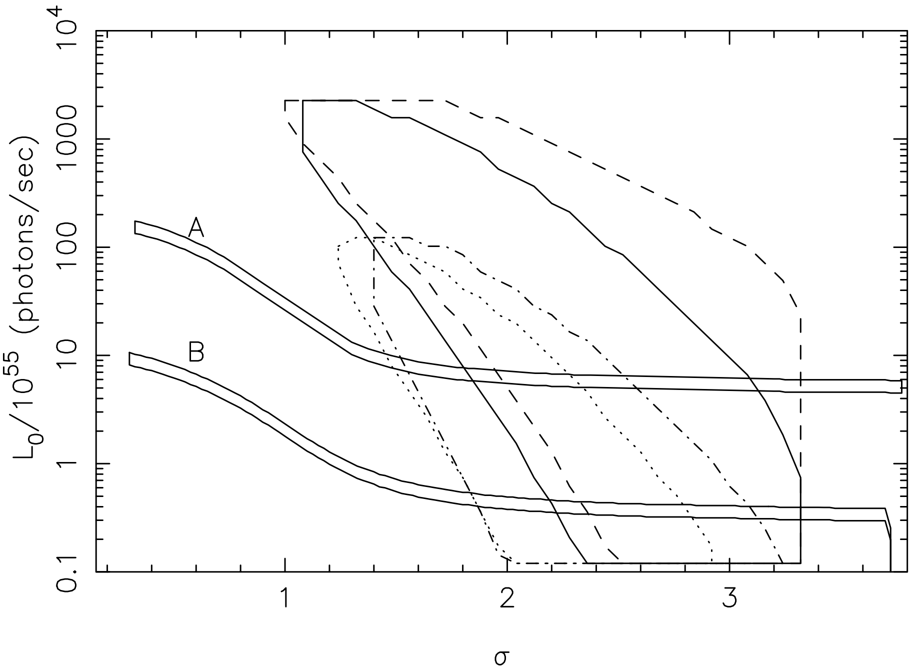

Figure 1. The results for the log-normal luminosity function are shown. The narrow regions (A, B) come from the N–F analysis and represent the region of K-S probability $P_{ks} > 0.01$ for the consistency between observed and theoretical number count-flux relation. We show the curves for no-evolution (B) and strong evolution (A) models. The broader regions (corresponding to $\approx$ 99% confidence level) come from afterglow analysis. They correspond to: no evolution model with no beaming correction (solid line), no evolution model with beaming correction (dotted line), strong evolution model with no beaming correction (dashed line) and strong evolution model with beaming correction (dot-dashed line).

For our analysis we take $z_{\max} = 5$ and $F_{\min} = 0.05$. The results are not very sensitive to the values of $z_{\max}$, $F_{\min}$. The joint probability is:

$$P(z, F; a_i)dFdz = \frac{N(z, F)}{\mathcal{N}} dzdF. \tag{4}$$

The likelihood that the observed set of 16 GRBs arise out of any assumed luminosity function is given by:

$$\mathcal{L}(a_i) = \prod_{j=1}^{16} P(z, F; a_i). \tag{5}$$

We need to maximize $\mathcal{L}(a_i)$ with respect to the parameters, $\{a_i\}$. Fig. 1 shows the results of such an exercise for log-normal distribution indicating regions where $\mathcal{L}(a_i)$ exceeds 10^{-4} times the value at the maximum (i.e., $\approx$ 99% confidence level). Also note that the allowed regions become narrower after beaming correction has been applied.

Table 1. Probable redshift range: IPN GRBs .

GRB	Peak flux ph/cm^2/s	$\langle z \rangle$ for L_0(sec^{-1}) 10^{55}	10^{56}	Limiting magnitude	Z-range (mean $\pm 1\sigma$)
GRB 920720	15.437	0.16	0.42	B = 22.8	0.26 – 0.62
GRB 920517	38.757	0.11	0.29	B = 22.0	0.19 – 0.53
GRB 920525	22.64	0.14	0.36	V = 22.7	0.28 – 0.64
GRB 920325	13.75*	0.17	0.44	R = 20.9	0.18 – 0.5

*Flux was converted from the observed 25–100 keV range to the BATSE range (50–300 keV) using the method discussed in Bhargavi (2001).

2.1 *Estimation of redshifts*

Using the best-fit parameters $10^{55}\,\mathrm{sec}^{-1} \leq L_0 \leq 10^{56}\,\mathrm{sec}^{-1}$ and $2 \leq \sigma \leq 3$ for log-normal distribution, where L_0 is the average photon luminosity and σ is the width of the luminosity function, we calculate the average redshift and the variance of the expected redshift of the GRB of a given flux as follows:

$$\langle z \rangle = \int_0^\infty z p(z)\, dz\,; \quad \sigma = \int_0^\infty (z - \langle z \rangle)^2 p(z) dz \tag{6}$$

In Table 1 we show fluxes of 4 IPN GRBs and the range of their redshifts (columns 3 & 4). The redshifts lie in the range 0.1–0.4 when L_0 is varied between 1 and 10 in units of $10^{55}\,\mathrm{sec}^{-1}$. The variances are close to the mean value.

Similarly, we estimate the average redshift and variance for a sample of galaxies in a magnitude-limited sample. The relation between apparent magnitude m and absolute magnitude M is:

$$M = m - 25 \log_{10}(r/1\,\mathrm{Mpc}) - 2.5 \log_{10}(1+z) - m_K(z, \lambda) \tag{7}$$

m_K is the K-correction for galaxies and is a function of the redshift and the wavelength λ of the observed band. We apply these from Coleman, Wu & Weedman (1980). Given the absolute magnitude, the luminosity ($\mathrm{erg\,sec}^{-1}$) in different wave bands can be calculated using:

$$L_\lambda = L_\odot \times 10^{[0.4 \times (C - M_\lambda)]}. \tag{8}$$

Here $L_\odot = 4 \times 10^{33}$ is the bolometric luminosity of the Sun. The value of C has been taken to be 5.41, 4.79 and 4.49 respectively for B, V and R band filters.

The luminosity function of galaxies in B-band and its evolution for $z \leq 1$ is taken from Loveday *et al.* (1992) and Lilly *et al.* (1995). The luminosity function in other wave-bands can be obtained by using the spectral energy distribution given by Yoshii & Takahara (1988). For simplicity we assume the galaxy spectral distribution to remain unchanged for $z \leq 1$.

The redshift range for a given magnitude limit for the four IPN fields is given in column 6 of Table 1. The range refers to the 1σ deviation from the mean redshift. Comparing this with the redshift range in columns 3 & 4 of Table 1 we notice that the redshift range corresponding to the limiting magnitude of observed field overlaps with the redshift range from which the GRBs originate in all four cases. Therefore the GRB host might lie in the observed field.

If GRBs are associated with galaxies then it is natural to ask whether the observed fields have any plausible candidates for the GRB hosts. Most of the previous studies assumed GRBs to be standard candles, while our study shows that the GRB luminosity function is quite broad. This basically means that the redshift range from which the GRBs originate is also quite broad, as is evidenced by Table 1. Therefore some of the objects seen inside the error boxes could be the host, but we cannot rule out the possibility of the host being fainter than the magnitude limit of the survey. Moreover, since the z ranges compatible with the survey limits are marginal to the actual distribution of measured z, it is not likely that the host is detected in all the 4 error boxes.

Acknowledgements

This talk is based on part of the work carried out for my Ph. D. thesis. I thank my thesis adviser, Prof Ramanath Cowsik for the guidance and useful comments on this manuscript; Dr Shiv Sethi (HRI, Allahabad) for discussions and help in the analysis of luminosity functions of GRBs; Drs. F Vrba & A Henden (USNO, Flagstaff) for providing the calibration data on IPN fields.

References

Bhargavi, S. G. 2001, in *An investigation into the sources associated with the GRB phenomenon*, Ph. D. thesis (Mangalore University).
Coleman, G. D., Wu, C., Weedman, D. W. 1980, *Ap. J. S.*, **43,** 393.
Hurley, K. *et al.* 2000, *Ap. J.*, **533,** 884.
Laros, J. G. *et al.* 1998, *Ap. J. S.*, **118,** 391.
Larson, S. B. 1997, *Ap. J.*, **491,** 86.
Lilly, S. J. *et al.* 1995, *Ap. J.*, **455,** 108.
Loveday, J. *et al.* 1992, *Ap. J.*, **390,** 338.
Sethi, S. & Bhargavi, S. G. 2001, *A & A* **345,** 10.
Vrba, F. J. *et al.* 1995, *Ap. J.*, **446,** 115.
Yoshii, Y. & Takahara, F. 1988, *Ap. J.*, **326,** 1.

J. Astrophys. Astr. (2002) **23,** 129–135

An Exact Solution of the Gamma Ray Burst Arrival Time Analysis Problem

S. Sinha *ISRO Satellite Center, Bangalore 560 017, India*

Abstract. An analytical solution of the GRB arrival time analysis is presented. The errors in the position of the GRB resulting from timing and position errors of different satellites are calculated. A simple method of cross-correlating gamma ray burst time-histories is discussed.

Key words. Gamma Ray Bursts—triangulation.

1. Introduction

Most GRB detectors (with the exception of BATSE) have practically no angular resolution one can speak of. The positions of GRB sources in the celestial sphere are determined accurately (a few arc minute error box) from the arrival times of the GRB photon front at widely spaced detectors onboard several different satellites that constitute what is known as an inter-planetary network (IPN). *Numerical* solutions of this Arrival Time Analysis problem have been developed and are in use since many years (K. Hurley, pvt. comm.). In the present work an *analytical* solution of this arrival time analysis (triangulation) problem of GRBs is described. The error in the determined position of the GRB source that results from position and timing errors of different satellites is also calculated. A simple method of cross-correlating two given GRB time-histories is discussed.

2. Method of calculation

If the positions of the satellites and the timings are exactly known, the GRB position may be determined exactly, i.e., it will be a point on the celestial sphere. In practice, however, there are uncertainties both in the positions of the satellites and in the timings. These uncertainties result in a corresponding uncertainty in the position of the GRB. Hence, the GRB source can be located only within an error box, the size of which is determined by the uncertainties in satellite positions and the timings. Using the timing information from two widely separated spacecrafts an annulus in the sky may be obtained. Using a third satellite two different annuli are obtained that intersect each other and result in two error boxes. If there is a fourth non-coplanar satellite in the network, then, using this information the ambiguity between the two error boxes may be resolved and a unique positional error box is obtained for the source of the detected GRB.

Sometimes multiple GRB monitors are flown on a single satellite. Using the relative intensities of detection, a coarse position is derived. This itself may remove the degeneracy between the two error boxes. Otherwise, earth occultation of one of the two directions also might be used for the same purpose. In that case the fourth satellite is not absolutely essential. On the other hand, having a network of a large number of widely separated satellites with on-board GRB monitors with good timing accuracy helps in determining very accurate source positions.

3. Determination of the mean radii of the annular rings

Let us consider three different satellites with their mean positions given in the geocentric equatorial co-ordinate frame, namely, r_i, α_i, δ_i where $i = 1, 2, 3$. r_i is the radial distance of the ith satellite from the geocenter, α_i is the right ascension and δ_i is the declination. Let t_i be the mean arrival time of the burst at the ith satellite. We transform r_i, α_i, δ_i by the following prescription, $r_i \Rightarrow r_i, \alpha_i \Rightarrow \phi_i, (90^o - \delta_i) \Rightarrow \theta_i$ (θ_i is the North Polar distance of the satellite). This coordinate system will be referred to as the original (O) system. It is a geocentric reference system in which the X-axis is the line $O\gamma$ where γ is the first point of Aries and the Z-axis points towards the celestial North pole.

$$\mathbf{r_{12}} = \mathbf{r_1} - \mathbf{r_2} \tag{1}$$

where $\mathbf{r_{12}}$ is the vector from the satellite which saw the burst second to the satellite which saw the burst first. The X-component of $\mathbf{r_{12}}$ is

$$r_{12x} = r_1 \sin\theta_1 \cos\phi_1 - r_2 \sin\theta_2 \cos\phi_2. \tag{2}$$

The Y- and Z-components of $\mathbf{r_{12}}$ are defined likewise. The three components of $\mathbf{r_{12}}$ in this spherical polar coordinate system are:

$$r_{12} = sqrt(r_{12x}^2 + r_{12y}^2 + r_{12z}^2), \tag{3}$$

$$\theta_{12} = \cos^{-1}(r_{12z}/r_{12}), \tag{4}$$

$$\phi_{12} = \tan^{-1}(r_{12y}/r_{12x}). \tag{5}$$

The relative time delay between the arrivals of the GRB front at the two satellites is

$$\Delta t_{12} = t_2 - t_1. \tag{6}$$

The mean radius of the annulus around $\mathbf{r_{12}}$ in which the GRB source is located is given by

$$\theta_{sp12} = \cos^{-1}(c * \Delta t_{12}/r_{12}) \tag{7}$$

(refer to Fig. 1a) where c is the velocity of light. Similarly, the mean radius of the annulus around $\mathbf{r_{13}}$ in which the GRB source is located is (when satellites 1 and 3 are considered),

$$\theta_{sp13} = \cos^{-1}(c * \Delta t_{13}/r_{13}) \tag{8}$$

where Δt_{13} is the time delay observed between detectors 1 and 3.

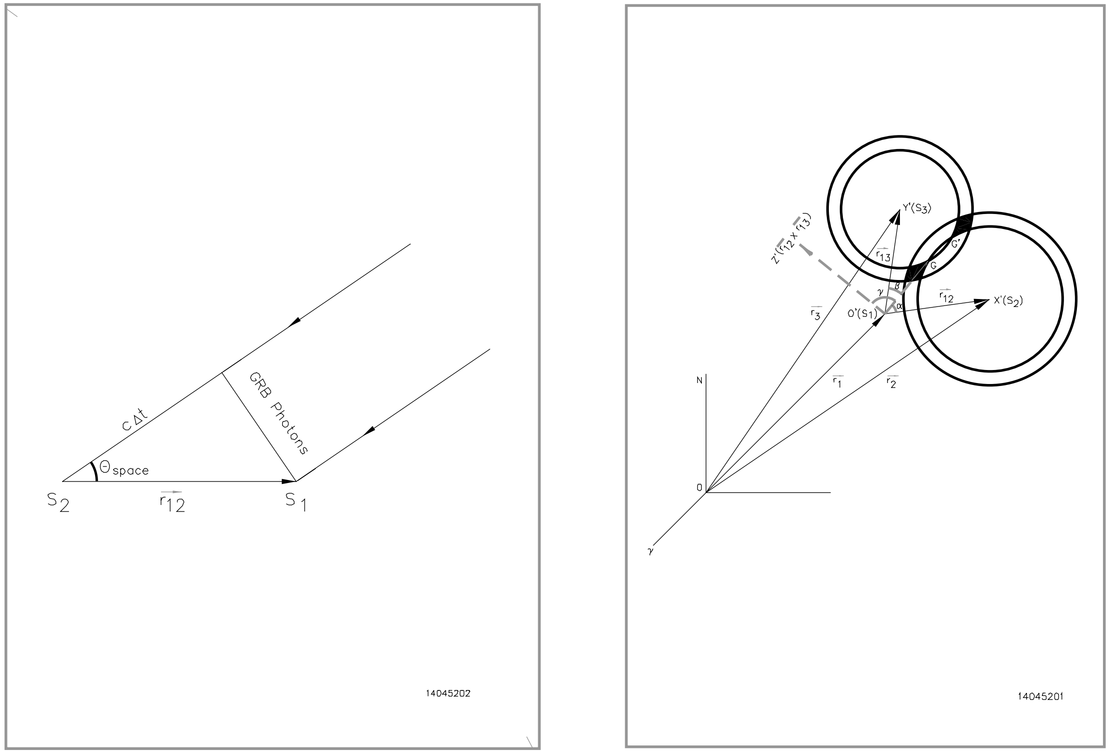

Figure 1. **(a)** Determination of the mean radius (θ_{space}) of the annular ring from the relative time delay of GRB arrivals at two satellites S_1 and S_2 separated by a distance r_{12}. **(b)** $O\gamma N$ is the geocentric coordinate system (O is the geocentre, γ is the first point of Aries and N is the celestial north pole). $O'X'Y'Z'$ is the oblique coordinate system, where $\mathbf{OO}'$, $\mathbf{OX}'$ and $\mathbf{OY}'$ are the position vectors of the three satellites 1, 2 and 3 respectively. $\mathbf{O'Z'}$ points along the vector ($\mathbf{r_{12}Xr_{13}}$). The two circles (having radii θ_{sp12} and θ_{sp13} respectively) intersect at two points G and G'. The GRB source is located in one of the two shaded error boxes (the degeneracy is removed by using a fourth non coplanar satellite). The vector $\mathbf{OG}$ makes angles α, β and γ with the three axes ($\mathbf{r_{12}}$, $\mathbf{r_{13}}$, and $\mathbf{r_{12}Xr_{13}}$) of the oblique coordinate system.

4. Determination of the widths of the annular rings

The error in θ_{sp} (the radius of the annulus) resulting from the uncertainty in time of arrival of the GRB ($\delta\Delta t_{ij}$) is given by

$$\mathrm{d}\theta_{spT} = (c * \delta(\Delta t_{ij}))/(r_{ij} * \sin(\theta_{sp})). \tag{9}$$

The magnitude of the error in the position vector $\mathbf{r_i}$, $\mathrm{d}\mathbf{r_i}$ is

$$\mathrm{mod}(\mathrm{d}\mathbf{r_i}) = sqrt(\mathrm{d}r_i^2 + r_i^2 \mathrm{d}\alpha_i^2 \cos^2\delta_i + r_i^2 \mathrm{d}\delta_i^2) \tag{10}$$

where $r_i = \mathrm{mod}(\mathbf{r_i})$. The maximum error in position is given by $\mathrm{d}\mathbf{r} = \mathrm{d}\mathbf{r_i} + \mathrm{d}\mathbf{r_j}$. The error in the radius of the annulus resulting from this position error of the two satellites is given by

$$\delta\theta_{spPOS} = (\mathrm{d}r_i + \mathrm{d}r_j)/(r_{ij} * \sin(\theta_{spij})). \tag{11}$$

The total width of the annulus (resulting from both timing as well as position uncertainties) is, therefore,

$$\delta\theta_{sp} = 2 * (\delta\theta_{spPOS} + \delta\theta_{spT}). \tag{12}$$

The two boundaries of the annulus are given by $\theta_{\mathrm{spin}} = \theta_{sp} - \delta\theta_{sp}$ and $\theta_{\mathrm{spout}} = \theta_{sp} + \delta\theta_{sp}$.

5. Calculation of the points of intersection

The two annuli intersect at totally eight points (two sets of four points each). Each set of four points constitute the four corners of an error box. The GRB source is located in one of these two error boxes. An oblique co-ordinate system (Fig. 1b) is chosen in which the three axes are along $\mathbf{r_{12}}(O'X')$, $\mathbf{r_{13}}(O'Y')$ and $\mathbf{r_{12}} X \mathbf{r_{13}}(O'Z')$, (the three satellites S_1, S_2 and S_3 are located at the points O', X' and Y' respectively). The angles $Y'O'Z' = \lambda = Z'O'X' = \mu = 90^o$ and $X'O'Y' = \nu$ where $\cos\nu$ may be calculated as

$$\sin\theta_{12}\cos\phi_{12}\sin\theta_{13}\cos\phi_{13} + \sin\theta_{12}\sin\phi_{12}\sin\theta_{13}\sin\phi_{13} + \cos\theta_{12}\cos\theta_{13} = \cos\nu. \tag{13}$$

Equation (13) is obtained by forming the dot product of the two unit vectors along $\mathbf{r_{12}}$ and $\mathbf{r_{13}}$. The vectors $\mathbf{r_{12}}$ and $\mathbf{r_{13}}$ are completely known in terms of the original $(O\gamma N)$ co-ordinate system. Let us consider one of the points of intersection, viz. that between the two inner circles. The direction cosines of the unit vector that joins the origin to this point of intersection (with respect to the oblique axes, $O'X'Y'Z'$) are $\cos\theta_{\mathrm{spin}}(\theta_{sp12in} = \theta_{sp12} - \delta\theta_{sp12})$, $\cos\theta_{sp13in}(\theta_{sp13in} = \theta_{sp13} - \delta\theta_{sp13})$ and X (unknown) respectively. Let us denote these three direction cosines by $\cos\alpha$(α to be distinguished from right ascension), $\cos\beta$ and $\cos\gamma$ respectively. $\cos\gamma$ is unknown and may be calculated from the following relation (Bell 1960)

$$\begin{vmatrix} 1 & \cos\nu & \cos\mu & \cos\alpha \\ \cos\nu & 1 & \cos\lambda & \cos\beta \\ \cos\mu & \cos\lambda & 1 & \cos\gamma \\ \cos\alpha & \cos\beta & \cos\gamma & 1 \end{vmatrix} = 0 \tag{14}$$

which is equivalent to

$$\cos^2\alpha + \cos^2\beta + \cos^2\gamma \sin^2\nu - 2\cos\nu\cos\alpha\cos\beta = 1 - \cos^2\nu \tag{15}$$

(under the assumption $\lambda = \mu = 90^\circ$, i.e., $\cos\lambda = \cos\mu = 0$, $\sin\lambda = \sin\mu = 1$). This is the relation satisfied by the direction cosines of any line. The two distinct values of $\cos\gamma$ obtained from this relation correspond to the two different points of intersection between the two inner circles. Hence all the three angles, i.e., all the direction cosines are known in terms of the oblique co-ordinate system $(O'X'Y'Z')$. Next, a transformation is necessary to calculate the direction cosines, i.e. the angles Θ, Φ with respect to the original $(O\gamma N)$ co-ordinate system from the direction cosines with respect to the oblique co-ordinate system. This is done in the following manner.

Let the unit vector in the original $(O\gamma N)$ co-ordinate frame be denoted by **V**. Its three components in the original co-ordinate system are $\sin\Theta\cos\Phi$, $\sin\Theta\sin\Phi$ and $\cos\Theta$ respectively. The matrix **A** that transforms this unit vector **V** (in the reference frame O) to the unit vector $\mathbf{V}'$ (say), in the oblique reference frame O' is given by

$$\begin{pmatrix} \sin\theta_{12}\cos\phi_{12} & \sin\theta_{12}\sin\phi_{12} & \cos\theta_{12} \\ \sin\theta_{13}\cos\phi_{13} & \sin\theta_{13}\sin\phi_{13} & \cos\theta_{13} \\ \sin\theta_{12}\sin\phi_{12}\cos\theta_{13} & \sin\theta_{13}\cos\phi_{13}\cos\theta_{12} & \sin\theta_{12}\cos\phi_{12}\sin\theta_{13}\sin\phi_{13} \\ -\sin\theta_{13}\sin\phi_{13}\cos\theta_{12} & -\sin\theta_{12}\cos\phi_{12}\cos\theta_{13} & -\sin\theta_{12}\sin\phi_{12}\sin\theta_{13}\cos\phi_{13} \end{pmatrix}.$$

The three elements of the last row are to be normalised by dividing each element by $sqrt(\Sigma_{j=1,3}A^2_{3j}$. This is necessary since the norm of the vector $\mathbf{r_{12}}$ X $\mathbf{r_{13}}$ is not unity. In this case, the vector $\mathbf{V}'$ is known and the components of the vector **V** are to be determined. This is done by the inverse transformation

$$\mathbf{V} = \mathbf{A^{-1}}\mathbf{V}'. \tag{16}$$

The inverse of the transformation matrix **A**, $\mathbf{A^{-1}}$ is calculated. The three components of the vector **V** are determined from the three components of the vector $\mathbf{V}'$ (in the oblique co-ordinate system) using the following relationships.

$$\mathbf{V_i} = \Sigma_{j=1,3}\mathbf{A^{-1}}_{ij}\mathbf{V'_j}. \tag{17}$$

Here $\mathbf{V'_1} = \cos\alpha$, $\mathbf{V'_2} = \cos\beta$ and $\mathbf{V'_3} = \cos\gamma$. The calculated values of $\mathbf{V_i}$ are transformed to α (right ascension) and δ (declination) as follows: $\delta = 90.0^\circ - \Theta$ where $\Theta = \cos^{-1}(\mathbf{V_3})$. and $\Phi = \tan^{-1}(\mathbf{V_2}/\mathbf{V_1})$. If Φ becomes less than 0 than $\Phi = \Phi + 360.0^o$; $\alpha = \Phi$. Thus the right ascension and declination of the intersection point is known in the original $(O\gamma N)$ co-ordinate system. In this manner the co-ordinates of each corner of the error box may be determined. It is to be noted that these errors are one standard deviation errors.

6. Determination of timing uncertainties: Cross-correlations of GRB time-histories

Since a given time interval Δt is equivalent to a spatial interval of $\Delta l = c * \Delta t$, the timing uncertainties, in general, contribute more to the final GRB error box size.

Therefore, it is very crucial to determine the relative time delay between two spacecrafts as precisely and accurately as possible. The relative time delay and its error are determined by doing cross-correlations between the two GRB time-histories. Various methods of cross-correlations are used in practice (K. Hurley, pvt. comm.). We describe below the chi-square method. Generally, the integration time scales and the energy bands for any two GRB detectors are different. Rebinning of high resolution data is, therefore, necessary in order to make the integration times equal. The GRB time-histories are selected such that the energy bands are either the same or are very nearly so, since the time-history of a given GRB recorded by a given detector varies with the energy band selected. The counting rates for different detectors are different and they are either scaled up or down as needed. The χ^2 is calculated as

$$(\chi^2)_i = \Sigma_{j=1,m}(A_{i+j-1} - B_j)^2/(A_{i+j-1} + B_j) \tag{18}$$

where A_k and B_l represent the two time-histories (background subtracted). m is the number of integration time bins in one (say, the short one) of the time-histories. n is the number of time bins in the other (longer) time-history. The length (duration) of a GRB time-history depends on the sensitivity of the detector. Here $i = 1, 2, \ldots, n - k$. The degrees of freedom $\nu = m - 1$. The value of χ^2 is calculated by shifting one of the time-histories with respect to the other, one bin at a time. The relative time-delay obtained between the two time-histories when the χ^2 is minimum is the required quantity. The true minimum of the χ^2 and the corresponding time lag are determined by interpolation. The uncertainty (say, 3 sigma) in the time lag is calculated by determining the points on either side for which the $\chi^2 = \chi^2_{\rm min} + \chi^2_1(\alpha)$ where α is the significance.

7. Discussion

The present method of solving the arrival time analysis (triangulation) problem of GRBs is straightforward and conceptually simpler than the *numerical* methods. It should be possible to adapt this method to determine arrival directions of Extensive Air Showers (EAS) in Ultra High Energy (UHE) or in Very High Energy (VHE) gamma ray astronomy experiments that use the Atmospheric Cerenkov Wavefront Sampling Technique (Majumdar *et al.* 2002). Plane fronts of relativistic particles or visible cerenkov photons respectively are fitted using a rather complicated χ^2 -minimisation method to determine the arrival directions of EAS in these experiments.

8. Conclusion

An analytical method to determine the position of a GRB source from the timings of arrival of the GRB at different satellites and their position co-ordinates has been presented. The errors (one standard deviation) resulting in the esimated position of the GRB are calculated from the position and timing errors of different satellites. A simple method of cross-correlating gamma ray burst time-histories has been described. Usefulness of the present method of triangulation has been discussed.

Acknowledgements

I am indebted to Prof. Kevin Hurley for several clarifications and for providing the test IPN data to check my procedure. I thank Prof. P. V. RamanaMurthy for his very useful suggestions to improve the manuscript of this paper.

References

Bell R. J. T. 1960 *An Elementary Treatise on Co-ordinate Geometry of Three Dimensions* 3rd edition (Macmillan and Co.)

Hurley, K. *Cross-correlating Gamma Ray Burst time-histories*, Proc. 2nd Huntsville Workshop (AIP 307), 1993, p 687 (eds) G. J. Fishman, J. J. Brainerd & K. Hurley.

Majumdar P. *et. al*. 2002 *Bull. Astr. Soc. India* **30**, 389–395.

J. Astrophys. Astr. (2002) **23,** 137–141

A Circular Statistical Method for Extracting Rotation Measures

S. Sarala & Pankaj Jain *Physics Department, IIT, Kanpur 208 016, India.*

Abstract. We propose a new method for the extraction of Rotation Measures from spectral polarization data. The method is based on maximum likelihood analysis and takes into account the circular nature of the polarization data. The method is unbiased and statistically more efficient than the standard χ^2 procedure.

Key words. Polarization—methods: data analysis—galaxies: magnetic fields.

1. Circular statistical method

Polarizations of radio waves from cosmologically distant sources undergo Faraday Rotation upon propagation through galactic magnetic fields. The observed orientation of the linearly polarized component of the electromagnetic wave $\theta(\lambda)$ can be written as

$$\theta(\lambda) = \theta_0 + (RM)\,\lambda^2 \tag{1}$$

where RM is the Rotation Measure and θ_0 is the intrinsic position angle of polarization (IPA). The extraction of RM is ambiguous since the observed polarization is defined only up to additions of $n\pi$, where n is an integer.

In the present paper we propose an alternate method for the extraction of RM and IPA from data. This procedure is based on maximum likelihood for distributions defined to be invariant under angular coordinate changes. The von Mises (vM) distribution serves as a prototype for the statistical fluctuations for circular data. It is given by

$$f(\theta; RM, \theta_0) = \frac{\exp\left[\kappa \cos 2(\theta - RM\lambda^2 - \theta_0)\right]}{\pi I_0(\kappa)}\,, \tag{2}$$

where κ is a measure of the concentration of population and is related to the error in measurement of the polarization angle. The best fit parameters RM, θ_0 can be obtained by maximizing the log likelihood of the spectral polarization data $\theta(\lambda)$. Maximising the log likelihood is equivalent to minimizing (Sarala and Jain 2001)

$$\chi^2_{\rm cir} = \sum_{i=1}^{N} \frac{1 - \cos 2\left[\theta_i - \theta_0 - (RM)\,\lambda_i^2\right]}{1 - \cos 2\Delta\theta_i} \tag{3}$$

where $\Delta\theta_i$ is the error in the measurement of angle θ_i.

We can obtain the distribution of the polarization angle by making the reasonable assumption that the electric field components follow a normal distribution

$$p(E_1, R_2) = \frac{\det(\mathbf{R})}{(\pi^2)} \exp\left(-\sum_{i,j=1}^{2} E_i^* R_{ij} E_j\right) .$$

E_1, E_2 are the right and left circularly polarized components of the electric field. R_{ij} are the parameters of the distribution. By making a change of variables such that $E_j = a_j \exp(i\phi_j)$ and integrating over the rest of the variables we obtain the distribution for linear polarization angle $\theta = (\phi_1 - \phi_2)/2$ as

$$p_{MB}(\theta) = \frac{(1-\xi^2)}{\pi(1-\mu^2)^{3/2}} \left[\mu \sin^{-1}\mu + \frac{\pi}{2}\mu + (1-\mu^2)^{1/2}\right] \tag{4}$$

where $\mu = \xi \cos(2\theta - 2\overline{\theta})$. Here $\xi^2 = 1 - |R_{12}|^2/R_{11}R_{22}$ $(0 \leq \xi \leq 1)$ and $\overline{\theta}$ are the parameters of the distribution which measure the concentration and mean value of the population respectively. The distribution $p_{MB}(\theta)$ is called as MacDonald-Bunimovitch (MB) distribution (MacDonald 1949; Bunimovitch 1949). We again maximize the log likelihood, $\ln \mathcal{L} = \sum_{i=1}^{N} \ln[p_{MB}(\theta_i)]$ taking the results obtained with von Mises distribution as an initial guess. This distribution requires a two dimensional maximization as it is not possible to eliminate θ_0 analytically.

The von Mises as well as the normal distribution are somewhat similar to the $p_{MB}(\theta)$ in the limit when the population is strongly concentrated near the mean value, i.e. in the limit when the parameter $\xi \to 1$. But MB distribution does not decay exponentially and hence there is large probability for θ to undergo large fluctuations. If ξ is significantly different from one, these distributions differ significantly over the entire range as shown in Fig. 1.

2. Results and discussion

We apply our procedure to the spectral polarization data given in the catalogue compiled by Tabara & Inoue (1980) for 701 sources. In Fig. 2 we show $\chi^2_{\rm cir}$ as a function of RM for two randomly selected sources. We find that $\chi^2_{\rm cir}$ has several local minima. These minima correspond to the standard ambiguity in the determination of RM due to $n\pi$ ambiguity in the polarization angle. Tabara & Inoue (1980) resolve the $n\pi$ ambiguity by searching the minimum in χ^2 over a limited range of RM which is selected on the basis of the galactic latitude b of the source. If $\cot|b| < 2$ then $|RM| \leq 200 rad/m^2$, else the range is extended to $100 \cot|b|\ rad/m^2$. We also use the same range of RM in order to search for the global minimum. In most cases we find that our results are in good agreement with the ones given in Tabara & Inoue (1980), which have been obtained using the standard linear fit. Overall the MB distribution gives results which are considerably different from $\chi^2_{\rm cir}$ and χ^2 for 28 and 35 sources respectively. Large differences arise since the different procedures prefer different $n\pi$ combinations in these cases.

We next compare the reliability of estimates provided by the circular method using the MB distribution with those given by the linear method. For this purpose we generate artificial spectral polarization data for 1000 sources at four different wavelengths. The

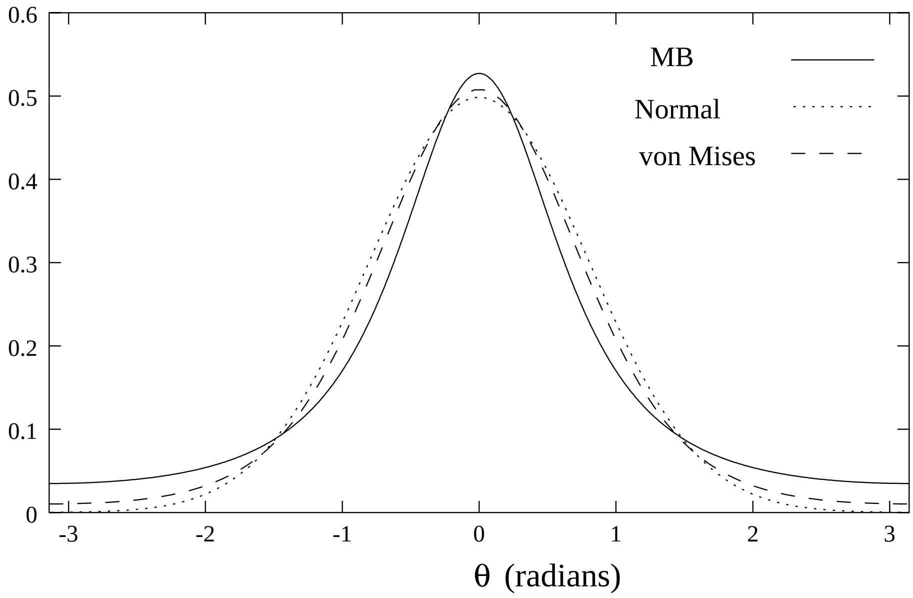

Figure 1. Comparison of the normal distribution ($\sigma = 0.8$) with von Mises, and the MB distribution, (equation 4). The parameters of the von Mises and MB were determined by requiring that the least square difference between them and the normal distribution is minimum.

rotation measure for these sources was generated from a gaussian distribution and the IPA was generated randomly over an interval of 0 to π. The error in the polarization at each of the wavelengths is assumed to be 10 degrees. The artificial data are then used to estimate the RM and IPA using both the linear method and the circular method with the MB distribution. In both the methods we choose that solution for which the RM is closest to the RM value that was used in generating the artificial data. Let RM_L and RM_{MB} be the estimates given by the linear and MB method respectively. The mean and median of the square differences, $(RM_{Li} - RM_i)^2$ where i refers to the source number, for the linear estimate are equal to 103.6 and 30.5 $(rad/m^2)^2$ respectively. The corresponding values for the MB distribution are 54.4 and 17.6 $(rad/m^2)^2$. Hence we clearly see that the MB distribution gives a better estimate of rotation measure in comparison with the linear method.

We next determine whether the MB method provides a better description of the observed polarization data. We are interested in determining how the rotation measure estimate changes as we delete some of the data points. For this purpose we iteratively delete the data points for each of the source. If the source originally contained n data points then after iterative deletion we obtain n data sets each with $n - 1$ data points. We determine the rotation measure for all of these data sets using both the MB and the linear method. For both methods we choose that solution for each of the data sets which gives RM closest to the one given in the original set. We then compute the mean and median of the standard deviations for the entire set of sources. The mean and median for the MB distribution is equal to 6.90 and 1.77 in units of rad/m^2 while for the linear method they are 9.11 and 2.71 respectively. Hence we see that the MB distribution provides a more efficient estimate for rotation measure. We might have anticipated this result since the polarization data is known to have very large fluctuations. These

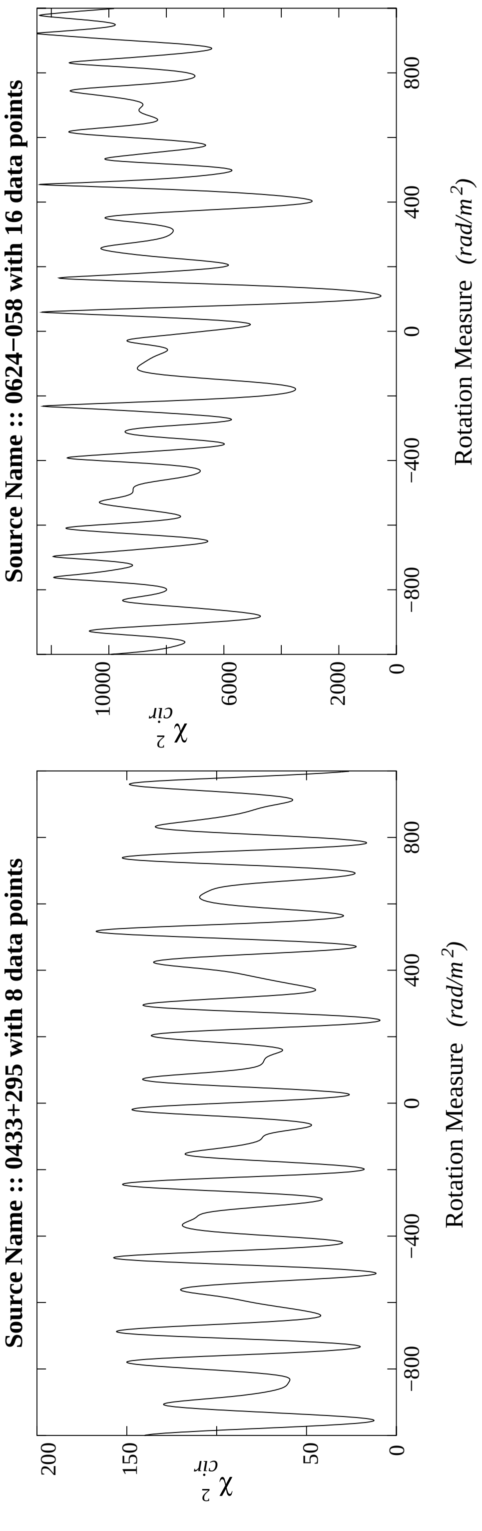

Figure 2. A representative sample of results showing $\chi^2_{\rm cir}$ as a function of the Rotation Measure.

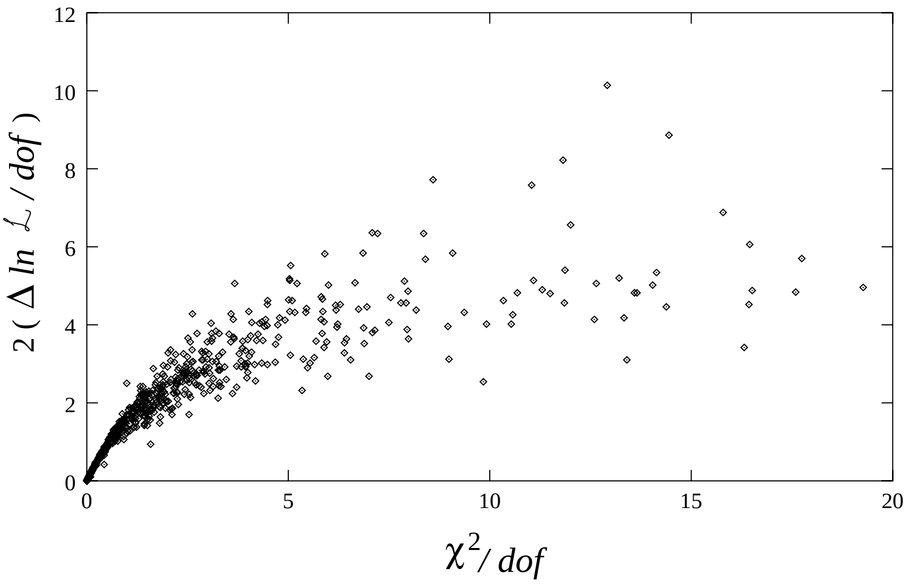

Figure 3. Comparison of the goodness of fit of linear and circular method with MB distribution.

can be easily interpreted in terms of the very large tail of the MB distribution which implies that there is relatively high probability for the polarization to deviate from its central value as shown in Fig. 1.

The goodness of fit for the MB distribution, $\Delta \ln \mathcal{L}$, is defined as

$$\Delta(\ln \mathcal{L}) = \sum_i^N (\ln[p_{\rm MB}(0; 0, 0)] - \ln[p_{\rm MB}(\theta_i; RM, \theta_0)])$$

where the sum is over all the spectral data points for a particular source and $p_{MB}(\theta_i; RM, \theta_0)$ is the MB distribution with the mean angle $\overline{\theta}_i = RM\lambda_i^2 + \theta_0$.

In Fig. 3 we compare the χ^2/dof obtained using the linear method with the analogous measure of the goodness of fit for the MB distribution, $2(\Delta \ln \mathcal{L}/dof)$ for all the sources. For small values of $\chi^2/dof < 1$ we find that $2(\Delta \ln \mathcal{L}/dof) \approx \chi^2/dof$. As χ^2/dof becomes much larger than one we find that $2(\Delta \ln \mathcal{L}/dof)$ is considerably smaller than χ^2/dof. This happens since the MB distribution has a large tail and allows larger fluctuations, which seem to be inherent in the polarization data. We conclude that the MB distribution provides an unbiased and efficient method to extract RM from polarization data.

References

Bunimovitch, V. I. 1949, *Zhur. Tekh. Fiz.*, **19,** 1231.
MacDonald, D. K. C. 1949, *Proc. Camb. Phil. Soc.*, **45,** 368.
Sarala, S., Jain, P. 2001, (to be published in *MNRAS*)
Tabara, H., Inoue, M. 1980, *Astron. Astrophys. Suppl. Ser.*, **39,** 379.

J. Astrophys. Astr. (2002) **23,** 143–147

Standing Shocks around Black Holes and Estimation of Outflow Rates

Santabrata Das & Sandip K. Chakrabarti *S N Bose National Center for Basic Sciences, Block - JD; Sector - III, Salt Lake, Kolkata - 98, West Bengal, India.*
e-mail: sbdas@bose.res.in chakraba@bose.res.in

Abstract. We self-consistently obtain shock locations in an accretion flow by using an analytical method. One can obtain the spectral properties, quasi-periodic oscillation frequencies and the outflow rates when the inflow parameters are known. Since temperature of the CENBOL decides the spectral states of the black hole, and also the outflow rate, the outflow rate is directly related to the spectral states.

Key words. Accretion—accretion disk—black hole physics—shock waves—outflows.

1. Introduction

In the two component advective flow (TCAF) model the sub-Keplerian flow flanks the Keplerian flow above and below the equatorial plane and these two components merge to make a single component sub-Keplerian flow close to the black hole (Chakrabarti & Titarchuk 1995). The two components mix close to a black hole, and may form shocks. In the post-shock region, the specific energy ($\mathcal{E}$) and the specific angular momentum (λ) of the sub-Keplerian flow are estimated by dynamically mixing these two components. We analytically calculate the shock locations for a set of initial parameters following the procedure used by Das, Chattopadhyay & Chakrabarti (2001a) (hereafter, DCC01a and references therein). Around the shock, incoming sub-Keplerian matter slows down due to the centrifugal barrier and becomes hotter. This CEntrifugal pressure supported BOundary Layer (CENBOL) region is responsible for the generation of the outflowing winds and jets, the rate of which is estimated knowing the properties of the CENBOL. CENBOL is also found to be responsible to explain the spectral state transitions and the Quasi-Periodic Oscillations (Chakrabarti 1996).

2. Basic model

We consider a thin, axisymmetric steady flow on the equatorial plane of a Schwarzschild black hole described by the Paczyń'ski-Wiita pseudo-Newtonian potential (Paczyński & Wiita 1980). In the accretion process, we assume, the viscous stress is negligible. The governing equations in the accretion flow are in Chakrabarti (1989). We assume the radial distances, velocities and times are measured in units of Schwarzschild radius $r_g = 2GM/c^2$, velocity of light c and r_g/c respectively. G and M are the gravitational constant and mass of the black hole respectively.

A sub-Keplerian flow with a positive energy passes through the X-type outer sonic point, becomes super-sonic and forms a shock depending on whether the Rankine-Hugoniot shock conditions are satisfied or not. The analytical calculation for the shock locations has been already done (DCC01a) and we use these results to compute the mass outflow rate due to hydrodynamic processes alone.

For some inflow parameters, when the shock conditions are not satisfied but entropy at the inner sonic point is higher than that at the outer sonic point, the shock starts oscillating with a time period $T_s(\sim x_s/\vartheta_s)$, where x_s and ϑ_s are the shock location and velocity of matter at the post-shock region (DCC01a). The observed quasi-periodic oscillation frequencies are comparable to $1/T_s$.

In the pre-shock region, matter is cooler. The free-fall (energy $\mathcal{E} \sim 0$) velocity is $\vartheta(x) = \left[\{x^2 - \lambda^2(x-1)\}/\{x^2(x-1)\}\right]^{1/2}$, where, x is the radial distance and λ is the specific angular momentum of the flow. At the shock, the compression ratio is described as, $R = \frac{\Sigma_+}{\Sigma_-}$. Here, Σ is the vertically integrated density of the matter and the subscripts "-" and "+" refer to the quantities before and after the shock.

We assume that the thermal pressure is negligible in comparison to the ram pressure in the cool pre-shock region. In the post-shock region, the temperature is roughly constant and we consider the region as isothermal in nature. The isothermal sound speed in this region is given by, $C_s^2 = W_+/\Sigma_+ = (R-1)\vartheta_-^2/R^2$, where, W is the vertically integrated thermal pressure and the second equality is obtained from the pressure balance condition for the shock (Das *et al.* 2001b, hereafter DNCC01b).

In general, the outflow is originated from the inner part of the accretion disk and the CENBOL is likely to deposit radiation momentum into it (see, Chattopadhyay & Chakrabarti, this volume). A useful assumption is that the outflow is isothermal at least up to the sonic point. There may be some angular momentum transport in the outflow due to radiative viscosity but presently we are not considering it. This is to make the problem simple and we believe that these effects will not change the result dramatically.

We consider the outflow geometry to be conical in nature. Various conservation equations are discussed in DCC01a. The mass outflow rate ($R_{\dot{m}}$) is defined as the ratio of the outgoing matter in the vertical direction to incoming matter coming through the disk. The analytical expression for that is given by (DNCC01b),

$$R_{\dot{m}} = \frac{\Theta_{\text{out}}}{\Theta_{\text{in}}} \left[\frac{x_s^2(x_s-1}{x_s^2 - \lambda^2(x_s-1)}\right]^{-1/2} \frac{RC_s x_c^2}{x_s(x_s-1)} \exp(-f), \tag{1}$$

where, $f = \frac{1}{2} - \frac{1}{2C_s^2}\frac{x_s - x_c}{(x_s-1)(x_c-1)}$.

Here, Θ_{out} and Θ_{in} are the solid angles subtended by the outflow and the inflow at the origin. Subscripts "s" denote the quantities at the shock and subscripts "c" denote the same at the sonic point in the outflow. The result is similar to that obtained in Chakrabarti (1999) where the angular motion of the inflow was ignored. The general behavior of the mass outflow rate remains unaltered when we consider an adiabatic outflow (DCC01a). In all these cases, $R_{\dot{m}}$ is only a function of R and λ. Since these are computed from the inflow parameters, the mass outflow rate becomes a function of the inflow parameter for a given flow geometry.

In Fig. 1, we show the general behavior of the analytical solution of the mass outflow rate as a function of the compression ratio when only the sub-Keplerian component

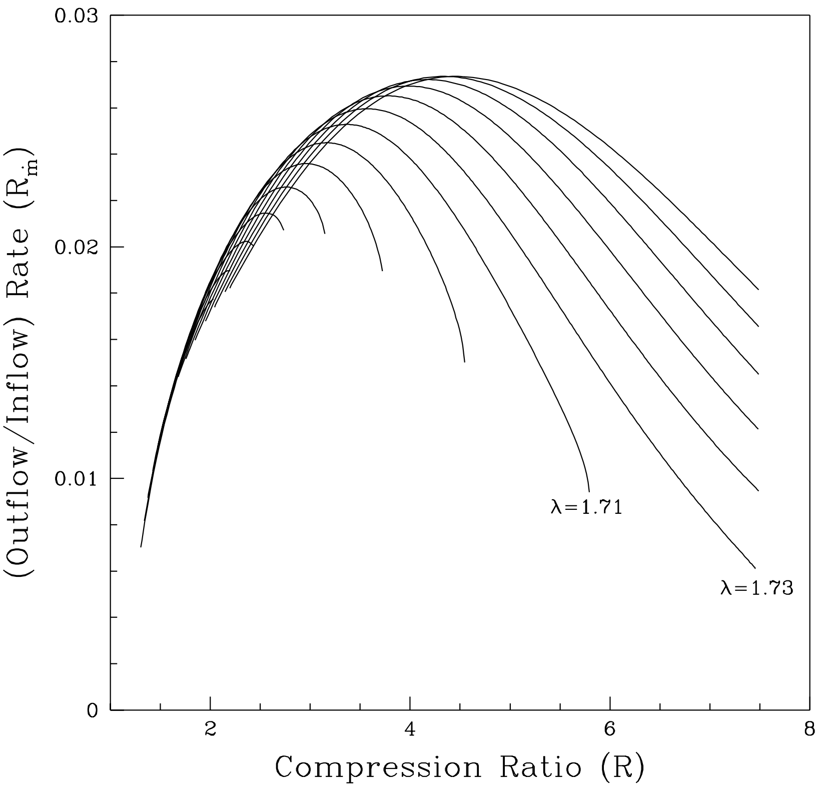

Figure 1. Variation of the ratio of the outflow to inflow rates $R_{\dot{m}}$ with the compression ratio R for various angular momentum (λ). λ varies from 1.57 (right) to 1.79 (left). Curves are drawn at intervals of $d\lambda = 0.02$(DNCC01b).

is considered. Outflow rate is negligible when the shock is weak ($R \sim 1$) and first increases and then decreases gradually as $R \rightarrow 7$ which corresponds to a very strong shock. In the intermediate shock strength, $R_{\dot{m}}$ is maximum. These features can be explained in the following way. A strong shock forms far away from black hole and though the CENBOL area is large, the temperature of that region is low which results in a small outflow rate. A weak shock forms close to the black hole and matter velocity is very high but the CENBOL area is very small. So the product is again low. There is a peak at about $R \sim 4$ and $R_{\dot{m}}$ is about 2.8% (assuming a half angle of 10^0 for both the disk and the jet). The peak of each curve increases monotonically for increasing λ due the increase of density of the CENBOL. Thus the outflow is thermally as well as centrifugally driven.

There are ample evidences that the spectral properties of black holes can be easily explained when the disk matter consists of both the sub-Keplerian and the Keplerian matter (Smith *et al.* 2001 and Smith, Heindl & Swank 2002). In Fig. 2, we present the mass outflow rate when a two component flow is considered. We plot the Keplerian and the sub-Keplerian disk rates in units of the Eddington accretion rate in the right and upper panel respectively. It is clear that the outflow rate steadily increases upward as Keplerian rate decreases and spectrum goes to harder state. For weak shocks, when the Keplerian rate is high, the post-shock region cools down and outflow rate is negligible.

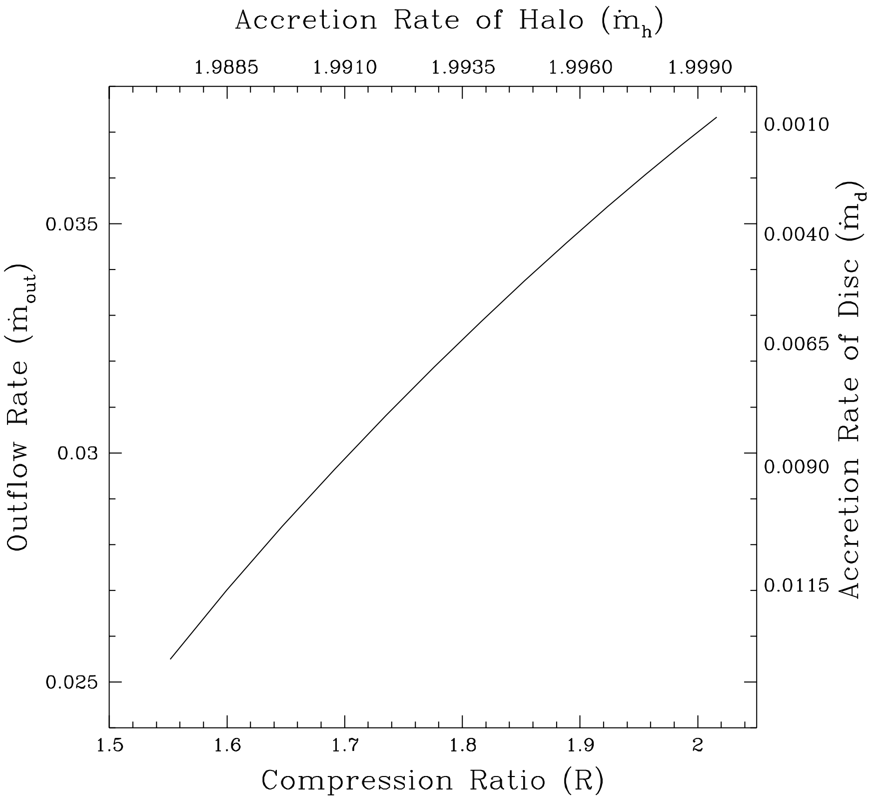

Figure 2. Variation of outflow rates (left axis) with compression ratio. Keplerian and sub-Keplerian accretion rates are plotted in the right and upper panel (DNCC01b).

This indicates that the softer states produce low outflow rates. There is increasing evidence that this is precisely what is happening in galactic microquasars (Klein-Wolt *et al.* 2001; Corbel *et al.* 2001). It is likely that in AGNs also such a behaviour would be observed.

Acknowledgement

This work is partly supported by a project (Grant No. SP/S2/K-14/98) funded by the Dept. of Science and Technology, Govt. of India.

References

Chakrabarti, S. K. 1989, *Ap. J.*, **347,** 365.
Chakrabarti, S. K., Titarchuk, L. G. 1995, *Ap. J.* **455,** 623.
Chakrabarti, S. K. 1996, *Ap. J.*, **464,** 664.
Chakrabarti, S. K. 1999, *A&A*, **351,** 185.
Corbel *et al.* 2001, *Ap. J.*, **554,** 43.
Das, S., Chattopadhayay, I., Chakrabarti, S. K. 2001a, *Ap. J.* **557,** 983 (DCC01a)
Das, S., Nandi, A., Chattopadhayay, I., Chakrabarti, S. K. 2001b, *A& A*, **379,** 683 (DNCC01b)

Klein-Wolt, M. *et al.* 2001, *ApSSS*, **276,** 291.
Paczyński B., Wiita P. J., 1980, *A&A*, **88,** 23.
Smith, D. M., Heindl, W. A., Swank, J. H. 2002, *Ap. J.*, **569,** 362.
Smith, D. M., Heindl, W. A., Markwardt, W. A., Swank, J. H. 2001, *Ap. J.*, **554L,** 41.

J. Astrophys. Astr. (2002) **23,** 149–153

Radiatively Driven Winds from Effective Boundary Layer around Black Holes

Indranil Chattopadhyay & Sandip K. Chakrabarti *S. N. Bose National Centre for Basic Sciences, Block-JD, Sector-III, Kolkata 98.*
e-mail: indra@bose.res.in chakraba@bose.res.in

Abstract. Matter accreting onto black holes suffers a standing or oscillating shock wave in much of the parameter space. The post-shock region is hot, puffed up and reprocesses soft photons from a Keplerian disc to produce the characteristic hard tail of the spectrum of accretion discs. The post-shock torus is also the base of the bipolar jets. We study the interaction of these jets with the hard photons emitted from the disc. We show that radiative force can accelerate outflows but the drag can limit the terminal speed. We introduce an equilibrium speed v_{eq} as a function of distance, above which the flow will experience radiative deceleration.

Key words. Accretion—accretion disc—black hole physics— winds—outflows.

1. Introduction

Rotating matter spirals onto the black hole to form a temporary depository called the accretion disc. As supersonic matter approaches the compact object centrifugal pressure becomes comparable to the gravitational pull. If the Rankine-Hugoniot shock conditions are satisfied the flow may suffer a thin shock (Chakrabarti 1996). Post-shock flow becomes hotter at roughly the virial temperature $kT_p \sim GM/r_s$, where G, M, r_s, k, T_p are the gravitational constant, mass of the black hole, Bolzmann constant and proton temperature respectively. This causes the flow to puff up in the form of a torus. The soft photons processed in the outer cool Keplerian disc is intercepted by this puffed up post-shock region. Chakrabarti and Titurchuk (1995, hereafter CT95) showed that the intercepted soft photons are reprocessed (inverse-Comptonized) by the hot electrons of post-shock torus and produces the characteristic hard tail of the spectrum. Hence the presence or absence of this post-shock flow, will determine whether the black hole candidate will be in the hard or the soft state.

Chakrabarti and his collaborators (Chakrabarti 1998, 1999; Das & Chakrabarti 1999; Das *et al.* 2001) showed that this post-shock tori (hereafter, CENBOL $\equiv$ CENtrifugal pressure supported BOundary Layer) is also the source of jets. The excess thermal pressure in CENBOL, drives a part of the infalling matter along the axis of symmetry as jets or winds around compact objects. Hence CENBOL acts as an effective boundary layer around black holes. This effective boundary then acts as both the source of hot photons as well as the source of jet matter. We are interested to study the interaction of these two.

Radiatively driven winds in various contexts have been studied by several workers. Icke (1980) studied radiatively driven gas flows from a Keplerian disc (Shakura & Sunyaev 1973), though the drag term was neglected. Sikora & Wilson (1981) showed that radiations from thick disc can collimate the outflow but radiation drag reduces its terminal velocity. Icke (1989) calculated the terminal speed of radiatively driven outflows above a Keplerian disc, in presence of radiation drag and found it to be $0.451c$ (where, c is the velocity of light). Fukue (1996) considered a rotating flow over such a disc and found the terminal speed to be lower. All the major works on this field has been done either by considering a geometrically thin, Keplerian disc or a hot thick disc. They also consider a cold jet, i.e., they ignored the pressure gradient term in the momentum balance equation. We, however, have included the pressure gradient term also. Chattopadhyay & Chakrabarti (2000a, 2000b) have already showed that the acceleration due to radiative momentum deposition is impressive if the radiation drag term is excluded. In this paper, we want to study the issue of radiative acceleration in presence of radiation drag. We consider a class of solutions called the advective discs (Chakrabarti 1996) which have a cold outer thin disc ($T \sim 10^7$K) and inner region could be hot ($T \sim 10^{9-10}$K) and a puffed up torus (CENBOL), which is approximately a thick disc (with advective corrections incorporated). We consider radiative acceleration of outflows coming from the CENBOL region of such a disc. In Compton effect, the energy transferred from a photon per scattering is given by $\Delta\nu/\nu \sim (4kT_e - h\nu)/\nu$. Thus electrons have to be cooler to receive energy from photons emitted by the CENBOL.

For simplicity, we assume the outflow to be conical and inviscid and electron scattering to be the dominant energy transport mechanism. The equation of motions are taken from (Mihalas & Mihalas 1984). The radiative flux and the energy density are calculated following Chattopadhyay & Chakrabarti (2000b).

2. Radiatively driven winds and terminal velocity v_{eq}

In our analysis, the acceleration mechanism considered are, **(1)** thermal pressure and **(2)** the radiative force. If only the first mechanism was chosen it would have been Bondi-type outflow, where the specific energy of the flow would have a positive Bernoulli constant. The terminal velocity achieved would be $\frac{1}{2}v_\infty^2 \sim na_{in}^2 - 1/2(z_{in}-1)$, where, n, v_∞, a_{in}, $-1/2(z_{in}-1)$ are the polytropic index, terminal velocity, initial sound speed, gravitational potential (psuedo-Newtonian, see, Paczýnskii-Wiita 1980) at the initial injection point. We see that, v_∞ is of the order of initial sound speed. If we now add the radiative acceleration the terminal velocity should increase, because the radiative work done (i.e., $\int_{z_{in}}^{\infty}(\mathcal{D}_z - 2v\mathcal{E})dz$, where the first term inside the parenthesis is the radiative acceleration and the second one is the radiative drag term) onto the outflow will increase the terminal velocity. Fig. 1(a) shows the variation of v_{1000} (v at $z = 1000r_g$; r_g is the Schwarzschild radius) with initial energy of the flow. The general behaviour is that the acceleration of the outflow increases with the radiative intensity of the disc, but for a very high initial energy, the dependence of v_{1000} on the intensity is weak as the radiative work done is negligible compared to E_{in}. For a very cold flow, radiative force may impart enough momentum onto the flow so that even bound matter may also be freed to join the outflow. In Fig. 1(b) the solution topology of a radiatively driven outflow with an initially bound energy is compared with only

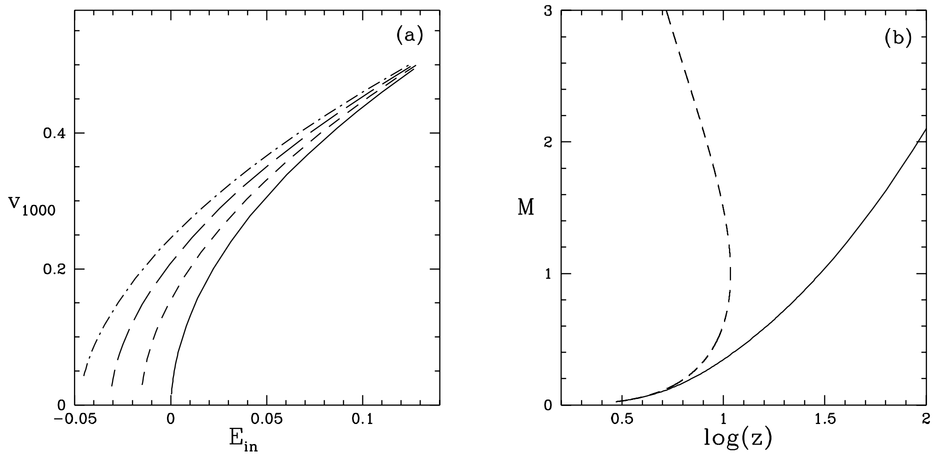

Figure 1. **(a)** Comparison of (v_{1000}) with initial energy (E_{in}) of the flow. Various curves represent flows acted on by radiation momentum deposition from inflow with $\dot{M}_{acc} = 15\dot{M}_{Edd}$ (dash-dot), with $\dot{M}_{acc} = 10\dot{M}_{Edd}$ (long-dashed), with $\dot{M}_{acc} = 5\dot{M}_{Edd}$ (short-dashed) and Bondi-type (solid) outflow. **(b)** Comparison of the variation of Mach number (M) with $\log(z)$. The solid curve represents the outflow acted on by radiation deposition due to $\dot{M}_{acc} = 5\dot{M}_{Edd}$. The dashed curve represents the outflow driven only by the thermal energy. Initial parameter is, $E_{in} = -0.002$ at $z_{in} = 3$.

thermally driven outflow. Radiatively driven flow is found to be transonic while the other dives back on to the black hole.

The radiative deceleration term (drag) is proportional to both the bulk velocity (v) and the radiation energy density ($\mathcal{E} \propto$ radiation energy density) at a given point. Hence there is an equilibrium velocity above which there would be radiative deceleration, whose expression is $v_{eq} = \mathcal{D}_z/(2v\mathcal{E})$. In Fig. 2(a), the variation of v_{eq} is shown. To exhibit the acceleration/deceleration mechanism of radiative force, the injection velocity $v_{in} > v_{eq}(z_{in})$. The flow is decelerated upto z_1. In the region $z_1 < z < z_2$, there is acceleration and again $v(z_2) = v_{eq}(z_2)$. In the region $z > z_2$, there should be deceleration, but it is not evident from Fig. 2(b). On the other hand, Fig. 2(c) shows that in the region $z > z_2$ there is deceleration but both the radiation flux and its energy density decreases to such a low value, that the deceleration is negligible. If one plots the specific energy of the flow, the decrease in this region due to the radiative deceleration is also shown to be negligible. This shows that v_{eq} is the upper limit of v_∞ for cold plasma, in absence of gravity. Thus we give a general form of terminal velocity; $1/2(v_\infty^2) \leq 1/2(v_{eq}^2) + E_{in}$.

3. Conclusions

The radiative force can accelerate outflows to a maximum velocity of $0.5c$ but if there is enough thermal energy the terminal velocity could be higher and in principle there is no limit to the final velocity. Galactic microquasars such as SS433, GRS1915+105 etc. do show jets with velocities up to $0.98c$. We believe that these could be accelerated by radiative process.

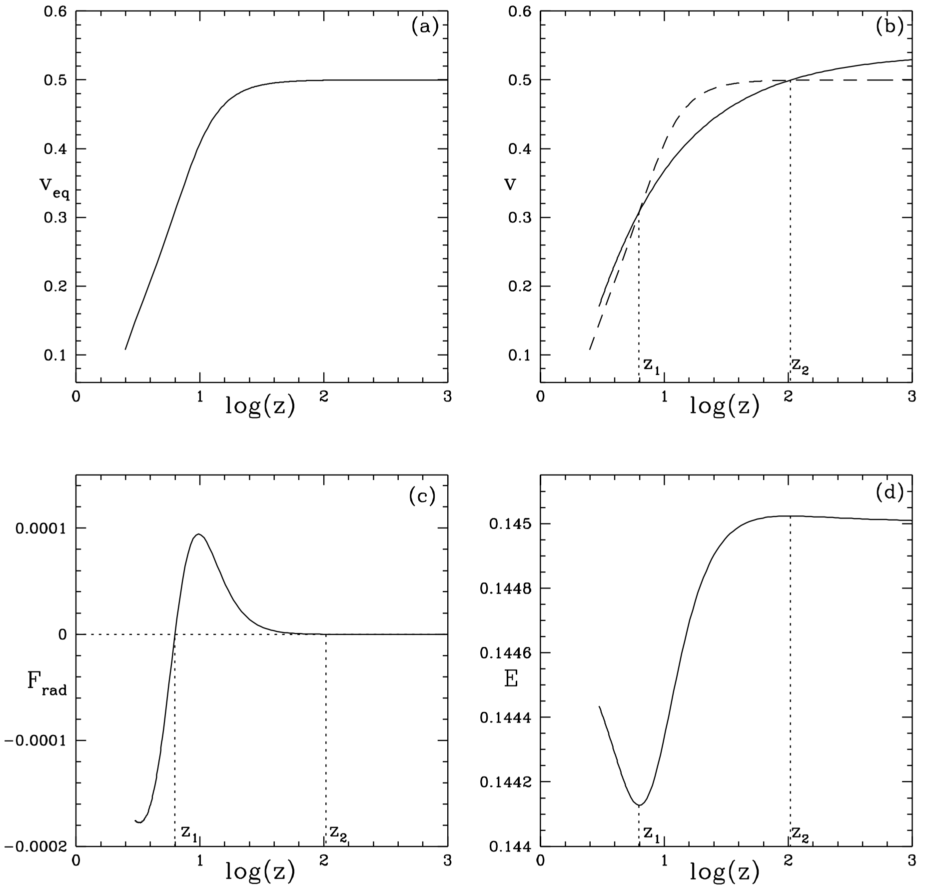

Figure 2. **(a)** Variation of v_{eq} as a function of z **(b)** Comparison of variation of bulk velocity v (solid) with v_{eq} (short-dashed) as a function of z. $v_{in} = 0.17$ at $z_{in} = 2.96$. $v_{eq}(z_{in}) < v_{in}$. The outflow topology (solid) is acted on by RAMOD corresponding to $\dot{M}_{acc} = 5\dot{M}_{Edd}$. **(c)** The net radiative force (F_{rad}) is presented as a function of z. **(d)** Comparison of E of the outflow in the previous case.

References

Chakrabarti, S. K., Titarchuk, L. 1995, *Ap. J.*, **455,** 623.
Chakrabarti, S. K. 1996, *Ap. J.*, **464,** 664.
Chakrabarti, S. K. 1998, in *Proceedings of Observational Evidence For Black Holes In The Universe*, (ed.) S. K. Chakrabarti (Kluwer Academic Publishers)
Chakrabarti, S. K. 1999, *A&A*, **351,** 185.
Chattopadhyay, I., Chakrabarti, S. K. 2000a, *IJMP-D*, **9(1),** 57.
Chattopadhyay, I., Chakrabarti, S. K. 2000b, *IJMP-D*, **9(6),** 717.
Das, T. K., Chakrabarti, S. K. 1999, *Class. Quant. Grav*. **16,** 3879.
Das, S., Chattopadhyay, I., Nandi, A., Chakrabarti, S. K. 2001, *A&A*, **379,** 683.
Fukue, J. 1996, *PASJ*, **48,** 631.
Icke, V. 1980, *Astron. J.*, **85(3),** 329.
Icke, V. 1989, *A&A*, **216,** 294.

Mihalas, D., Mihalas, B. W. 1984, *Foundations of Radiation Hydrodynamics* (Oxford University Press)
Paczyński, B., Wiita, P. 1980, *A&A*, **88,** 23.
Sikora, M., Wilson, D. B. 1981, *MNRAS*, **197,** 529.
Shakura, N. I., Sunyaev, R. A. 1973, *A&A*, **24,** 337.

J. Astrophys. Astr. (2002) **23,** 155–164

Interaction of Accretion Shocks with Winds

Kinsuk Acharya[1], Sandip K. Chakrabarti[2,1] & D. Molteni[3]

[1]*Centre for Space Physics, P-61 Southend Gardens, Kolkata 700 084, India.*
[2]*S. N. Bose National Center for Basic Sciences, JD Block, Salt Lake, Kolkata 700 098, India.*
[3]*University of Palermo, Via Archirafi 36, I-90123, Italy.*

Abstract. Accretion shocks are known to oscillate in presence of cooling processes in the disk. This oscillation may also cause quasi-periodic oscillations of black holes. In the presence of strong winds, these shocks have oscillations in vertical direction as well. We show examples of shock oscillations under the influence of both the effects. When the shocks are absent and the flow is cooler, the wind becomes weaker and the vertical oscillation becomes negligible.

Key words. Black hole physics—accretion—winds—shock waves—hydrodynamics.

1. Introduction

In a black hole accretion, the flow must be sub-Keplerian close to the horizon and the specific angular momentum is almost constant. As a result, the centrifugal force dominates over gravity and a centrifugal barrier dominated boundary layer (CENBOL) appears (see, Chakrabarti 1996, and references therein) close to a black hole. Chakrabarti & Titarchuk (1995) pointed out that this CENBOL is the illusive ‘Compton Cloud’ and the hard X-rays observed from black hole candidates are emitted from it. Later, Chakrabarti (1999) made a bold proposal that perhaps most of the outflows and jets are emanated from CENBOL also and computed the outflow rate from the inflow rate self-consistently. It was shown that outflow rates strongly depend on the strength of the standing shock which caused the CENBOL formation and in soft states of black hole, when shocks are absent, the outflow also disappears.

Shock solutions themselves have been found to be stable in the absence of cooling (Chakrabarti & Molteni 1993). Time-dependent simulations showed that shocks could oscillate in presence of cooling (Molteni, Sponholz & Chakrabarti, 1996 [MSC96]) or winds (Ryu, Chakrabarti & Molteni, 1997). These simulations were carried out using only the upper half of a disk because of computational constraints. When both halves were included, a new kind of instability was observed: the winds interacted with the accretion flow and the flow becomes bent with respect to the equatorial plane (Molteni *et al.* 2001).

We now investigate shock oscillations in both radial and vertical directions. Cooling rate determines the location and radial oscillation frequency of shocks and winds determine the vertical oscillations.

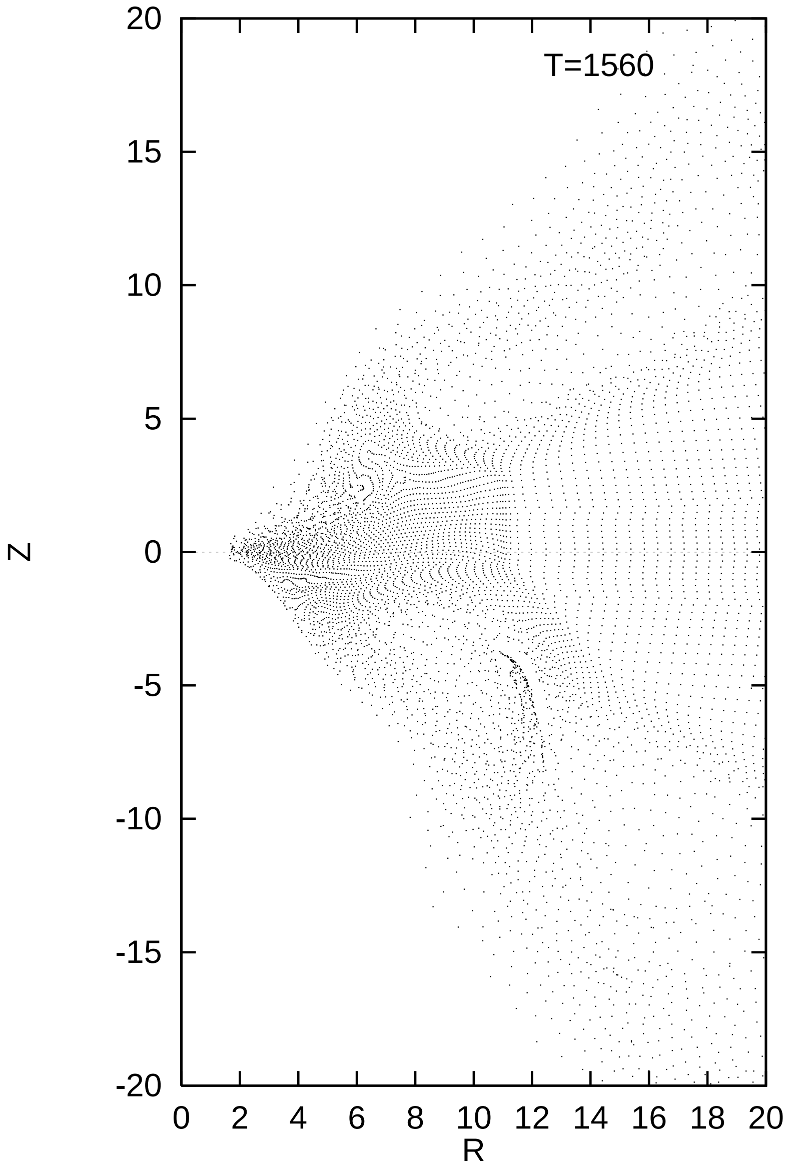

Figure 1. Oscillating shocks at various times (Marked) for $\rho(r_o) = 2.02 \times 10^{-14}$ gm cm^{-3}.

2. Results

Simulation was carried out using Smoothed Particle Hydrodynamics (SPH). Matter was injected in both the halves (upper and lower). The accretion rate was varied by varying the density at the injection point, which we chose to be $r_o = 50r_g$ where, $r_g = 2GM/c^2$ is the Schwarzschild radius. Unless otherwise stated, we use the followings at r_o: **(a)** $\gamma = 5/3$, **(b)** radial velocity $v_r = 0.126c$, **(c)** sound speed $a = 0.04$, **(d)** thickness $h(r_o) = 14.75$ (obtained from vertical equilibrium at $r(o)$) and **(e)** specific

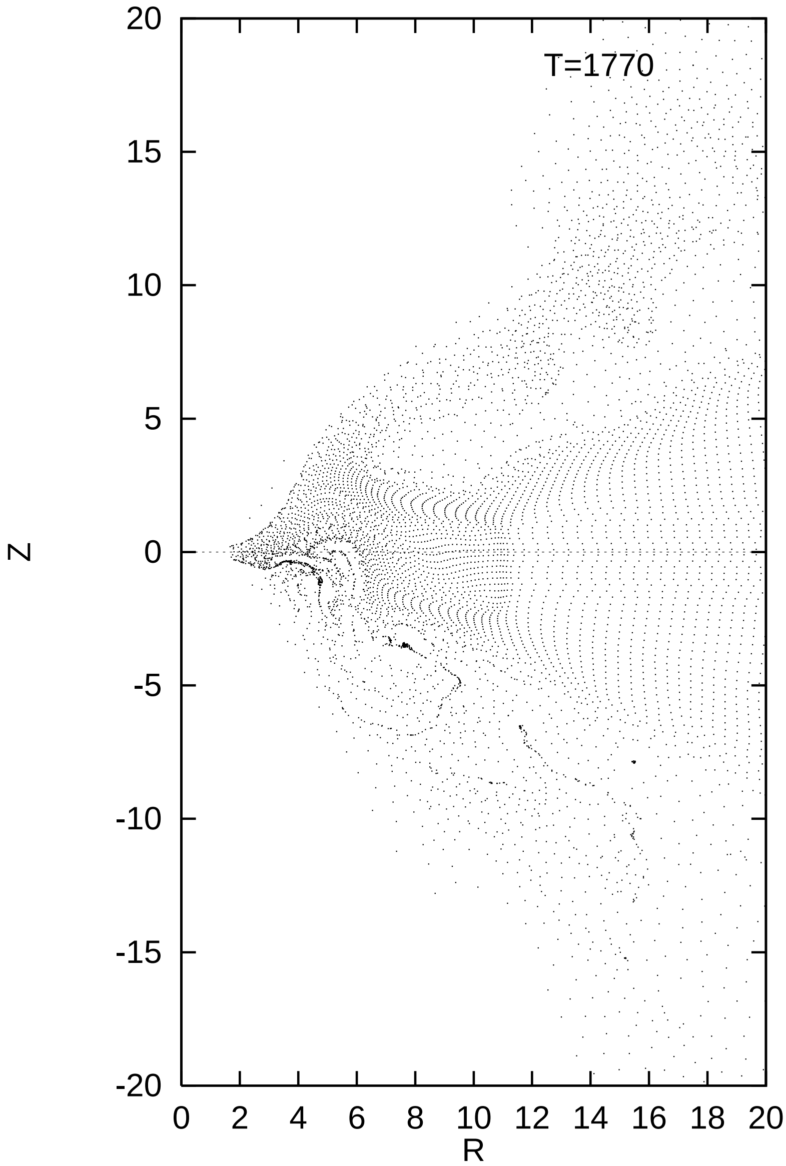

Figure 1. (*Continued*)

angular momentum $\lambda = 1.75$. For $\rho(r_o) = 10^{-15}$ gm cm^{-3}, the accretion rate for a 10^8 solar mass black hole is $0.5 M_\odot$ yr^{-1}.

In Fig. 1, we show the nature of the shock at three different times of simulations when $\rho(r_o) = 2 \times 10^{-14}$ gm cm^{-3}. The times are marked in each figure. Note the vertical as well as the horizontal motion of the shock in these figures.

The oscillation causes variation of thermal energy content in the flow. The energy release will be proportional and may manifest themselves as quasi-periodic oscillations (QPO) observed in galactic and extra-galactic black hole candidates. As an example,

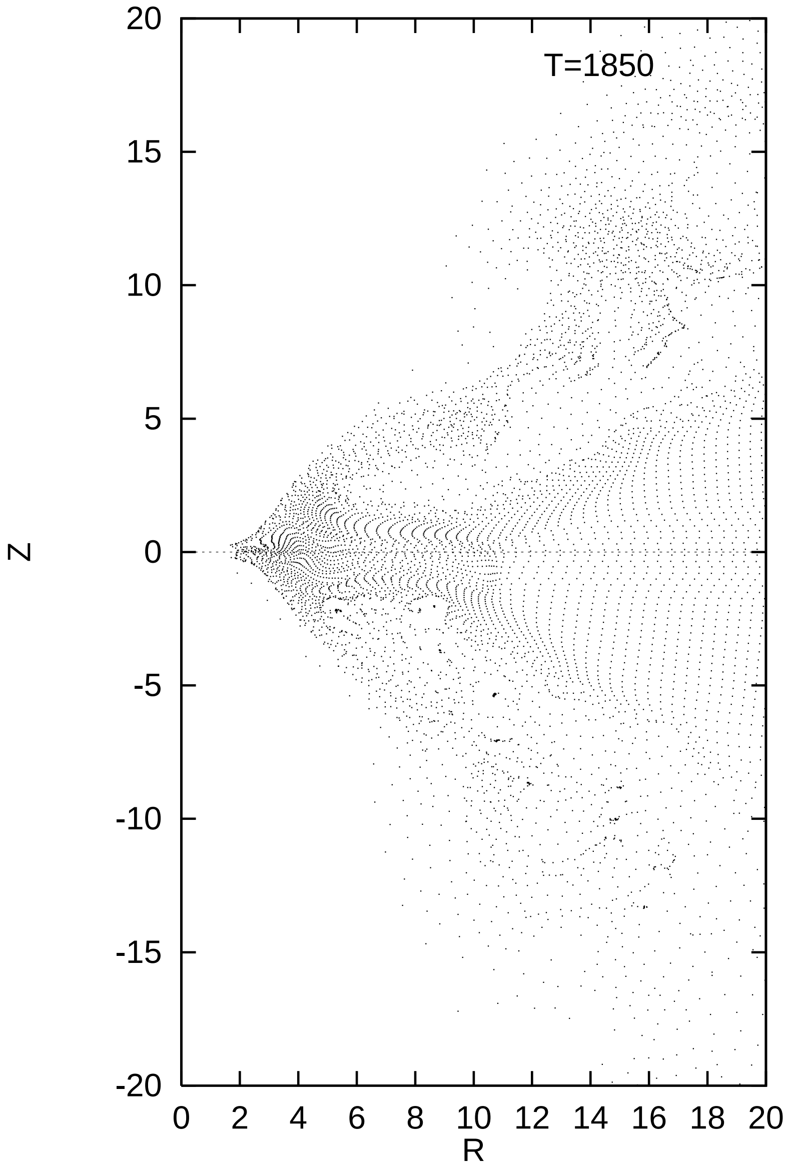

Figure 1. (*Continued*)

in Fig. 2, we plot thermal energy and its Power Density Spectrum (PDS) (we chose black hole mass $M = 10^8 M_\odot$, angular momentum $l = 1.78$, $\rho(r_o) = 0.95 \times 10^{-14}$). We clearly see evidence of QPO with period $\sim$ 10days as is expected from scaling of $\sim$ 0.1s periods for stellar black holes ($M \sim 10M_\odot$). By varying injection parameters one can obtain various types of light curves from our time dependent simulations.

With the increase of $\rho(r_o)$ the cooling rate increases. As MSC96 showed, the oscillation of shocks occur when the cooling timescale $\mathcal{E}/\dot{\mathcal{E}}$ is comparable with the infall

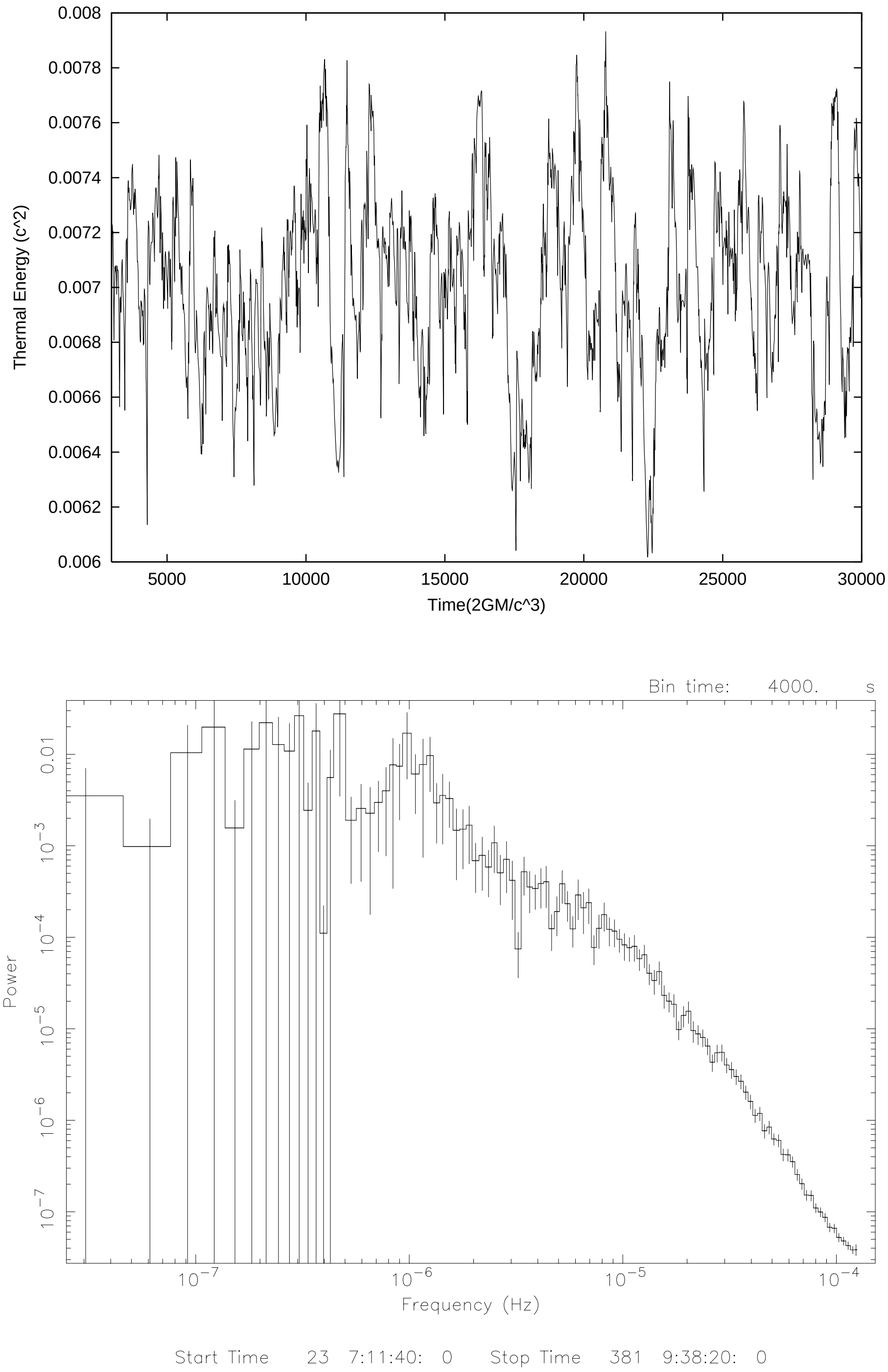

Figure 2. Example of variation of the thermal energy with time **(a)** and its Power Density Spectra **(b)**. Note the presence of quasi-periodic oscillation at 10^{-6}Hz.

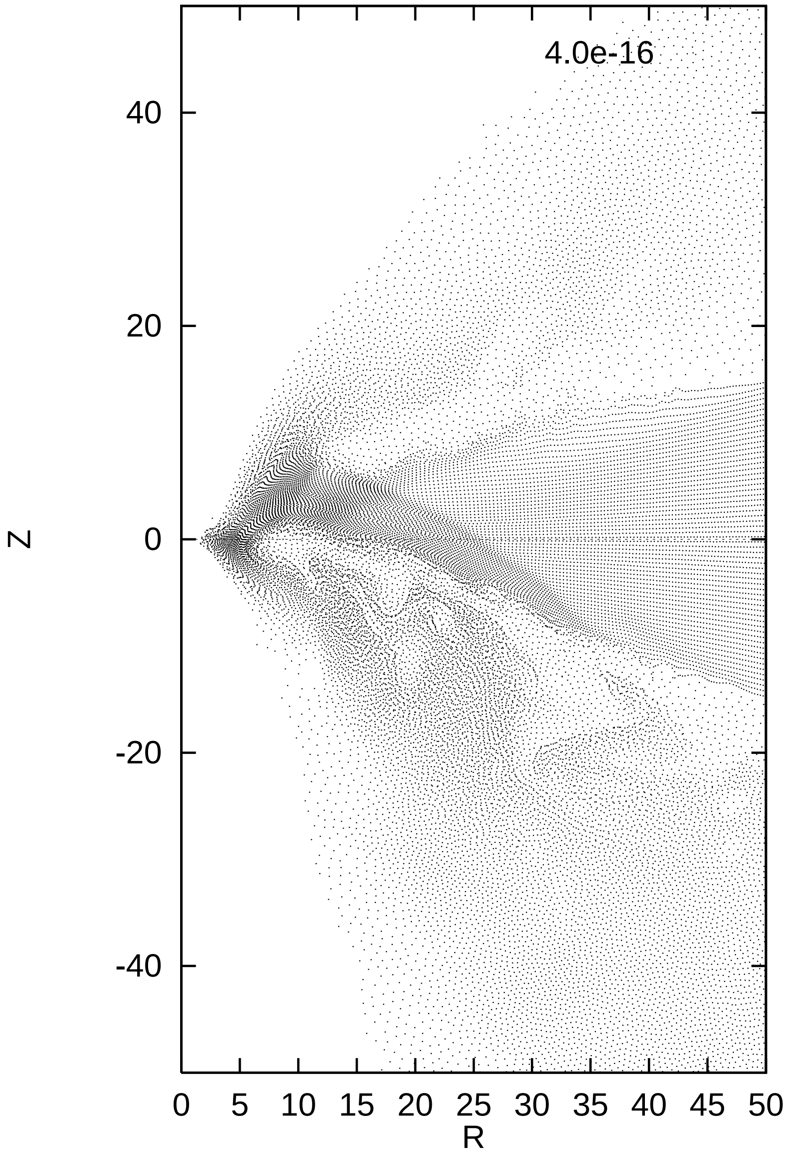

Figure 3(a). Vertical and horizontal oscillations for various densities (marked).

timescale in the CENBOL r/v. Thus it is expected that in certain range of $\rho(r_o)$, the oscillation will occur and the frequency of oscillation should increase with the cooling rate. In Fig. 3, we showed results of simulations with varying accretion rate ($\rho(r_o)$ is marked in each box) In Fig. 3(a) there is no shock but the CENBOL is hot and it produces winds which interact with the disk causing vertical oscillations. In Fig. 3(d), the shock is not present and the CENBOL region is cooler due to a large cooling rate. As a result, the outflow is weak and hence even the vertical oscillation is absent. In the intermediate cases, the shock approaches the black hole as accretion rate is increased and

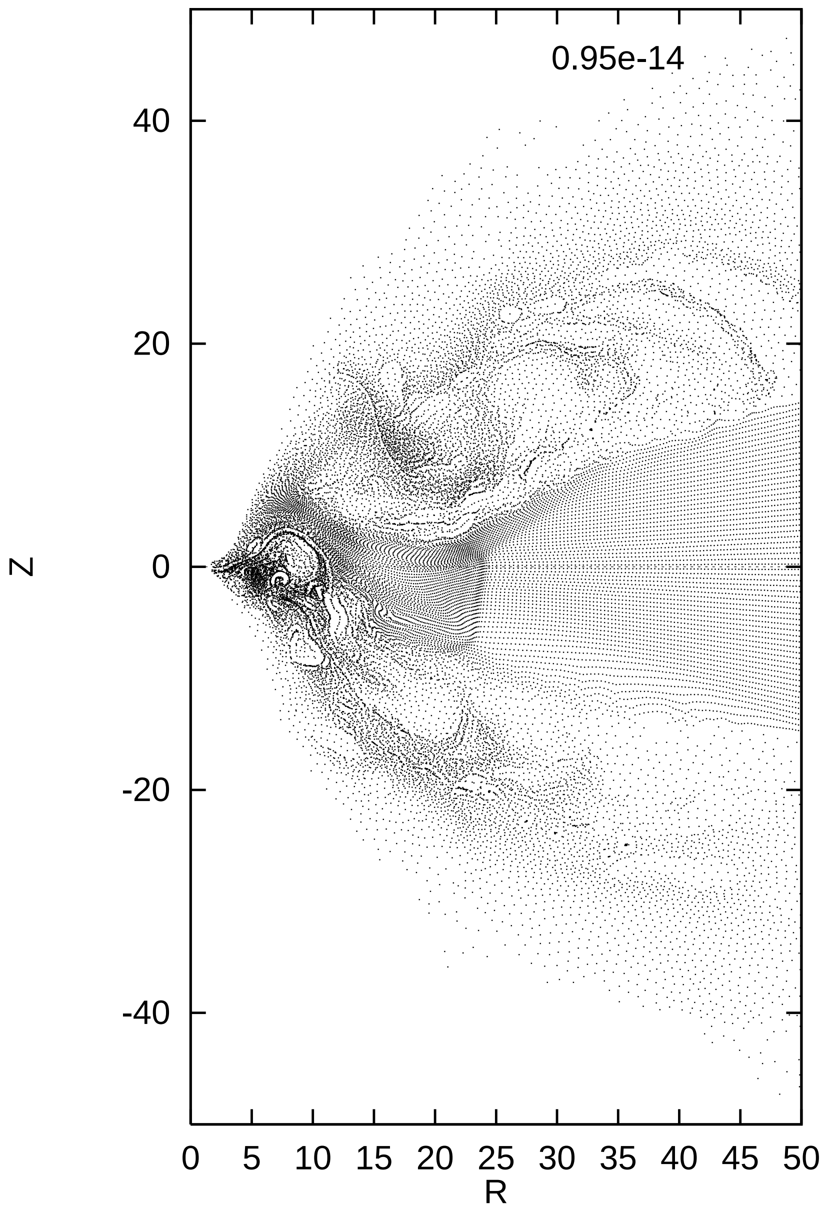

Figure 3(b).

oscillates with higher frequencies. Unlike other models of QPO (e.g., Nowak & Lehr 1998; Rodriguez *et al.* 2002) our model is capable of switching from QPO/No-QPO state in cooling time scale which could be very short for Compton cooling. Details of the results are submitted elsewhere (Chakrabarti, Acharya & Molteni, in preparation).

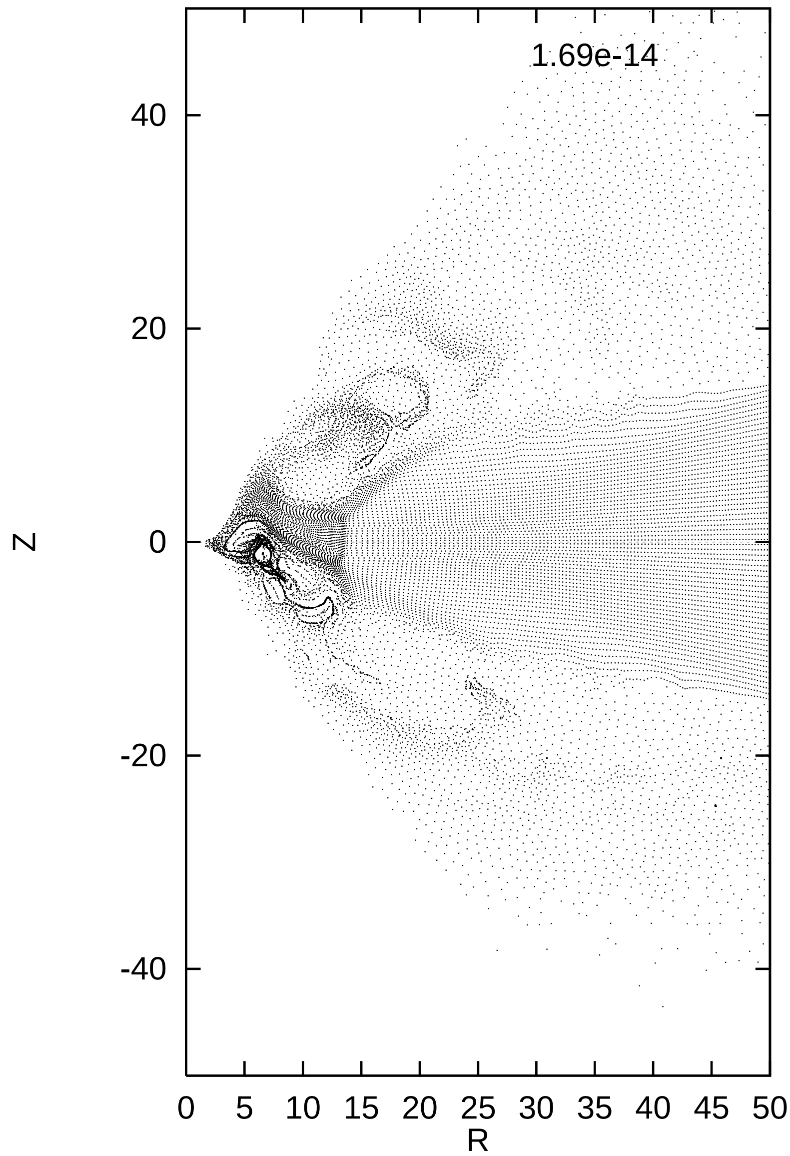

Figure 3(c).

3. Concluding remarks

A considerable power is present in QPOs observed in the accretion disk with oscillating shock waves. This phenomenon may be responsible for the observed QPO in galactic and extra-galactic black hole systems. This work is partly supported by the ISRO project on 'Quasi-Periodic Oscillations in Black Hole Candidates'.

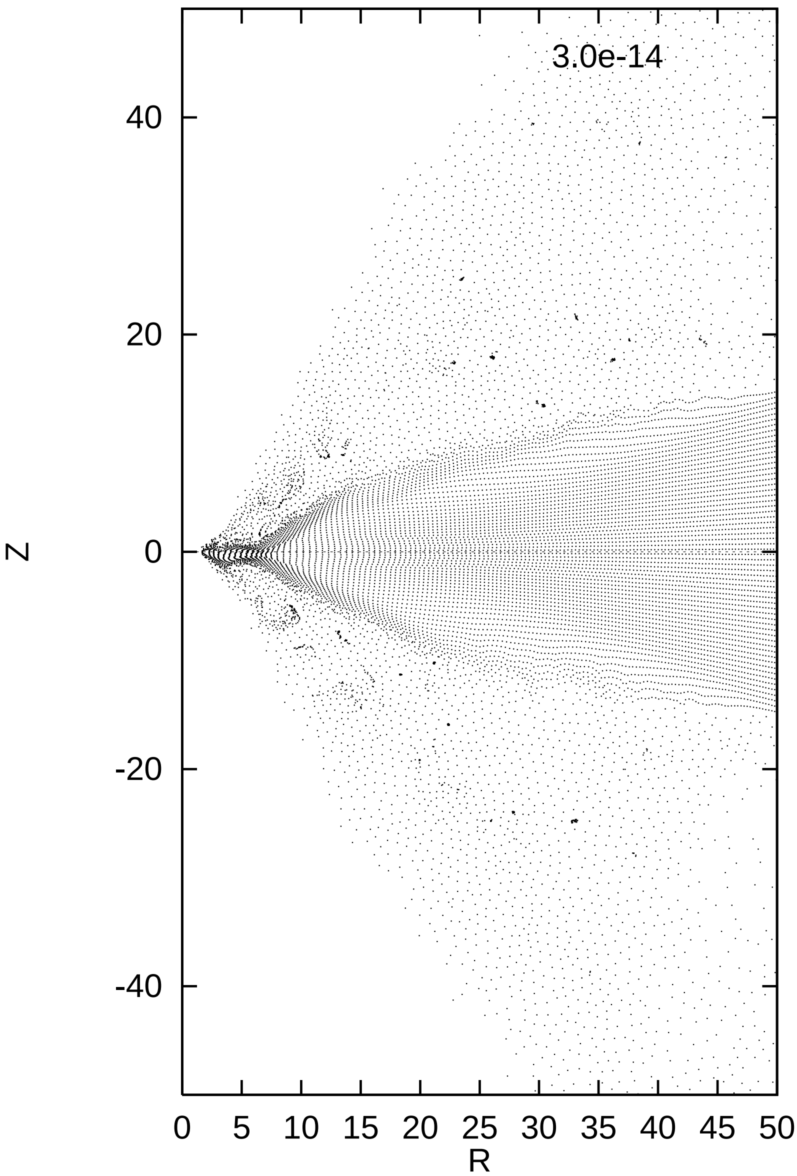

Figure 3(d).

References

Chakrabarti, S. K. 1996, *Ap. J.*, **464,** 664.
Chakrabarti, S. K. 1999, *A&A*, **351,** 185.
Chakrabarti, S. K., Molteni, D. 1993, *Ap. J.*, **417,** 671.
Chakrabarti, S. K., Titarchuk, L. G. 1995, *Ap. J.*, **455,** 623.
Molteni, D., Acharya, K., Kuznetsov, O., Bisikalo, D., Chakrabarti, S. K. 2001, *Ap. J.*, **563,** L57.
Molteni, D., Sponholz, H., Chakrabarti, S. K. 1996, *Ap. J.*, **457,** 805.

Nowak, M., Lehr, D. 1998 in '*Theory of Black Hole Accretion Disks*' (eds.) M. A. Abramowicz, G. Bjornsson, J. E. Pringle, p. 233
Rodriguez, J., Varnier, P., Tagger, M., Durouchox, P. 2002, *A&A*, 38.
Ryu, D., Chakrabarti, S. K., Molteni, D. 1997, *Ap. J*, **474,** 378.

J. Astrophys. Astr. (2002) **23,** 165–171

Tracking the Shadows through GMRT

D. Narasimha[1], N. Kanekar[2] & J. N. Chengalur[2]

[1]*Tata Institute of Fundamental Research, Mumbai 400 005.*
[2]*NCRA, Tata Institute of Fundamental Research, Pune 411 007.*

Abstract. The structures of faint high redshift galaxies cannot be observed directly. But if a luminous quasar is located farther along their line of sight, high resolution absorption lines offer a valuable and reliable probe to their structure. GMRT is suited to monitor the absorption spectra, if the redshifted neutral hydrogen or OH doublet fall in one of the windows of the telescope. We present the OH doublet absorption spectra for the system B0218+357, taken at GMRT this year at resolution of approx. 9.5 km/sec with an rms noise of the order of 1 mJy. Based on our study of the OH doublet and 21cm neutral hydrogen line we infer that, in the lensing spiral galaxy of B0218 + 357, neutral hydrogen and OH coexist in tenous clouds and there is possibly a hole in the central part of the galaxy. In contrast, the gas is seen in high density clouds in the lens in an otherwise similar system PKS1830-211.

Key words. Gravitational lens, molecular absorption lines, quasar—B0218 + 357.

1. Introduction

Gravitational lensing has opened up a new probe to the structure of high redshift galaxies using their absorption lines. A typical spiral galaxy at redshift upwards of 0.5 will have sufficient projected surface mass density to cause multiple images of suitably located background source, though it might be too faint for detailed direct observations. However, when it is along the line of sight to a quasar forming multiple images of the background source, the copious amount of neutral or low ionization gas in the intervenous galaxy gives rise to absorption lines in the multiple images. A comparison of the relative strength, doppler width and profile as well as difference in the doppler velocity of the lines along the images will provide valuable information about the dynamics as well as structure of the galaxy. For instance, from the relative strengths of the multiple radio lines of OH, the star formation history or the distribution of gas can be inferred.

B0218+357 is a well-studied gravitational lens system having radio ring (Patnaik *et al.* 1993), for which many mm molecular absorption lines have been detected. It consists of two images of a flat spectrum radio source (AGN) separated by 340 milliarcseconds and the Einstein ring has a diameter of 335 milliarcseconds. The AGN at a redshift of 0.96 is lensed by a spiral galaxy of I magnitude 20 at a redshift of 0.685. The time delay between the images has been measured to be 11 days. This lens could be very useful to determine the large scale geometry of the Universe because of the moderate redshift of the lens and a relatively low redshift of the source with respect to the lens. The inferred Hubble constant or other predictions for an Open Universe without cosmological constant and a Flat Universe with a cosmological constant will be considerably different for this lens system. It is possible to construct reasonable lens model for the system using a high sensitivity EVN+MERLIN image of the system at 1.7 GHz and accurate position of VLBA scale substructures (Narasimha, Patnaik & Porcas, in preparation).

High sensitivity and high resolution observations of the absorption lines in radio provide valuable probe of the lens in the following way: (1) From a chemical diagnostic of the various radicals like OH and doppler width of the individual lines formed within a cloud, the star formation history of the galaxy can be traced. (2) Measuring rotation curve of the lensing spiral galaxy at high redshift (Chengalur *et al* 1999). For a single component lens, the images as well as radio ring can constrain the lens model accurately; but in a spiral galaxy the bulge, disk and possible halo simultaneously act as lens for subarcsecond images; consequently, models explaining the observed features of the radio ring and images at a specified single redshift can differ from each other by an unknown mass of the dark halo which will change the time delay between the images without affecting any other observables. The absorption lines due to the images as well as ring in the system can be used to directly infer the gravitational potential of the lens galaxy and hence break this degeneracy. Accurate diagnostic of the rotation curve requires determination of the doppler position of the absorption lines due to the two compact images and a shallow absorption trough due to the ring which becomes strong at low frequencies.

2. Analysis of 21cm neutral hydrogen line

Redshifted neutral hydrogen 21 cm line was observed at Westerbork telescopes by A G de Bruyn in July 1998. The 3.48 km/sec/channel spectrum and its decomposition is displayed in Fig. 1. The broad but shallow component of the absorption profile due to the radio ring at approx 10 mJy level is evident in spite of the rms noise of 1 mJy. It is tempting to identify the two narrow features in the profile as due to the compact images. However, the position of the absorption line is not at the centre of the radio ring and hence, neither of the features is likely to be due to the Image B. Instead, we interpret the two main features as lines arising from the two VLBA components of Image A. The derived line of sight rotation velocity at 0.18 arcsecond from the lens centre is approximately 70 km s^{-1}. Since the lens is at an inclination of the order of 25 to 35 degrees, the total rotation velocity should be 150 km s^{-1} at this radius.

3. GMRT observations

The first OH observation of B0218+357 was carried out at GMRT during 1999, but due to the high noise level of about 10 mJy, only the broad lines could be identified. Consequently, the observations were repeated on the 17th and 27th of June, 2001, with the standard 30 station FX correlator as the backend. A total bandwidth of 4 MHz was used for the observations, to include both the main OH transitions (at rest

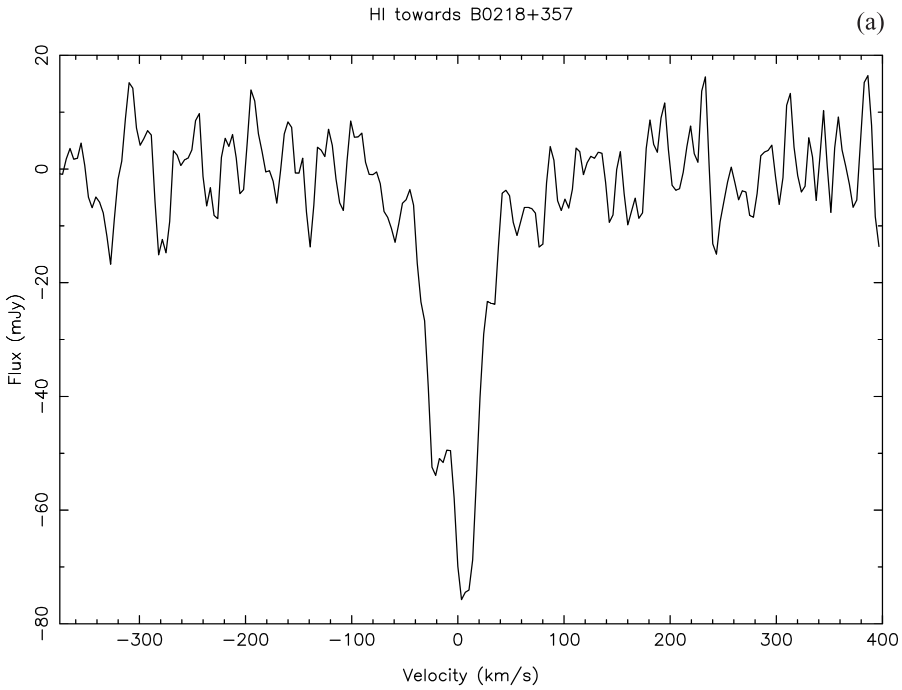

Figure 1. **(a)** Westerbork HI spectrum towards 0218+357. The spectrum has a resolution of ~ 3.48 km s^{-1}.

frequencies of 1665.403 MHz and 1667.359 MHz). This was further sub-divided into 128 channels, yielding a velocity resolution of $\sim$ 9.4 km s^{-1} on each run. Twenty three and seventeen antennas were available for the observations on the 17th and the 27th respectively, due to various debugging and maintenance activities. The standard calibrator 3C48 was used to carry out absolute flux and bandpass calibration. Total on-source times were three and five hours on the first and second observing runs respectively.

The data were converted from the telescope format to FITS and analysed in AIPS. Data from the two days were analysed separately. Continuum emission was subtracted by fitting a linear polynomial to the U-V visibilities, using the AIPS task UVLIN. The continuum-subtracted data were then mapped in all channels and spectra extracted at the quasar location from the resulting three-dimensional data cube. The spectra of the two epochs were corrected to the heliocentric frame outside AIPS and then averaged together. The flux density of B0218+357 was measured to be 1.64 Jy at both epochs. Earlier experience with the GMRT indicates that the flux calibration is reliable to $\sim$ 15%, in this observing mode.

The final GMRT OH spectrum towards 0218+357 is shown in Fig. 2. The RMS noise is 1.1 mJy, per 9.4 km/sec/channel; note that the spectrum has not been smoothed. Both OH transitions are clearly visible; the peak absorption occurs at heliocentric frequencies of 988.56 MHz and 989.72 MHz, corresponding to redshifts $z = 0.68467 \pm 0.00005$ and $z = 0.68468 \pm 0.00005$ for the 1665 MHz and 1667 MHz transitions respectively.

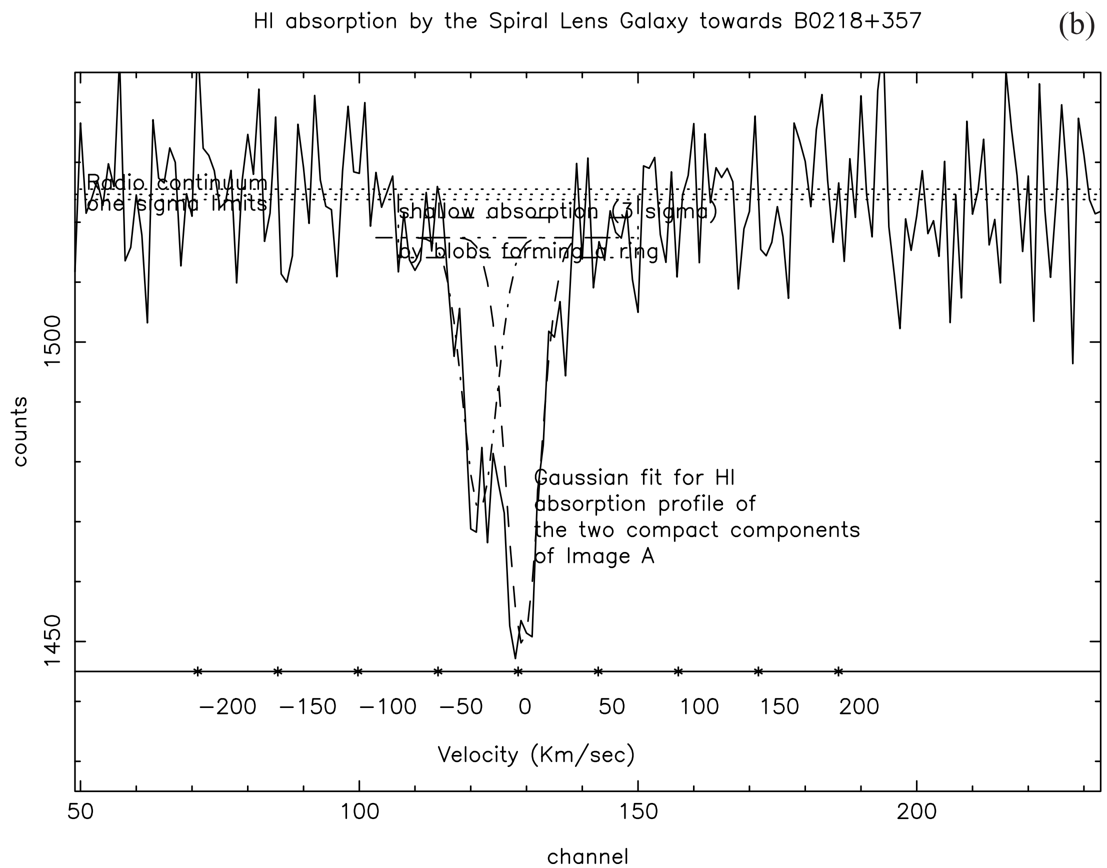

Figure 1. **(b)** Decomposition of the HI 21 cm line profile into main absorption feature in front of Image A as well as shallow absorption trough due to the radio ring. The best fit continuum and the shallow absorption level are shown along with the Gaussian main lines. The x-axis is the Doppler velocity with respect to the heliocentric frequency while the y-aixs is the observed flux in mJy.

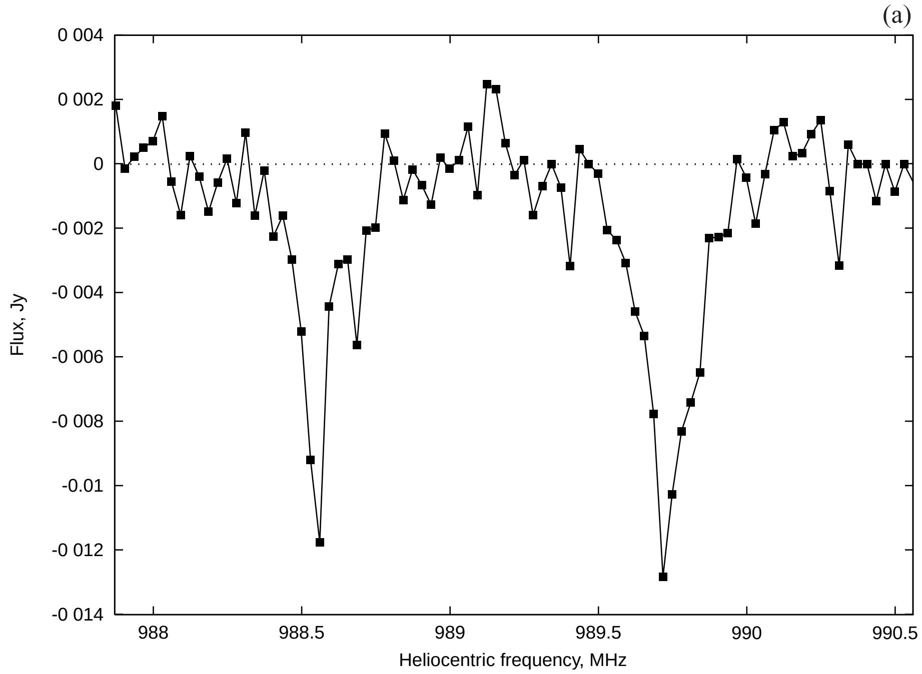

Figure 2. **(a)** GMRT 4 MHz OH spectrum towards 0218+357. The x-axis is heliocentric frequency, in MHz. The spectrum has a resolution of $\sim$ 9.4 km s^{-1}.

4. Analysis of the OH line profiles and results

The spectral decomposition shown in Fig. 2 is similar to the HI line. In spite of the poor velocity resolution, absorption due to the radio ring can be extracted from both the OH lines at a doppler width of around 70 km s^{-1}. The inferred velocity at 1.4 kpc radial distance is between 120 and 160 km/sec, consistent with the HI value. But, like the HI line, absorption in front of Image B at the centre of the ring is absent in both the OH lines. So, the bulge of the lensing spiral galaxy appears to have a hole, a fact noted by Wiklind & Combes (1995).

The OH doublet have identical strengths as well as doppler width in front of Image A. Both the doppler position and velocity match well with the HI line. The inference is that neutral hydrogen and molecular gas appear to coexist, but in tenous clouds where radiative equilibrium is established through infra–red pumping. This is in contrast with PKS1830-211, where a similar spiral galaxy at redshift of 0.89 has OH doublet of nearly 9:5 strength coexisting with neutral hydrogen, indicating that higher density gas clouds permeate the galaxy.

Acknowledgements

The OH observations were carried out with GMRT of TIFR.

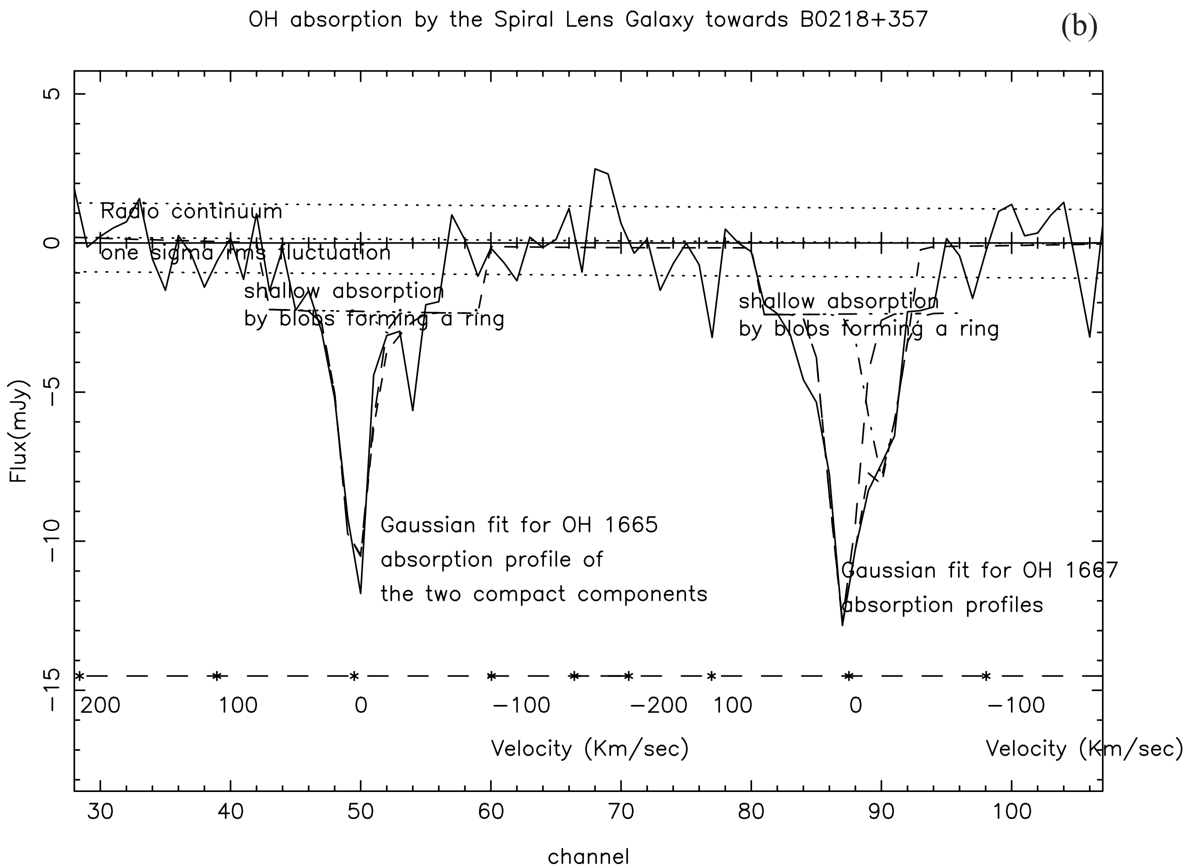

Figure 2. **(b)** Decomposition of the GMRT spectra into the main OH absorption feature in front of Image A as well as shallow absorption trough due to the radio ring. The best fit continuum and shallow absorption level are shown along with the Gaussian main lines. The x-axis is the Doppler velocity with respect to the heliocentric frequency while the y-axis is the flux in mJy.

References

Chengalur, J., de Bruyn, A. G., Narasimha, D. 1999, *A&A*, **343,** L79.
Patnaik, A. R. *et al* 1993, *MNRAS*, **261,** 435.
Wiklind, T., Combes, F. 1995, *A&A*, **299,** 382.

J. Astrophys. Astr. (2002) **23,** 173–183

Connecting Global to Local Parameters in Barred Galaxy Models

N. D. Caranicolas *Department of Physics, Section of Astrophysics, Astronomy and Mechanics, University of Thessaloniki, 540 06 Thessaloniki, Greece.*
e-mail: caranic@helios.astro.auth.gr

Received 2002 March 26; accepted 2002 November 14

Abstract. We present connections between global and local parameters in a realistic dynamical model, describing motion in a barred galaxy. Expanding the global model in the vicinity of a stable Lagrange point, we find the potential of a two-dimensional perturbed harmonic oscillator, which describes local motion near the centre of the global model. The frequencies of oscillations and the coefficients of the perturbing terms are not arbitrary but are connected to the mass, the angular rotation velocity, the scale length and the strength of the galactic bar. The local energy is also connected to the global energy. A comparison of the properties of orbits in the global and local potential is also made.

Key words. Galaxies: barred—orbits—global and local parameters.

1. Introduction

We consider the barred galaxy model described by the potential

$$\Phi(r,\phi) = -\frac{M_d}{(r^2+\alpha^2)^{1/2}} - \frac{M_b}{\{r^2[1+(b^2-1)\sin\phi^2]+c_b^2\}^{1/2}}, \tag{1}$$

where r, ϕ are polar coordinates. Here M_d is the mass, α is the scale length of the disk while M_b , c_b and $b > 1$ is the mass, the scale length and the strength of the bar, respectively. In the system of galactic units used in this paper, the unit of length is $1kpc$ the unit of time is 0.97746×10^8 yr and the unit of mass is $2.325 \times 10^7\, M_\odot$. The velocity and the angular velocity units are 10 km/s and 10 km/s/kpc, respectively while G is equal to unity. Our test particle is a star of mass $= 1$. Therefore, the energy unit (per unit mass) is $100\,(\mathrm{km/s})^2$. In these units the values of the parameters are $\alpha = 12$ kpc, $b = 2$, $c_b = 1.5$ kpc, $M_d = 9500$ and $M_b = 3000$. It is evident that we consider a galaxy with a massive bar.

We shall consider the case when the bar rotates clockwise at a constant angular velocity Ω_b. The corresponding Hamiltonian, which is known as the Jacobi integral, in rectangular cartesian coordinates x, y, reads

$$H_J = \frac{1}{2}(p_x^2+p_y^2)+\Phi(x,y)-\frac{1}{2}\Omega_b^2(x^2+y^2) = \frac{1}{2}(p_x^2+p_y^2)+\Phi_{\mathrm{eff}}(x,y) = E_J, \tag{2}$$

where p_x, p_y are the momenta, per unit mass, conjugate to x and y

$$\Phi_{\mathrm{eff}}(x,y) = -\frac{M_d}{\sqrt{x^2+y^2+\alpha^2}} - \frac{M_b}{\sqrt{x^2+b^2y^2+c_b^2}} - \frac{1}{2}\Omega_b^2(x^2+y^2), \tag{3}$$

is the effective potential and E_J is the numerical value of the Jacobi integral. If we expand the effective potential (3) in a Taylor series near the centre we shall find a potential describing local motion.

The aim of the present work is:

- to find connections between global and local parameters and
- to study and compare the properties of global and local motion.

In particular, we shall express the coefficients of the local potential in terms of the global physical quantities entering potential (3). A connection of the global to local energy will be also presented.

The properties of orbits in the global model are studied in section 2. In section 3 we present the local potential, the connection between the local and global parameters and the properties of the local motion. We close with a discussion and the conclusions of this work, which are presented in section 4.

2. Orbits in the global model

Figure 1 shows contours of the constant effective potential (3), when $\Omega_b = 1.25$ in the above mentioned galactic units, which is equivalent to 12.5 km/s/kpc. One observes

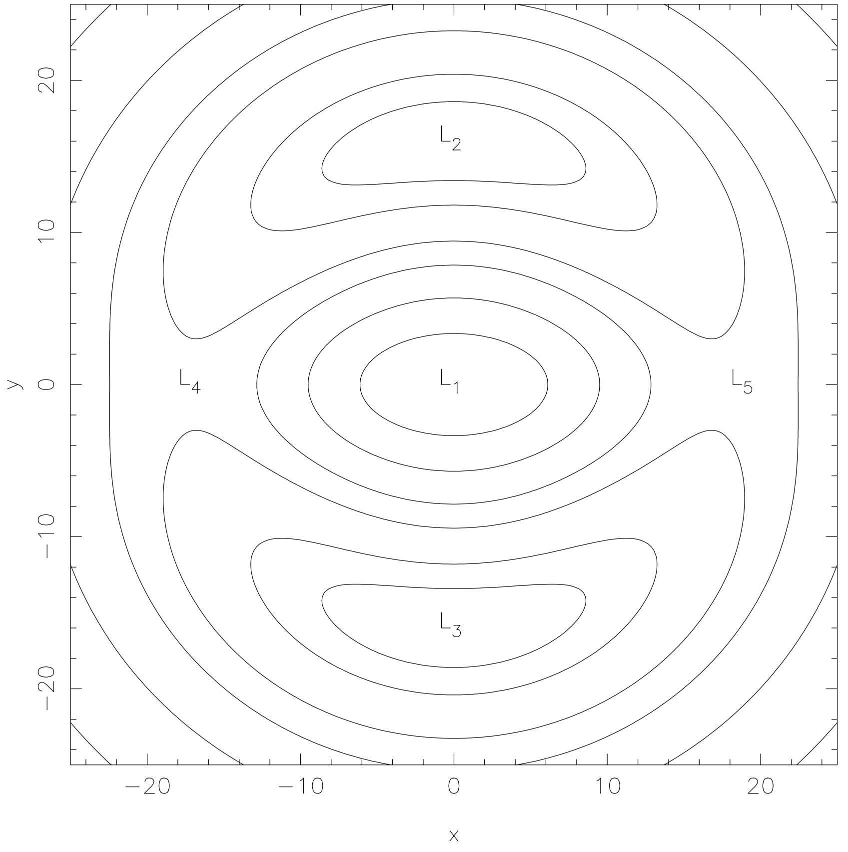

Figure 1. Contours of the constant effective potential (3) when $\Omega_b = 1.25$. The values of the parameters are $\alpha = 12$ kpc, $b = 2$, $c_b = 1.5$ kpc, $M_d = 9500$ and $M_b = 3000$. One observes that there are five stationary points marked L_1 to L_5.

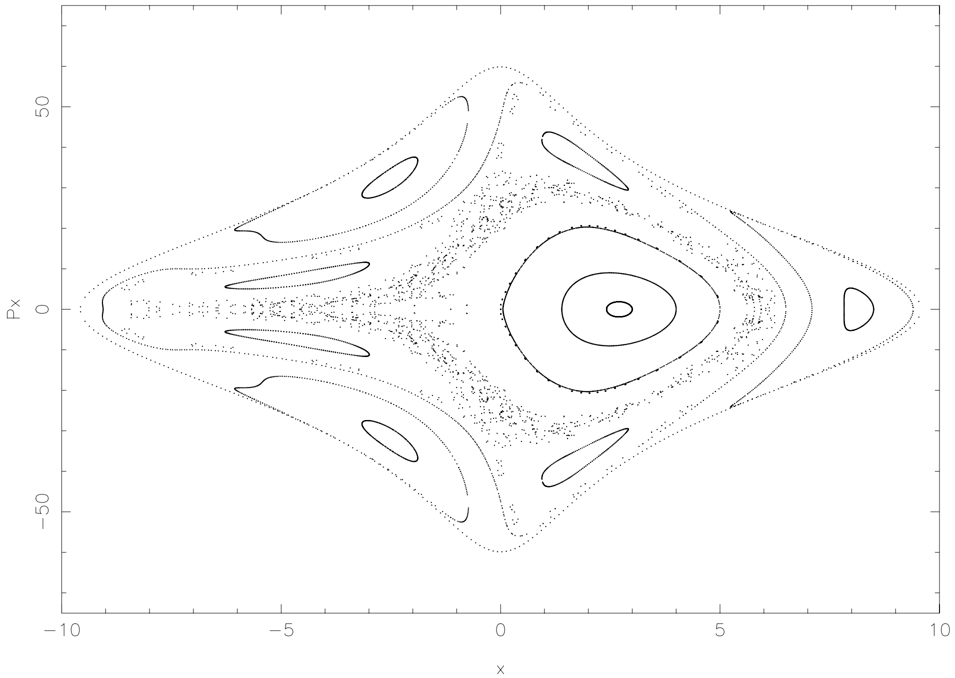

Figure 2. The $x - p_x$ phase plane for the global Hamiltonian (2) when $E_J = -1000$. The values of the parameters are as in Fig. 1.

that there are five stationary points, marked L_1 to L_5, at which

$$\frac{\partial \Phi_{\rm eff}}{\partial x} = 0\,, \qquad \frac{\partial \Phi_{\rm eff}}{\partial y} = 0. \tag{4}$$

These points are called "Lagrange points". The central stationary point L_1 is a minimum of $\Phi_{\rm eff}$. In the other four points L_2, L_3, L_4, L_5 it is possible, for the test particle, to travel in a circular orbit while appearing to be stationary in the rotating frame. For this orbit the centrifugal and gravitational force precisely balance. The stationary points L_4, L_5 on the x-axis are saddle points while L_2, L_4 are maxima of the effective potential. The annulus bounded by the circles through L_2, L_3 and L_4, L_5 is known as the "region of corotation" (see Binney & Tremaine 1987). It is important to note that the region of corotation is located somewhere at the end of the galaxy described by the model (3).

We now proceed to study the properties of orbits in the potential (3). Orbits are found by integrating numerically the equations of motion

$$\ddot{x} = -2\Omega_b \dot{y} - \frac{\partial \Phi_{\rm eff}}{\partial x}, \quad \ddot{y} = 2\Omega_b \dot{x} - \frac{\partial \Phi_{\rm eff}}{\partial y}, \tag{5}$$

where the dot indicates derivative with respect to the time.

In order to visualise the properties of motion we use the $x - p_x$, $y = 0$, $p_y \geq 0$ Poincare phase plane of the Hamiltonians (2). The results for $E_J = -1000$ are shown in Fig. 2. There are regular orbits, forming the nearly circular invariant curves, as well

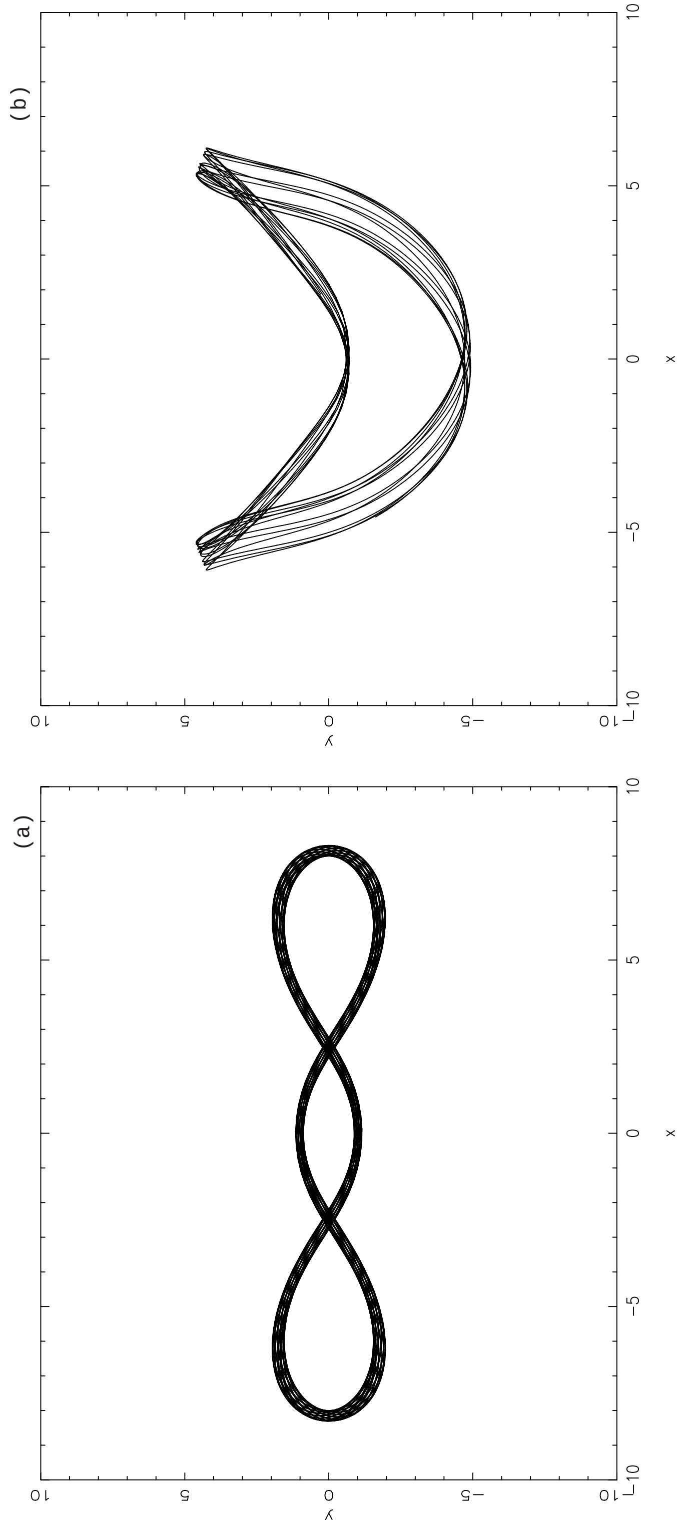

Figure 3. (*Continued*)

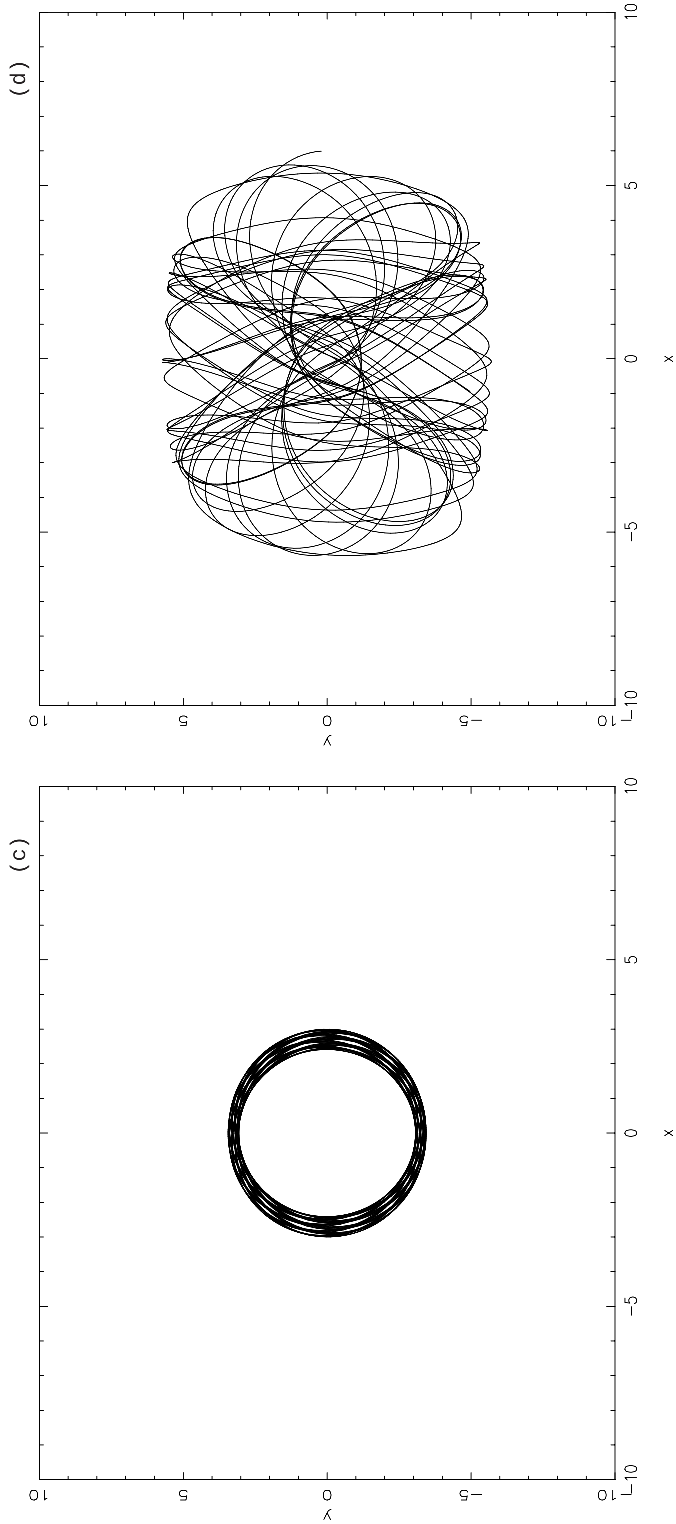

Figure 3(a–d). Orbits in the global Hamiltonian (2). The values of parameters are as in Fig. 2.

as sets of islands and chaotic orbits producing a chaotic region. The outermost curve is the limiting curve defined by the equation

$$\frac{1}{2}p_x^2 + \Phi_{\mathrm{eff}}(x) = E_J. \tag{6}$$

Figure 3(a–d) shows four typical orbits. The orbits shown in Fig. 3(a) produce the set of the three outer islands. It is evident that those elongated orbits support the bar. The orbit shown in Fig. 3(b) produces two of the inner islands while the orbit given in Fig. 3(c) produces the central invariant curves that are topologically circles. The chaotic region are produced by the orbit shown in Fig. 3(d). It is clear that the three last types of orbits support the disk. It is important to note that for the values of the parameters used, chaotic motion is present only when $c_b < 1.7$ kpc while for $c_b = 1.7$ kpc the chaotic region is negligible (see Caranicolas & Innanen 1991).

For small values of the energy the phase plane is quite different. Fig. 4 shows the $x - p_x$ phase plane when $E_J = -2700$. It is evident that, here, we have motion taking place near the stable Lagrange point L_1. The motion is regular and one observes only one kind of invariant curves. The invariant curves are topological circles closing around one unique invariant point. The corresponding orbits are box-orbits. Those forming the outer invariant curves belong to elongated boxes that support the bar while, as we approach the "central" invariant point, the boxes become more rectangular.

3. Orbits in the local potential

The local potential can be found by expanding the effective potential (3) in a Mc-Laurin series near the stable Lagrange point L_1, which coincides with the origin. Doing so,

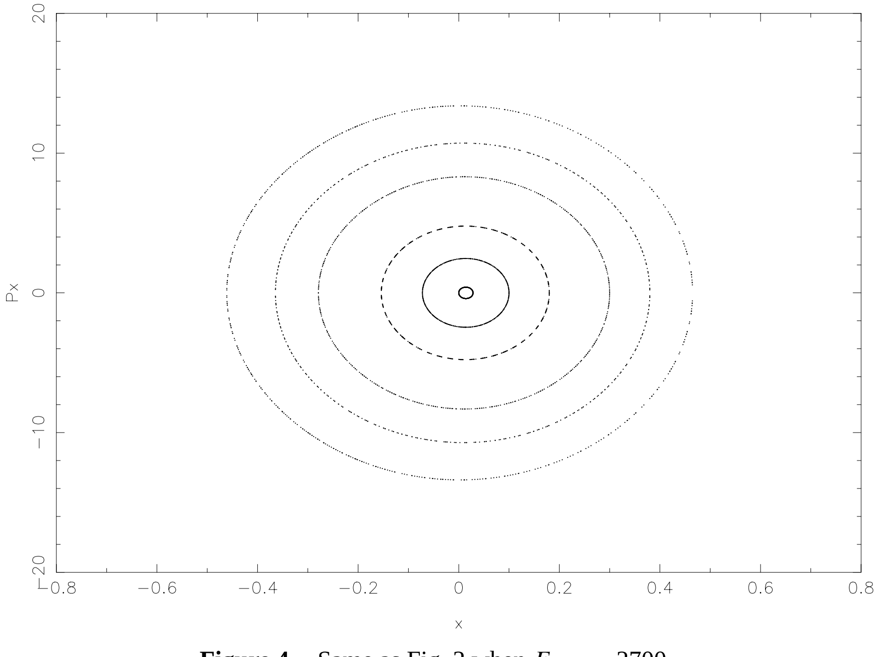

Figure 4. Same as Fig. 2 when $E_J = -2700$.

we obtain the local effective potential which reads

$$\begin{aligned} U_{\rm eff}(\Delta x, \Delta y) = U_{\rm eff}(0,0) &+ \frac{1}{2}A(\Delta x)^2 + \frac{1}{2}B(\Delta y)^2 \\ &- \frac{3}{8}[\alpha_1(\Delta x)^4 + 2\alpha_2(\Delta x)^2(\Delta y)^2 + \alpha_3(\Delta y)^4] \\ &- \Omega_0^2[(\Delta x)^2 + (\Delta y)^2]/2, \end{aligned} \tag{7}$$

where we have set

$$U_{\rm eff} = \frac{\alpha}{M_d}\Phi_{\rm eff}, \tag{8}$$

in order to avoid large numbers. Writing, for convenience, $x = \Delta x$, $y = \Delta y$, $V_{\rm eff} = U_{\rm eff}(x, y) - U_{\rm eff}(0,0)$, equation (7) becomes

$$V_{\rm eff} = \frac{1}{2}Ax^2 + \frac{1}{2}By^2 - \frac{3}{8}[\alpha_1 x^4 + 2\alpha_2 x^2 y^2 + \alpha_3 y^4] - \Omega_0^2(x^2 + y^2)/2, \tag{9}$$

where

$$\begin{aligned} &A = \frac{1}{\alpha^2} + \frac{\alpha M_b}{M_d c_b^3}\ ,\ B = \frac{1}{\alpha^2} + \frac{\alpha b^2 M_b}{M_d c_b^3}\ ,\ \alpha_1 = \frac{1}{\alpha^4} + \frac{\alpha M_b}{M_d c_b^5}, \\ &\alpha_2 = \frac{1}{\alpha^4} + \frac{\alpha b^2 M_b}{M_d c_b^5}\ ,\ \alpha_3 = \frac{1}{\alpha^4} + \frac{\alpha b^4 M_b}{M_d c_b^5}\ ,\ \Omega_0^2 = \frac{\alpha \Omega_b^2}{M_d}. \end{aligned} \tag{10}$$

One observes, from equation (10), that the coefficients of the local effective potential are functions of the physical quantities entering the global effective potential.

The local Hamiltonian is

$$H_L = \frac{1}{2}(X^2 + Y^2) + V_{\rm eff}(x, y) = h_L, \tag{11}$$

where X, Y are the local momenta, per unit mass, conjugate to x and y while h_L is the numerical value of the local energy. We now come to connect the global energy E_J to the local energy h_L. Note that $E_{J0} = \Phi_{\rm eff}(0,0)$ defines a point in the (x, y) plane while $E_J = \Phi_{\rm eff}(x, y)$ defines a curve in the same plane. The global motion takes place inside this curve which is known as the zero velocity curve. At the same time $h_{L0} = V_{\rm eff}(0,0)$ defines a point in the (x, y) plane while $h_L = U_{\rm eff}(x, y)$ defines a curve inside which the local motion takes place. This second curve is the local zero velocity curve. We consider only bounded motion, that is the zero velocity curves are always closed curves. The local energy h_L is connected to the global energy through the relation

$$\begin{aligned} h_L = U_{\rm eff}(x, y) - U_{\rm eff}(0,0) &= \frac{\alpha}{M_d}[\Phi_{\rm eff}(x, y) - \Phi_{\rm eff}(0,0)] \\ &= \frac{\alpha}{M_d}(E_J - E_{J0}). \end{aligned} \tag{12}$$

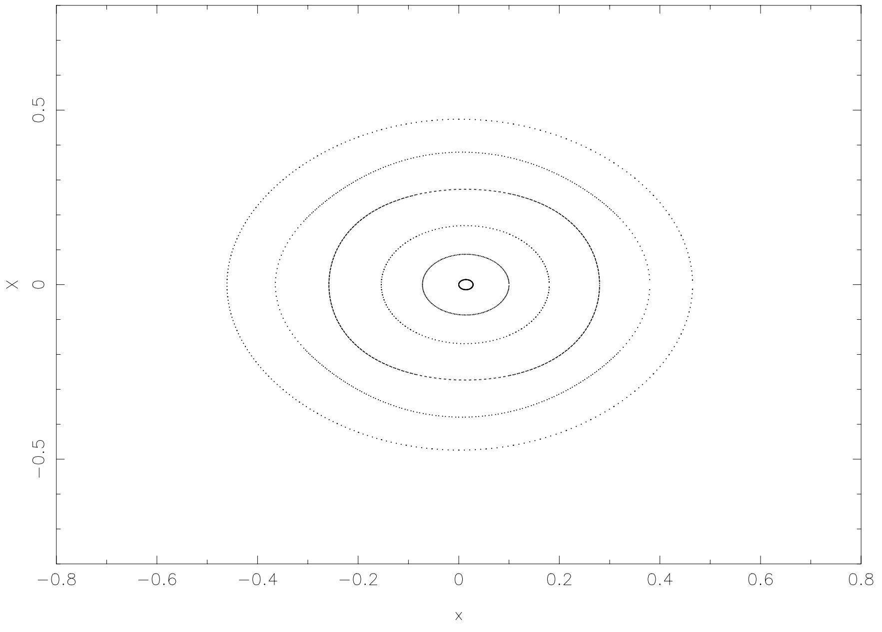

Figure 5. The $x - X$ phase plane for the local Hamiltonian (11) when $h = h_L = 0.11578$.

We now come to study the properties of local motion. For the adopted values of the global parameters and $\Omega_b = 1.25$, we find $A = 1.13$, $B = 4.50$, $\alpha_1 = 0.50$, $\alpha_2 = 2.00$, $\alpha_3 = 7.98$, $\Omega_0 = 0.044$. Using the value $E_J = -2700$ we find $h_L = 0.11578$. Fig. 5 shows the $x - X$ ($y = 0$, $Y > 0$) phase plane for the local motion. The motion is regular and one observes invariant curves that are topologically circles closing around a "central" invariant point. It is clear, that no resonant orbits are present although the ratio of the unperturbed frequencies is a rational number, namely $A^{1/2}/B^{1/2} = 1/2$. As the similarity between Figs 4 and 5 is obvious one can say that the behaviour of orbits in the local system Hamiltonian (11) is similar to that of orbits in the global Hamiltonian (2).

Figure 6 shows the $x - X$ phase plane for the local motion when $h = 0.36 > h_L$. Here things look quite different. In addition to the invariant curves closing around the "central" invariant point, one observes four sets of islands. These islands are produced by quasi periodic orbits starting near the corresponding stable periodic orbits. These periodic orbits are the well known figure-eight periodic orbits. We shall come to this point later in this section.

It is natural for the reader to ask: why for this value of local energy the properties of orbits of the local system are different from those of the corresponding global potential? The answer is the following: The expansion (9) is valid only when

$$\frac{x^2 + b^2 y^2}{c_b^2} << 1. \tag{13}$$

When $h_L = 0.11578$ we have $x \le x_{\max} = 0.47$, $y \le y_{\max} = 0.23$. For the above values of x and y (13) is always true when $b = 2$, $c_b = 1.5$ kpc. On the other hand, if one chooses $h = 0.36$, then $x \le x_{\max} = 0.95$, $y \le y_{\max} = 0.48$ and relation (13) is not valid for the same values of b and c_b. Therefore, it is obvious that the properties of

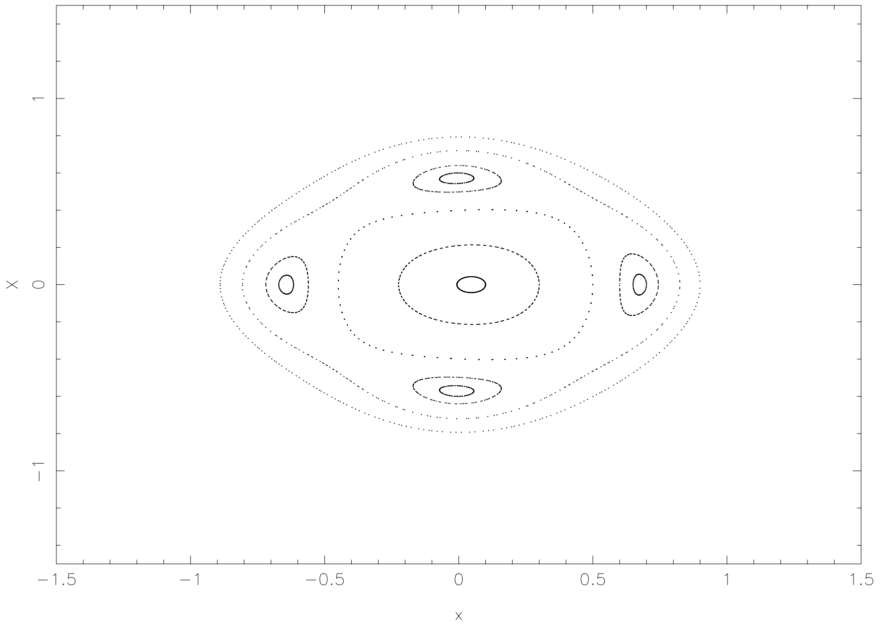

Figure 6. Same as Fig. 5 when $h = 0.36$.

orbits in the local system are the same to the properties of orbits, in the global system, only when the local energy is small enough such as relation (13) to hold. If we increase the value of energy then resonant periodic orbits appear. These orbits are stable figure-eight orbits. Near these orbits start the figure-eight quasi periodic loop orbits, which support the bar structure in the central parts of the galaxy.

It is also important to note that, for a given value of global energy, there corresponds a value of local energy through relation (12). It is obvious that this local energy does not have a meaning, if relation (13) is not satisfied. In order to observe the resonant figure-eight orbits, one must use larger values of energy for the local potential. Numerical experiments suggest that the figure-eight orbits appear for values of h about twice as large as h_L. On the other hand we must emphasise that the chaotic regions, if any, are negligible. Indeed we made many numerical calculations for energies up to the energy of escape in the local potential. Our numerical calculations have shown that the area of the phase plane covered by the quasi periodic figure-eight orbits increases while no chaotic phenomena were observed. The energy of escape for the local potential (see Caranicolas & Varvoglis 1984) is given by the relation

$$h_{\mathrm{esc}} = \frac{(B - \Omega_b^2)^2}{6\alpha_3}. \tag{14}$$

Note that, because we always study bounded motion, we must have $h_L \leq h \leq h_{\mathrm{esc}}$.

4. Discussion

During the last decades a large number of papers have been devoted to the study of dynamics of barred galaxies (see e.g. Freeman 1966; Zang & Hohl 1978; Miwa &

Noguchi 1981; Toomre 1981; Carnevali 1983; Papayannopoulos & Petrou 1983; Petrou 1984; Sparke & Sellwood 1987; Combes *et al.* 1990; Sundin & Sandelius 1991).

In the present work we have tried to find connections between the parameters of a model describing global motion in a barred galaxy and the corresponding parameters of the local potential. The local potential comes by expanding the global effective potential near the centre of the galaxy. It was shown that the local parameters and the corresponding local energy are functions of the global parameters and the global energy.

Numerical calculations in the global model suggest that, in addition to the regular orbits, there is a significant part of orbits that is chaotic. It was observed that chaotic orbits to appear need small values of the scale length of the bar. For small values of the global energy the motion is regular and all orbits are box orbits. The same is true for the local motion when relation (13) is satisfied. In other words, the properties of global and local motion are similar for small values of the global energy, which consequently give, through (12), small values for the local energy h_L.

Furthermore, we must note that in the global model the resonant orbits of type b as well as the chaotic orbits of type d carry stars in the central parts of the galaxy. Therefore we have an increasing density near L_1. It is interesting to observe that a large number of high energy stars passing near L_1 are in chaotic orbits. The other two types of orbits a and b do not contribute in the central density.

Increasing the value of energy in the local model gives rise to resonant figure-eight orbits. The present and previously derived results support the idea that these orbits seem to be important for the local barred galaxy models. With the term local barred galaxy models we mean those that are made from perturbed harmonic oscillators. The following reasons make these orbits important for galactic bars:

- It is evident that the figure-eight orbits support the barred structure.
- Starting from the figure-eight orbits and using the theory of the Inverse Problem, one can construct a local potential based on perturbed harmonic oscillators which reproduce the above orbits (see Caranicolas 1998; Caranicolas & Karanis 1998).
- Figure-eight orbits were observed not only in self consistent models (Miller & Smith 1979) but also in the present local model which comes from the realistic potential (1).

It is also important to notice that the figure-eight orbits appear for values of the energy h much more larger than the local energy h_L. Looking this fact from a physical point of view, one can say that the figure-eight orbits can be considered as a product of a particular activity near the centre of barred galaxies.

Acknowledgement

The author would like to thank an anonymous referee for useful comments.

References

Binney, J., Tremaine, Sc. 1987, *Galactic Dynamics*, (Princeton, New Jersey: Princeton University press)

Caranicolas, N. D., Varvoglis, Ch. 1984, *Astron. Astrophys.* **141**, 383.

Caranicolas, N. D., 1998, *Astron. Astrophys.* **332**, 88.

Caranicolas, N. D., Karanis, G.I. 1998, *A& SS* **259**, 45.

Caranicolas, N. D., Innanen, K.A. 1991, *A.J.* **102**, 1343.
Carnevali, P. 1983, *Ap. J.* **265**, 701.
Combes, F., Dupraz, C., Cerin, M. 1990, In: *Dynamics and Interactions of Galaxies*, (ed.) R Wielen (Berlin: Springer) p. 205
Freeman, K.C. 1966, *MNRAS* **134**, 15.
Miller, R., Smith, B.F. 1979, *Ap. J.* **227**, 785.
Miwa, T., Nochuchi, M. 1998, *Ap. J.* **499**, 149.
Papayannopoulos, Th., Petrou, M. 1983, *Astron. Astrophys.* **119**, 21.
Petrou, M. 1984, *MNRAS* **211**, 283.
Sundin, M., Sundelius, B. 1991, *Astron. Astrophys.* **245**, L5.
Sparke, S.L. , Sellwood, J.A. 1987, *MNRAS* **225**, 653.
Toomre, A. 1981, In: *The Structure and Evolution of Normal Galaxies*, (eds) S. M. Fall, I. Lyndell-Bell, (Cambridge University Press)
Zang, T.A., Hohl, F. 1978, *Ap.J.* **226**, 521.

J. Astrophys. Astr. (2002) **23,** 185–196

TreePM: A Code for Cosmological N-Body Simulations

J. S. Bagla *Harish-Chandra Research Institute, Chhatnag Road, Jhunsi, Allahabad 211 019, India.*
e-mail: jasjeet@mri.ernet.in

Received 2002 June 13; accepted 2002 November 14

Abstract. We describe the TreePM method for carrying out large N-Body simulations to study formation and evolution of the large scale structure in the Universe. This method is a combination of Barnes and Hut tree code and Particle-Mesh code. It combines the automatic inclusion of periodic boundary conditions of PM simulations with the high resolution of tree codes. This is done by splitting the gravitational force into a short range and a long range component. We describe the splitting of force between these two parts. We outline the key differences between TreePM and some other N-Body methods.

Key words. Gravitation—methods: numerical—cosmology: large scale structure of the universe.

1. Introduction

Observations suggest that the present universe is populated by very large structures like galaxies, clusters of galaxies etc. Current models for formation of these structures are based on the assumption that gravitational amplification of density perturbations resulted in the formation of large scale structures. In absence of analytical methods for computing quantities of interest, numerical simulations are the only tool available for study of clustering in the non-linear regime. The last two decades have seen a rapid development of techniques and computing power for cosmological simulations and the results of these simulations have provided valuable insight into the study of structure formation.

The simplest N-Body method that has been used for studying clustering of large scale structure is the Particle Mesh method (PM hereafter). The genesis of this method is in the realisation that the Poisson equation is an algebraic equation in Fourier space, hence if we have a tool for switching to Fourier space and back, we can calculate the gravitational potential and the force with very little effort. It has two elegant features in that it provides periodic boundary conditions by default, and the force is softened naturally so as to ensure collisionless evolution of the particle distribution. However, softening of force done at grid scale implies that the force resolution is very poor. This limits the dynamic range over which we can trust the results of the code between a few grid cells and about a quarter of the simulation box (Bouchet & Kandrup 1985; Bagla & Padmanabhan 1997. Many efforts have been made to get around this problem, mainly in the form of P^3M (Particle-Particle Particle Mesh) codes (Efstathiou *et al.*

1985; Couchman 1991). In these codes, the force computed by the particle mesh part of the code is supplemented by adding the short range contribution of nearby particles, to improve force resolution. The main problem with this approach is that the particle-particle summation of the short range force takes a lot of time in highly clustered situations. Another, more subtle problem is that the force computed using the PM method has anisotropies and errors in force at grid scale – these errors are still present in the force calculated by combining the PM force with short range corrections (Bouchet and Kandrup 1985).

A completely different approach to the problem of computing force are codes based on the tree method. In this approach we consider groups of particles at a large distance to be a single entity and compute the force due to the group rather than sum over individual particles. There are different ways of defining a group, but by far the most popular method is that due to Barnes & Hut (1986). Applications of this method to Cosmological simulations require including periodic boundary conditions. This has been done using Ewald's method (Ewald 1921; Rybicki 1986; Hernquist, Bouchet & Suto 1991; Springel, Yoshida & White 2001). Ewald's method is used to tabulate the correction to the force due to periodic boundary conditions. This correction term is stored on a grid (in relative separation of a pair of particles) and the interpolated value is added to the pairwise force.

Some attempts have been made to combine the high resolution of a tree code with the natural inclusion of periodic boundary conditions in a PM code by simply extending the P^3M method and replacing the particle-particle part for short range correction with a local tree (Xu 1995).

In this paper we present a hybrid N-Body method that attempts to combine the good features of the PM and the tree method, while avoiding the problems of the P^3M and the TPM methods. Our approach is to divide force into long and short range components using partitioning of unity, instead of taking the PM force as given. This allows us greater control over errors, as we shall see below.

The plan of the paper is as follows: Section 2 introduces the basic formalism of both the tree and PM codes. Section 2.3 gives the mathematical model for the TreePM code. We analyse errors in force for the TreePM code in section 3. Computational requirements of our implementation of the TreePM code are discussed in section 4. A discussion of the relative merits of the TreePM method with respect to other N-Body methods follows in section 5.

2. The TreePM method

2.1 *Tree code*

We use the approach followed by Barnes & Hut (1986). In this, the simulation volume is taken to be a cube. The tree structure is built out of cells and particles. Cells may contain smaller cells (subcells) within them. Subcells can have even smaller cells within them, or they can contain a particle. We start with the simulation volume and add particles to it. If two particles end up in the same subcell, the subcell is geometrically divided into smaller subcells until each subcell contains either subcells or at most one particle. The cubic simulation volume is the root cell. In three dimensions, each cubic cell is divided into eight cubic subcells. Cells, as structures, have attributes like total mass, location of centre of mass and pointers to subcells. Particles, on the other hand have the traditional attributes like position, velocity and mass. More details can be found in the original paper (Barnes & Hut 1986).

Force on a particle is computed by adding contribution of other particles or of cells. A cell that is sufficiently far away can be considered as a single entity and we can just add the force due to the total mass contained in the cell from its centre of mass. If the cell is not sufficiently far away then we must consider its constituents, subcells and particles. Whether a cell can be accepted as a single entity for force calculation is decided by the cell acceptance criterion (CAC). We compute the ratio of the size of the cell d and the distance r from the particle in question to its centre of mass and compare it with a threshold value

$$\theta = \frac{d}{r} \leq \theta_c. \tag{1}$$

The error in force increases with θ_c. There are some potentially serious problems associated with using $\theta_c \geq 1/\sqrt{3}$, a discussion of these is given in Salmon & Warren (1994). One can also work with completely different definitions of the CAC (Salmon & Warren 1994; Springel, Yoshida & White 2001). Irrespective of the criterion used, the number of terms that contribute to the force on a particle is much smaller than the total number of particles, and this is where a tree code gains in terms of speed over direct summation.

We will use the Barnes and Hut tree code and we include periodic boundary conditions for computing the short range force of particles near the boundaries of the simulation cube. Another change to the standard tree walk is that we do not consider cells that do not have any spatial overlap with the region within which the short range force is calculated. We also use an optimisation technique to speed up force calculation (Barnes 1990).

2.2 *Particle mesh code*

A PM code is the obvious choice for computing long range interactions. Much has been written about the use of these in cosmological simulations (e.g., see Hockney & Eastwood 1988) so we will not go into details here. PM codes solve for the gravitational potential in the Fourier space. These use Fast Fourier Transforms (FFT) to compute Fourier transforms, and as FFT requires data to be defined on a regular grid the concept of mesh is introduced. The density field represented by particles is interpolated onto the mesh. Poisson equation is solved in Fourier space and an inverse transform gives the potential (or force) on the grid. This is then differentiated and interpolated to the position of each particle in order to calculate the displacements. Use of a grid implies that forces are not accurate at the scale smaller than the grid cells. A discussion of errors in force in a PM code can be found in Efstathiou *et al.* (1985) and elsewhere (Bouchet & Kandrup 1985; Bagla & Padmanabhan 1997). The error in force can be very large at small scales but it drops to an acceptable number beyond a few grid cells, and is negligible at large scales.

We use the Cloud-in-Cell weight function for interpolation. We solve the Poisson equation using the natural kernel, $-1/k^2$; this is called the poor man's Poisson solver (Hockney & Eastwood 1988). We compute the gradient of the potential in Fourier space.

2.3 *TreePM code*

We now turn to the question of combining the tree and the PM code. We wish to split the inverse square force into a long range force and a short range force. The gravitational potential can be split into two parts in Fourier space (Ewald 1921).

$$\begin{aligned}\varphi_k &= -\frac{4\pi G \varrho_k}{k^2}, \\ &= -\frac{4\pi G \varrho_k}{k^2} \exp\left(-k^2 r_s^2\right) - \frac{4\pi G \varrho_k}{k^2} \left(1 - \exp\left(-k^2 r_s^2\right)\right), \\ &= \varphi_k^l + \varphi_k^s,\end{aligned} \tag{2}$$

$$\varphi_k^l = -\frac{4\pi G \varrho_k}{k^2} \exp\left(-k^2 r_s^2\right), \tag{3}$$

$$\varphi_k^s = -\frac{4\pi G \varrho_k}{k^2} \left(1 - \exp\left(-k^2 r_s^2\right)\right), \tag{4}$$

where φ^l and φ^s are the long range and the short range potentials, respectively. The splitting is done at the scale r_s. G is the gravitational coupling constant and ϱ is density. The expression for the short range force in real space is:

$$\mathbf{f}^s(\mathbf{r}) = -\frac{Gm\mathbf{r}}{r^3} \left(\operatorname{erfc}\left(\frac{r}{2r_s}\right) + \frac{r}{r_s\sqrt{\pi}} \exp\left(-\frac{r^2}{4r_s^2}\right)\right). \tag{5}$$

Here, erfc is the complementary error function. These equations describe the mathematical model for force in the TreePM code. The long range potential is computed in the Fourier space, just as in a PM code, but using equation (3) instead of equation (2). This potential is then used to compute the long range force. The short range force is computed directly in real space using equation (5). In the TreePM method this is computed using the tree approximation. The short range force falls rapidly at scales $r \gg r_s$, and hence we need to take this into account only in a small region around each particle.

We have plotted the long range and the short range force (equation (5)) as a function of r in Fig. 1 to show their dependence on scale. We have chosen $r_s = 1$ here. The short range force closely follows the total force up to about $2r_s$ and then falls rapidly, its magnitude falls below 1% of the total force by $5r_s$. The long range force reaches a peak around $2r_s$. It makes up most of the total force beyond $3.5r_s$. It falls with scale below $2r_s$, becoming negligible below $r_s/2$.

Evaluation of special functions for calculating the short range force can be time consuming. To save time, we compute an array containing the magnitude of the short range force. The force between any two objects, particle-cell or particle-particle, is computed by linearly interpolating between the nearby array elements multiplied by the unit vector $\mathbf{r}$. It is necessary for the array to sample the force at sufficiently closely spaced values of r in order to keep error in interpolation small.

3. Error estimation

In this section we will study errors in force introduced by various components of the TreePM code. We will only list salient points here and the reader is referred to a more comprehensive study for details (Bagla & Ray 2002).

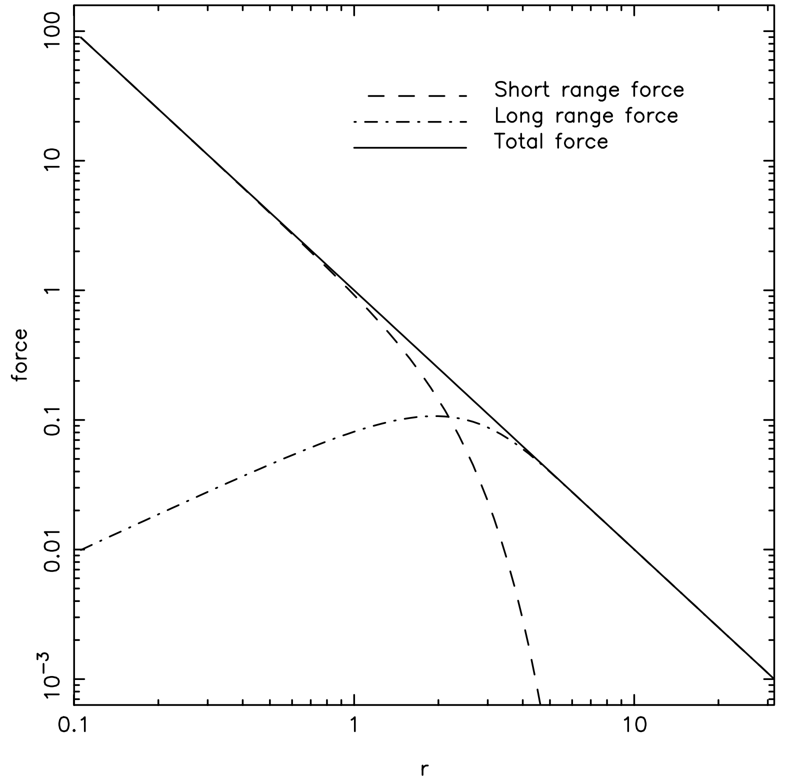

Figure 1. This figure shows the long and the short range force as a function of scale. The inverse square force is shown by the thick line, the long range force by dot-dashed line and the short range force by the dashed line. We have taken $r_s = 1$ here.

We start by estimating the error in force due to one particle. The long range force of a particle is calculated using the PM method, but using equation (3) instead of equation (2). The cutoff at high wave numbers largely removes the effect of the grid and we find that the dispersion in the long range force is very small, e.g., for $r_s \geq 1$ grid length the dispersion is smaller than 1% of the total force at all scales. There is a systematic offset in the long range force that is larger than the dispersion. This offset is induced by the interpolating function, and can be corrected (White 2000; Bagla & Ray 2002) by de-convolving the square of the interpolating function (we need to interpolate twice). This deconvolution does not affect the dispersion in any significant manner.

There are no errors in computing the short range force for one particle, hence the only source of errors is in the calculation of the long range force in this case. All the errors arise due to anisotropies in the long range force. The errors in the long range force increase as we approach small scales, but the contribution of the long range force to the total force falls sharply below $2r_s$ and hence the errors also drop rapidly. There is a peak in errors around $2r_s$–$3r_s$, and for $r_s = 1$ maximum rms error in force of one particle is 1% of the total force.

In calculating the total force, we added the short range force to the long range force at all scales. However, this is not necessary as beyond some scale, the contribution of small scale force to the total force drops to a negligible fraction of the total force. We will call the scale up to which we add the small scale force as $r_{\rm cut}$. The short range force is just below 1% of the total force at $r_{\rm cut} = 5r_s$. We choose this value of $r_{\rm cut}$ for the TreePM code.

The other source of error is the tree approximation that we use for computing the short range force. The first correction term is due to the quadrapole moment of the particle distribution in the cell, however the magnitude of this error is larger than in the inverse square force due to a more rapid variation in force with distance. In the worst case, this error can be more than twice the error in the corresponding case of inverse square force (Bagla & Ray 2002). In more generic cases, errors due to this effect tend to cancel out and the net error is small.

Apart from this effect, there is also a dispersion introduced by the tree approximation. The magnitude of this dispersion varies monotonically with θ_c.

One factor that we have to weigh in is that the execution time is small for large θ_c and small $r_{\rm cut}$. Given these considerations, the obvious solution is to choose the smallest r_s and the largest θ_c that gives us a sufficiently accurate force field.

It is important to estimate the errors in a realistic situation, even though we do not expect errors to add up coherently in most situations. We test errors for two distributions of particles: a homogeneous distribution and a clumpy distribution. For the homogeneous distribution, we use randomly distributed particles in a box. We use 262144 particles in a 64^3 box for this distribution. We compute the force using a reference setup ($r_s = 4$, $r_{\rm cut} = 6r_s$, $\theta_c = 0$) and the setup we wish to test ($r_s = 1$, $r_{\rm cut} = 5r_s$, $\theta_c = 0.5$). It can be shown that the errors in the reference setup are well below 0.5% for the entire range of scales (Bagla & Ray 2002). We compute the fractional error in force acting on each particle, this is defined as,

$$\epsilon = \frac{|\mathbf{f} - \mathbf{f}_{\rm ref}|}{|\mathbf{f}_{\rm ref}|}. \tag{6}$$

Figure 2 shows the cumulative distribution of fractional errors. The curves show the fraction of particles with error greater than ϵ. The thick line shows this for the homogeneous distribution. Error ϵ for 99% of particles is less than 3.5%. Results for the clumpy distribution of particles are shown by the dashed line. We used the output of a CDM simulation (Fig. 3a) run with the TreePM code. Errors in this case are much smaller, as compared to the homogeneous distribution, as in the case of tree code (Hernquist, Bouchet & Suto 1991). Error ϵ for 99% of particles is around 2%, as compared to 3.5% for the homogeneous distribution.

There are two noteworthy features of this figure. One is that the error for the homogeneous distribution is higher. The main reason for this is similar to that in tree codes, though the effect is much smaller here. When we are dealing with a homogeneous distribution, the total force on each particle is very small because forces due to nearly identical mass distributions on opposite sides cancel out. This near cancellation of large numbers gives rise to errors that decrease as the net result of these cancellations grows. In a tree code, we calculate the force due to all the particles in the simulation box whereas in the TreePM method we add up the contribution of only those within a sphere of radius $r_{\rm cut}$. This is the reason for the difference in these two curves being much less pronounced than the corresponding curves for the tree code (Hernquist, Bouchet & Suto 1991).

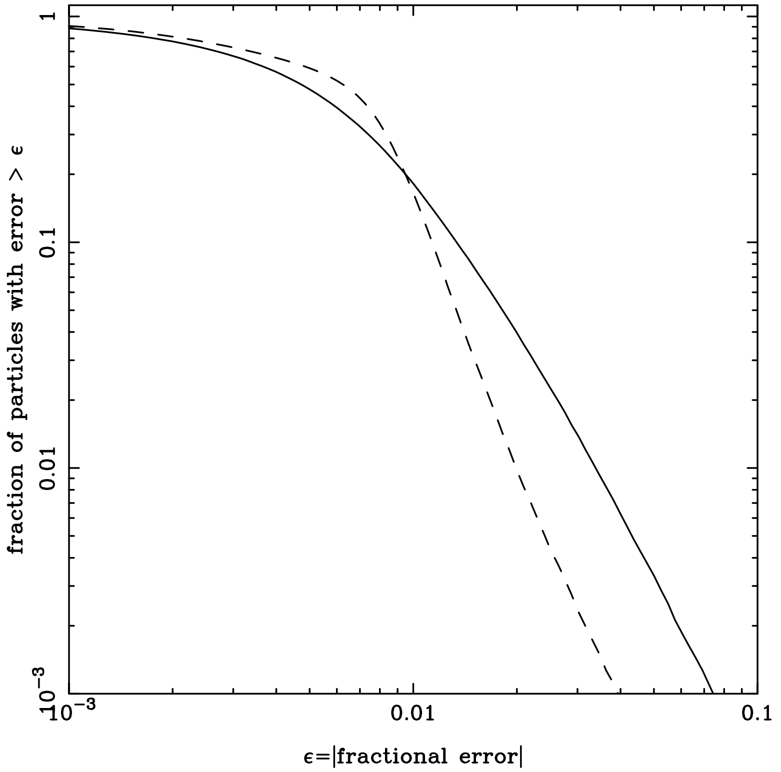

Figure 2. This figure shows the distribution of errors. The variation of the fraction of particles with error greater than a threshold, as a function of the threshold error is plotted. Thick line marks the error for a homogeneous distribution of particles and the dashed line shows the same for a clumpy distribution. These errors were measured with respect to a reference force, determined with a very conservative value of r_s, $r_{\rm cut}$ and θ_c. This panel shows that 99% of the particles have fractional error in force that is less than 3.5% for the homogeneous distribution and around 2% for the clumpy distribution.

The other feature is that the shape of the curves for the homogeneous distribution and the clumpy distribution is different. This is because we begin to see the effect of the error due to tree approximation in case of clumpy distribution. In case of the homogeneous distribution, the distribution of particles is close to isotropic around any given particle and hence the error cancels out. This error can be controlled by reducing θ_c.

We end this section with a brief comparison of the TreePM code with a PM code. We ran a simulation of the sCDM model (262144 particles, $64h^{-1}$Mpc box) with a PM code (Bagla & Padmanabhan 1997) and with the TreePM code discussed here. Fig. 3 shows a slice from these simulations; Fig. 3(a) shows the simulation with the TreePM code and Fig. 3(b) shows the same for a PM code. The large scale structures are the same in the two but there are significant differences at small scales. The halos are much more compact in the TreePM simulation, and large halos show more substructure. These differences are also clear in the two point correlation function $\bar{\xi}(r)$ plotted in Fig. 4. The thick line shows the correlation from the TreePM simulation and the dashed line shows the same for the PM simulation. As expected from Fig. 3 and from general considerations,

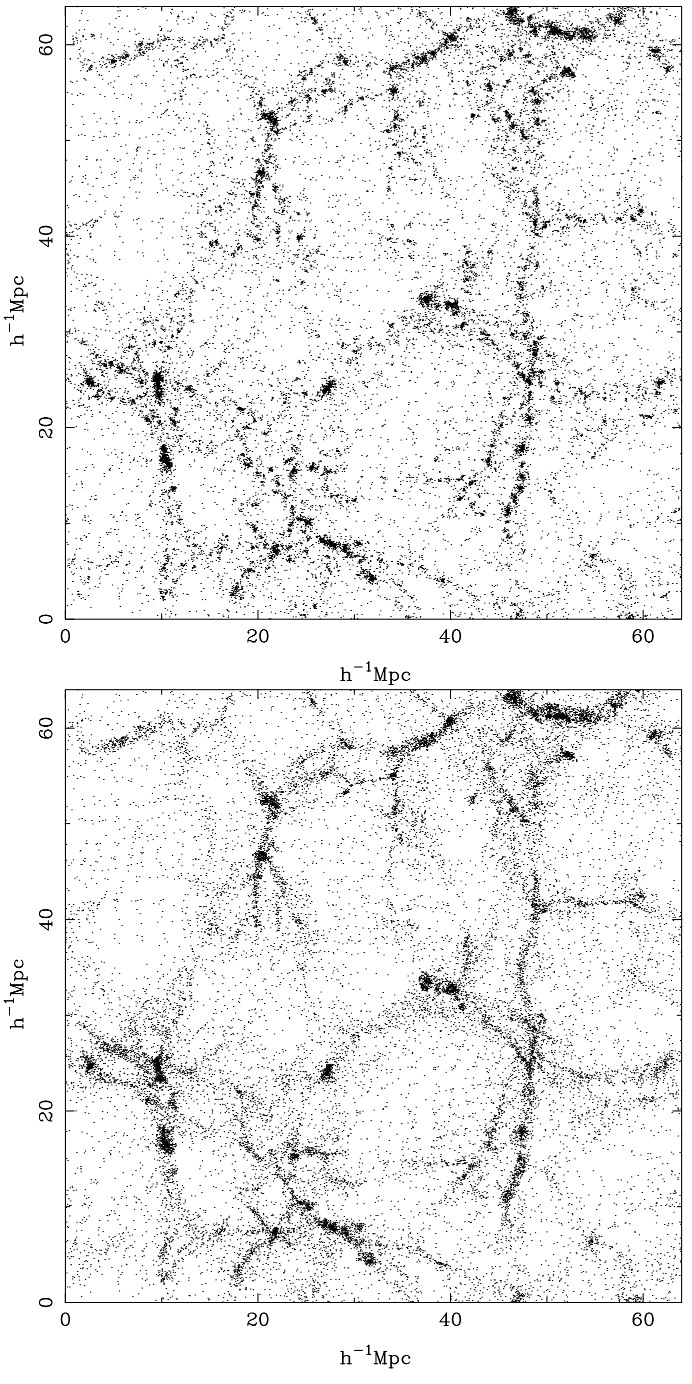

Figure 3. This figure shows a slice from a simulation of the sCDM model. The top panel shows the slice from the TreePM simulation. For comparison, we have included the same slice from a PM simulation of the same initial conditions in the lower panel. The large scale structures are the same in the two but there are significant differences at small scales. The halos are much more compact in the TreePM simulation, and large halos show more substructure. This is to be expected because of the superior resolution of the TreePM code.

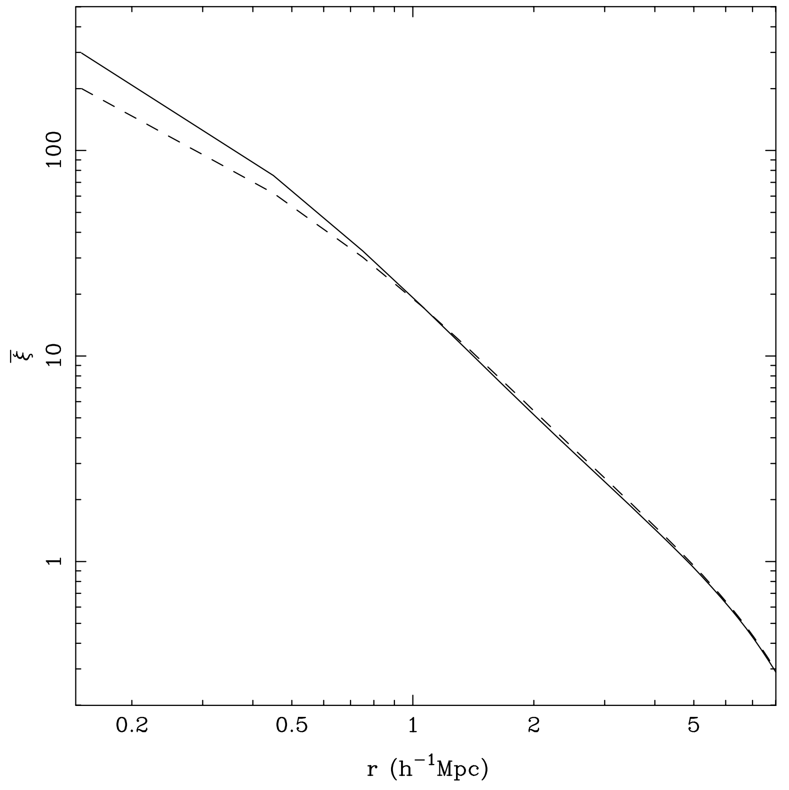

Figure 4. This figure shows the averaged correlation function $\bar{\xi}(r)$ as a function of scale. The thick line shows this quantity for the TreePM simulations and the dashed line shows the same for the PM simulation. These two match at large scales but the PM simulation underestimates the clustering at small scales.

the correlation function in the TreePM simulation matches with that from the PM simulation at large scales, but at small scales, the TreePM simulation has a higher correlation function.

We have checked the accuracy of evolution by checking the rate of growth for the correlation function in the linear regime and also by looking for scale invariance of the correlation function for power law models. For more details please see Bagla & Ray (2002).

4. Computational resources

In this section, we describe the computational resources required for the present implementation of the TreePM code. Given that we have combined the tree and the PM code, the memory requirement is obviously greater than that for either one code. We need four arrays for the PM part, the potential and the force. The rest is exactly the same as a standard Barnes & Hut tree code. With efficient memory management, we need less than 160 MB of RAM for a simulation with 128^3 particles in a 128^3 mesh for most part. In the absence of memory management, this requirement can go up to

Table 1. Time taken by the code, per time step per particle. Column 1 lists the number of particles. Columns 2, 3, 4 and 5 list the time taken (per time step per particle) by the TreePM code for an unclustered and a clustered particle distribution. Column 6 lists the same number for a tree code for an unclustered distribution of particles. All the times are in milli seconds.

N_{particle}	Time (ms)	Time (ms)	Time (ms)	Time (ms)	Time
	TreePM unclustered P-4	TreePM unclustered PIII	TreePM unclustered Alpha	TreePM clustered Alpha	tree unclustered Alpha
32768			0.57	0.59	2.94
262144			0.78	0.80	3.75
2097152	0.34	0.89	1.22	1.28	6.03

250 MB. These are the numbers for floating point numbers, if we use double precision variables then this requirement goes up by a factor of two.

Table 1 lists the time required per time step per particle for three values of the number of particles. These were run on a 533MHz Alpha workstation (EV5) and compiled with the native F90 compiler, a 1GHz Pentium III desktop or a 1.6GHz P-4 and compiled with the Intel F90 compiler. Column 1 lists the number of particles and columns 2, 3 and 4 list the time per step per particle for an unclustered distribution. This number increases much slower than the total number of particles, as expected from the theoretical scaling of $O(N \ln N)$.

Column 5 of the table gives the same number for a highly clustered particle distribution, similar in clustering strength to that shown in Fig. 3. Column 6 lists the time per step per particle taken by the tree code for the particle distribution used in column 4. It is clear that the TreePM code is faster than the tree code by a factor of about 4.5. It is also clear that this code performs well even on inexpensive hardware.

The performance of this code can be improved further by including features like individual time steps for particles. It is expected that adding individual time steps will improve the performance by a factor of two or more.

5. Comparison with other methods

Among other codes that try to augment the performance of PM codes are the P^3M (Efstathiou *et al.* 1985; Couchman 1991) codes and the TPM code (Xu 1995). Following subsections compare TreePM with these codes.

5.1 *P^3M and AP^3M*

There are two main differences between the P^3M codes (Efstathiou *et al.* 1985; Couchman 1991) and the TreePM code presented here. One is that most P^3M codes use the natural cutoff provided by the grid for the long range force, i.e., these take the PM force to be the long range force. Hence errors in the PM force are present in the P^3M force. In contrast, the TreePM code uses an explicit cutoff that allows us to limit errors near the grid scale.

The second difference is in terms of the time taken for adding the short range correction as a function of clustering. In both instances, the short range force is added for particles within a fixed radius r_{cut}. This process is of order $O(Nnr_{\mathrm{cut}}^3(1+\bar{\xi}(r_{\mathrm{cut}})))$ for the P^3M method, where N is the number of particles in the simulation, n is the number density of particles and $\bar{\xi}(r_{\mathrm{cut}})$ is the average number of excess particles around a particle, here excess is measured compared to a homogeneous distribution of particles with the same number density. At early times this reduces to $O(Nnr_{\mathrm{cut}}^3)$, but at late times, when the density field has become highly non-linear ($\bar{\xi}(r_{\mathrm{cut}}) \gg 1$), it becomes $O(Nnr_{\mathrm{cut}}^3\bar{\xi}(r_{\mathrm{cut}}))$. As the density field becomes more and more clumpy, the number of operations required for computing the short range force increases rapidly. This is to be compared with the number of operations required for adding the short range correction in the TreePM code: $O(N\log(nr_{\mathrm{cut}}^3(1+\bar{\xi}(r_{\mathrm{cut}}))))$. The linear and the non-linear limits of this expression are $O(N\log(nr_{\mathrm{cut}}^3))$ and $O(N\log(nr_{\mathrm{cut}}^3\bar{\xi}(r_{\mathrm{cut}})))$, respectively. Thus the variation in the number of operations with increase in clustering is much less for TreePM code than for a P^3M code. The problem is not as severe as outlined for the Adaptive P^3M code (Couchman 1991) but it still persists. Therefore the TreePM code has a clear advantage over the P^3M and AP^3M code for simulations of models where $\bar{\xi}(r_{\mathrm{cut}})$ is very large.

In turn, P^3M codes have one significant advantage over TreePM, these require much less memory. This gives P^3M codes an advantage on small machines and for simulations of models where $\bar{\xi}(r_{\mathrm{cut}})$ is not much larger than unity.

5.2 *TPM*

Before we go into the differences between the TreePM and TPM methods, we would like to summarise the TPM method (Xu 1995) here.

The TPM method is an extension of the P^3M method in that the PM force is taken to be the long range force and a short range force is added to it. Tree method is used for adding the short range correction instead of the particle-particle method. There are some further differences, e.g., correction is added only for particles in high density regions implying that the resolution is non-uniform. At each time step, high density regions are identified and a local tree is constructed in each of these regions for computing the short range correction. Thus, there are two clear differences between the TreePM and the TPM method:

- The TPM code uses the usual PM force to describe the long range component. In contrast, the TreePM code uses an explicit cutoff (r_s).
- TreePM treats all the particles on an equal footing, we compute the short range (equation (5)) and the long range force for each particle. In the TPM code, the short range force is computed only for particles in the high density regions.

6. Discussion

Preceeding sections show that we have developed a new method for doing cosmological N-Body simulations with a clean mathematical model. The model splits force into long and short range forces using a parameter r_s. By choosing this parameter judiciously, in conjunction with two other parameters that arise in the implementation of this model (r_{cut} and θ_c) we can obtain a configuration that matches our requirements for the error budget.

It is possible to devise a more complex scheme for splitting the force into two parts but the one we have chosen seems to be the optimal scheme from the point of view of errors in force calculation as well as CPU time (Bagla and Ray 2002).

Apart from improving control over errors, the TreePM code also leads to a significant gain in speed over the traditional tree code.

TreePM code is also amenable to parallelisation along the lines of (Dubinski 1996), and is likely to scale well because the communication overhead is much more limited. Work in this direction is in progress and will be reported elsewhere (Bagla 2002).

Acknowledgement

I would like to thank Rupert Croft, Lars Hernquist, Suryadeep Ray, Volker Springel and Martin White for insightful comments and discussions. Part of the work reported in this paper was done while the author was at the Harvard-Smithsonian Center for Astrophysics.

References

Bagla, J. S., Padmanabhan, T. 1997, *Pramana – Journal of Physics* **49**, 161.
Bagla, J. S., Ray, S. 2002, (manuscript in preparation).
Bagla, J. S. 2002, To appear in proceedings of *Numerical Simulations in Astrophysics* 2002.
Barnes, J. E. 1990, *J. Comp. Phys.* **87**, 161.
Barnesm, J., Hut, P. 1986, *Nature* **324**, 446.
Bouchet, F. R., Kandrup, H. E. 1985, *ApJ* **299**, 1.
Couchman, H. M. P. 1991, *ApJL* **368**, L23.
Dubinski, J. 1996, *New Astronomy* **1**, 133.
Efstathiou, G., Davis, M., Frenk, C. S., White, S. D. M. 1985, *ApJS* **57**, 241.
Ewald, P. P. 1921, *Ann. Physik* **64**, 253.
Hernquist, L. 1987, *ApJS* **64**, 715.
Hernquist, L., Bouchet, F. R., Suto, Y. 1991, *ApJS* **75**, 231
Hockney, R. W., Eastwood, J. W. 1988, *Computer Simulation using Particles*, (New York: McGraw Hill)
Rybicki, G. B. 1986, in *The Use of Supercomputers in Stellar Dynamics*, (ed.) P. Hut & S. McMillan (Berlin: Springer), p.181
Salmon, J. K., Warren, M. S. 1994, *J. Comp. Phys.* **111**, 136.
Springel, V., Yoshida, N., White, S. D. M. 2001, *New Astronomy* **6**, 79.
White, M., 2000, Private communication.
Xu, G. 1995, *ApJS* **98**, 355.

J. Astrophys. Astr. (2002) **23,** 197–212

Spectral Measurements of Cyg X-3: A Thermal Source Embedded in Hot Plasma within a Cold Shell

R. K. Manchanda *Tata Institute of Fundamental Research, Homi Bhabha Road, Colaba, Mumbai 400 005, India.*
e-mail: ravi@tifr.res.in

Received 2002 August 23; accepted 2002 October 21

Abstract. The attempts at unified model fitting to explain the spectral variations in Cyg X-3 suggest equally probable fits with a combination of an absorbed blackbody and a separately absorbed power law with an exponential cut-off or a composite of absorbed free-free emission with a power law hard X-ray component apart from the iron emission line. These seemingly ordinary but ad hoc mixtures of simple X-ray emission mechanisms have a profound implication about the geometry of the X-ray source. While the first set suggests a black-hole nature of the compact object, the second combination is consistent with a neutron star binary picture. The spectral variability at hard X-ray energies above 30 keV can provide crucial input for the unified picture. In this paper, we present spectral observations of Cyg X-3, made in our on-going survey of galactic and extragalactic X-ray sources in the 20–200 keV energy region, using Large Area Scintillation counter Experiment. The data show a clear power-law photon spectrum of the form $\frac{dN}{dE} \sim E^{-2.8}$ in the 20 to 130 keV energy range. A comparison with earlier data suggests that the total number of X-ray photons in the entire 2–500 keV energy band is conserved at all time for a given luminosity level irrespective of the state. We propose that this behaviour can be explained by a simple geometry in which a thermal X-ray source is embedded in a hot plasma formed by winds from the accretion disk within a cold shell. The high/soft and low/hard X-ray states of the source are simply the manifestation of the extent of the surrounding scattering medium in which the seed photons are Comptonized and hot plasma can be maintained by either the X-ray driven winds or the magneto-centrifugal winds.

Key words. Low mass X-ray binaries—X-ray sources—Cyg X-3.

1. Introduction

Cyg X-3 is not only the most luminous binary system but can be classified as a class unto itself. The emission spectrum of the source extends from radio, infrared, X-ray to GeV gamma ray energies. In the X-ray energy band source exhibits both a 'high' state and a 'low' state with X-ray luminosity of the source varying between 2 and 10×10^{37} ergs s^{-1} for a source distance of 8.5 kpc. A hard X-ray spectrum, a 4.8^{h} period with an asymmetric light curve and quasi-periodic oscillations with a period of few hindered seconds are the key temporal characteristics of the source. The quasi-periodic oscillations seen in the Cyg X-3 have the highest power at periods between 50 and 1500 sec and this is in complete contrast with the observations of other QPO sources where the excess power in the power density spectrum lies in the 1–50 Hz (van der Klis & Jenson 1985; Kitamoto *et al.* 1992). Despite a large number of data obtained since 1968, and the observations of a variety of temporal and spectral features from the source, the true nature of the source geometry and the X-ray emission mechanism still remains unresolved (see review by Bonnet-Bidaud & Chardin 1988; White *et al.* 1992).

In the X-ray band, the main spectral characteristics of the source include a black-body/power law spectrum at low energies attenuated by a large hydrogen column density, a simple power law spectrum above 20 keV (Rao *et al.* 1991; Chitnis *et al.* 1993; Dal Fiume *et al.* 2000) and an emission line feature at 6.5 keV arising from the iron line, which is more predominant during the low/hard state (Kitamoto *et al.* 1994a). The presence of an X-ray halo up to $\sim 2^\circ$ was seen in the Ginga data (Kafuko *et al.* 1994) and recent measurement of the halo with Chandra observatory (Predehl *et al.* 2000) reveal that surface brightness profile in the 5–7 keV and 1–3 keV band extends to a radial distance of 3° and 6° respectively. These data clearly point to the very large amount of surrounding material, which can also lead to build up effects due to multiple Compton scattering. The high resolution spectroscopy in the 1–10 keV using Chandra observatory shows a rich discrete emission line spectrum, which also implies an origin in the photo-ionization driven excitation of the surrounding medium (Paerels *et al.* 2000).

Cyg X-3 is not visible in the optical and UV band, probably due to its position in the galactic plane, but is clearly seen in the infrared band above 1 μm and shows clear 4.8^h binary modulation. Near simultaneous measurements in the IR and X-ray band with UKRIT and OSSE data show a fair degree of similarity in the binary light curve, thereby suggesting generic relations between the two (van Kerkwijk 1993; Matz *et al.* 1996). The source is also bright at the millimeter and centimeter wavelength and on occasions exhibits giant radio flares accompanied with relativistic outflow with velocity 0.3 c (Newell *et al.* 1998). At higher gamma ray energies there is no credible detection of the flux between 35 and 1000 MeV (Mori *et al.* 1997). Positive detection of sources in the TeV and PeV energy bands have been reported on several occasions, however, data were never confirmed in subsequent searches. Similarly, claims have been presented for the detection of 12.59 msec pulsation from the source at energies above $E > 100$ TeV however, no pulsation was observed in later attempts (Chadwick *et al.* 1985; Bhat *et al.* 1988; Chardin & Gerbier 1989; Rannot *et al.* 1994).

The 4.8^h period of the non-eclipsing light curve is typical of the low mass X-ray binaries. The observations of the Doppler shift in the He and N lines in the infrared spectrum of the companion suggest that the primary component is a Wolf Rayet star (van Kerkwijk *et al.* 1992, 1996). If the proposed association of Cyg X-3 with the Wolf-Rayet star is true, then Cyg X-3 is the shortest period binary among the known High Mass Binary Systems. A phase-on system geometry of the binary is inferred from the absence of 4.8^h modulation in the radio jets (Ogley *et al.* 2001). The true nature of the compact object in Cyg X-3 is however still unresolved. The system is generally believed to be a neutron star even though possibility of a black hole candidate has been discussed in literature (Schmutz *et al.* 1996; Ergam & Yungelson 1998).

2. Payload and the observations

The balloon-borne payload consists of an X-ray telescope made up of three modules of scintillation detectors having both passive and active shielding and fitted on a fully steerable alt-azimuth mount. Each of the detector modules has a geometrical area of 400 cm^2 and the thickness of the prime detector is 4 mm. Since the sensitivity limit in a scintillation counter mainly arises from the detector background generated by Compton scattering of high energy photons, the detector modules are a specially designed combination of thin and thick large area NaI(Tl) scintillation counters arranged in back to back geometry (Manchanda 1998). The 3σ sensitivity of the LASE telescope in the entire energy range up to 200 keV is $\sim 1 \times 10^{-6}\,\mathrm{cm^{-2}s^{-1}keV^{-1}}$ for a source observation of 10^4 sec. The response matrix of each detector is constructed from the pre flight calibration of the detectors at different X-ray line energies using a variety of radioactive sources Am^{241}, Ba^{133}, Cd^{109}. To calibrate the high energy end of chosen energy range, we used highly accurate 'divide by two' attenuators in the detector outputs and observed the 300 keV and 357 keV lines from Ba^{133}. The field of view of each module is $4.5^o \times 4.5^o$ and is defined by demountable mechanical slat collimator specially designed with a sandwiched material of Lead, Tin and Copper effective up to 250 keV. Each module along with its collimator is further encased with a passive shield. Each detector is designed as a stand-alone unit with independent on-board subsystems for HV power and data processing. LASE payload is fully automatic with an on-board star tracker and requires no ground control during the flight. The details of the detector design, associated electronics, control subsystems and in-flight behaviour of instrument is presented elsewhere (D'Silva *et al.* 1998).

The balloon flight was launched on 30th March 1997 from Hyderabad, India (cutoff rigidity 16.8 GV) and reached a ceiling altitude of 3.3 mbs. Two detector modules were used for source observations during this flight. A number of X-ray sources Her X-1, GR 1744-28, GS 1843 + 00, GRS 1905 + 105, Cyg X-1 and Cyg X-3 were observed during the experiment. Cyg X-3 was in the field of view of the two detectors for a total period of 50 minutes during 0430 to 0530 UT. The background was derived from two observations of a blank field before and after the source pointing. The present observation of the source corresponds to MJD 50536.2 and corresponds to the binary phase of $\phi \sim 0.7376$ using the ephemeris of $T_o = \mathrm{JD}\ 2440\,949.896 \pm .0009$ and $P_0 = .19968354 \pm 1.5 \times 10^{-7}$ d.

3. Results and discussion

A total excess of 30,000 photons due to Cyg X-3 was obtained in the two detectors during the entire observations and corresponds to a combined statistical significance of 60σ in the 20–165 keV energy band. The source contribution was divided in 12 energy bins and corrected for the atmospheric absorption of 3.3 mbs. corresponding to the altitude, window transmission, detection efficiency and the energy resolution of each detector. An additional correction of 10% due to the systematic effects was applied to data below 26 keV. The combined deconvolved hard X-ray spectrum of the source is shown in Fig. 1. It is seen from that, that the entire data can be fitted to a single power law of the form $\frac{dN}{dE} = KE^{-\alpha}\ \mathrm{ph\ cm^{-2}s^{-1}keV^{-1}}$. The best fit model parameters for a single power law are; $K = 16.3 \pm 1.6$ and $\alpha = -2.74 \pm 0.13$ for $\chi^2 \sim 0.17$ per degree

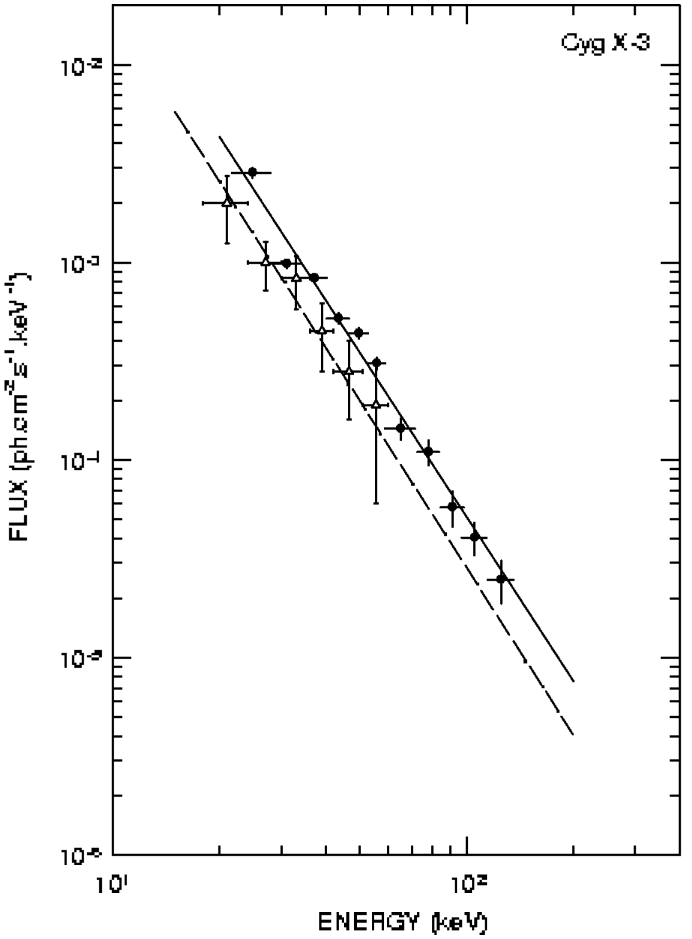

Figure 1. Hard X-ray spectra of Cyg X-3. Solid line represents the best fit to the data. The data of Rao *et al.* (1991) is shown for comparison (Δ).

of freedom. In Fig. 1, we have also plotted the phase averaged spectral data points of Cyg X-3 obtained by Rao *et al.* (1991) using a xenon filled proportional counter telescope for comparison and their best fit spectral shape $11.3\,E^{-2.8}$ (dotted line). It is clear from the figure that two data sets are in complete agreement in spectral shape and with a small change in magnitude representing the activity level of the source on the corresponding epoch. The estimated luminosity of the source in 20–200 band corresponding to our observations is 2×10^{37} ergs/sec, assuming a source distance of 10 kpc.

The arrival time of each accepted event, from any of the detector modules in the LASE payload is time-tagged with an accuracy of 25 μsec relative to the telemetry frame sync using UT time reference. For the analysis of timing properties of the Cyg X-3, we computed the arrival time of each photon and searched for the coherent pulsed emission at 12.6 msec once reported from the UHE data using XRONOS folding routine. Search was made between 11 and 13 msec using 100 steps. The data from two detectors were analyzed independently and co-added. No statistical

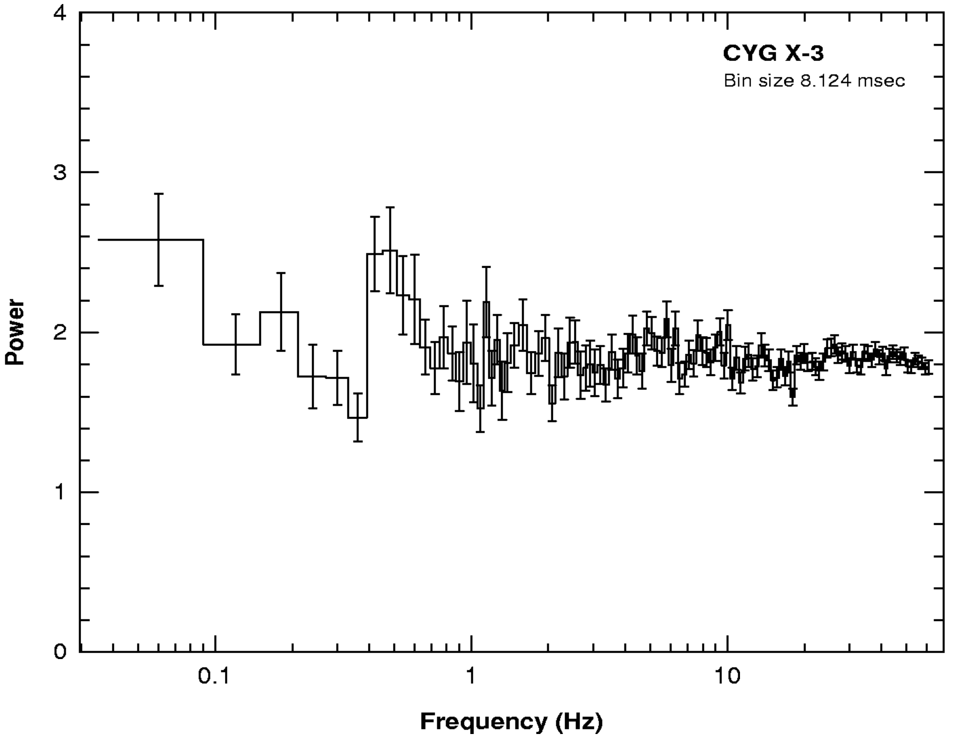

Figure 2. Power density spectrum using FTOOLS.

significant peak was found around the pulsar period of 12.57 msec. Similarly to search for the 121 sec transient period, we binned the data in 1 sec intervals and used the folding routine. Once again no clear single peak with large residual power was seen in the data. To look for the high frequency Quasi-periodic oscillations in our data, we rebinned the data with 8.1 msec resolution and reanalyzed the observed photons using FTOOLS. The power density spectrum is shown in Fig. 2. It is clear from the figure that there is no evidence of any dominant frequency in our data, however, a feature at 0.5 Hz is indicted but its significance is limited due to low statistics.

To determine the activity level of Cyg X-3 corresponding to the spectral and temporal data presented above, we have plotted X-ray light curves of the source taken from the archival data in Fig. 3. The top panel in Fig. 3 shows the X-ray light curve of the source from BATSE data on board CGRO in the 20–120 keV band. The all sky monitor data on-board RXTE in the 2–6 keV band is shown in the bottom panel. The expanded view in each panel is shown in the inset. The arrow in the figures indicates the epoch of the present observation of the source. It is seen from the figure that in the hard X-ray region, Cyg X-3 was close to its normal quiescent phase during the present observations. In the soft X-ray band however, the X-ray emission appears close to a flare like behaviour.

A simple power-law nature of the hard X-ray emission during the quiescent state as seen in Fig. 1, suggests a non-thermal origin for the X-ray photons. The hard X-ray emission in Cyg X-3 is believed to originate in the Inverse Compton scattering process of the low energy photons (Sunyaev & Titarchuk 1980; Liang & Nolan

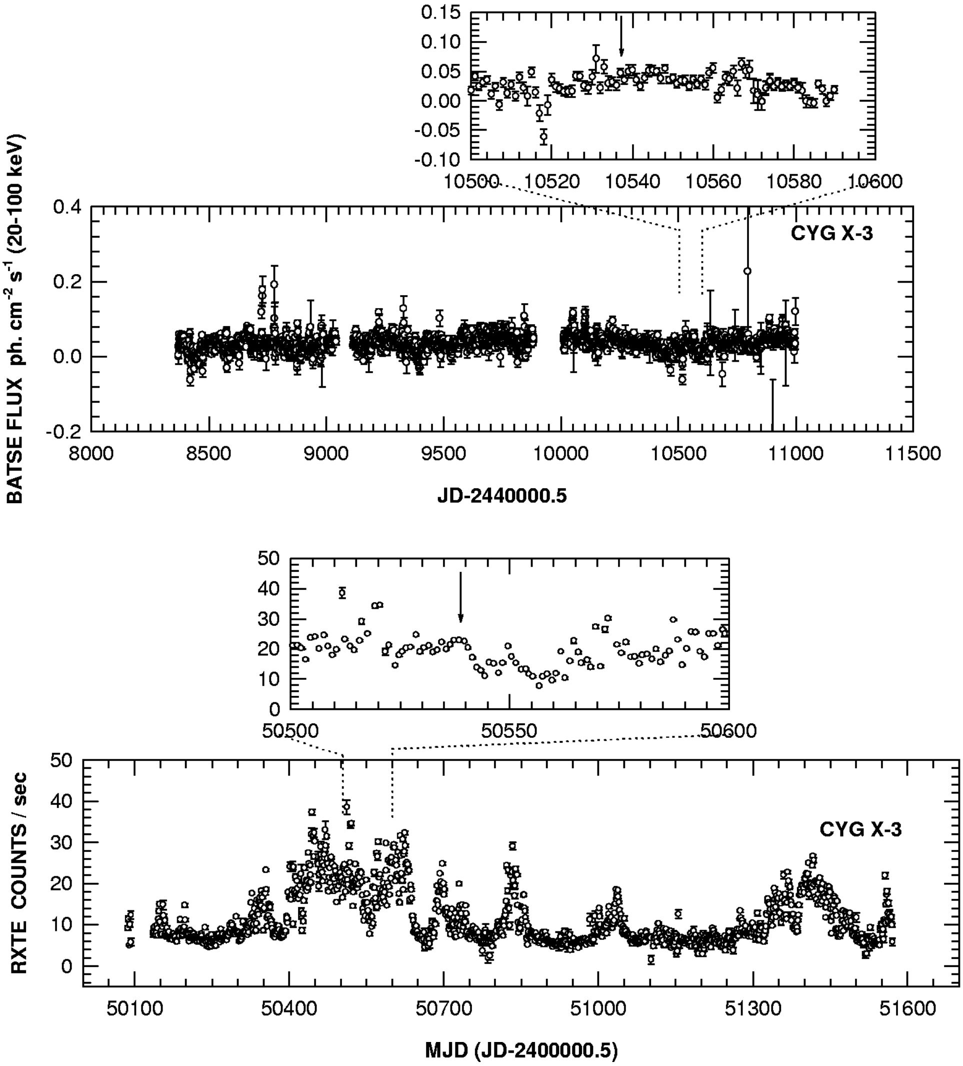

Figure 3. X-ray light curve of Cyg X-3 as seen in BATSE (upper panel) and RXTE data. The arrow indicates the epoch of the present observation.

1984). Comptonization of the low energy photons can provide a natural mechanism for the emission of high energy photons. During Comptonization the seed photons are upgraded in energy and the increase in photon energy on average during each scattering is given by $\frac{\nu'}{\nu} \sim 1 + \frac{4}{3}[\gamma^2 - 1]$. Therefore, multiple scattering even by a Maxwellian electron gas can lead to very high photon energies. But the final spectral shape will be determined by the energy spectrum of the electrons and the seed photons. In such a scenario, the spectral characteristics of the source should differ substantially during the active phase compared with the present observations. In figure 4 we have plotted the hard X-ray spectrum of the source during the flare state seen in OSSE data (Matz *et al.* 1994) and the high state data from HEXE (Maisack *et al.* 1994). The OSSE data correspond to the high state viewing period 7 during August 8–15, 1991 (MJD 48476) just after the major radio flare. The HEXE data corresponds to the observations in May 1988. The dotted line in the figure gives the combined fit to both the data sets. It is seen from the figure that during the flare mode the hard X-ray spectrum of the source continues to be a power law but does have a much steeper spectrum with a spectral index 3.25 ± 0.15.

3.1 *Model geometry*

To arrive at a unified model of the source it is essential that all the observed features of the sources be put in proper perspective. The first attempt in this direction was made by White & Holt (1982) who modeled the observed HEAO-A2 data with a multi-parameter fit arising out of different emission mechanisms. A different set of parameters was obtained by Nakamura *et al.* (1993) while fitting the Ginga data in the 2–30 keV. Rajeev *et al.* (1994) tried to fit a similar model using EXOSAT data along with high energy measurements in the 20–60 keV band (Rao *et al.* 1991). In these models, a one-to-one comparison of the observed spectra has been carried out for data collected at different epochs. The complexity of the model can be judged from the summary of the derived parameters in these models, in which ad hoc emission/absorption features are introduced to improve the χ^2 value of the fit to the data. A functional fit to the observed high energy X-ray spectral data in the extended energy region up to 200 keV is not possible with the derived parameters of these models.

It is also clearly seen from the light curves presented in Fig. 3, that integral luminosity of the source does vary continuously and it is either uncorrelated or at best anti-correlated between the soft and hard X-ray bands. In addition, the source also exhibits asymmetric 4.8^h binary light curve. Therefore, any attempt to construct a unified model by a detailed comparison between different observations not made simultaneously can lead to art-effects. Even the simultaneous observations with different detectors in the broad energy band are prone to systematic effects. For example, the best fitted iron line energy from Ginga data is 6.53 ± 0.03 (Kitamoto *et al.* 1994a) and does not change with the intensity state. For the EXOSAT data the best fit iron line energy peak during high state is 6.95 ± 0.03 (Willingale *et al.* 1985). Similarly, in the case of Ginga data, the estimated value of N_H is the $3 \times 10^{22}\,\mathrm{cm}^{-2}$ and is the same during high and low states, while the derived numbers for EXOSAT data are not only higher by a factor ~ 1.5 but also vary by a factor of 3 between two states of the source (Nakamura *et al.* 1993). The absolute values of different parameters during a multi parameter fit is also a sensitive function of the number of parameters and their weightage factor. Therefore, only global properties can be used to delineate X-ray emission mechanism and the source geometry. In Fig. 5, we have plotted the observed spectral data in the 2–500 keV energy range. The low energy data corresponding to 2–30 keV band is taken from the Ginga observations of Nakamura *et al.* (1993). The data points correspond to both high and low states of the source. The most surprising feature of Fig. 5 is that the spectral index in the hard X-ray region as inferred earlier for the two luminosity states of the source appears to be a natural extension of the low energy data. A careful observation of the data shown in the figure suggests that the integral number of X-ray photons in the entire energy band of 2–500 keV are conserved during the two intensity states for a given activity level of the source. This conclusion leads to very fundamental changes in our understanding of the source geometry.

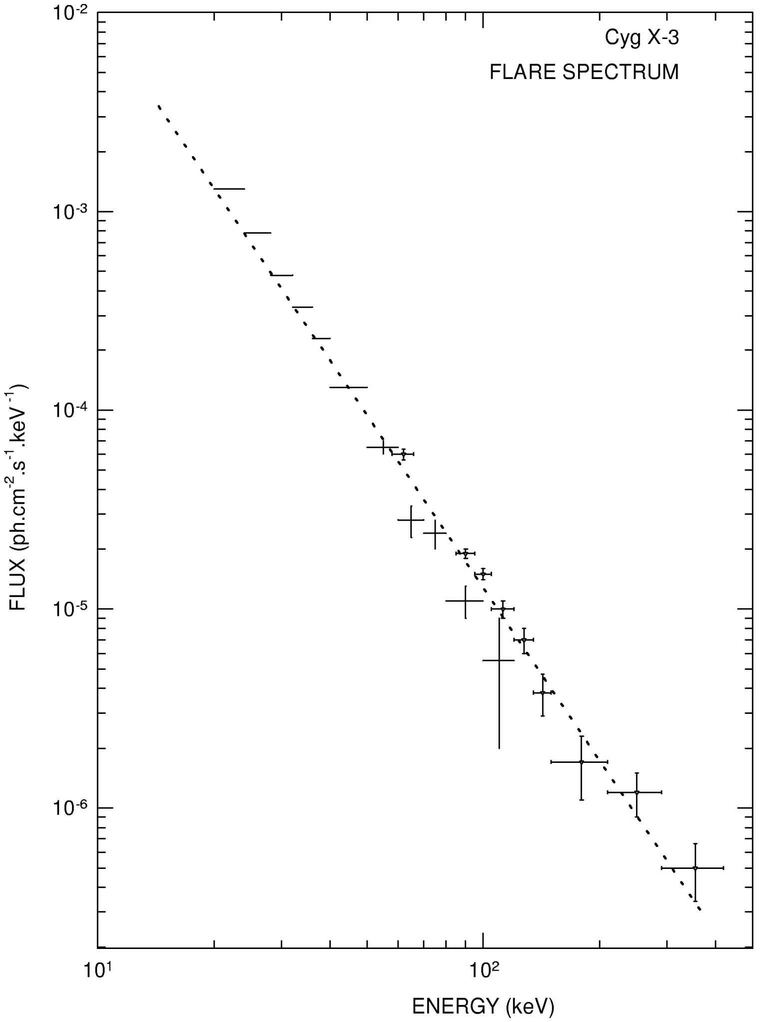

Figure 4. Hard X-ray spectrum of Cyg X-3 during flare period.

The prime factors which determine the X-ray emission mechanism and the accretion geometry of the source do depend to some extent on the nature of the compact object. In the case of a black hole or a low magnetic field neutron star, the X-ray emission is believed to arise in the inner edges of the accretion disk. In the case of a neutron star with strong magnetic field, the photon emission from the hot spot at the polar cap is considered as the most probable cause. The source luminosity and its temporal behaviour at macroscopic scale is a direct result of the variation in the accretion rate. In the standard model for accretion in binary system the transfer of the mass from the primary to the compact object takes place either through the Roche lobe overflow or by the stellar wind. Since the accreting gas will have intrinsic angular momentum, a Keplarian disk will be formed around the compact object and the falling matter releases the gravitation potential energy, which heats the gas and emits radiation. The exact spectral behaviour of the emergent photons will be determined by the accretion geometry, dominant heating and cooling mechanism, optical thickness of the gas in

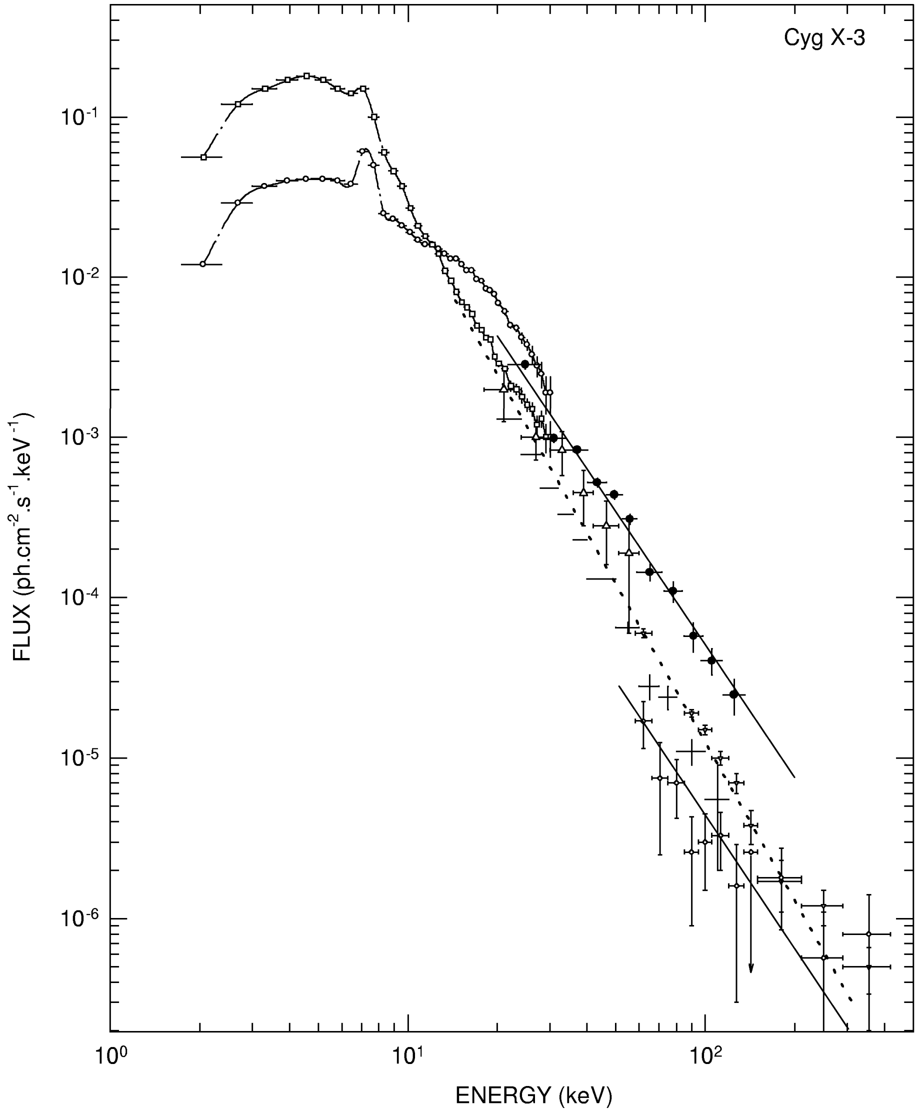

Figure 5. A compilation of the spectral data of Cyg X-3 in the 2–500 keV range. ○ Nakamura *et al.*, △ Rao *et al.*, — — — HEXE, + OSSE, ● Present data. Solid lines represent the best fit power law band corresponding to the different activity levels in quiescent phase.

the emission region, net heating and cooling rates, radiation pressure, magnetic fields and the boundary conditions at large distance as well as stellar surface. (Shapiro & Teukolsky 1983; King 1997). Thus a unified model leading to the emergent spectrum will reflect the dominance of one or more processes in the emission geometry. In the specific case of accretion on to a black hole compact object, the ultrasoft and the soft X-ray excess in the 2–10 keV energy region is expected due to the fact that the main cooling mechanism near to the surface of black hole is almost 100% advection (Chen *et al.* 1997; Narayan & Yi 1994, 1995a, 1995b) and the electron temperature does not rise to very high kT value.

While the long term X-ray variability of the source depends on the rate of accretion coupled to dynamical nature of the companion, the spectral and other temporal features need to be understood in terms of the standard model of accreting neutron star. In the case of Cyg X-3, the model parameters in the low energy region are derived by fitting the observed spectra with a large number of parameters with or without any physical connection to the natural changes expected during the change in the source activity. For example, in their attempt to make a unified fit to 2–30 keV data Nakamura *et al.* (1993) use a 13 parameter fit. The components include, a free-free emission spectrum, a black body spectrum, iron emission line and an ad hoc absorption edge at 9 keV and a variable absorbing medium for the line and continuum. To explain the hard X-ray measurements presented in section 2, it is essential to include further assumptions in these unified models. Even though some of the global features are clearly seen in the composite data shown in Fig. 5, the ensemble of a large number of parameters is too artificial. A simple composite model based on the global properties of the source will provide a natural geometry for the emission region. The observed global features as seen in various figures are summarized in Table 1.

Table 1. Summary of the observed spectral parameters of Cyg X-3.

	High state	Low state
α_1 in hard X-rays	3.25 ± 0.1	2.3 ± 0.1
E_{Fe} [keV]	6.53 ± 0.03	6.53 ± 0.02
EW_{Fe} [keV]	1.1	2
Estimated Compton scattered contribution (1–50 keV) 10^{-9} ergs cm^{-2}s^{-1}	3.8	4.4

We propose that the seed photons and the low energy continuum spectrum of Cyg X-3 is produced in a free-free emission process (Becket *et al.* 1978; Blisset *et al.* 1981) in the 2–500 keV band and the resultant spectrum is further modified by the Comptonization of the low energy photons (Sunyaev & Titarchuck 1980). In a hot tenuous plasma bremsstrahlung and recombination losses are small and the energy exchange between electrons and photons is controlled by the multiple scattering. For $4kT_e > h\nu$, the seed photons are upgraded in energy and a composite power law spectrum emerges due to the superposition of the photons scattered by differing number of times. The spectral index will thus be determined by the average number of scattering per photon. In a non-relativistic plasma where $kT_e \ll m_e c^2$ and $\tau \gg 1$, the average number of scattering for the seed photon $n_s \sim \tau^2$. Clearly the optical depth of the scattering envelope will control the hard X-ray spectrum. We have plotted sample simulated spectra obtained through Comptonization of the low energy photons in weakly relativistic plasma in Fig 6. The curves correspond to two optical depths of $\tau \sim 0.1$ and $\tau \sim 1$ are computed using Monte-Carlo method (Pozdnyakov *et al.* 1983).

It is seen from the figure that an increase in the optical depth of the plasma cloud leads to flattening of the emergent spectrum as well as deficit in the low energy band. The curves are normalized to the observed of Cyg X-3 at 10 keV. Therefore, the observed power law nature of the hard X-ray spectrum and reduction in the low energy photons during the low/hard state of Cyg X-3 can thus be accounted as due to the enlargement of

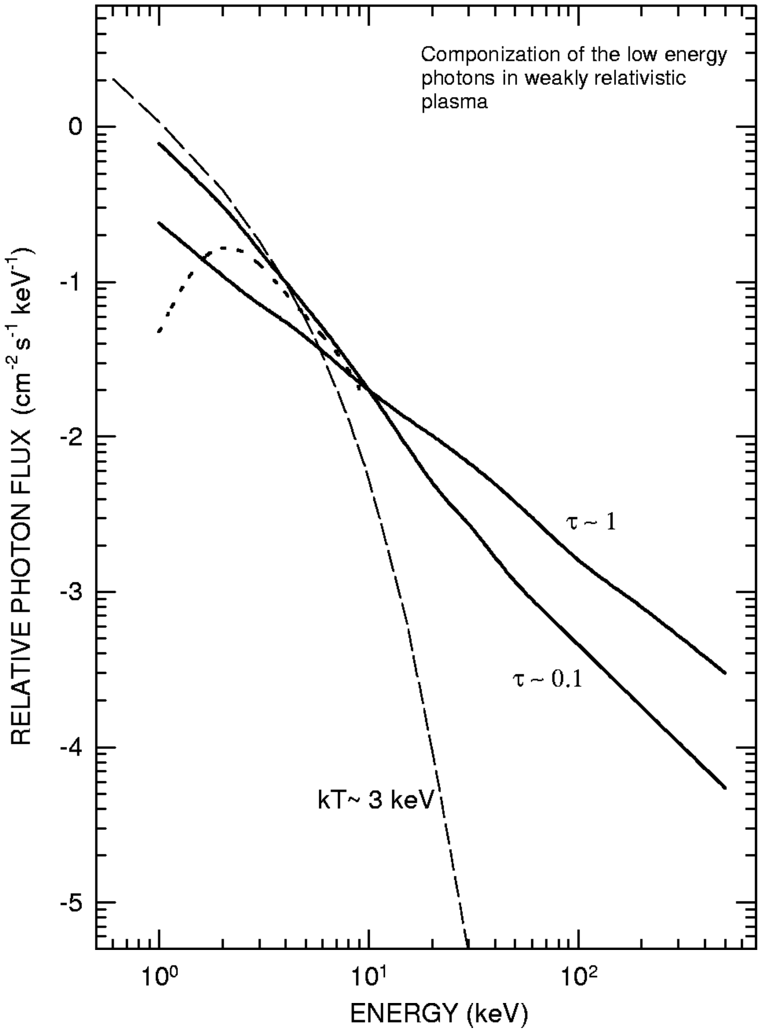

Figure 6. Sample curves for Comptonized low energy photons in a cloud of weekly relativistic plasma for two values of optical depths and differing number of scattering.

the surrounding cloud of relativistic plasma. A lower mean energy of the iron emission line at 6.53 ± 0.02 keV also supports the presence of the hot plasma cloud. In such a model, the flux of 6.5 keV iron emission line will also be proportional to the optical depth of the scattering cloud and the line energy will be independent of the intensity state of the source. Therefore, during the low/hard state, the larger optical depth will lead to the increased equivalent width of the line. The observed data shown in table 1, clearly supports this hypothesis.

In Fig. 6, we have also plotted a free-free emission spectrum with kT $\approx$ 3 keV. The data are normalized at 6 keV. It is seen from the figure that apart from the contribution arising from the iron emission line, a thermal emission from a hot plasma does represent the general spectral behaviour of the source in the low energy band and could provide the necessary seed photons for Comptonization. A non-exponential, gradual

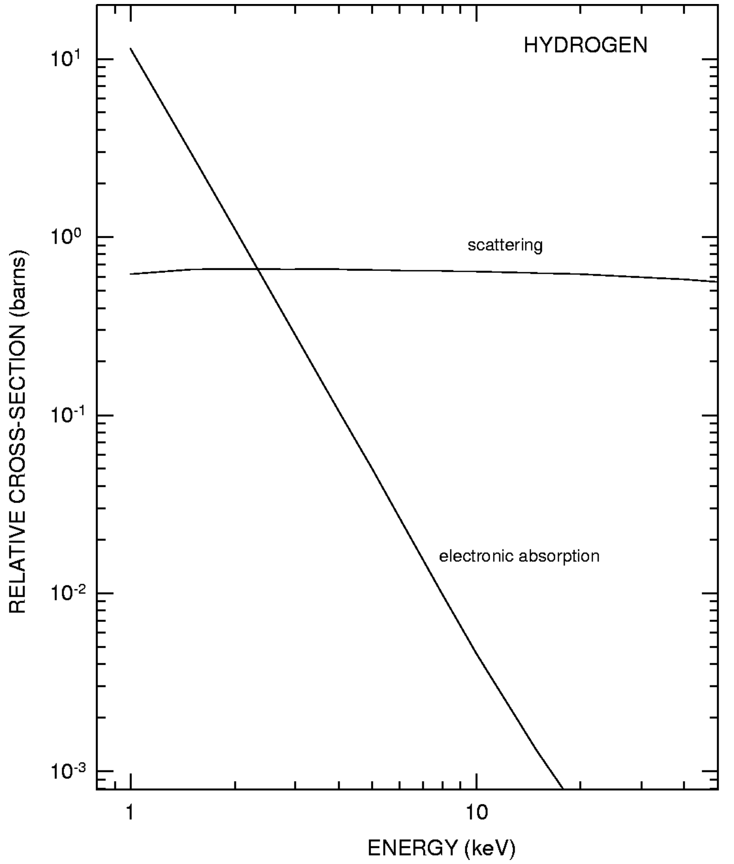

Figure 7. Attenuation cross section vs. photon energy for hydrogen.

turn-around in the observed spectrum below 5 keV as seen in figure 5, can be easily reproduced by a cold hydrogenous shell. The presence of a cold matter around the source is clearly indicated by the asymmetry of the light curve both in the X-ray and infrared bands (Kitamoto *et al.* 1994b). In the case of hydrogen, the electronic absorption cross section for photons is only dominant below 3 keV as shown in Fig. 7. Above 3 keV, photon interactions only lead to degrading the photon energy as opposite to total loss. The shape of resultant spectrum is thus radically modified due to multiple Compton scattering compared to the simple exponential attenuation (Manchanda 1976). In Fig. 6, the dotted line shows the expected low energy behaviour of the spectrum including the build-up effect due to multiple Compton scattering in a cold shell of thickness 0.5 gm.cm^{-2}(3×10^{26}). It is clearly seen from Fig. 6 that computed curves account for the global features in the observed X-ray spectrum of source as seen in Fig. 5.

Two important questions which need to be addressed in support of the proposed model are, the origin and maintenance of the hot plasma cloud surrounding the hot spot and the presence of the cold matter in the line of sight. The two mechanisms which easily give rise to the hot plasma cloud are the X-ray driven wind or the winds driven by the poloidal magnetic field. The dynamics of Compton heated winds and coronae that may form above an accretion disk irradiated by an intense X-ray flux at critical and super critical luminosities have been discussed in the literature (Begelman *et al.* 1983; and Jones & Raine 1980). Evidence of an X-ray driven wind was seen in strong optical emission with weak P Cyg profiles early in the outburst of V404 Cygni (Wagner *et al.* 1991). Optically thin thermal bremsstrahlung in the X-ray driven hot wind at $\sim 10^6$ K has been proposed to explain the infrared excess observed from the black-hole transient A0620-00. Similarly the correlated H_α excess to the X-ray luminosity of GX $1+4$ has been explained by the reprocessing of the EUV flux generated from the free-free emission in the wind (Manchanda *et al.* 1995). The observed X-ray luminosity $L_x \approx 10^{37} - 10^{38}$ erg s^{-1} of Cyg X-3 corresponds to a mass accretion rate $\dot{M} \sim 10^{17} - 10^{18}$ g s^{-1}. The radius and temperature of the outer region of the accretion disk formed by this accreted matter are respectively given by

$$R_{\text{disk}} > 3.2 \times 10^3 \dot{M}_{17}^{\frac{2}{3}} r_s \quad \text{and} \quad T_s \sim 2 \times 10^7 \dot{M}_{17}^{\frac{1}{4}} \left(\frac{r}{r_s}\right)^{-\frac{3}{4}}$$

for a neutron of mass 1.4 $M_\odot$ and radius $r_s \sim 10^6$ cm (Shapiro & Teukolsky 1983). For a value of $R_{\text{disk}} \sim 10^{10} - 10^{11}$ cm, the outer layer should radiate at a black body temperature of $T \leq 10^4 - 10^5$ K. The total emissivity due to the wind can be written as;

$$4\pi \int_0^\infty J_\nu d\nu = 1.435 \times 10^{-27} T^{1/2} n_e^2 \text{ erg cm}^{-3} \text{ s}^{-1}.$$

For a temperature $T \sim 10^5$ K the total contribution from the wind is estimated to be $\leq 2 \times 10^{35}$ erg s^{-1} for $n_e^2 V \sim 10^{60}$. Thus the X-ray driven winds can sustain the hot plasma necessary for Compton upgrading of the low energy X-ray photons.

An alternate mechanism which can drive the hot plasma is the wind caused by centrifugal motion of the magnetized plasma in the disk. Presence of transient radio jets for Cyg X-3 have been discussed in literature (Manchanda *et al.* 1993; Mirabel & Rodriguez 1994; Miduszewski *et al.* 1998, 2001). A magneto-centrifugal wind has been discussed as the underlying mechanism for the spurting jets in which the ionized particles within the accretion disk are out along magnetic field lines that ultimately twist into a helical shape along the rotational axes of the disk. Orbital energy from the accretion disk is thus dissipated in propelling the polar jets (Königl A. 1989). Detailed models for the origin of the MHD wind and its collimation into a jet from the surface of Keplarian accretion disks have been discussed in literature (Pelletier & Pudritz 1992; King & Kolb 1999). A geometrical model involving magnetocentrifugal wind is consistent with the episodes of jet ejection observed in Cyg X-3 (Miduszewski *et al.* 1998). The steady state angular momentum equation of an axisymmetric accretion disk threaded by the magnetic field and undergoing viscous stress depends upon the angular momentum of the accreting matter $\rho u_p \Omega r^2$, the ordered magnetic energy density in the disk $\frac{r B_\phi B_p}{4\pi}$ and the viscous torque τ_{visc}. For a dipole field, the B_ϕ is taken as B_z. We propose that poloidal magnetic field in the accretion disk grows on arbitrary time scale depending upon the accretion rate and the development of instabilities in the disk and when sufficiently strong, this component can then drive the magneto-centrifugal wind and even the ejection of a jet. It has been shown that poloidal magnetic flux may be dragged radially inward by the accreting gas until its dissipative escape, driven by the gradient in magnetic pressure limits its growth. Provided that the magnetic field makes an angle of less than 60° with the radius vector at the disk in Keplarian motion,

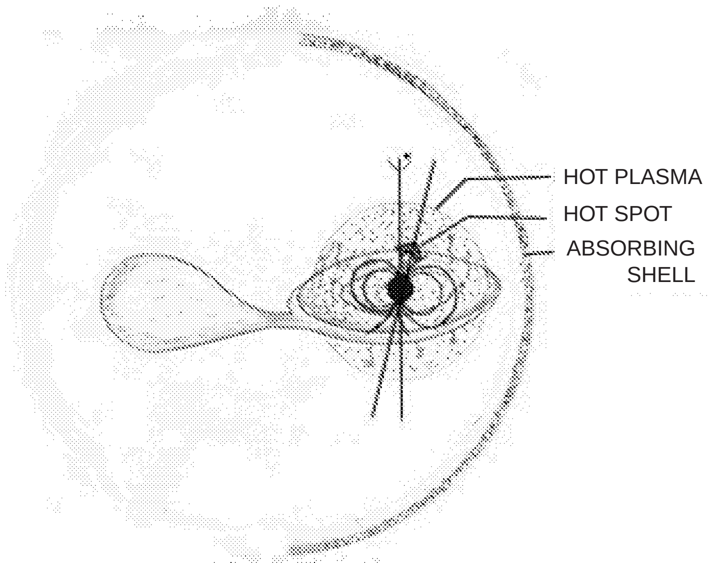

Figure 8. A schematic diagram of the geometrical model.

it will be energetically favorable for gas to leave the disk in a centrifugally driven wind (Blandford 1989; Königl & Ruden 1992).

The origin of the large amount of cold material made of mostly hydrogenous matter in the line sight may be connected with the Wolf-Rayet nature of the companion star. High velocity strong winds are the observed characteristics of WR stars. It is therefore, conceivable that outside the capture radius in a wind-fed geometry, a cold shell may be formed at the interaction boundary of the wind and the primordial hydrogenous material swept by the WR wind.

In summary, a simple thermal source embedded in a relativistic plasma within a cold shell can easily reproduce the observed spectral features of Cyg X-3. The spectral index and the intensity of the iron emission line being dependent on the optical depth of the relativistic cloud. We have made no attempt to derive the set parameters which can fit the observed data shown in Fig. 5 as the observations were made at very different epochs. The absence of the coherent pulsation and the assumption of the neutron star with strong magnetic field giving polar emission considered in our model do not pose any problem. A cartoon picture depicting emission geometry in Cyg X-3 is shown in Fig. 8. It is seen from the figure that in a general case, the value of viewing angle θ, angle of the emission cone α and the angle between the rotation and magnetic axis of the compact object β do control the observance of any pulsation or its shape. The absence of pulsation and the binary modulation in the radio jet in Cyg X-3 suggests that the viewing angle must be $< \beta$ with respect to the rotation axis.

Acknowledgements

I thank Sarvashri J. A. R. D'Silva, P. P. Madhwani, N. V. Bhagat, B. G. Bagade and Ms. N. Kamble for their support in the fabrication of the payload and flight support. I also thank the staff at the TIFR balloon facility, Hyderabad for fabricating the balloon and conducting a successful balloon flight. I also gratefully acknowledge the RXTE and BATSE teams for making their data public on their respective web sites.

References

Becker, R. H., Robinson-Saba, J. L., Boldt, E. A., Holt, S. S., Pravado, S. H., Serlimitsos, P. J., Swank, J. H. 1978, *Ap.J.*, **224**, L113.

Blisset, R. J., Mason, K. J., Culhane, J. L. 1981, *MNRAS*, **194**, 77.

Begelman, M. C., McKee, C. F., Shields, G. A. 1983, *Ap.J.*, **271**, 70.

Bhat, P. N., Ramana Murthy, P. V., Vishwanath, P. R. 1988, *JApA*, **9**, 155.

Blandford, R. D. 1989, In: *Theory of Accretion Disks*, (ed.) P. Meyer, W. Duschl, J. Frank and E. Meyer-Hofmeister (Dordrecht: Kluwer), 35.

Bonnet-Bidaud, J. M., Chardin, G. 1988, *Phys. Rep.*, **170**, 326.

Chadwick, P. M., Dipper, N. A., Dowthwaite, J. C., Gibson, A. I., Harrison, A. B. 1985, *Nature*, **318**, 642.

Chardin, G., Gerbier, G. 1989, *A& A*, **210**, 52.

Chen, X., Abramowicz, M. A., Lasota, J. 1997, *Ap.J.*, **485**, L75.

Chitnis, V. R., Agrawal, P. C., Manchanda, R. K., Rao, A. R. 1993, *BASI*, **21**, 555.

D'Silva, J. A. R., Madhwani, P. P., Tembhurne, N., Manchanda, R. K. 1998, *NIM*, **A412**, 342.

Dal Fiume, D., Palazzi, E., Orlandini, M., Nicastro, L., Del Sordo, S. 2000, *IAUC*, **7393**.

Ergam, E., Youngelson, Lev R. 1998, *A& A*, **333**, 151.

Jones, B. C., Raine, D. J. 1980, *A& A* **81**, 128.

Kitamoto, S., Kawashima, K., Negoro, H., Miyamoto, S., White, N. E., Nagase, F., 1994a, *PASJ*, **46**, L105.

Kitamoto, S., Mizobuchi, S., Yamashita, K., Nakamura, H. 1992, *Ap.J.*, **384**, 263.

Kitamoto, S., Miyamoto, S., Waltman, E. B., Fiedler, R. L., Johnston, K. J., Ghigo, F. D. 1994b, *A& A*, **281**, 85.

Kafuko, S., Yamaguchi, S., Yamaguchi, M., Kawai, N., Matsuoka, M., Koyama, K., Kifune, T. 1994, *MNRAS*, **268**, 437.

King, A. 1997, In: *Accretion Disks - New Aspects*, (Springer-Verlag.) p 356.

King, A. R., Kolb, U. 1999, *MNRAS*, **305**, 654.

Königl, A. 1989, *Ap.J.*, **342**, 208.

Königl, A., Ruden, S. P. 1992, In: *Protostars and Planets III*, (eds) E. H. Levy, & J. I. Lunine, (University of Arizona Press).

Liang, E. P., Nolan, P. L. 1984, *Space Sci. Rev.*, **38**, 353.

Manchanda, R. K. 1976, *IJRSP*, **5**, 13.

Manchanda, R. K. 1998, *Adv. Sp. Res.*, **21**, 1019.

Manchanda, R. K., Waldron, L., Sood, R. K. 1993, *PASAu*, **10**, 208.

Manchanda, R. K., Lawson, W. A., Grey, D. J., Sood, R. K., Sharma, D. P., James S. 1995, *A& A*, **293**, 29.

Mirabel, I. F., Rodriguez, L. F. 1994, *Nature*, **375**, 464.

Mori, M., Bertsch, D. L., Dingus, B. L., Esposito, J. A. *et al.* 1997, *Ap.J.*, **476**, 842.

Matz, S. M., Garabelsky, D. A., Purcell, W. R., Ulmer, *et al. AIP Conference Proceedings* (ed.) S. Holt & S. D. Charles, 1994, **308**, p. 263

Matz, S. M., Fender, R. P., Bell Burnell, S. J., Groove, J. E., Strickman, M. S. 1996, *A& A Suppl.* **120**, 235.

Maisack, M., Kendziorra, E., Pan, H., Skinner, G., Englhauser, J., Reppin, C., Efremov, V., Sunyaev, R. 1994, *Ap J Suppl*, **92**, 473.

Miduszewski, A. J. *et al.* 1998, In: *ASP Conf* (eds.) J. A. Zeusus, G. B. Taylor & J. M. Wrobel, **144**.

Miduszewski, A. J., Rupen, M. P., Hjellming, R. M., Pooley, G. G., Waltman, E. B. 2001, *Ap.J.*, **533**, 766.

Newell, S. J., Garrett, M. A., Spencer, R. E. 1998, *MNRAS*, **293**, L17.

Nakamura, H., Matsuoka, M., Kawai, N., Yosihada, A., Miyoshi, S., Kitamoto, S., Yamashita, K. 1993, *MNRAS*, **261**, 353.

Narayan, R., Yi I. 1994, *Ap.J.*, **428**, L13.

Narayan, R., Yi I. 1995a, *Ap.J.*, **444**, 213.
Narayan, R., Yi I. 1995b, *Ap.J.*, **452**, 710.
Ogley, R. N., Bell Burnell, S. J., Spencer, R. E., Newell, S. J. *et al.*, 2001, *MNRAS*, **326**, 349.
Paerels, F., Cottman, J., Sako, M., Liedahl, D. A. *et al.*, 2000, *Ap.J.*, **533**, L135.
Pelletier, G., Pudritz, R. E. 1992, *Ap.J.*, **394**, 117.
Pozdnyakov, L. A., Sobol, I. M., Sunyaev, R. A. 1983, *Space Sci. Rev.*, **2**, 189.
Predehl, P., Burtwitz, V., Paerels, F., Trumper, J. 2000, *A& A*, **357**, L25.
Rajeev, M. R., Chitnis, V. R., Rao, A. R., Singh, K. P. 1994, *Ap.J.*, **424**, 376.
Rannot, R. C., Bhat, C. L., Tickoo, A. K., Sapru, M. L., Senecha, V. K., Kaul, V. K. 1994, *Ap& SS*, **219**, 221.
Rao, A. R., Agrawal, P. C., Manchanda, 1991, *A& A*, **241**, 127.
Schmutz, W, Gebelle, T. R., Schild, H. 1996, *A& A*, **311**, L25.
Shapiro, S. L., Teukolsky, S. A. 1983, In: *Black holes, White dwarfs & Neutron stars*, (John Wiley & Sons).
Sunyaev, R. A., Titarchuk, L. G. 1980, *A& A*, **86**, 121.
van Kerkwijk, M. H., Charles, P. A., Gebelle, T. R. *et al.* 1992, *Nature*, **355**, 703.
Van Kerkwijk, M. H. 1993, *A& A*, **276**, L9.
Van Kerkwijk, M. H., Gebelle, T. R., King, D. L., van der Klis, van Paradijs, 1996, *A& A*, **314**, 521.
van der Klis, M., Jensen, F. A. 1985, *Nature*, **313**, 768.
Wagner, R. M., Bertram, R., Starrfield, Sumner G., Howell, Steve B., Kreidl, Tobias J., Bus, S. J., Cassatella, A., Fried, R., 1991, *Ap.J.*, **378**, 293.
White, N. E., Holt, S. S. 1982, *Ap.J.*, **257**, 318.
White, N. E., Nagase, F., Parmar, A. N. 1992, In: *X-ray Binaries*, (ed.) Lewin, Paradijs & van den Heuvel (Cambridge. Univ. Press), 1.
Willingale, R., King, A. R., Pounds, K. A. 1985, *MNRAS*, **215**, 295.

J. Astrophys. Astr. (2002) **23,** 213–233

Fast Transition between High-soft and Low-soft States in GRS 1915 + 105: Evidence for a Critically Viscous Accretion Flow

S. Naik[1], A. R. Rao[1] & Sandip K. Chakrabarti[2]

[1] *Tata Institute of Fundamental Research, Homi Bhabha Road, Mumbai, 400 005, India.*
[2] *S. N. Bose National Center for Basic Sciences, Salt Lake, Calcutta, 700 091, India.*

Abstract. We present the results of a detailed analysis of RXTE observations of class ω (Klein-Wolt *et al.* 2002) which show an unusual state transition between high-soft and low-soft states in the Galactic microquasar GRS 1915 + 105. Out of about 600 pointed RXTE observations, the source was found to exhibit such state transition only on 16 occasions. An examination of the RXTE/ASM data in conjunction with the pointed observations reveals that these events appeared as a series of quasi-regular dips in two stretches of long duration (about 20 days during each occasion) when hard X-ray and radio flux were very low. The X-ray light curve and colour-colour diagram of the source during these observations are found to be different from any reported so far. The duration of these dips is found to be of the order of a few tens of seconds with a repetition time of a few hundred seconds. The transition between these dips and non-dips which differ in intensity by a factor of $\sim$ 3.5, is observed to be very fast ($\sim$ a few seconds). It is observed that the low-frequency narrow QPOs are absent in the power density spectrum (PDS) of the dip and non-dip regions of class ω and the PDS is a power law in the 0.1 – 10 Hz frequency range. There is a remarkable similarity in the spectral and timing properties of the source during the dip and non-dip regions in this set of observations. These properties of the source are distinctly different from those seen in the observations of other classes. This indicates that the basic accretion disk structure during both dip and non-dip regions of class ω is similar, but differ only in intensity. To explain these observations, we invoke a model in which the viscosity is very close to critical viscosity and the shock wave is weak or absent.

Key words. Accretion, accretion discs — binaries: close — black hole physics — stars: individual: GRS 1915 + 105 — X-rays: stars

1. Introduction

The Galactic microquasar GRS 1915 + 105 was discovered in 1992 with the WATCH instrument on-board the GRANAT satellite (Castro-Tirado *et al.* 1992). Subsequent radio observations led to the identification of a superluminal radio source at a distance of 12.5 $\pm$ 1.5 kpc ejecting plasma clouds at $v \sim 0.92c$ (Mirabel & Rodriguez 1994). Since the discovery, the source has been very bright in X-rays, emitting at a luminosity of more than 10^{39} erg s^{-1} for extended periods. It exhibits peculiar types of X-ray variability characteristics (Greiner *et al.* 1996) which have been interpreted as the instabilities in the inner accretion disk leading to the infall of matter into the compact object (Belloni *et al.* 1997). Strong variability is observed in X-ray, radio and infrared over a wide range of time scales. Observations with the Burst and Transient Source Experiment (BATSE) on the *Compton Gamma Ray Observatory* have revealed the highly variable nature of the source in the hard X-rays. The intensity variations of as much as 3 Crab have been observed on time scales from seconds to days (Muno *et al.* 1999). The X-ray emission is characterized by quasi-periodic oscillations (QPOs) at centroid frequencies in the range of 0.001–67 Hz (Morgan *et al.* 1997). It is found that the intensity dependent narrow QPOs are a characteristic property of the low-hard state (Chen *et al*. 1997). Based on extensive X-ray studies, Muno, Morgan & Remillard (1999) classified the behavior of the source into two distinct states, spectrally hard-state with the presence of narrow QPOs, dominated by a power-law component and the soft-state with the absence of QPOs, dominated by thermal emission. Attempts have been made to connect the observed radio characteristics in GRS $1915+105$ like jets and superluminal motion with the X-ray emission from the accretion disk (Naik & Rao 2000; Naik *et al.* 2001 and references therein). They have interpreted the observed soft dips in the X-ray light curves of the source as the evacuation of matter from the accretion disk and superposition of a series of such dip events produce huge radio flares in the source.

An extensive study of all the publicly available RXTE pointed observations from 1996 January to 1997 December lead to a classification into 12 different classes on the basis of structure of the X-ray light curve and the nature of the colour-colour diagram (Belloni *et al.* 2000). According to this classification, the source variability is restricted into three basic states, a low-hard state with invisible inner accretion disk (C), a high-soft state with visible inner accretion disk (B) and a low-soft state with spectrum similar to the high-soft state and with much less intensity (A). Belloni *et al.* (2000) suggested that the state transition between two canonical states (B and C) takes place through a hint of state A. During the transition between low-hard (C) and high-soft (B) states, the source shows the properties of state A for a duration of about a few seconds. Longer duration (≥ 20 s) of state A (soft-dip) has been observed during the transition from low-hard state to high-soft state in class β (after the spike in the X-ray light curve) and in the observations of class θ when the source exhibits the properties of low-hard state (C) during the non-dip regions. Recently, Klein-Wolt *et al.* (2002) have discovered an unusual state transition between high-soft and low-soft states in the microquasar GRS $1915+105$. This type of transition between two different intensity states was not observed in any other black hole binaries. The low-soft state (state A) is a rare occurrence in Galactic Black hole sources. In GRS $1915+105$ it appears briefly (for a few seconds) during the rapid state transition between states C and B as well as during the soft dips seen during the variability classes β and θ (in the nomenclature of Belloni *et al.* 2000), which are associated with high radio emission (Mirabel *et al.* 1998; Naik & Rao 2000; Naik *et al.* 2001). On rare occasions, long stretches of state A are also seen in this source (the variability class ϕ). Recently, Smith *et al.* (2001) reported a sudden transition from a spectrally hard state to soft state with much lower intensity in GRS $1758-258$. Though transition from low-hard to high-soft states are seen in many Galactic black hole candidate sources, a transition between two different intensity states (high and low) with similar physical parameters of the accretion disk was not observed in GRS $1915+105$ or in any other black hole binaries.

The extremely variable nature of the microquasar GRS 1915 + 105 is restricted within three canonical spectral states A, B, and C. (as described above). The source is observed to be in spectral state C, (low-hard state) for wide time ranges starting from hundreds of seconds to tens of days to a few months whereas the source remains in the spectral state B, (high-soft state) only for a few occasions (Rao *et al.* 2000). These properties are also seen in other Galactic black hole binaries. The broad-band spectra of the source obtained from the observations with the Oriented Scintillation Spectroscopy Experiment (OSSE) aboard the *Compton Gamma Ray Observatory* along with the simultaneous observations with RXTE/PCA during lowest X-ray fluxes (low-hard state C; 1997 May 14 – 20) and highest X-ray fluxes (high-soft state B; 1999 April 21 – 27) are well fitted by Comptonization of disk blackbody photons in a plasma with both electron heating and acceleration (Zdziarski *et al.* 2001). Although the RXTE/PCA observation during 1999 April 21 – 27 is of class γ which is not a pure high-soft state B rather a combination of states A and B, the overall spectrum is dominated by the high-soft state B. During the above period, the hard X-ray photon flux in 20 – 60 keV energy range with BATSE is also found to be very low ($\sim$ 0.03 photons cm^{-2} s^{-1}) which indicates the source spectrum to be soft. On a careful analysis of the RXTE/PCA observations which show high frequency QPO with constant centroid frequency of 67 Hz, arising in the inner accretion disk of the black hole binary (Morgan *et al.* 1997), it is found that these observations are of classes λ, μ, γ. δ with spectral state of high-soft state B. As these properties are associated with the inner accretion disk of the black hole, it is interesting to study the RXTE/PCA observations during the high-soft states with low value of hard X-ray photon flux with BATSE in detail.

In this paper, we present the evidence of fast transitions between two different X-ray intensity states with similar spectral and timing properties in GRS 1915 + 105. A detailed spectral and timing analysis is presented which shows that the low-soft state is very different from the spectral state A seen during other variability classes. We have tried to explain the observed peculiar state transition in GRS 1915 + 105 on the basis of the presence of an accretion disk with critical viscosity which causes the appearance and disappearance of sub-Keplerian flows out of Keplerian matter.

2. Analysis and results

We have made a detailed examination of all the publicly available RXTE pointed observations on GRS 1915 + 105 in conjunction with the continuous monitoring of the source using RXTE/ASM. Based on the X-ray light curve and the hardness ratio, we could identify most of the pointed observations into the 12 variability classes suggested by Belloni *et al.* (2000), and associate the global properties of the source with other characteristics like radio emission (see Naik & Rao 2000). During these investigations a new variability class was found to be occurring during two time intervals, 1999 April 23 – May 08 (MJD 51291–50306) and 1999 August 23 – September 11 (MJD 51410–51432), respectively. This new class which is called as class ω (Klein-Wolt *et al.* 2002), was observed in a total of 16 pointed RXTE observations and is characterized by a series of dips of duration of 20–95 s and repetition rate of 200–600 s.

To compare and contrast the X-ray properties of the source during this new class with other reported classes, we show, in Fig. 1, the X-ray light curve of the source obtained with RXTE/ASM in 1.3 – 12.1 keV energy range (top panel) with the hard X-rays photon flux in 20 – 60 keV energy range (bottom panel). The data for hard

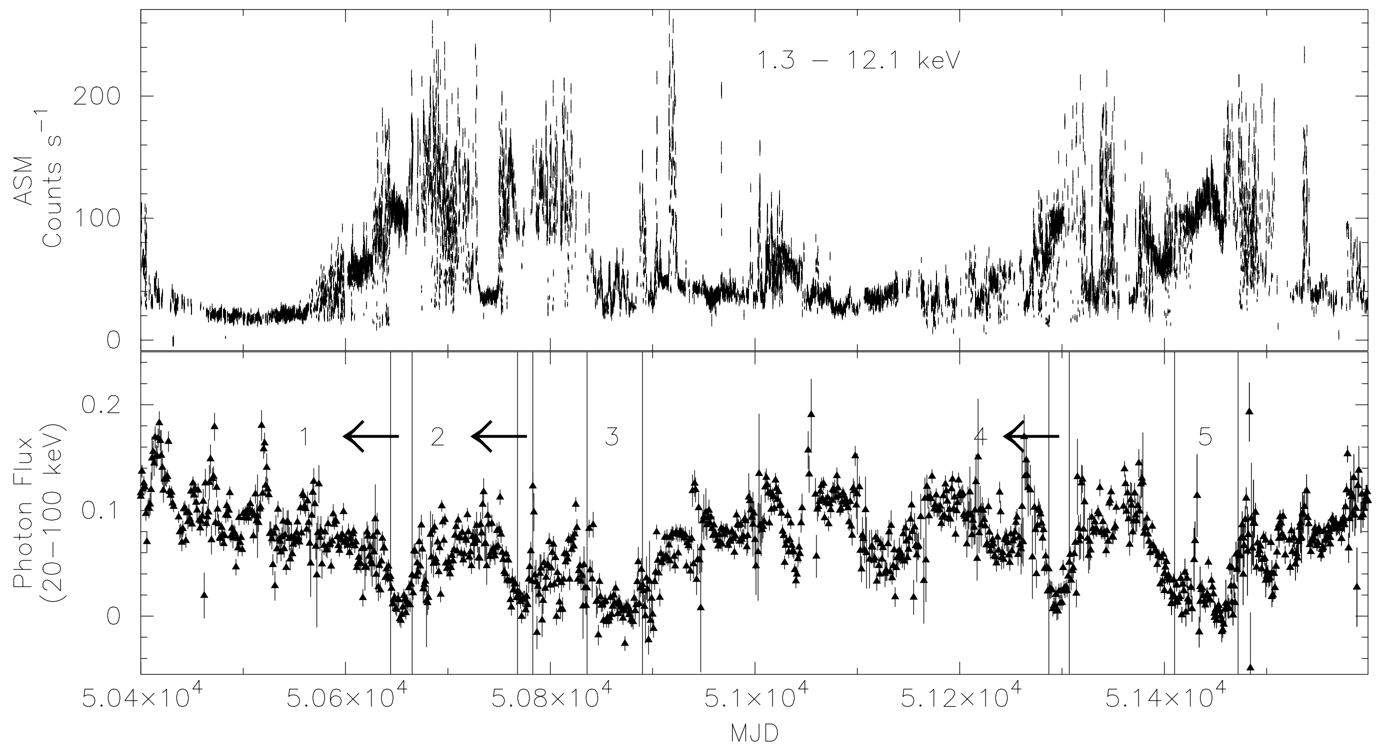

Figure 1. The X-ray light curve for GRS 1915 + 105 with RXTE/ASM in the energy range 1.3 – 12.2 keV is shown in the upper panel with the hard X-ray photon flux in the energy range 20 – 60 keV with BATSE in the bottom panel. The regions (1), (2), (3), (4), and (5) in the bottom panel indicate the presence of the long duration ($\geq$ 10 days) soft-spectral states of the source when the hard X-ray photon flux of the source is $\sim$ 0.03 photons cm^{-2} s^{-1}.

X-rays were taken from the Burst and Transient Source Experiment (BATSE) on the *Compton Gamma Ray Observatory*. We have selected the time range (MJD 50400 – 51600) during which the X-ray (1.3 – 12.1 keV), radio and hard X-ray (20 – 60 keV) data are available. We have selected five regions of durations of more than about 10 days when the hard X-ray photon flux is ~ 0.03 photons cm^{-2} s^{-1}. These regions are marked by vertical lines in the bottom panel of Fig. 1.

To examine the variation in the source flux at different energy bands (X-ray, radio, and hard X-ray photon flux), we have plotted in Fig. 2, the ASM light curve in 1.3 – 12.2 keV energy range (top panel), radio flux density at 2.25 GHz (middle panel), and the hard X-ray photon flux (bottom panel) during above five different regions. The start time of RXTE pointed observations during these five intervals and the class (Belloni *et al.* 2000) to which these observations belong to, are marked in the bottom panel of the figure. The average ASM count rate, average flux density at 2.25 GHz, spectral index and the hard energy photon flux during all these five regions are given in Table 1. From the table, it is observed that the average ASM count rate during first, second and fifth regions are $\sim$ 100 counts s^{-1} and $\sim$ 80 counts s^{-1} during fourth region whereas the count rate is too low ($\sim$ 40 counts s^{-1}) during the third region. It is observed that the rms variation in the source count rate is maximum during the third region. However, the radio flux density at 2.25 GHz and the hard X-ray photon flux are found to be indifferent during all these five intervals. From a careful analysis of the RXTE pointed observations during these five intervals, it is found that the RXTE observations are of class γ (regions 1, 2, and two observations in region 3), class ϕ (region 3), class δ (half of the region 5) and class ω (new class; regions 4 and 5). These observations and the classes are indicated in the bottom panel of Fig. 2. The X-ray light curves of the RXTE pointed observations in 1999 April – May and 1999 August – September (class ω) which show a quasi-regular and distinct transition between two different X-ray intensity states (dip and non-dip) are different from the reported 12 different classes.

Out of about 600 RXTE pointed observations, there are only 16 occasions when the source shows the unusual transition between two different intensity states (class ω). We emphasize here that these 16 observations occur only during two occasions (51290 – 50306 and 51410 – 51433 MJD ranges) when the hard X-ray flux was low (as described above). We have shown, in Fig. 3, the X-ray light curve for one such observation carried out on 1999 April 23 (Obs. ID: 40403-01-07-00). The panel (a) in the figure shows the RXTE/PCA light curve of the source in 2 – 60 keV energy band (normalized to 5 Proportional Counter Units (PCUs)) whereas the panels (b) and (c) show the hardness ratios HR1 (the ratio between the count rate in the energy range 5 – 13 keV to that in 2 – 5 keV) and HR2 (the ratio between the count rates in the energy range 13 – 60 keV and 2 – 13 keV), respectively. In panels (d), (e), and (f), we have shown the source light curves (normalized to 5 PCUs) in 2 – 5 keV, 5 – 13 keV, and 13 – 60 keV energy bands respectively. The average value of source count rate in different energy bands during the dip, non-dip, and the total light curves are given in Table 2 along with the hardness ratios HR1 and HR2. From Fig. 3 and Table 2, it can be seen that the variability in the source flux is low during the dips in all the energy bands. It is, however, observed that the source variability decreases at high energy bands. An intensity difference by a factor of ≥ 3 is observed between the non-dip and dip regions at low energy bands which ~ 2 at hard X-ray bands. This indicates that the change in the source flux during dip and non-dip regions are significant in soft X-

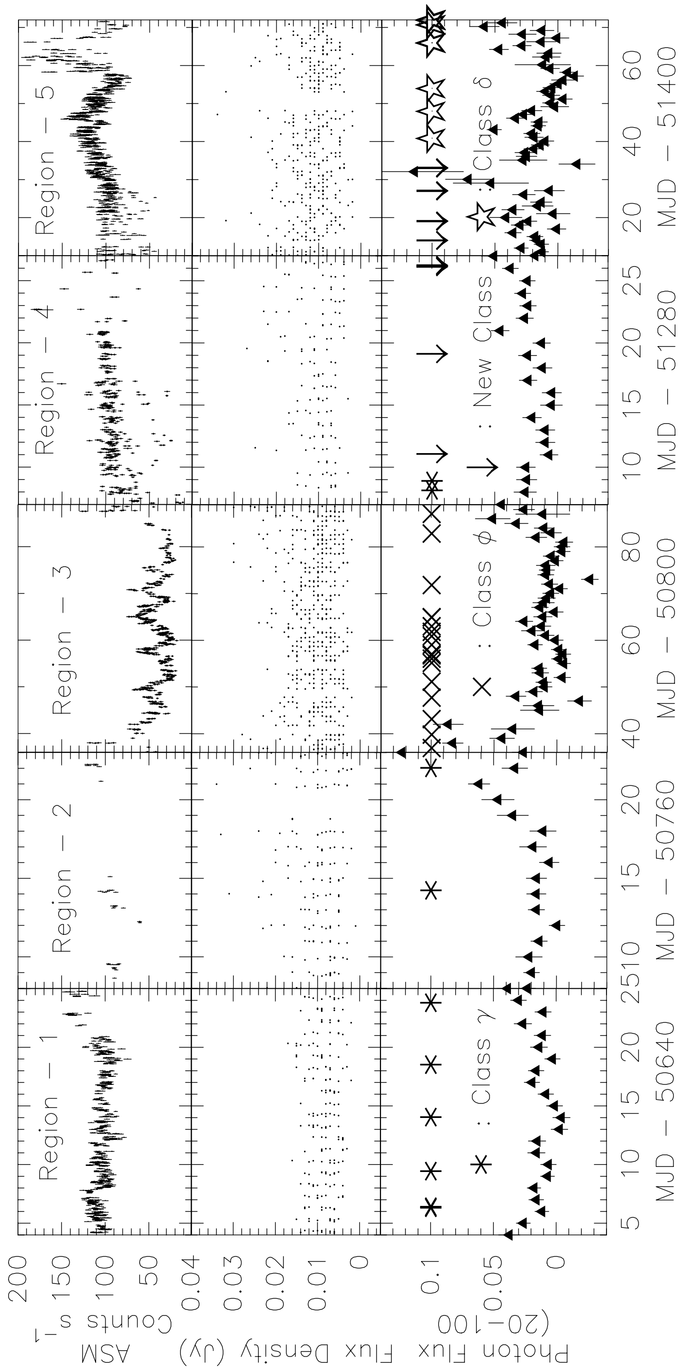

Figure 2. The X-ray light curve for GRS 1915 + 105 with RXTE/ASM in the energy range 1.3–12.2 keV during the 5 different regions marked in Fig. 1 (bottom panel) is shown in the upper panel with the radio flux at 2.25 GHz (second panel) and hard X-ray photon flux in the energy range 20 − 60 keV with BATSE (bottom panel). The start time of RXTE pointed observations during these five intervals are indicated by different markers in the bottom panel of the figure.

Table 1. Statistics of five different regions shown in Fig. 2.

	Region – 1	Region – 2	Region – 3	Region – 4	Region – 5
ASM Count rate[1]	103.4 ± 2.8	91.3 ± 6.7	37.6 ± 7.4	78.9 ± 11.7	102.8 ± 6.5
Flux density[2]	0.009 ± 0.0002	0.011 ± 0.0006	0.011 ± 0.0002	0.011 ± 0.0005	0.011 ± 0.0003
Spectral Index	-0.11 ± 0.05	-0.15 ± 0.06	-0.25 ± 0.03	-0.06 ± 0.06	$+0.07 \pm 0.04$
Photon flux[3]	0.014 ± 0.002	0.022 ± 0.006	0.009 ± 0.003	0.023 ± 0.003	0.018 ± 0.002

[1] The average ASM count rate obtained from the Dwell data and the quoted errors are the rms deviations from the average count rate.
[2] Flux density in mJy at 2.25 GHz.
[3] Hard X-ray flux from BATSE in photons $cm^{-2}\ s^{-1}$.

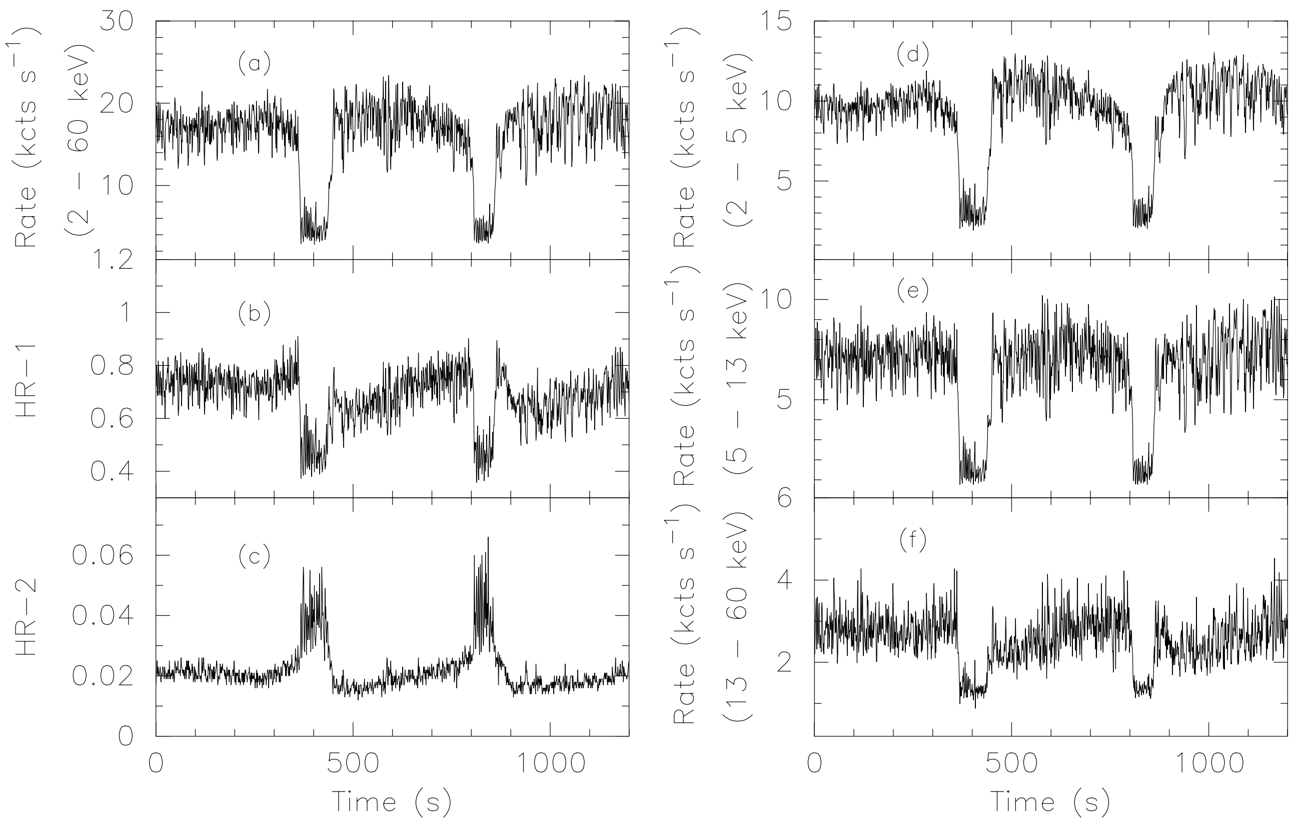

Figure 3. Light curve (2 – 60 keV energy range for 5 PCUs) of GRS 1915 + 105 for the RXTE/PCA pointed observation on 1999 April 23 (new class ω) is shown along with the hardness ratios HR1 (count rate in 5 – 13 keV / count rate in 2 – 5 keV energy range) and HR2 (count rate in 13 – 60 keV / count rate in 2 – 13 keV energy range). The light curves at 2 – 5 keV, 5 – 13 keV, and 13 – 60 keV energy bands are shown in the right panels. Low values of HR1 (≤ 1.0) and HR2 (≤ 0.06) indicate the softness of the spectrum during both the dip and non-dip regions.

Table 2. Statistics of the non-dip and dip regions shown in Fig. 3.

Energy range (in keV)	Average count rate[1] Non-dip region	Dip region	Total (dip and non-dip)	Flux Ratio[2]
$2-5$	9744 ± 46	3171 ± 95	8991 ± 68	3.1 ± 0.1
$5-13$	7147 ± 55	1593 ± 78	6298 ± 57	4.5 ± 0.22
$13-60$	2787 ± 23	1393 ± 29	2511 ± 17	2.0 ± 0.05
$2-60$	17239 ± 101	4938 ± 175	15603 ± 125	3.5 ± 0.13

[1] Average count rate (in counts s^{-1}).
[2] Ratio between the average count rate during the non-dip region to the dip region.

ray bands which decreases significantly in hard X-ray bands. The low intensity dips are characterized by HR1 and HR2 in 0.35 – 0.55 and 0.03 – 0.06 ranges respectively whereas the non-dip regions are characterized by HR1 and HR2 in 0.6 – 0.8 and 0.15 – 0.25 ranges respectively. The observed differences between the hardness ratios HR1 and HR2 during the dip and non-dip regions are not significant enough to highlight the difference in the spectral properties of the source.

The duration of the dips in the light curves of all the 16 RXTE pointed observations of class ω which show the unusual transition between two different intensity states, lies in the time range of 20 – 95 s whereas the non-dip regions last for 200 – 525 s. Although the duration of the dips was high in the beginning of the observations during both the occasions, sparse RXTE pointed observations restrict us to present any statistical picture of the duration and the repetition period of these dips. Figure 3 shows that the HR1 is low during the dips.

To study the timing properties of the source, we have generated the power density spectrum (PDS) in 2 – 13.1 keV energy band for the dip (low intensity state) and non-dip (high intensity state) regions of all 16 selected RXTE/PCA pointed observations. It is found that the low frequency narrow QPOs are absent in the PDS of both dip and non-dip regions of all the observations. We have fitted the PDS of both the dips and non-dip regions with a power-law in frequency ranges 0.1 – 1 Hz and 1 – 10 Hz. It is found that there is no significant difference in the power law index during both the intensity states. The only distinguishing feature of the two intensity states is the higher rms variability in both the frequency bands during the low intensity (dip) state compared to the high intensity (non-dip) state. Figure 4 shows the PDS of the two different regions of the RXTE/PCA pointed observation on 1999 April 23. From the figure, it is found that the PDS during both the regions are a featureless power law in 0.1 – 10 Hz range.

We have attempted a wide band X-ray spectroscopy of the dip and non-dip regions of the RXTE observation of the source on 1999 August 23 (Obs. ID : 40703-01-27-00). The data for the dip region were selected when the source count rate was less than $\leq$ 3000 counts s^{-1} (for 2 PCUs) in 2 – 60 keV energy range and non-dip region when the count rate was $\geq$ 5000 counts s^{-1}. We have generated 128 channel energy spectra from the standard 2 mode of the PCA and 64 channel spectra from HEXTE for the dip and non-dip regions. Standard procedures for data selection, background estimation and response matrix generation have been applied. Systematic error of 2% has been added to the PCA spectral data. We have used the archive mode data from

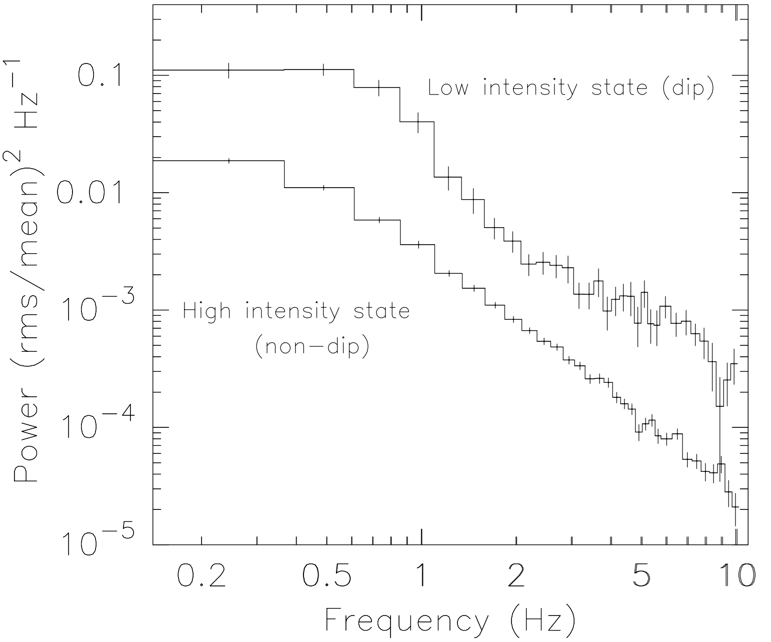

Figure 4. PDS of the source GRS 1915 + 105 in the energy range of 2 – 13 keV for high-soft and low-soft states of the X-ray light curve obtained from RXTE/PCA on 1999 April 23. The absence of the narrow QPO in the frequency range of 0.1 – 10 Hz is clear. The normalized power at a given frequency is high for the low-soft (dip) state and is low for the high-soft state (non-dip).

Cluster 0 of HEXTE for better spectral response. The spectra were re-binned at higher energy band to fewer number of channels in order to improve the statistics. 3 – 50 keV energy range PCA data and 15 – 180 keV energy range HEXTE data are used for spectral fitting. The dip and non-dip spectra are fitted with the standard black hole models (Muno *et al.* 1999) consisting of "disk-blackbody and a thermal-Compton spectrum", "disk-blackbody and a power-law", and "disk-blackbody, a power-law and a thermal-Compton spectrum" with a fixed value of absorption by intervening cold material parameterized as equivalent hydrogen column density, N_H at 6×10^{22} cm^{-2}. From the spectral fitting, it is observed that the model with disk-blackbody, a power-law, and a thermal-Compton spectrum as model components fits very well with the data during both the dip and non-dip regions. It is observed that the source spectrum is similar in hard X-ray energy bands ($\geq$ 50 keV) for both the dip and non-dip regions. The fitted parameters for the best fit model during two different regions along with the 2 – 50 keV source flux for each model components are given in Table 3. Assuming the distance of the source as 12.5 kpc, we have calculated the luminosity of the source in 3 – 60 keV energy band to be $\sim 7.83 \times 10^{38}$ ergs s^{-1} and 2.2×10^{38} ergs s^{-1} for non-dip and dip regions respectively. The parameters in the table show the similarities in the properties of the accretion disk during two different intensity states. From the results of the spectral fitting, we found that the spectrum of the source is soft with similar parameters of the accretion disk during both the different intensity states. We have shown, in Fig. 5, the energy spectra obtained from the RXTE/PCA and HEXTE observations of the source with the fitted model ("disk-blackbody, a power law and a thermal Compton spectrum) during two different intensity states. The upper panel in

Table 3. Spectral parameters during high-soft and low-soft states of class ω of GRS 1915 + 105 for the model "disk-blackbody, a power law and a thermal Compton spectrum".

X-ray intensity state	Reduced χ^2	$kT_{\rm in}^1$ (keV)	kT_e^2 (keV)	Γ_x^3	Inner disk radius (km)	L^4 ergs s^{-1}
High-soft (non-dip)	0.68 (76 dof)	$1.7^{+0.05}_{-0.06}$	$2.5^{+0.13}_{-0.15}$	$2.9^{+0.2}_{-0.97}$	42^{+5}_{-3}	7.83×10^{38}
Low-soft (dip)	0.68 (66 dof)	$1.55^{+0.03}_{-0.05}$	$4.05^{+0.042}_{-0.045}$	$2.03^{+0.1}_{-0.1}$	25^{+6}_{-3}	2.2×10^{38}

$^1kT_{in}$: Inner disk temperature.
^2kT_e : Temperature of the Compton cloud.
$^3\Gamma_x$: Power-law photon index.
^4L : Luminosity of the source in 3 – 60 keV energy range, assuming the distance of the source to be 12.5 kpc.

Fig. 5 shows the the energy spectrum and the best fit model for the non-dip region of class ω whereas the bottom panel shows the spectrum and the fitted model for the dip regions. From the figure, it is observed that the dip and non-dip spectra are dominated by the thermal component.

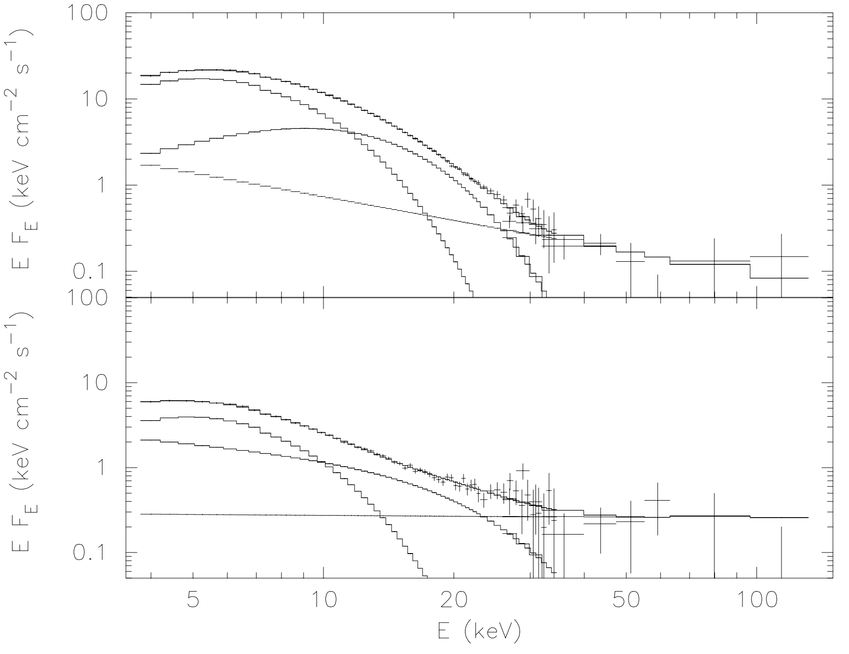

Figure 5. The observed count rate spectrum of GRS 1915 + 105 during high-soft (non-dip) and low-soft (dip) states of the new class ω obtained from RXTE/PCA and HEXTE data. A best-fit model consisting of a disk blackbody, a power-law, and a thermal Compton spectrum is shown as histogram with the data.

In order to investigate the structure of the inner accretion disk during the observed unusual transition between two different intensity states, we have calculated the characteristic radius of the inner disk ($R_{col} = D_{10\,\mathrm{kpc}}\sqrt{N_{bb}/cos\theta}$) from the normalization parameter of the disk blackbody (N_{bb}). Assuming the distance of the source to be 12.5 kpc ($D_{10\,\mathrm{kpc}} = 1.25$), and an inclination angle (θ) equal to that of the radio jets, 70°, the radius of the inner accretion disk is found to be 41 ± 7 km during the non-dip (high intensity state) and 25 ± 3 km during the dip (low intensity state) regions. The temperature of the inner accretion disk during the dip and non-dip regions are found to be 1.54 and 1.72 keV respectively. Using these values, we have estimated the ratio of the total flux from the disk ($F_{bb} = 1.08 \times 10^{11} N_{bb} \sigma T_{col}^4 \mathrm{ergs}^{-1}\mathrm{cm}^{-2}$ s, where σ is the Stephan-Boltzmann constant) during non-dip and dip regions to be ~ 3.9 which is observed from the X-ray light curves. From this analysis, we conclude that the observed transition between the different intensity states is associated with the change in temperature of the inner accretion disk without any change in the radius.

3. Comparison between various spectral states

The spectral and temporal properties of the source were studied by Rao *et al*. (2000) when the source was making a slow transition from a low-hard state (C) to a high-soft state (B) in about three months. Rapid state transitions between the above two canonical spectral states were also observed when the source was exhibiting a series of fast variations, which can be classified as bursts (Rao *et al*. 2000). It was pointed that the spectral and timing properties of the source during the short duration B and C states are identical to those seen during the long duration B and C states. Fast transition between low-hard (C) and low-soft states (A) was also observed when the light curve of the source contains a series of X-ray soft dips (Naik *et al*. 2001). Although Belloni *et al*. (2000) have classified the RXTE/PCA observations of low-hard states into four different sub-classes ($\chi 1$, $\chi 2$, $\chi 3$, and $\chi 4$), there is not much difference in the temporal and spectral properties of the source during the observations of these four sub-classes. During the observations of class ϕ, the source remains in low-soft state (A) whereas during all other classes, it is observed that the source remains in high-soft spectral state (B) or makes transition between the spectral states B and C, and C and A. Although the transition between the spectral states B and A is seen during the observations of a few classes, the duration of the spectral state A is in the order of a few seconds. However, the transition between the states A and B as observed during the observations of class ω where the source remains in state A for a few tens of seconds is different. As both the spectral states A and B are characterized by the soft spectrum with inner accretion disk extending towards the black hole event horizon, the difference in the observed transition between these two states needs a detailed comparison between these three states along with the low-soft state observed during the class ω.

According to the Belloni *et al*. (2000) classification, the source variability ranges from a steady emission for long durations like in classes ϕ, χ to large amplitude variations in classes λ, κ, ρ, α. Short periodic flickering with different amplitudes is seen during the observations of classes γ, μ and δ. During the observations of classes θ, β, and ν, the amplitude variation is accompanied by soft X-ray dips with duration of a few tens of seconds to hundreds of seconds. It is observed that the properties of the source during the observations of class α are similar to those during the combined classes ρ and χ (Naik *et al*. 2002). However, the RXTE pointed observations which

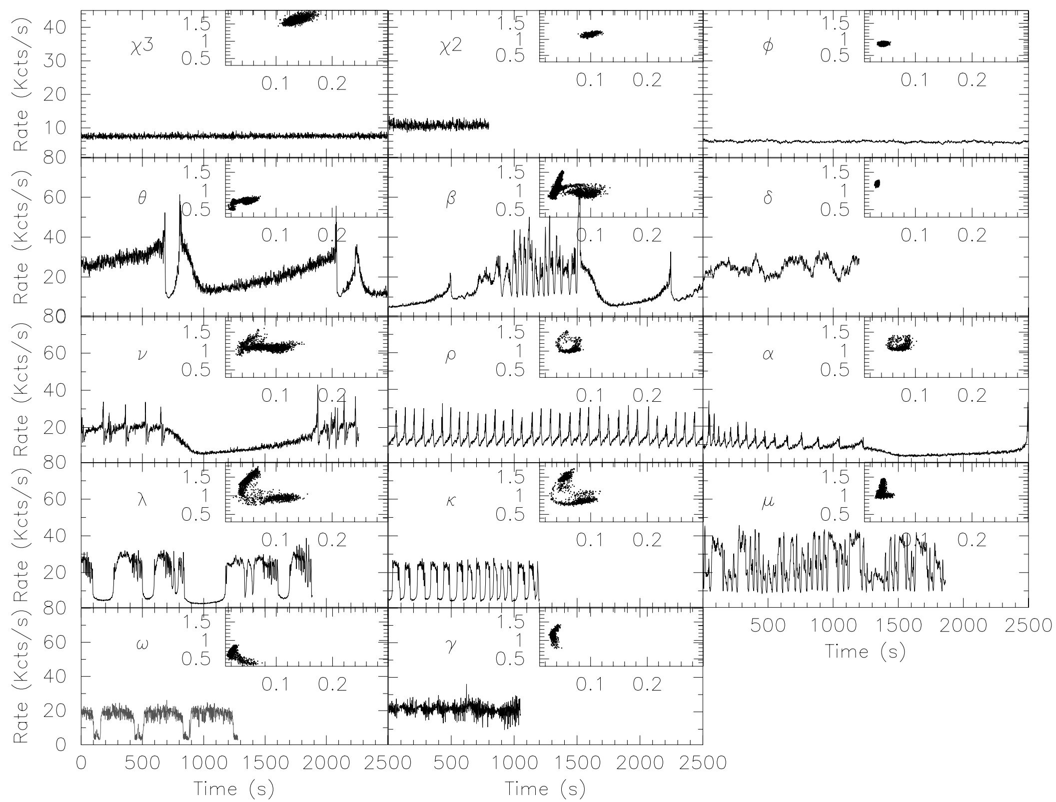

Figure 6. X-ray light curves (2 – 60 keV energy range) and colour-colour diagram (HR1 vs HR2) of GRS 1915 + 105 for observations of all classes (Belloni *et al.* 2000) are shown along with the observation of class ω. The insets in each figure shows the colour-colour diagram, HR1 in the Y-axes and HR2 in the X-axes (see text). The Obs. Ids of the data used are $\chi 3$: 20402-01-50-01, $\chi 2$: 20402-01-04-00, ϕ : 30703-01-08-00, θ : 40702-01-03-00, β : 20402-01-44-00, δ : 20402-01-42-00, ν : 10408-01-41-00, ρ : 20402-01-03-00, α : 20402-01-28-00, λ : 20402-01-37-01, κ : 20402-01-33-00, μ : 20402-01-45-01, ω : 40403-01-07-00, and γ : 20402-01-40-00.

show the unusual transition between two different intensity states (class ω) are found to be different from all the other classes. The absence of strong variability in the X-ray light curve, the presence of soft-dips with similar spectral properties as the non-dip regions prompted to investigate the similarities/differences in the source properties during various low and high intensity states with little variability in the X-ray light curve of the reported 12 different classes of RXTE observations.

We have selected one RXTE observation from all the X-ray classes and, in Fig. 6, we have shown the light curves and colour-colour (HR1 vs HR2) diagram of the selected observations. From the figure, it is observed that observations of classes ϕ, δ and ω are characterized by the absence of strong variability in the light curve with HR1 ≤ 1 and HR2 ≤ 0.06 which indicate the softness of the spectrum of the source. Although the observations of classes $\chi 2$ and $\chi 3$ also show less variability in the X-ray light curves, the spectrum of the source is hard with HR1 ≥ 1 and HR2 ≥ 0.1. Comparing the structure of the light curves and colour-colour diagram of all these observations, it is found that the observations which show the unusual intensity transition (class ω) is different from the observations of other classes. We have examined the uncertainty in the value of HR1 (about 0.3) due to the different gains of PCUs at different epochs. But the general trend in the hardness ratios remain unaffected by the change in gains.

To study the spectral properties of the source during these different classes, we have attempted a wide band X-ray spectroscopy of all the RXTE observations which show a gradual change from a high-soft to low-hard state and characterized by a sharp soft dip with low variability (β and θ) and observations which show steady behavior during the orbit of RXTE ($\chi 2$, $\chi 3$, ϕ, and δ) along with one of the observation showing the unusual state transition (class ω). We have selected the radio-quiet low-hard state of class $\chi 2$, radio-loud low-hard state of class $\chi 3$, and the high-soft (non-dip) state of the observations of class ω. Standard procedures for data selection, background estimation and response matrix generation have been applied. We have used the data in the same energy range such as 3 – 50 keV energy range PCA data and 15 – 180 keV energy HEXTE data for spectral fitting. The spectra of all three different classes of observations are fitted with all the three models which were used for the dip and non-dip regions (described in the previous section). The fitted parameters for different models are given in Table 4. Examining the parameters in the table, it is found that "disk-blackbody and a thermal-Compton spectrum" model is suitable for the radio-quiet low-hard state (class $\chi 2$) and "disk-blackbody, a power-law and a thermal-Compton spectrum" model is suitable for the radio-loud low-hard state (class $\chi 3$) and the high state (non-dip) of the observations which show the unusual transition between two intensity states.

To compare the deviations of the spectral parameters of the source during the various low state observations with the above described three well fitted models for the observations of classes $\chi 2$, $\chi 3$, and the non-dip region of the observation showing the peculiar state transition, we analyzed the source spectrum during various dips observed in other classes of RXTE observations along with a few low variability high-state observations of classes ϕ and δ. We have selected data for the low-hard dip of class β (before the spike in the light curve), low-soft dip of class θ which is identical to the dip observed (after the spike) in the light curve of class β, low-intensity observation of class ϕ and high-soft state of class δ. To investigate the similarities in the spectral properties of the source during the above X-ray observations, we have used

Table 4. Spectral parameters during classes $\chi 2$, $\chi 3$, and ω (non-dip) of GRS 1915+105.

X-ray class	Reduced χ^2	$kT_{\rm in}^1$ (keV)	kT_e^2 (keV)	τ^3	Γ_x^4	Count rate HEXTE	PCA
Model: Disk blackbody + thermal-Compton spectrum							
$\chi 2$ (RQ[5])	1.353	1.348	20.01	3.047	− − −	62.58	4093
$\chi 3$ (RL[6])	8.26	4.068	12.54	4.159	− − −	78.22	4902
ω (High state)	2.035	2.056	4.415	6.489	− − −	71.08	8547
Model: Disk blackbody + power-law							
$\chi 2$ (RQ)	5.313	0.156	− − −	− − −	2.519	− − −	− − −
$\chi 3$ (RL)	33.24	0.156	− − −	− − −	2.636	− − −	− − −
ω (High state)	2.505	2.205	− − −	− − −	3.457	− − −	− − −
Model: Disk blackbody + power-law + thermal-Compton spectrum							
$\chi 2$ (RQ)	1.367	1.349	20.01	3.047	2.52	− − −	− − −
$\chi 3$ (RL)	1.736	2.58	4.464	46.56	2.606	− − −	− − −
ω (High state)	0.68	1.71	2.532	25.42	2.91	− − −	− − −

[1]kT_{in} : Inner disk temperature.
[2]kT_e : Temperature of the Compton cloud.
[3]τ : Optical depth of the Compton cloud.
[4]Γ_x : Power-law photon index.
[5]RQ : Radio-quiet.
[6]RL : Radio-loud.

"disk-blackbody and a thermal-Compton spectrum" and "disk-blackbody, a power-law and a thermal-Compton spectrum" models to fit the spectra. All the spectral parameters other than the normalizations are fixed for the models which are well-fitted with the data during the radio-quiet low-hard state (class $\chi 2$), radio-loud low-hard state (class $\chi 3$) and the high state of the observations of the class ω. The fitted parameters are shown in Table 5. Comparing the fitted parameters in Table 5, it is observed that the model for the high-soft state of class ω fits better with the spectra during the dip of the class ω (marked as A' in Table 5), soft-dip of class θ and the observation of class δ whereas the $\chi 2$ model fits better with the spectrum of the low-hard dip of class β. From the table, it is also noticed that the spectrum of the observation of class ϕ does not fit any of the models and needs more investigations on the spectral properties of the source. We can draw two important conclusions from the spectral analysis:

- the low soft state seen during class ω, though generically can be classified as spectral state A, it is distinctly different from the long duration spectral state A (class ϕ) and short duration A states seen during class θ etc.
- the spectral shape during the low soft state is similar to the high soft state (with the same set of spectral components).

Hence we can conclude that the high-soft and low-soft states of the observations of class ω do not have any significant difference in the physical parameters of the accretion

Table 5. Spectral parameters during various classes of GRS 1915 + 105.

Model[1]	Normalization[2]	ω_{dip}(A[3])	β_{low}(C[4])	θ_{low}(A[4])	ϕ(A[5])	δ(B[6])
$\chi 2$ (RQ[7])	dbb	351.8	118.5	1605	478.4	2511
	co	3.169	7.835	9.259	1.624	5.824
	Reduced χ^2	9.96	2.71	24.09	37.35	173.7
$\chi 3$ (RL[8])	dbb	13.27	3.6673E-10	38.48	9.710	57.77
	co	0.000	4.8426E-33	0.000	0.000	0.000
	po	0.747	13.97	4.314	2.0348E-33	0.000
	Reduced χ^2	53.39	8.41	27.66	108.46	127.3
ω (RQ)	dbb	81.97	4.6E-25	316.2	103.9	316.2
(High state)	co	4.8E-14	7.5E-25	0.068	0.000	6.8E-02
	po	10.0	27.0	28.63	4.790	28.63
	Reduced χ^2	0.84	135.4	2.02	37.23	2.02

[1] : Model $\chi 2$: Model "Disk-blackbody + CompST" with $kT_{in} = 1.348$ keV, $kT_e = 20.01$ and $\tau = 3.047$
Model $\chi 3$: "Disk-blackbody + Power-law + CompST" with $kT_{in} = 2.580$ keV, $kT_e = 4.464$, and $\tau = 46.56$ and $\Gamma = 2.606$
Model ω : "Disk-blackbody + Power-law + CompST" with $kT_{in} = 1.709$ keV, $kT_e = 2.532$ keV and $\tau = 25.42$ and $\Gamma = 2.912$.
[2] : dbb = Disk blackbody normalization, co = thermal-Compton spectrum normalization, and po = power-law normalization.
[3] : Low-soft state of new class.
[4] : Low-hard state.
[5] : Soft state.
[6] : High-soft state.
[7] : Radio-quiet.
[8] : Radio-loud.

disk of the black hole except the normalization factors and hence these two different intensity states are identical in the spectral and temporal properties of the source and different from the observations of any other reported classes.

4. Discussion

The X-ray observation of Galactic black hole candidates reveal four different spectral states such as

- *"X-ray very high"* state with quite high soft X-ray flux and an ultra-soft thermal of multi-color blackbody spectrum of characteristic temperature $kT \sim 1$ keV and a power-law tail with photon-index $\Gamma \sim 2 – 3$ with approximate X-ray luminosity at Eddington limit,
- *"X-ray high, soft"* state with similar characteristic temperature kT and a weak power-law tail but with lower luminosity (by a factor of $\sim 3 – 30$),
- *"X-ray low, hard"* state with a single power-law spectrum with photon-index $\Gamma \sim 1.5 – 2$ with a typical X-ray luminosity of less than 1% of Eddington, and

- *"X-ray off or quiescent"* state with very low level emission with uncertain spectral shape at a luminosity $L_X < 10^{-4}$ of Eddington limit (Grebenev *et al.* 1993; van der Klis 1995). However, it is rare to observe a source exhibiting all the four spectral states.

4.1 *Fast transition between high-soft and low-hard states*

Galactic black hole binaries remain in a canonical spectral state with similar properties for considerably long durations ($\sim$ a few months). This suggests the general stable nature of the accretion disk. Though the microquasar GRS 1915 + 105 shows extended low-hard states as seen in other Galactic black hole candidates, the state transition between the low-hard state and high-soft state occurs in a wide range of time scales. Attempts have been made to explain the observed state transitions when the source shows regular periodic bursts in the X-ray light curves. Belloni *et al.* (1997) have tried to explain the repeated patterns (burst/quiescent cycle) in the X-ray light curve as the appearance and disappearance of the inner accretion disk. They have shown that the outburst duration is proportional to the duration of the previous quiescent state. Taam *et al.* (1997) have attempted to describe these transitions in the framework of thermal/viscous instabilities in the accretion disk. They have argued that the geometry of the accretion disk in GRS 1915 + 105 consists of a cold outer disk extending from radius $r_{in} \sim 30$ km to infinity and a hot, optically thin inner region between $r = 3$ km and r_{in}. They have interpreted the spectral changes between low-hard and high-soft states as arising due to the change in the value of inner disk radius. Nayakshin *et al.* (2000) tried to explain the observed temporal behavior of GRS 1915 + 105 invoking the model of standard cold accretion disk with a corona that accounts for the strong nonthermal X-ray emission and plasma ejections in the jet when the source luminosity approaches the Eddington limit. This model qualitatively explains the observed cyclic features in the light curves (classes ρ, α, and λ), the dependence of the overall evolution and the values of the cycle times on the time-averaged luminosity, and the fact that the transitions between the states can be very much shorter than the corresponding cycle time. This model also successfully explains the ejections of plasma into radio jets and the associated dip features (class β) seen in the X-ray light curves of the source.

Rao *et al.* (2000) have observed a slow transition from an extended low-hard state to a high-soft state ($\sim$ 3 months) in 1997 March−August. Fast transition (a few seconds) between the two spectral states is observed during many occasions when the source exhibits irregular bursts (Rao *et al.* 2000), soft dips (Naik *et al.* 2001) in the X-ray light curves. Chakrabarti *et al.* (2000) interpreted the observed spectral transition in GRS 1915 + 105 in the light of advective disk paradigm which includes self-consistent formation of shocks and out-flows from post-shock region. The observed fast transition between the two canonical spectral states implies the solutions for the accretion disk during two states exist for similar net (i.e., sum of the Keplerian and sub-Keplerian) $\dot{m}$. This is because the time scale of fast transition ($\sim$ 10 s) is not sufficient for the readjustment of the accretion disk at the outer edge to create a significant change in $\dot{m}$.

4.2 *Fast transition between high-soft and low-soft states*

The Galactic microquasar GRS 1915 + 105 remains in the low-hard state for extended periods and switches from the low-hard state into a high-soft state in a wide range of time-scales. During the low-hard state, the source spectrum is dominated by the non-thermal component and the inner edge of the accretion disk lies far away from the black hole event horizon. However, during the high-soft state, the spectrum is dominated by the thermal component and the inner edge of the accretion disk extends towards the event horizon. The Compton cloud which is responsible for the Comptonization of the soft X-ray photons during the low-hard state vanishes during the high-soft state. The X-ray flux has a significant contribution from the non-thermal component during the low-hard state whereas the thermal component is dominated over by the non-thermal component during the high intensity soft states. The transition between the above two canonical spectral states takes place because of the infall of matter from the inner accretion disk into the black hole and presence and absence of the Compton cloud. However, the observed transition between the high-soft and low-soft states (present work) without any significant change in the geometry of the accretion disk is interesting new phenomenon. We try to explain this observed feature invoking a model where the viscosity parameter of the accretion disk is very close to the critical viscosity.

We observed a factor of ~ 3.5 difference in the X-ray flux in 2 – 60 keV energy range during the high-soft (non-dip) and low-soft (dip) states of class ω. If this could be due to the decrease in the mass accretion rate, according to ADAF, the source spectrum during this low intensity state should be hard which is not the case. The softness of the source spectrum during the low state (dip) of class ω makes it clear that the observed change in intensity during these states (dip and non-dip) cannot be due to the change in mass accretion rate at the outer edge. Although similar change in X-ray flux during the dip and non-dip regions was observed in the light curves of the black hole candidates GRO J1655–40 and 4U 1630–47 (Kuulkers *et al.* 1998), these dips are different from those observed in GRS $1915 + 105$. In earlier cases, the source spectra during the dips were heavily absorbed by some intervening material. The spectra during the dips when fitted by a model with power law and absorbed disk blackbody as the model components, the equivalent hydrogen column densities (N_H) for the two sources were found to be $27 \times 10^{22}\,\mathrm{cm}^{-2}$ and $34 \times 10^{22}\,\mathrm{cm}^{-2}$ respectively which are about one order higher in magnitude than the interstellar absorption column densities ($N_{H_{\mathrm{int}}}$). The values of N_H were very high ($\geq 76 \times 10^{22}\,\mathrm{cm}^{-2}$) for both the sources when the spectra were fitted with a model with blackbody and absorbed disk blackbody as model components. However, the source spectra during the dips (low-soft state) in GRS $1915 + 105$ are well described by “disk blackbody, power law and a thermal Compton-spectrum” model without any absorbing medium other than $N_{H_{\mathrm{int}}}$. Hence, the decrease in X-ray intensity during the dips cannot be explained by absorption by the intervening medium. As the source is radio-quiet during the observations of this class, the decrease in X-ray intensity cannot be explained by the evacuation of matter from the accretion disk which causes flares in radio and infrared bands.

The observed unusual transition between two different intensity states in GRS $1915 + 105$ is attributed to the change in the temperature of the inner accretion disk without incorporating any significant change in the inner radius. The inner accretion disk during the high intensity state (non-dip) is hotter than the low intensity state (dip). The duration of the observed dips and non-dips are in the range 20 – 95 s and 200 – 550 s. If the variation in the intensity between two dips and non-dips are due to the emptying and replenishing of the inner accretion disk caused by a viscous thermal instability, then the viscous time can be explained by (Belloni *et al.* 1997)

$$t_{\mathrm{vis}} = 30\alpha_2^{-1} M_1^{-1/2} R_7^{7/2} \dot{M}_{18}^{-2} s \tag{1}$$

where $\alpha_2 = \alpha/0.01$, R_7 is the radius in units of 10^7 cm, M_1 is the mass of the compact object in solar masses, and $\dot{M}_{18}$ is the accretion rate in units of 10^{18} g s^{-1}. Using all these parameters, Belloni *et al.* (1997) found that the model agrees with the data with a relation of the form $t_q \propto R^{7/2}$, where t_q is the time interval for the quiescent phase. Applying the values of the radius of the inner accretion disk during the dip to the above expression, the duration of the derived quiescent (dip) period does not match with the observed dip duration. These results manifest that the above model cannot explain the the observed transition between two intensity states.

We attempt to explain the observed phenomenon of state transition between different intensity states in GRS 1915 + 105 by invoking the two component advective flow (TCAF) model of Chakrabarti & Titarchuk (1995) which consists of two major disk components

- standard, optically thick disk component produced from the Keplerian or the sub-Keplerian matter at the outer boundary and
- quasi-spherical and axisymmetric sub-Keplerian halo component.

The advantage of this model is that the soft and hard X-ray radiations are formed self-consistently from the same accretion disk without invoking any adhoc components such as the plasma cloud, hot corona, etc. whose origins have never been clear. According to this model, the temperature of the Keplerian disk increases with the increase in the accretion rate of Keplerian disk. The increase in the number of soft photons intercepted by the post-shock region results in reducing its temperature. Assuming Comptonization as the dominant mechanism for cooling, the expression for the electron temperature T_e can be given as

$$T_e = \frac{T_{es} r_s}{r} e^{C_{\mathrm{comp}}(r^{3/2} - r_s^{3/2})} \tag{2}$$

where C_{comp} is a monotonically increasing function of optical depth assuming a constant spectral index, r_s is the shock location and T_{es} is the electron temperature at r_s. For $C_{\mathrm{comp}} > r_s^{-3/2}$, the cooling due to Comptonization overcomes geometrical heating and T_e drops as the flow approaches the black hole. According to this model, a disk with completely free (Keplerian) disk and (sub-Keplerian) halo accretion rates for a black hole of mass $M = 5M_{\odot}$, exhibits multiplicity in spectral index (when both the rates are fixed) or multiplicity in disk accretion rate when the spectral index is similar (see, Fig. 3a of Chakrabarti & Titarchuk, 1995). In the observation described in this paper, there is no evidence for a large variation of the spectral index. This signifies that though there is not enough time for a change in the total rate (as the transition between the high-soft and low-soft states takes place within a time range of $\leq$ 10 s), individually, Keplerian and sub-Keplerian rates may have been modified. This is possible if the Shakura-Sunyaev viscosity parameter α is very close to the critical value ($\alpha \sim \alpha_c \sim 0.015$; Chakrabarti 1996). When α of the entire disk is well above α_c, the entire disk is pretty much Keplerian, except very close to the black hole ($r < 3r_g$, where r_g is the Schwarzschild radii). Similarly when α of the entire flow is well below α_c, the flow is sub-Keplerian with a possible standing or oscillating shock wave (Chakrabarti 1996). Since viscosity in a disk can change in a very small time scale (convective/turbulent time-scale in the vertical direction) it is not unlikely that the viscosity near the Keplerian-disk surface is very close to the critical value during the time when this new class is exhibited. The high-intensity state will then correspond to the ordinary Keplerian disk. Extraordinary laminary flow may reduce viscosity at some stage, and sub-Keplerian flow develops out of the Keplerian disk both above and below the Keplerian disk. This sub-Keplerian flow need not be hotter since excess soft photons from the underlying Keplerian disk cools it instantaneously. Temperature and intensity of the radiation from the Keplerian disk drops to the point that a thin outflow develops from the sub-Keplerian flow. This is the low intensity state. This wind is cooled down and is fallen back on the Keplerian disk, increasing the Keplerian rate, intensity and viscosity, thereby cutting off the wind and bringing the flow to the high intensity state again. Unlike the transition from State B to State C (as described by Belloni *et al.* 2000 and explained in Chakrabarti *et al.* 2000), where the sub-Keplerian flow may always be present, in the present case, the high intensity state need not have a sub-Keplerian component at all. The transition from one soft-state to another could in fact be due to the interesting change in topology of the flow at the critical viscosity.

5. Acknowledgements

Work of SN is partially supported by the Kanwal Rekhi Scholarship of the TIFR Endowment Fund. We thank the RXTE, BATSE, and NSF-NRAO-NASA GBI team for making the data publicly available. This research has made use of data obtained through the High Energy Astrophysics Science Archive Research Center Online Service, provided by the NASA/Goddard Space Flight Center. The Green Bank Interferometer is a facility of the National Science Foundation operated by the NRAO in support of NASA High Energy Astrophysics programs.

References

Belloni, T., Mendez, M., King, A. R., *et al.* 1997, *Ap. J.*, **488**, L109.
Belloni, T., Klein-Wolt, M., Mendez, M. *et al.* 2000, *A&A*, **355**, 271.
Castro-Tirado, A. J., Brandt, S., Lund, N. 1992, *IAU Circ.*, 5590.
Chen, X., Swank, J. H., Taam, R. E. 1997, *Ap. J.*, **477**, L41.
Chakrabarti, S.K., 1996, *Ap. J.*, **464**, 664.
Chakrabarti, S.K., Manickam, S.G., Nandi, A. *et al.* 2000, submitted to World Scientific (astro-ph – 0012525)
Chakrabarti, S.K., Titarchuk, L.G. 1995, *Ap. J.*, **455**, 623.
Grebenev, S.A., Sunyaev, R., Pavlinsky, M. *et al.* 1993, *A&AS*, **97**, 281.
Greiner, J., Morgan, E. H., Remillard, R. A. 1996, *Ap. J.*, **473**, L107.
Klein-Wolt, M., *et al.* 2002, MNRAS, (astro-ph/0112044)
Kuulkers, E., Wijnands, R., Belloni, T. *et al.* 1998, *Ap. J.*, **494**, 753.
Mirabel, I. F., Rodriguez, L. F. 1994, *Nat.*, **371**, 46.
Mirabel, I. F., Dhawan, V., Chaty, S. *et al.* 1998, *A & A*, **330**, L9.
Morgan, E.H., Remillard, R.A., Greiner, J. 1997, *Ap. J.*, **482**, 993.
Muno, M.P., Morgan, E.H., Remillard, R.A. 1999, *Ap. J.*, **527**, 321.
Naik, S., Rao, A.R. 2000, *A&A*, **362**, 691.
Naik, S., Agrawal, P.C., Rao, A.R. *et al.* 2001, *Ap. J.*, **546**, 1075.
Naik, S., Agrawal, P.C., Rao, A.R., Paul, B. 2002, *MNRAS*, **330**, 487.
Nayakshin, S., Rappaport, S., Melia, F. 2000, *Ap. J.*, **535**, 798.
Rao, A.R., Yadav, J.S., Paul, B. 2000, *Ap. J.*, **544**, 443.
Smith, D.M., Heindl, W.A., Markwardt, C.B., Swank, J.H. 2001, *Ap. J.*, **554**, L41.

Taam, R.E., Chen, X., Swank, J.H. 1997, *Ap. J.*, **485**, L83.
van der Klis, M. 1995, in *X-ray Binaries*, (ed.) W. Lewin, J. van Paradijs, & E. van den Heuvel (Cambridge: Cambridge Univ. Press) 252.
Zdziarski, A.A., Grove, J.E., Poutanen, J., *et al.* 2001, **554**, L45

J. Astrophys. Astr. (2002) **23,** 235–242

On the Relativistic Beaming and Orientation Effects in Core-Dominated Quasars

A. A. Ubachukwu* & A. E. Chukwude *Department of Physics and Astronomy, University of Nigeria Nsukka, Nigeria*
**Regular Associate of the Abdus Salam ICTP, Trieste Italy*

Received 2002 July 31; accepted 2002 December 11

Abstract. In this paper, we investigate the relativistic beaming effects in a well-defined sample of core-dominated quasars using the correlation between the relative prominence of the core with respect to the extended emission (defined as the ratio of core- to lobe- flux density measured in the rest frame of the source) and the projected linear size as an indicator of relativistic beaming and source orientation. Based on the orientation-dependent relativistic beaming and unification paradigm for high luminosity sources in which the Fanaroff-Riley class-II radio galaxies form the unbeamed parent population of both the lobe- and core-dominated quasars which are expected to lie at successively smaller angles to the line of sight, we find that the flows in the cores of these core-dominated quasars are highly relativistic, with optimum bulk Lorentz factor, $\gamma_{opt} \sim$ 6–16, and also highly anisotropic, with an average viewing angle, $\sim 9^\circ$–16°. Furthermore, the largest boosting occurs within a critical cone angle of $\approx 4^\circ$–10°.

Key words. Galaxies: active, jets, quasars: general.

1. Introduction

The phenomenology of active galactic nuclei (AGNs) involves a supermassive black hole which releases relativistic outflows of energetic particles by accretion of matter through an accretion disk surrounded by an optically thick torus. These relativistic outflows form well-collimated symmetric twin jets or beams that feed the radio lobes (Rees 1971; Blandford & Rees 1974; Scheuer 1974; Blandford & Königl 1979). The interaction of the head of the beams/jets with the intergalactic medium produces the observed synchrotron lobe emission (Scheuer 1977). The classification of AGNs depends on the power and geometry of the central engine as well as the jet/disk orientation with respect to our line of sight. (e.g., Antonucci 1993; Gopal-Krishna 1995; Falcke *et al.* 1995a,b; Urry & Padovani 1995). Thus, many properties of quasars and AGNs can be attributed to relativistic Doppler and geometric projection effects at small angles to our line of sight.

In low frequency surveys, the emission from high luminosity extragalactic radio sources is usually dominated by the lobe which has steep spectra (spectral index, $\alpha \geq 0.5$, $S_\nu \sim \nu^{-\alpha}$). These sources include the lobe-dominated quasars (LDQs) and Fanaroff & Riley (1974) class-II (FRII) galaxies. The lobe emission is usually assumed to be isotropic so that radio source samples selected on the basis of their lobe emission should be orientation-unbiased. This means that, for the lobe-dominated sources, the ratio of the core flux density to that of the lobe (R) should usually not exceed unity (i.e., $R \leq 1$).

In contrast, high frequency source samples appear to be dominated by their core emissions so that radio sources selected from high frequency surveys tend to contain mostly core-dominated sources characterized by flat spectra ($\alpha < 0.5$) due to synchrotron self-absorption. These high luminosity radio sources are largely quasars and are called core-dominated quasars (CDQs). For these sources, the core emission depends on the viewing angle and can be Doppler boosted if the source axis is oriented close to the line of sight (i.e., $R > 1$). In addition, the projected linear sizes (D) of the CDQs are expected to be foreshortened due to geometrical projection effects at small viewing angles. The notable exception to the core-dominated objects observable at high frequencies are the compact steep spectrum sources which are of galactic dimensions and whose radio properties appear to be less dependent on orientation (Fanti *et al.* 1990).

Several statistical tests have been carried out which confirmed that R is indeed a good statistical measure of relativistic beaming in the cores of high luminosity sources (e.g., Orr & Browne 1982; Kapahi & Saikia 1982; Hough & Readhead 1989; Saikia & Kulkarni 1994; Saikia *et al.* 1995). In previous papers (Ubachukwu 1998; 2002, hereafter paper I), we studied the statistical consequences of relativistic beaming and geometric projection effects in high luminosity lobe-dominated sources using their observed $R - D$ data. In this follow-up paper, we wish to extend the $R - D$ analysis to their core-dominated counterparts.

2. Doppler boosting and geometrical projection effects in core-dominated sources

The simplest relativistic beaming and radio source unification model predicts that both the projected linear size, D, and the core dominance parameter, R, should depend on the viewing angle according to the following equations;

$$D = D_0 \sin\phi, \tag{1}$$

and

$$R = f\gamma^{-n}[(1 - \beta\cos\phi)^{(-n+\alpha)} + (1 + \beta\cos\phi)^{(-n+\alpha)}], \tag{2}$$

where D_0 is the intrinsic size of the source, f is the ratio of the intrinsic core luminosity to the unbeamed extended luminosity, β is the velocity of the radiating material in units of the velocity of light, α is the spectral index and $\gamma = (1 - \beta^2)^{-1/2}$ is the bulk Lorentz factor. The exponent n depends on whether the radiating material consists of a continuous jet ($n = 2$) or blobs ($n = 3$); in general $2 \leq n \leq 3$ if the emission is isotropic in the rest frame of the source. For the purposes of the present study which involves the core-dominated sources, we shall assume $\alpha = 0$ throughout. At small angles to the line of sight, relativistic beaming in active galactic nuclei (the ratio of the observed core luminosity to it's emitted value) is fundamentally characterized by the Doppler factor given by,

$$\delta = [\gamma(1 - \beta\cos\phi)]^{-1}. \tag{3}$$

Generally, the relativistic beaming hypothesis is based on two parameters, the bulk Lorentz factor/jet velocity (γ/β) and the viewing angle, ϕ. Equation (2) therefore suggests that the distribution of R should provide us with an indication of the range of values of viewing angle as well as the Lorentz factor which can be used to test specific beaming models once f is known. Consequently, the median angle to the line of sight can be calculated from the median value (R_m) of the R-distribution (from equation (2)) through

$$\cos\phi_m \approx 1 - \left(\frac{2^{n-1}R_m}{R_T}\right)^{-1/2} \tag{4}$$

(for $\gamma >> 1$), where $R_T = \frac{2f}{\gamma^n}$ is the value of R at $\phi = 90^\circ$ (i.e., the value of R for a source whose jet axis lies along the plane of the sky). The last equation is actually to a first approximation and is applicable to beamed sources whose radio axes are expected to lie close to the line of sight.

In addition, equation (3) has the implication that, for angles between $\phi = 0^\circ$ and some critical angle, ϕ_{crit}, the relativistic boosting is optimized and this can be obtained by setting $\frac{\mathrm{d}\delta}{\mathrm{d}\beta} = 0$. This yields (e.g., Vermeulen & Cohen 1994; Ubachukwu 1999)

$$\phi_{\text{crit}} \approx \sin^{-1}\left(\frac{1}{\gamma_{\text{opt}}}\right), \tag{5}$$

where γ_{opt} is the Lorentz factor which can be derived from equation (2) as

$$\gamma_{\text{opt}} \approx \left[\frac{1}{2^{n-1}}\left(\frac{R_{\max}}{R_T}\right)\right]^{1/2n}. \tag{6}$$

Here, $R_{\max} = R(\phi = 0^\circ) \approx f(2\gamma)^n$.

Furthermore, comparing equation (1) with equation (2) shows that R should be anti-correlated with D. A graph of R against D for a well-defined source sample is expected to yield,

$$R = R_{\max} - mD. \tag{7}$$

The last two equations suggest that we can deduce the value of the beaming parameter, γ, from the regression analyses of R on D for any assumed model once R_T is known for a given source sample. This of course presupposes that the observed $R - D$ correlation is entirely due to relativistic beaming. However, linear sizes of extragalactic radio sources have been known to undergo cosmological evolution (e.g., Barthel & Miley 1988; Kapahi 1989; Neeser *et al.* 1995), but whether the observed evolution is real or an artifact of the luminosity selection effects often present in most bright source samples is still unclear (see Singal 1993; Nilsson *et al.* 1993; Ubachukwu & Ogwo 1998). Nevertheless, this effect if present, should be accounted for before D could be used to test the relativistic beaming and radio source orientation scenarios. Following paper I, we test these expectations for a sample of core-dominated sources in the following section.

3. Analysis and results

The present analysis is based on a well-defined sample of powerful core-dominated sources compiled by Murphy *et al.* (1993). All of the sources have 5GHz core flux densities, $S > 1$ Jy. This sample consists of both BL Lacs and quasars which are variable sources. The quasar subsample, which is of interest for the present work, comprises 54 sources with complete R and D information.

The median value data for the R-distribution for the subsample is $R_m = 12.6$. Orr & Browne (1982) have shown that the R-distribution for radio loud quasars is consistent with $R_T = 0.024$, i.e., if the LDQs form the parent population of the CDQs. This would imply (from equation(4)), $\phi_m \approx 14^\circ$ for $n = 2$ or $\phi_m \approx 23^\circ$ for $n = 3$. However, as noted by Padovani & Urry (1992), and Urry & Padovani (1995), there appear to be too few LDQs to form the parent population of the CDQs. In fact, Barthel (1989, 1994) has used the relative number densities and size distributions of radio galaxies and quasars in the $3CR$ sample of Laing *et al.* (1983) to argue that high luminosity radio galaxies and quasars are the same objects seen from different orientation angles. We shall therefore adopt $R_T = 0.003$ which appears to be consistent with the FRII-LDQ-CDQ unification scheme for high frequency surveys (see Padovani & Urry 1992; Simpson 1996; Morganti *et al.* 1997; paper I). Using $R_T = 0.003$ together with $R_m = 12.6$ in equation (4) gives $\phi_m \approx 9^\circ$ for $n = 2$ or $\approx 16^\circ$ for $n = 3$.

To check for possible evolutionary effects, we show the R - z and D - z plots in Fig. 1 and Fig. 2 respectively (where z is the redshift and D is in Kpc). The two plots show no discernible trend. Linear regression analyses give correlation coefficient, $r \sim -0.2$, for each case implying a lack of any significant redshift dependence. Removal of the outlier, $1803 + 784$, weakens the correlation further (though not significantly) so we can hence conclude that evolution, if present, is negligible and proceed to use the R - D correlation to test the beaming hypotheses.

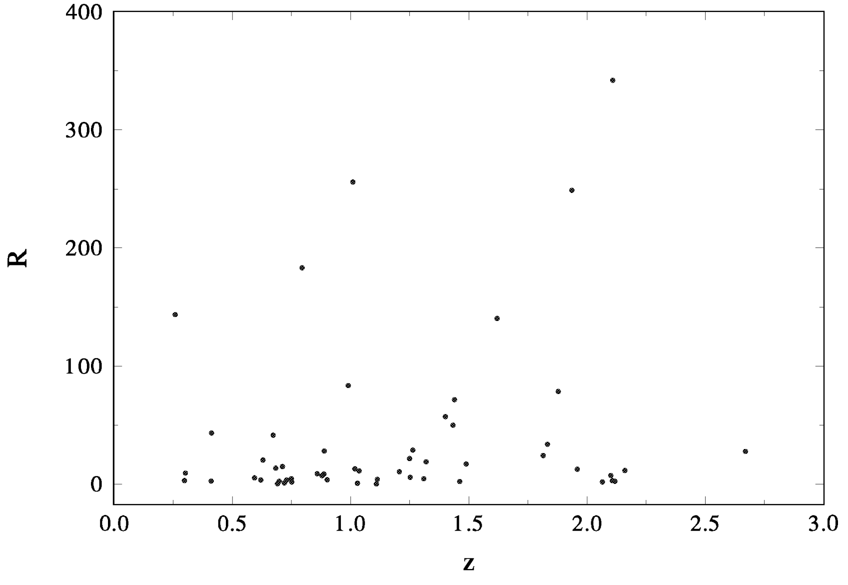

Figure 1. The graph of core dominance parameter against redshift.

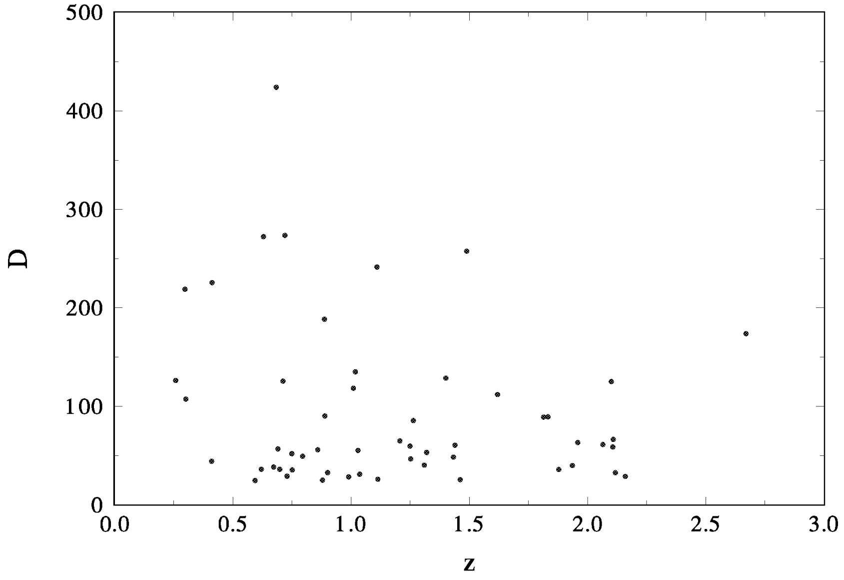

Figure 2. Projected linear size against redshift.

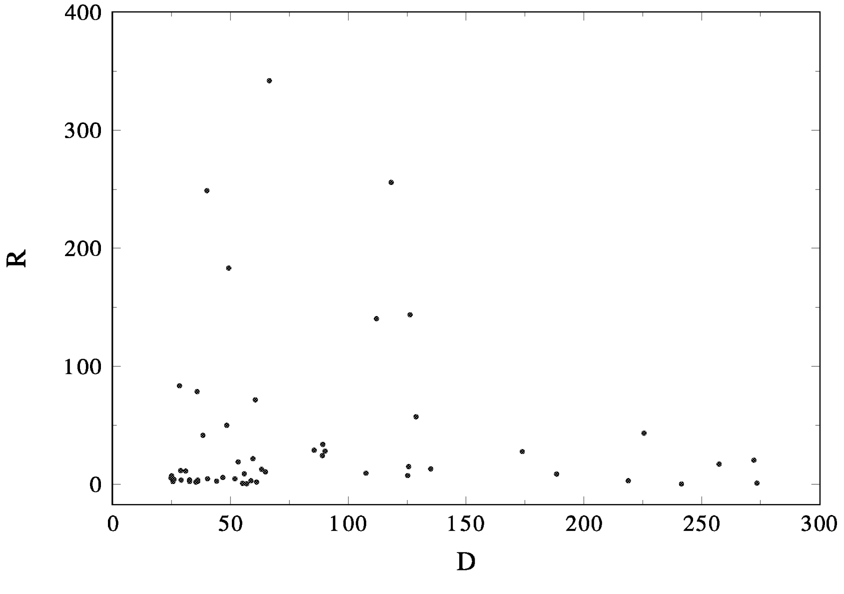

Figure 3. The plot of core dominance parameter against projected linear size.

Figure 3 shows the R - D plot for the present sample (without the outlier). Although the plot shows no obvious general trend, the upper envelope R - D function (which shows the locus of the maximum core dominance parameter as a function of the projected linear size) is well-defined. This function is usually attributed to relativistic beaming and geometric projection effects at small angles with respect to the line of sight (see Ubachukwu 1998; paper I). Linear regression analysis of the upper envelope R-data against D in four ranges of D: $D < 50$ kpc; $50 \leq D \leq 100$ kpc; $100 < D \leq$

150 kpc and $D > 150$ kpc, gives $R_{\max} = 375.64$ with $r \sim -0.9$. Using $R_{\max} = 375.64$ and $R_T = 0.003$ in equation (6) gives the bulk Lorentz factor (for optimum boosting), $\gamma_{\text{opt}} \approx 16$ and ~ 6 for $n = 2$ and 3 respectively. The corresponding critical beaming angle from equation (5) becomes, $\phi_{\text{crit}} \approx 4^\circ$ (for $n = 2$) or $\approx 10^\circ$ (for $n = 3$).

4. Discussion

Two main results can be derived from the analyses presented in the preceding section. These two results were based on the simple assumption that the relativistic beam emanating from AGNs is narrow and can be described with a single Lorentz factor, γ, once a flow model, which can either be in the form of a continuous jet ($n = 2$) or in form of individual blobs of plasma ($n = 3$), is adopted. Each of these models leads to different values of γ and viewing angle, ϕ. A more general situation may therefore be obtained in-between these two flow models ($2 \leq n \leq 3$) and this will form the basis for our discussion. It could be noted however, that smaller values of n imply higher γ-values but lower values of the viewing angle, ϕ. Furthermore, it was assumed that the Fanaroff-Riley class-II radio galaxies form the unbeamed parent population of both the LDQs and CDQs, with the latter being the most beamed counterpart (cf. Barthel 1989). However, analysis based on the Orr & Browne (1982) model in which the LDQs form the parent population of CDQs leads to a lower value of the Lorentz factor but a higher value of the orientation angle.

The first main result comes from the distribution of the core dominance parameter, R which shows that, on the average, CDQs are inclined at $\phi \approx 9^\circ$–16°, with respect to the line of sight. The second result is the presence of a strong anti-correlation between R and the apparent linear size, D for the upper envelope $R - D$ data. This correlation was shown to be consistent with an optimum Lorentz factor, $\gamma_{\text{opt}} \approx 6$–16, with corresponding critical beaming angle (i.e., the largest angle for optimum boosting), $\phi_{\text{crit}} \approx 4^\circ$–$10^\circ$. These results are all consistent with the orientation-dependent relativistic beaming and radio source unification paradigm in which the flows from the cores of CDQs are expected to be highly relativistic (even at large scales) and in which Doppler effects generate anisotropic radiation patterns at close angles to our line of sight. The results are also in quantitative agreement with previous works, as discussed below. But before that, a comparison of the results obtained in paper I with those found in the present analysis shows a much higher value of $R_{\max}$ (376) is inferred from the present CDR sample than that obtained from the LDQ sample of Paper I ($R_{\max} = 2.5$). Since $R_{\max} \approx 2R_T\gamma^4$, it follows that for a single value of R_T, a distribution of γ may be required with larger values being ascribed to the CDQs if they are to broadly fit into the FRII $-$ LDQ unification scheme. A simple consequence of this is that apparent jet velocities are higher for CDQs than for LDQs/FRIIs, due to their selection criteria: LDQ/FRII sample was randomly selected while the CDQ sample was selected based on the core emission (see Murphy 1990; Ubachukwu 1999). In fact, Ubachukwu (1999) has observed that the Lorentz factor and proper motion appear to be a factor of ~ 2 larger for core-selected quasars than for lobe-selected quasars.

Based on the assumption that the LDQs form the unbeamed parent population of radio loud quasars, Orr & Browne (1982) showed that the radio luminosity function of CDQs is consistent with a core Lorentz factor, $\gamma = 5$ (see also Kapahi & Saikia 1982; Hough & Readhead 1989). Similar result ($\gamma = 4$) was also obtained by Ubachukwu

(1999) based on the core dominance – proper motion data for LDQs as the parent population of CDQs (see Vermeulen 1995). However, as mentioned in the preceding section, there appears to be too few LDQs to form the parent population of the CDQs; the relativistic beaming and radio source unification hypotheses imply that the parent population must be larger. It is therefore more appropriate to derive the beaming and orientation parameters of CDQs based on the FRII radio galaxies as the parent population and not LDQs.

Padovani & Urry (1992), and Urry & Padovani (1995) have argued that if the high luminosity radio galaxies form the parent population of both the LDQs and CDQs then, it is not possible to fit the luminosity function with a single Lorentz factor but a distribution with a weighted mean, $\gamma_m \sim 11$. They showed that the CDQs should have their radio axes within $\sim 14^\circ$ (with an average $\sim 9^\circ$) of the line of sight. They also noted that high values of the Lorentz factor and lower values of n are necessary to provide better fit to the observed luminosity function. On the other hand, Ghisellini *et al.* (1993) used the synchrotron self-Compton model to estimate the value of γ from the observed and predicted X-ray flux densities and found $\gamma \approx 10$ and a viewing angle of $\sim 8^\circ$ for CDQs. Using the correlation between the accretion disk (UV) luminosity and the radio core emission of a sample of radio-loud quasars, Falcke (1995a) obtained a distribution of $3 \leq \gamma \leq 10$. These results are in close agreement with those obtained here.

5. Conclusion

We have investigated a simple statistical consequence of the relativistic beaming model in which, due to Doppler boosting and geometric projection effects at small viewing angles in core-dominated sources, the core dominance parameter, R, is expected to correlate inversely with the projected linear size, D, if the former is to be used as an orientation indicator. Our result shows a strong anti-correlation in the $R - D$ upper envelope data which offers both qualitative and quantitative support to the hypotheses that jets in core-dominated quasars are highly relativistic. This is consistent with the orientation-dependent relativistic beaming and unification paradigm for high luminosity radio sources in which the FRII radio galaxies form the parent population of the lobe- and core-dominated quasars, with the latter being the most beamed counterpart.

Acknowledgement

This work was done while AAU was visiting the Abdus Salam International Centre for Theoretical Physics as a Regular Associate. He is grateful to the Swedish International Development Agency (SIDA) for a generous contribution towards the visit.

References

Antonucci, R. 1993, *ARA&A*, **31**, 473.
Barthel, P. D. 1989, *Ap. J.*, **336**, 606.
Barthel, P. D. 1994, In: *The First Stromlo Symposium: Physics of Active Galaxies*, (ed.) G. V. Bicknell, M. A. Dopita, P. Quinn. (Cambridge: Cambridge Univ. Press) p. 175
Barthel, P. D., Miley, G. K. 1988, *Nat.*, **333**, 318.
Blandford, R. D., Königl, A. 1979, *Ap. J.*, **232**, 24.

Blandford, R. D., Rees, M. J. 1974, *MNRAS*, **169**, 395.
Falcke, H., Malkam, M. A., Biermann, P. L. 1995a, *A&A*, **298**, 375.
Falcke, H., Gopal-Krishna, Biermann, P. L. 1995b, *A&A*, **298**, 395.
Fanaroff, B. L., Riley, J. M. 1974, *MNRAS*, **167**, 13p.
Fanti, R., Fanti, C., Schilizzi, R. T., Spencer, R. E., Nan Rendong, Parma, P., van Breugel, W. J. M., Venturi, T. 1990, *A&A*, **231**, 333.
Ghisellini, G., Padovani, P., Celotti, A., Maraschi, L. 1993, *Ap. J.*, **407**, 67.
Gopal-Krishna 1995, *Proc. Natl. Acad. Sci.*, **92**, 11399.
Hough, D. H., Readhead, A. C. S. 1989, *AJ*, **98**, 1208.
Kapahi, V. K., Saikia, D. J. 1982, *JAA*, **3**, 465.
Kapahi, V. K. 1989, *Ap. J.*, **97**, 1.
Laing, R. A., Riley, J. M., Longair, M. S. 1983, *MNRAS*, **204**, 151.
Morganty, R., Oosterloo, T. A., Reynolds, J. E., Tadhunter, C. N., Migenes, V. 1997, *MNRAS*, **284**, 541.
Murphy, D. W. 1990, In: *Parsec-Scale Radio Jets.* (ed.) J. A. Zensus, & T. J. Pearson, (Cambridge: Cambridge Univ Press) p. 298
Murphy, D. W., Browne, I. W. A., Perley, R. A. 1993, *MNRAS*, **264**, 298.
Neeser, M. J., Eales, S. A., Law-Green, J., Leahy, J. P., Rawlings, S. 1995 *Ap. J.*, **451**, 76.
Nilsson, K., Valtonen, M. J., Jaakola, T. 1993, *Ap. J.*, **413**, 453.
Orr, M. J. L., Browne, I. W. A. 1982, *MNRAS*, **200**, 1067.
Padovani, P., Urry, C. M. 1992, *Ap. J.*, **387**, 449.
Rees, M. J. 1971, *Nat.*, **2229**, 312.
Saikia, D. J., Jeyakumar, S., Wiita, P. J., Sanghera, H., Spencer, R. E. 1995, *MNRAS*, **276**, 1215.
Saikia, D. J., Kulkarni, V. K. 1994, *MNRAS*, **270**, 897.
Scheuer, P. A. G. 1974, *MNRAS*, **166**, 513.
Scheuer, P. A. G. 1977, In: *Radio Astronomy and Cosmology, IAU Symp 74*, (ed.) D. L. Jauncy (Dordrecht: Reidel), p. 434.
Simpson, C. 1996, *Vistas Astron.*, **40**, 57.
Singal, A. K. 1993, *MNRAS*, **263**, 139.
Ubachukwu, A. A. 1998, *Ap&SS*, **257**, 23.
Ubachukwu, A. A. 1999, *Publ. Astron. Soc. Aust.*, **16**, 130.
Ubachukwu, A. A. 2002, *Ap&SS*, **279**, 251.
Ubachukwu, A, A., Ogwo, J. N. 1998, *AJP*, **51**, 143.
Urry, C. M., Padovani, P. 1995, *PASP*, **107**, 803.
Vermeulen, R. C. 1995, In: *Quasars and AGN: High Resolution Imaging*, (ed) M. H. Cohen & K. I. Kellermann (Washington DC: National Academy of Science), p. 11385
Vermeulen, R. C., Cohen, M. H. 1994, *Ap. J.*, **430**, 467.

J. Astrophys. Astr. (2002) **23,** 243–258

Spectral Variability in Hard X-rays and the Evidence for a 13.5 Years Period in the Bright Quasar 3C273

R. K. Manchanda *Tata Institute of Fundamental Research, Colaba, Mumbai 400 005, India*
e-mail: ravi@tifr.res.in

Received 2002 October 21; accepted 2002 December 12

Abstract. We report the observation of nearest quasar 3C273 made with LASE instrument on November 20th, 1998 as a part of our continuing programme of balloon borne hard X-ray observations in the 20–200 keV band using high sensitivity Large Area Scintillation counter Experiment. Our data clearly show a steep spectrum in the 20–200 keV with power law spectral index $\alpha = 2.26 \pm 0.07$. This is in complete contrast to the reported data from OSSE and BeppoSAX which suggest the value of 1.3 to 1.6 for the power law index in the X-ray energy band, but is quite consistent with the value derived for the high energy gamma ray data. A single power law fit in the X-ray and gamma ray energy bands points to a common origin of these photons and the absence of spectral break around 1 MeV as suggested in literature. We have reanalyzed the available data to study the temporal variability of the spectrum in the hard X-ray band. Our analysis reveals that 50 keV flux from the source, shows a strong modulation with a period of about 13.5 years. The analysis of the optical light curve of the source also supports the 5000 day period. We discuss the emission mechanism and the possible sites for X-ray photons along with the implications of the long term periodicity with respect to source geometry.

Key words. Galaxies: active galactic nuclei, jets, binary black hole system—quasars: individual 3C273—X-rays: galaxies.

1. Introduction

Among the large variety of active galactic nuclei, 3C273 is the nearest quasi stellar object with red shift $z = 0.158$. The source has been studied in detail in various energy bands and shows a large variety of morphological features. These include, a continuously fuelled curved inner jet with superluminal components observed in VLBI observations (Davis, Muxlow & Unwin 1991), an outer jet which is also visible in radio and optical wavelength other than the X-ray band and the UV excess (blue bump). The multiband spectrum of the source extends from radio to the GeV gamma rays region (Courvoisier *et al.* 1987) and can only be compared with the Crab Nebula, which also emits in the entire observable band. The spectral energy density distribution in 3C273 shows two broad peaks in the UV region ($\sim$ 10 eV) and the gamma ray energy band of 1–10 MeV (Ramos *et al.* 1997).

The X-ray emission from 3C273 in the soft X-ray band of 2–10 keV was first detected by Boyer *et al.* (1970). Since then the spectral observation of the source has been made in the X-ray and gamma ray energy bands, not only by balloon borne instruments (Pietsch *et al.* 1981; Bezler *et al.* 1984; Damle *et al.* 1987; Dean *et al.* 1990; Maisack *et al.* 1989, 1992) but also, by every X-ray payload launched on satellite missions till date i.e., HEAO-1 (Worrell *et al.* 1979; Primini *et al.* 1979), Einstein (Wilkes & Elvis 1987), SIGMA/GRANAT (Bassani *et al.* 1992), Ginga (Williams *et al.* 1992), ROSAT (Leach, McHardy & Papadakis 1995), EXOSAT (Turner *et al.* 1995) and ASCA (Cappi & Matsuoka 1997). The broadband data were obtained by OSSE (Johnson *et al.* 1995), COMPTEL (Hermsen *et al.* 1993) and EGRET (von Montigny *et al.* 1993) detectors on board CGRO and BeppoSAX (Grandi *et al.* 1997).

A temporal variability of the continuum emission from 3C273 in different energy bands is a regular feature of the source and has been discussed in literature (Courvoisier *et al.* 1987). Below 10 keV, the X-ray spectrum does show a large change in the spectral index on occasions, and can be fitted by a two component model in addition to a variable intensity weak and narrow Fe K_α emission line (Cappi & Matsuoka 1997). In the hard X-ray energy region of 20–200 keV, the spectrum generally follows a power law with a spectral index close to 1.5 however, a much steeper power index of 2.2 has also been reported in the archival data. The recent data from OSSE and BeppoSAX experiments show the canonical spectrum with index $1.4 < \alpha < 1.6$ except for a single observation of a flat spectrum with index 0.8 when the source intensity was lower by a factor of ~ 3. It was also noted from the Ginga data that the hard X-ray spectrum does not show any correlation with the flux variation in the 2–10 keV band. In the gamma ray energy band of 1 MeV to 1 GeV, the best fit spectral index is 2.4 (Litchi *et al.* 1994). From a comparison of the contemporary observations of the source made with the OSSE, COMPTEL and EGRET instruments, Johnson *et al.* (1995) have proposed a break in the source spectrum at around 1 MeV and steepening of the power index by ~ 1.

The X-ray emission in 3C273 is believed to arise by the synchrotron self Compton process (SSC) in the jets in which seed synchrotron photons are up scattered by interaction with the high energy electrons. X-ray and gamma ray emission in beamed relativistic jets in relation to BL Lac objects in general, and 3C273 in particular has been discussed in literature (Konigl 1981). The observation of soft X-ray excess below 1 keV in 3C273 and the flux variability below 10 keV, does suggest the presence of additional component which may arise from the thermal Comptonization of the soft photons originating in the accretion disc. The observation of the correlated variability in the medium energy X-rays and the K-band flux does however, suggest a generic relation between the two and a common emission process which also accounts for the bulk of X-ray photons emitted from the source (McHardy *et al.* 1999). The simultaneous multi-frequency observations in the radio and UV/Opt bands however, do not show a clear one-to-one correlation with the X-ray data (Ulrich *et al.* 1988).

The observed variability in the X-ray data of 3C273 is random and does not show any preferred time scales. ASM data on RXTE however, does show occasional flare like behaviour of the source. A $\sim 0.5\ d$ periodicity was first suggested from the Ariel 5 data (Marshall, Warwick & Pounds 1981). A comparison of the different data and the BATSE light curve in the 20–120 keV gives a variation in flux level by a factor ~ 2 over a period of months to years. A similar variation in the source flux over time scale of weeks was seen in the EXOSAT and Ginga data while the intensity variation by a factor of ~ 2 with a period of six months has been reported from the ROSAT data (Kim

2001). The observations of the source in the radio band show that new components are ejected into the inner jets ever since 2–4 years and thereby may result in the long term variation of the source. An existence of a 2 year period in the optical data of the source has been proposed by Fan *et al.* (2001). No definite periodic components have been found so far.

In this paper we report the hard X-ray spectral measurements of 3C273 made in the 20–200 keV band. The present measurements suggest that the entire X-ray and gamma ray emission from the source may arise in a single non-thermal process. We have re-analyzed the archival data by a new 'residual method' and conclude the presence of a long term variability of 13.5 years in the X-ray flux from the source. The re-analysis of the available optical data on the source also reveals the evidence of a similar long term period.

2. Present data

The spectral measurements were made during a balloon flight experiment using a large area scintillation counter telescope (LASE) operating in the 20–200 keV energy band. The X-ray telescope has a modular design and is optimized to make fast spectral and temporal measurement of cosmic X-ray sources in the hard X-ray band with very high sensitivity. The payload consists of three modules of scintillation detectors having both passive and active shielding and are fitted on a fully steerable alt-azimuth mount. Each of the three detector modules used in the experiment has a geometric area of 400 cm^2 and is specially configured in a back-to-back geometry. The field of view of each module is $4.5^\circ \times 4.5^\circ$ and is made with specially designed sandwiched material of tin, copper and lead. All modules have independent event-selection logic, onboard radioactive source calibration, PHA analyzer and the arrival time of the accepted events is recorded with a time resolution of 25 μsec. A 3σ threshold sensitivity of the LASE telescope in the entire energy range up to 200 keV is $\sim 1.5 \times 10^{-6}\ \mathrm{cm^{-2} s^{-1} keV^{-1}}$ for a source observation of 10^4 sec. The details of payload are given elsewhere (Manchanda 1998; D'Silva *et al.* 1998).

The observations were made on November 21st, 1998 from Hyderabad, S. India. The source observations were preceded and followed by off-source measurement from a nearby source free region. The total number of excess counts due to the source in all three detectors were 12418 during the source observation of 3540 sec and corresponds to a combined statistical significance of 20σ in the 35 to 160 keV energy band. The excess count rate spectrum was computed for the source and then corrected for the atmospheric absorption including multiple Compton scattering effects, window transmission and detector response functions. The spectra from all the three detectors were co-added. The observed photon spectrum is shown in Fig. 1. A single power law fit of the form $\frac{dN}{dE} = \mathrm{K\,E}^{-\alpha}\mathrm{ph.\ cm^{-2}s^{-1}keV^{-1}}$ to the spectral data above 35 keV gives the best fit model parameters of $K = 0.7$ and $\alpha = 2.26 \pm 0.07$ with a reduced χ^2 value of 0.2 corresponding to 7 degrees of freedom. The power law fit is shown in the figure with solid line. The data shown in the figure suggest a residual excess over the best fit line at about 120 keV, however, the total significance of the this feature is only $\sim 2\sigma$. It is also seen in the figure that high statistical significance of the individual data points for energies below 80 keV control the spectral index of the power law fit. The present observations correspond to MJD 2451137.

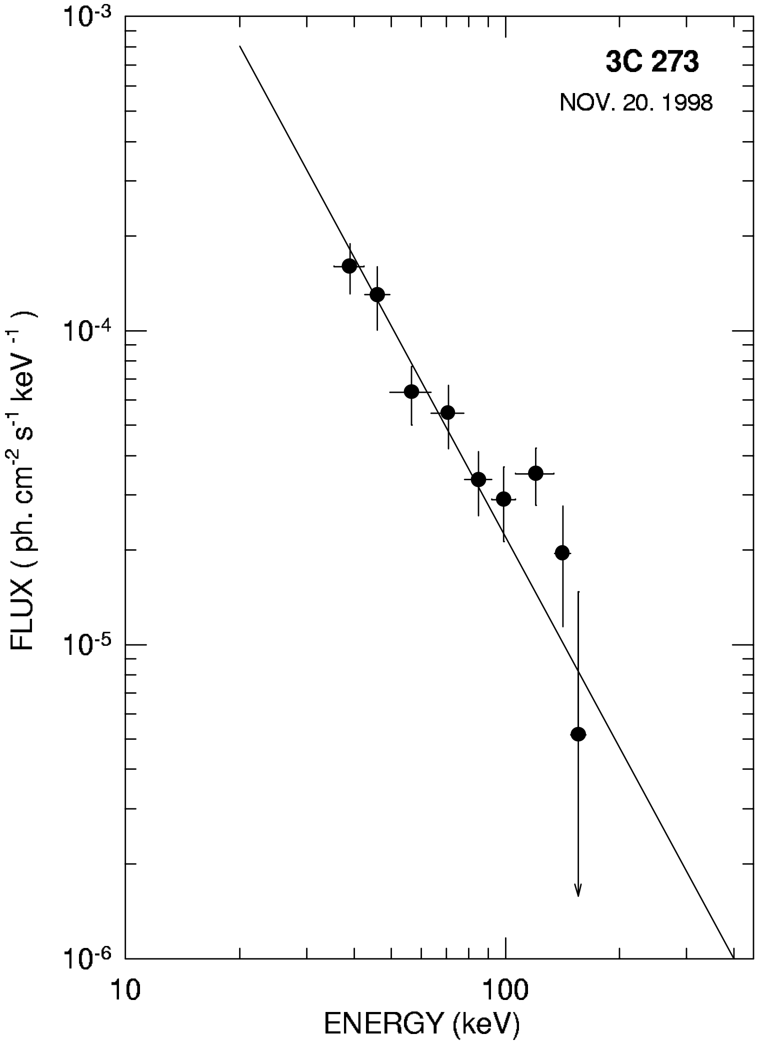

Figure 1. Hard X-ray spectrum of 3C273.

To determine the activity level of 3C273 corresponding to the spectral data presented above, and to illustrate the long term temporal behaviour of the source, we have plotted X-ray light curves taken from the archival data in Fig. 2. The left panel in the figure shows the X-ray light curve of the source from BATSE data on board CGRO in the 20–120 keV band. The all sky monitor data on-board RXTE in the 2–6 keV band is shown in the right panel. It is seen from the figure that in the hard X-ray band the source intensity does show gradual variation in intensity over long time scales and the source is clearly detectable even in the quiescent or normal phase. In the soft X-ray band however, the X-ray emission does show flare like behaviour on several occasions as is evident from the ASM data (right panel). It is also seen from the figure that present observations correspond to the normal state of the source.

A comparison of the present results with the earlier data in the hard X-ray ray band up to 300 keV is shown in Fig 3(a). The data shown in the figure correspond to the

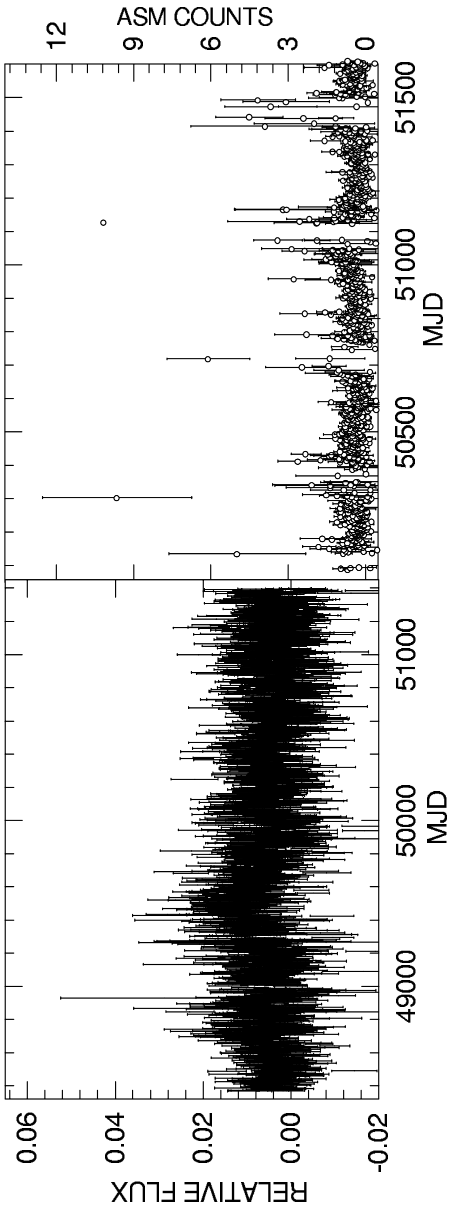

Figure 2. X-ray light curve of 3C273 as seen in BATSE (left panel) and RXTE data.

observations by SIGMA-Granat mission (Bassani *et al.* 1992), MIFRASO data (Dean *et al.* 1990) and OSSE detector on-board Compton/GRO observatory (Johnson *et al.* 1995). It is seen from the figure that present values of spectral flux in various energy bins is consistent with the SIGMA and MIFRASO data. The two dotted lines in the figure represent the high state and the low state spectra from OSSE data. It is seen in the figure that the present data is consistent with the high-state spectrum of the source from OSSE while the low state spectrum does vary significantly. The best fit power law index obtained from the present observations is also consistent with the data in the gamma ray energy region up to 10 GeV and is shown in Fig. 3(b). The gamma ray data in the figure corresponds to the observations made by COMPTEL and EGRET telescope (Hermsen *et al.* 1993, von Montigny *et al.* 1993). This in turn suggests a common emission mechanism for the high energy X-rays and gamma ray photons.

3. Spectral variability in hard X-rays

The compilation of the world data shown in Fig. 3, does appear to be consistent globally and the large scatter in the measured flux values at any given energy can be ascribed to the temporal variability as shown in Fig 2. However, when considered individually, the value of the measured spectral indices shows a large variation between 1.2 ± 0.17 and 2.26 ± 0.07. In order to find any correlation between the observed source luminosity and the spectral index as well as deduce the periodic behaviour of the source spectrum, we have devised the 'residual analysis' for the individual data sets. We have used the present measurement as the spectral template. The residuals are computed in each energy bin for different data and are shown in Fig. 4. We have split the world data in two parts i.e., pre and post 1983. In the case of earlier data the residuals were computed only at 50 keV and at 100 keV. The HEXE data are taken from Maisack *et al.* (1992). For convenience of plotting the data, the flux values were multiplied with $E^{-2.26}$. It is seen from the figure that data above 100 keV fit the mean spectra in all data sets thereby producing near zero residuals. Below 100 keV, high and low residuals are seen in different data sets. In the composite panel of pre 1983 data, once again the variability in the individual data sets is clearly visible. This analysis therefore, illustrates the possible spectral variability in 3C273 and that the observed variations are confined to energies below 100 keV in the hard X-ray region. This in turn suggests a two component origin for the hard X-ray photons, one of which exhibits temporal variations.

4. Long term periodicity in the source

In order to derive the long term period in 3C273, we have plotted the 50 keV flux (F_{50}) values as measured during different observations starting with the earliest measurements in Fig. 5. The choice of flux value at 50 keV is due to the fact that majority of the earlier measurements are made in balloon-borne observations and the systematic corrections are negligible at $\sim$ 50 keV. The pre 1990 compilation is taken from Bassani *et al.* (1992) and later high quality data corresponds to OSSE observations of the source. Apart from the short term variations, the data in the figure show a clear evidence of long term periodicity in the source. Assuming a sinusoidal functional form, an eye fit to the data gives a period of about 13.5 years ($\sim$ 5000 days). A similar plot

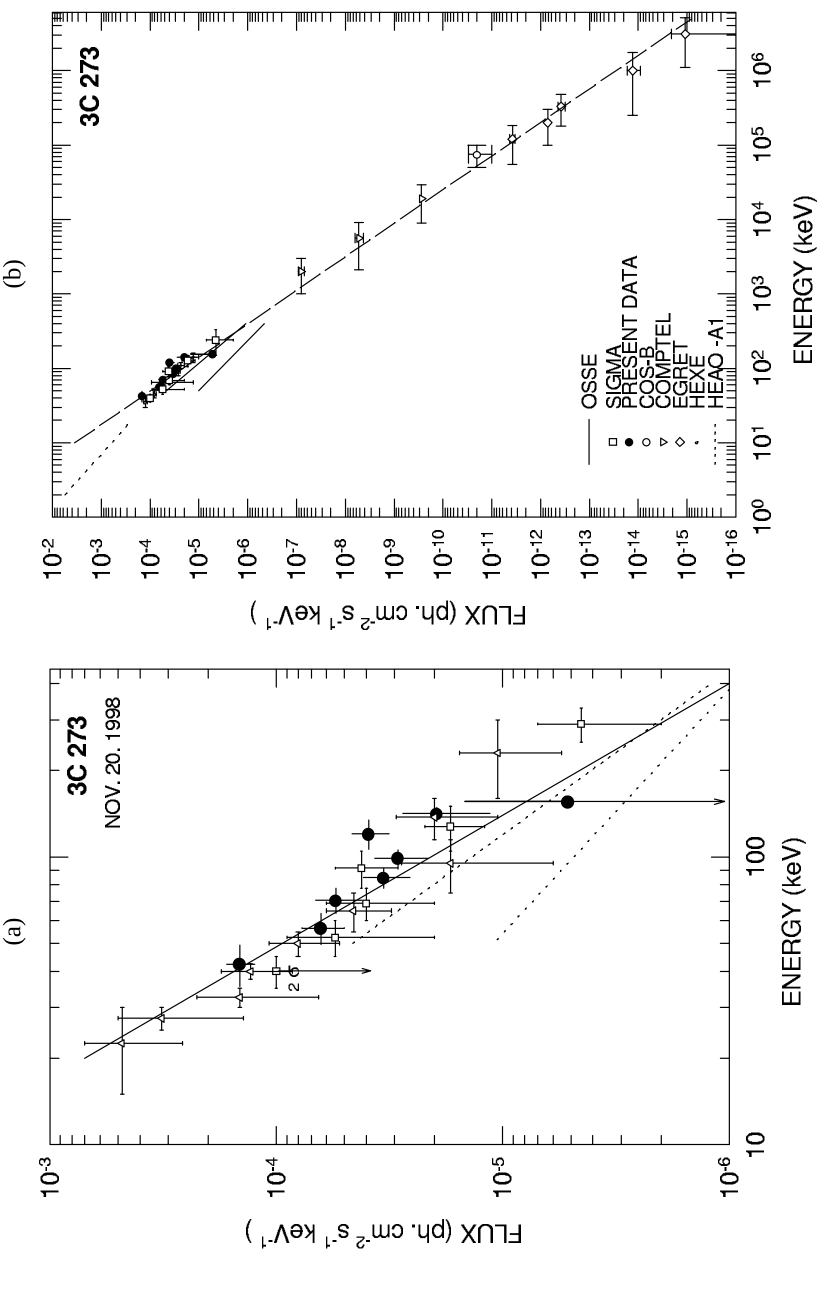

Figure 3. **(a)** Hard X-ray spectrum of 3C273. □ SIGMA, Δ MIFRASO, - - - OSSE, ● present data. Solid line, the best fit power law as in Fig. 1. **(b)** Photon spectrum in the entire X-ray and gamma ray energy band. The dotted line in the figure represents the extrapolation of best fit spectrum.

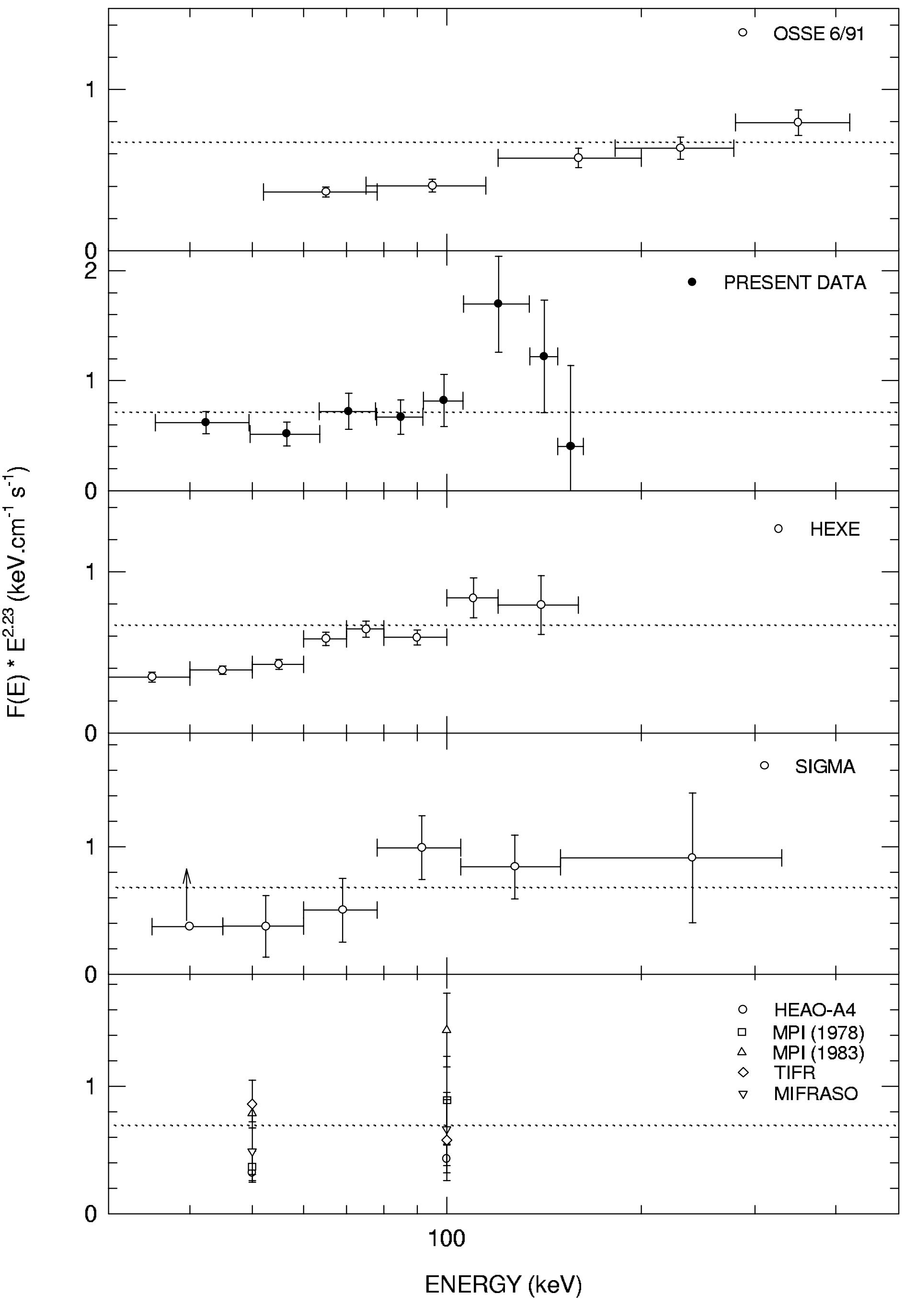

Figure 4. Plot for the spectral residuals for different data sets. Residuals are computed by taking $\alpha = 2.26$, as the best fit power index from keV to GeV energy band.

for the 100 keV flux, F_{100} did not show a clear period. Such a behaviour was expected on the basis of the variability plot shown in Fig. 4 in which the zero residuals were noted for data above 100 keV in all data sets. Similarly the long term periodicity is also not so apparent in the value of the spectral index as shown in the top panel in Fig. 5. The absence of long term period in the power law index can be ascribed to the emission mechanism for the hard X-ray photons and the temporal variation in the X-ray luminosity of the source. In addition, in a two component model, if the amplitude of the periodic component is small, the spectral index will remain mostly unchanged.

To search for additional evidence for the long term periodicity in 3C273 as inferred above, we have re-analyzed the optical brightness data of the source. The 110 year data base is due to Fan *et al.* (2001). The plot for the observed magnitude of the source versus modified Julian date is shown in Fig. 6 (left panel). The underlying long term variability can be clearly seen in the data. For searching the coherent periodicity in the optical data we used the XRONOS folding routine. The data were searched for periods between 3200 and 6000 days in 200 steps. The resultant power vs. period is shown in Fig. 6. (right panel). A broad peak centered around 4790 days is clearly visible in the figure. The large deviation of $\pm 205\ d$ in the determination of the period is due to short data base for long period searches. The presence of long term period in the optical data consistent with that inferred from the X-ray band clearly points to the true nature of the period.

5. Discussion

5.1 *Photon production and the emission sites*

A simple power-law nature of the spectrum in the entire X-ray and gamma ray region up to GeV as seen in figure 3, suggests a non-thermal origin for these photons and can arise either in pure synchrotron process or due to Synchrotron Self Compton process. The basic ingredient for this process to operate is the high energy relativistic electrons, which first give rise to the synchrotron seed photons and then up scatter these to higher energies in the case of SSC and if the seed photons have a power law spectrum, the emergent spectral index will be harder. In either of these processes a population of relativistic electrons is pre-requisite. The jets are the most suited geometry for the shock acceleration of the electron to very high energies. The detection of radio flux from the jets is itself an evidence of the presence of relativistic particles and *in situ* acceleration. The particle acceleration in the jets is believed to be due to shock wave at the interaction boundary of the expanding relativistic plasma and the ambient environment. During the shock acceleration a particle with velocity v gains a momentum $\simeq w/v$ every time it crosses the shock of velocity w. If the particles are scattered efficiently on both sides of the shock and stay trapped, the particle can reach relativistic energies provided the adiabatic losses are negligible. In case of the diffusive shock the maximum proton energy $E^p_{\max} \sim 10^{15}$ eV is attainable for a shock compression ratio of ~ 4 and reasonable values for other parameters (Mitra 1991). The shock acceleration of the particles transmits a power law spectrum and for a shock compression of $\sim$3–4 the exponent lies between 2 and 2.5.

The observed spectral energy density of 3C273 at higher energies is very large. Therefore, for Compton losses to be comparable to synchrotron energy loss the Lorenz factor for electrons, needs to be large compared with magnetic energy density. The

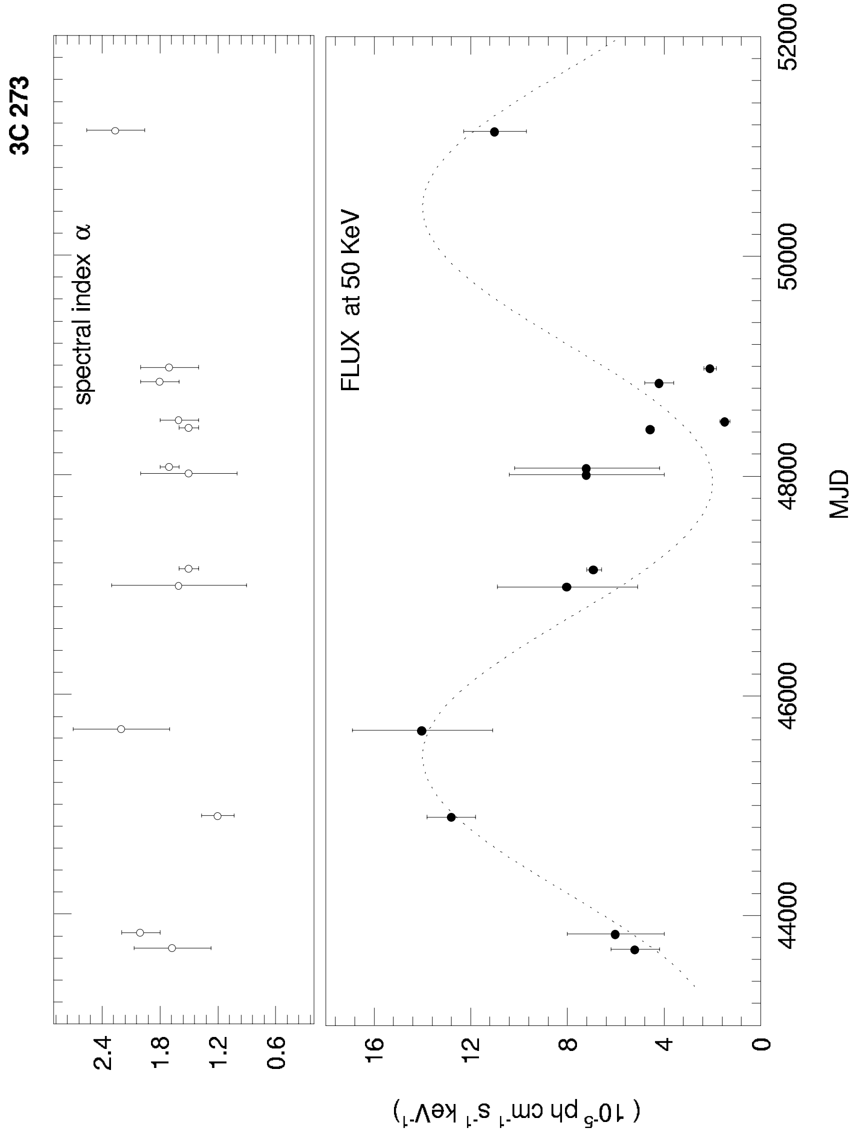

Figure 5. Long term variability of the X-ray flux from 3C273. The lower panel shows the measured flux values at 50 keV. Upper panel gives the best fit power law indices.

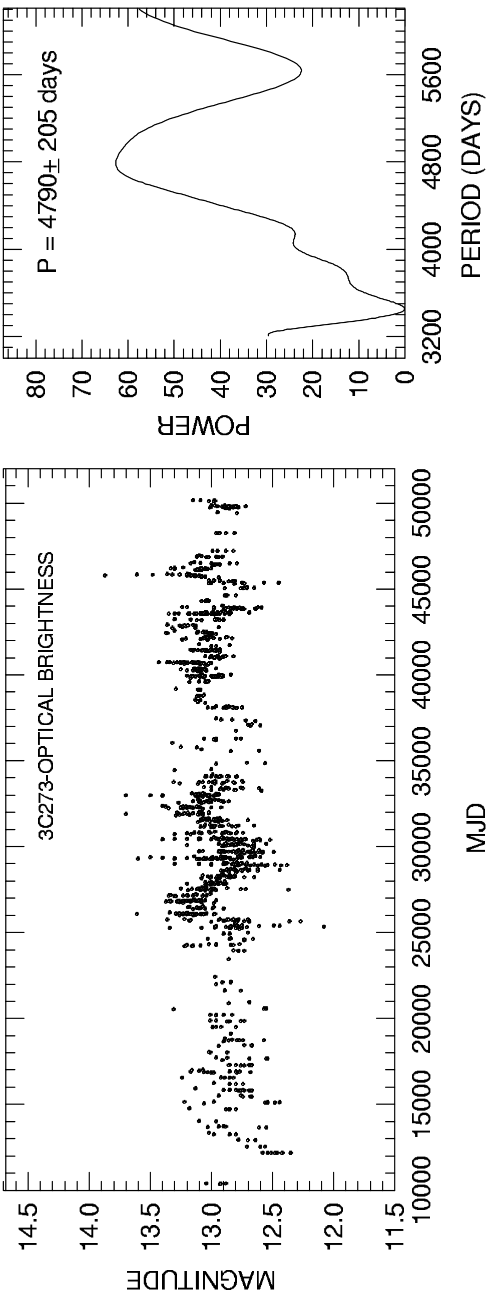

Figure 6. The optical light curve of 3C273 (left panel) and the periodogram obtained during the period analysis using XRONOS (right panel).

ratio of the energy losses of electrons in the synchrotron and synchrotron self Compton processes can be written as:

$$\frac{\dot{\gamma}_{\rm syn}}{\dot{\gamma}_{\rm ssc}} = \frac{B^2/8\pi}{\frac{1}{c}\int \mathcal{F}_\nu^{\rm syn} d\nu}$$

where the synchrotron luminosity $\mathcal{F}_\nu$ is given by (Ginzberg & Syrovatskii 1964);

$$\mathcal{F}_\nu\, d\nu = a'(\gamma)(e^3/mc^2)\left(3e/4\pi m^3 c^5\right)^{(\gamma-1)/2}\ (B_\perp)^{(\gamma-1)/2} L K_e\, \nu^{-(\gamma-1)/2} d\nu$$

for a power law electron spectrum of the form $N(E) = K_e\, E^{-\gamma}$ where $a'(\gamma) \sim 0.15$. For the SSC processes to operate successfully it is necessary to have magnetic field $B \leq 10^6 G$; which is an order of magnitude smaller than the inferred values. It is to be noted that photon emission from the jet requires a continuous injection of electrons into the jets and this can only take place if we assume a continuous flaring geometry as proposed in the case of Mkn 421 (Manchanda 2001). The gradual increase and decrease in the source flux over days to months is consistent with the jet emission model. A pure jet emission however, does not explain the large excess in the soft X-ray band below 1 keV and the occasional flare like behaviour observed in the ASM light curve of the source. Furthermore, the expected spectral energy distribution in the synchrotron or the SSC processes is a simple power law form while the observed distribution shows two broad peaks as noted earlier. In addition, the CHANDRA observations of the structure and the X-ray emission from the jet of 3C273 also suggest that in the soft X-ray region of 0.2–8 keV, only a part of the observed flux may be explained by the jet emission (Sambruna *et al.* 2001). The observation of a weak and a narrow Fe K_α line itself suggests the presence of an additional emission region in the source.

We therefore, propose that a photon emission arising from the accretion disk around the central black hole accounts for the remaining spectral features of the source. The temperature structure of a classical thin accretion disk is given by;

$$T^4 = \frac{3GM\dot{M}}{8\pi\sigma r^3}\left[1 - \left(\frac{r}{R_{\rm min}}\right)^{-1/2}\right]$$

and assuming that AGNs are accreting close to the Eddington rate with about 10% efficiency, the radial distribution of the temperature in the disk is given as:

$$T(r) \approx 6.3 \times 10^5 \left(\frac{\dot{M}}{M_{\rm edd}}\right)^{1/4} \left(\frac{M}{10^8 M_\odot}\right)^{-1/4} \left(\frac{r}{r_s}\right)^{3/4} {}^\circ K,$$

from which we expect a peak in the spectral energy distribution in the UV/soft X-ray region, which might in fact be the origin of the big blue bump seen in 3C273. The evidence for the accretions disks in AGNs is growing steadily i.e., the measurement of double peaked H_α profile in NGC 1097 (Storchi-Bergmann *et al.* 1997) and its variability can be interpreted as an evidence of the accretion disk and the binary nature of the central source similar to the observations in symbiotic stars. In fact, the simultaneity of the optical and UV flux in the case of AGNs suggests that these photons can not originate in the accretion process due to frequency dependence of the drift time scales and therefore, must originate by the reprocessing of X-ray photons in the cold matter of the accretion disk, which is also consistent with the observed equivalent width of the 6.4 keV Fe K_α line in these sources. The disk like Fe K_α line profile seen in Seyfert 1 galaxies, which is believed to arise in the gas rotation at relativistic speed in the Keplerian accretion disk does support the irradiation model. Hence, the observed Fe emission line profile and the correlation between the medium energy X-ray photons and the IR photons in K band in 3C273 can easily be accomplished in a model in which the accretion disk is irradiated by the downward moving hard X-ray photons external to the disk.

We further suggest that the underlying photons spectrum with $\alpha \sim 2.4$ as seen at the gamma ray energies is the true representative of the jet emission arising in non-thermal process. The UV bump is caused by the hot accretion disk. While the iron line is formed due to external irradiation of the disk. Additional contribution to the medium and hard energy X-ray bands will arise due to thermal Comptonization of the large number of available seed photons in the hot plasma surrounding the disk. Up grading of the low energy photons in Compton collisions with thermal electrons has been discussed in the case of galactic black hole candidate Cyg X-1 (Sunyaev & Titarchuck 1980). The added photon flux in the 2–100 keV band will thus give the observed spectral index between $1.2 < \alpha < 2.2$. An alternative process of X-ray emission due to external Compton process has been discussed in literature (Dermer & Schlickeiser 1993). However, the correlation between the K-band and the X-ray data suggests a common origin of these photons. As noted earlier, the multifrequency observations of 3C273 do not show any apparent temporal correlation in various bands. This is probably due to the fact that the large majority of the hard X-ray and gamma ray photons originate in the radio jet while the soft X-ray excess, the blue bump in UV are due to the accretion disk.

5.2 *Long term period and the source geometry*

Any proposed geometrical model with possible sites and the mechanism of photon emission must also explain the long term period of ~ 5000 days in 3C273 as discussed above. Long term periodicity of 23.1 ± 1.1 years for Mkn 421, 13.7 ± 1.3 year for ON 231, 12 years for OJ 287 and 6 years in the case of 3C345 have also been reported from the analysis of their optical data (Liu *et al.* 1995, 1997; Sillanpaa *et al.* 1988b; Unwin *et al.* 1997). Such times scales can only be associated with the activity of the central region of the host galaxy i.e., either the accretion disk or the central black hole system. The precession time scale in either case are too long to be observed and therefore, the observed periodic behaviour in 3C273 can only be explained either by the orbital period by assuming a binary black hole system in the center of the quasar or in terms of the thermal limit cycle (oscillations) time scale in slim accretion disk around the black hole, similar to the models suggested for other sources with long term variability (Sillanpaa *et al.* 1988a; Honma *et al.* 1991).

In the thermal limit cycle model, the nonlinear oscillations can originate in a thermally unstable region of the accretion disk, which are caused by the mass accretion rate above a critical limit. This model was first suggested to explain the bursts in dwarf novae and their S-curve behaviour (e.g., Ritter 1988; King *et al.* 1997,). These models have been extended to the accretion disks around neutron stars and black holes (Taam & Lin 1994; Matsumoto *et al.* 1989; Honma *et al.* 1991). In the thin disk models, the viscosity is the key factor which determines the stability of the inner parts of the accretion disk since the instability may set in for certain value of viscous stress when it is proportional to the total pressure (Shakura & Sunyaev 1976). A variety of stability criteria for the inner regions of the disk have been proposed in literature (Tam & Lin 1984; Abramowicz 1981; Lasota 1989). It has been recently shown that a limit-cycle behaviour of thermal instability can indeed occur only if there exists a high temperature stable equilibria, wherein the inner regions of the disk transits between optically thin and optically thick geometry (Lasota & Pelat 1991). The burst cycle time in this model is given by (Honma *et al.* 1991);

$$t_{\rm cyc} \sim 2\ t_{\rm burst} \sim 5 \times 10^3\ \alpha_{0.1}^{-0.62}\ M_8^{1.37}\ \ {\rm yrs.}$$

Assuming a typical value of $\alpha_{0.1} \sim 1$, the estimated mass of the central black hole necessary to obtain a long term period of 13.5 yrs is $M \simeq 10^6 M_\odot$. This value is two orders of magnitude smaller than the mass of the source required to explain the observed luminosity of the source.

We propose that central core of the 3C273 contains a super massive black hole binary system and the observed periodicity in the X-ray flux is due to the orbital period of the two components. The concept of super massive system of binary black holes in radio galaxies was first proposed by Begelman *et al.* (1980) to explain the observed precession of radio jets. Similarly, to explain the quasi-periodic behaviour of BL Lac OJ 287 in optical band and the radio features in 3C345, a binary black hole model has been proposed for these sources (Sillanpaa *et al.* 1988a; Lobanov & Roland 2002). The presence of a binary black hole system orbiting around their centre of mass in the AGNs, is likely to effect the gas dynamics in the accretion disk, which in turn will affect the gas emission features i.e., the broad emission lines (Begelman *et al.* 1980), narrow emission lines (Gaskell 1996) and even the Iron K_α emission line feature in the X-ray band (Yu & Lu 2001). There is a growing evidence of BBH systems in the active galactic nuclei. For example, observation double peaked Balmer lines of quasar OX 169 have been interpreted as due to binary black hole system (Stockton & Farnhem 1991). The observed complex line profile of 3C273 and its variability does support a binary black holes hypothesis for the source. A model involving a binary black hole system in circular orbit has also been invoked by Reiger and Manheim (2000) to explain the 23 day variability in Mkn 501, observed in the X-ray and TeV gamma rays energy bands (Protheroe *et al.* 1998; Hayashida *et al.* 1998; Nishikawa *et al.* 1999). While the implications of the generalized orbits for a binary black hole system are discussed by De Paolis *et al.* (2001). For a circular orbit, the orbital period P is given as (Yu & Lu 2001);

$$P \approx 210\ a_{0.1pc}^{3/2}\ \left(\frac{2\ M_8}{m_1 + m_2}\right)^{1/2}\ \ {\rm yrs,}$$

where: $a_{0.1pc}$ is the distance between two black holes in units of 0.1 pc and M_8, is the mass unit $10^8 M_\odot$. Assuming a binary separation of 0.01 pc and the observed period of 13.5 yrs in 3C273, the $m_1 + m_2 \approx 0.5 \times 10^8 M_\odot$. Core mass of $\sim 10^8 M_\odot$ is consistent with the inferred Eddington mass limit for the observed luminosity of $\sim 10^{46}$ ergs s^{-1} from the source.

In summary, the hard X-ray spectrum in 3C273 consists of two components. First, the underlying synchrotron emission from the jet which extends from radio energies to GeV photons and has a steep power with $\alpha \sim 2.3$ as measured in the present data. The second component consists of the disk emission which accounts for Iron K_α emission line and also contributes to continuum flux in the medium energy band. We have also presented evidence that the source exhibits a long term periodicity of 13.5 yrs, which is also present in the optical data of the source. We have also shown that the long term periodicity of the source can be explained by a binary black hole model for 3C273.

Acknowledgements

It is a great pleasure to acknowledge the support of the LASE team of J. A. R. D'Silva, P. P. Madhwani, N. V. Bhagat and Ms. N. Kamble for the fabrication of the payload and the successful balloon flight. I also thank Mr. S. Sreenivasan and the staff of the TIFR balloon facility at Hyderabad for the fabrication of the balloon and the successful balloon flight. BATSE and RXTE teams are gratefully acknowledged for making their data available on public archives. I sincerely thank Junhui Fan for providing the optical data of the source.

References

Abramowicz, M. A. 1981, *Nat.*, **294**, 235.
Bassani, L. *et al.* 1992, *Ap. J.*, **396**, 504.
Begelman, M. C., Blandford, R. D., Rees M. J., 1980, *Nat.*, **287**, 307.
Bezler, M., Kendziorra, E., Staubert, R. *et al.* 1984, *A & A*, **136**, 351.
Boyer, C. S., Lampton, M., Mack, J. 1970, *Ap. J.*, **161**, L1.
Courvoisier, T. J. L. *et al.* 1987, *A & A*, **176**, 21.
Cappi, M., Matsuoka, M., 1997, Proc. 2nd Integral workshop 'The Transparent Universe', (ed.) Winkler, Courvoisier & Durouchoucx, ESA, SP-382,
Cappi, M. and Matsuoka, M. Otani, M., Leighly, K. M. 1998, *PASJ*,
D'Silva, J.A.R. *et al.* 1998, *Nucl. Instrum. Methods*, **A412**, 34.
Damle, S. V., Kunte, P. K., Naranan, S. *et al.* 1987, *A & A*, **182**, L1.
Davis, R. J., Muxlow, T. W. B., Unwin, S. C. 1991, *Nat.*, **354**, 374.
Dean, A. J., Bazzano, A., Court, A. J. *et al.* 1990, *Ap. J.*, **349**, 41.
DePaolis, *et al.* 2002, *A & A*, **388**, 470.
Dermer, C. D., Schlickeiser, R. 1993, *Ap. J.*, **416**, 458.
Fan, J. H., Romero, G. E., Lin, R. G. 2001, *Acta Astronomica Sinica*, **42**, 9.
Gaskell, C. M. 1996, *Ap. J.*, **464**, L107.
Ginzberg, V. L., Syrovatskii, S. I. 1964, in *Origin of Cosmic Rays* (Pergamon Press)
Grandi, G. *et al.* 1997, *A & A*, **325**, L17.
Hayashida, N, Hirasawa, H., Ishikawa, F. *et al.* 1998, *Ap. J.*, **504**, L71.
Hermsen, W. *et al.* 1993, *A & A* **97**, 97.
Honma, F., Matsumoto, R., Kato, S. 1991, *PASJ*, **43**, 147.
Johnson, W.N. *et al.* 1995, *Ap. J.*, **445**, 182.
King, A. R., Frank, J., Kolb, U., Ritter, H. 1997, *Ap. J.*, **482**, 919.
Kim, C. 2001, *J. Astrophys. Astr.*, **22**, 283.
Konigl, A. 1981, *Ap. J.*, **243**, 700.
Lasota, J. P. 1989 In: (ed.) *Accretion disks and Magnetic fields in Astrophysics*, G. Belvedere, (Kluwer) p 273
Lasota, J. P., Pelat, D. 1991, *A & A*, **249**, 574.
Leach, C. M., McHardy, I. M., Papadakis, I. E., 1995, *MNRAS*, **272**, 221.
Litchi, G. G. *et al.* 1994, In: *The Second Compton Symposium*, (ed.) Fichtel, Gehrels & Norris, AIP, 611
Liu, F. K., Xie, G. Z., Bai, J. M. 1995, *A & A*, **295**, 1.
Liu, F. K., Liu, B. F., Xie, G. Z. 1997, *A & A*, **SS 123**, 569.

Lobanov, A. P., Roland, J. 2002, In: *Proc. 6th European VLBI network Symp.*, (ed.) Ross, Porcas, Labonov & Zensus, Bonn, p 121
Maisack, M. *et al.* 1989, *Proc. ESLAB Symp.*, **SP-296**, 975
Maisack, M., Kendziorra, E., Mony, B. *et al.* 1992, *A & A*. **262**, 433.
Manchanda, R. K. 1998, *Adv space Res.*, **21**, 1019.
Manchanda, R. K. 2001, *J. Astrophys. Astr.*, **22**, 145.
Maraschi, L. *et al.* 2000, *Adv. Space Res.*, **25**, 713.
Marshall, N., Warwick, R. S., Pounds, K. A. 1981, *MNRAS*, **194**, 987.
Matsumoto, R., Kato, S., Honma, F. 1989, In: *Theory of accretion disks*, (ed.) Meyer, Duschl, Frank and Meyer-Hofmeister, Kluwer, p 167
Mc Hardy, I., Lawson, A., Newsam, A. *et al.* 1999, *MNRAS*, **310**, 571.
Mitra, A. 1991, *Ap. J.*, **370**, 345.
Mushotzky, M. 1982, *Ap. J.*, **256**, 92.
Nishikawa, D., Hayashi, S. Chamoto, N. *et al.* 1999, *ICRC*, **3**, 26.
Pietsch, W., Reppin, C., Trumper, J. *et al.* 1981, *A & A*, **94**, 234.
Primini, F. A., Cooke, B. A., Dobson, C. A. *et al.* 1979, *Nat.*, **278**, 234.
Protheroe, J., Bhat, C. L., Fleury, P. *et al.* 1998, *ICRC*, **8**, 317.
Ramos, E., Kafatos, M., Fruscione, A. *et al.* 1997, *Ap. J.*, **482**, 167.
Reiger, F. M., Manheim, K. 2000, *A & A*, **359**, 948.
Ritter, H. 1988, *A & A*, **124**, 267.
Sambruna, R. M., Urry, C. M, Tavecchio, F. *et al.* 2001, *A & A*, **549**, L161
Shakura, N. I., Sunyaev, R. A. 1976, *MNRAS*, **175**, 613.
Sillanpaa, A., Haarala, S., Valtonen, M. J. 1988a, *et al. Ap. J.*, **325**, 628.
Sillanpaa, A., Haarala, S., Korhonen, T. 1988b, *A & A Suppl Ser.*, **72**, 347.
Stockton, A., Farnhem, T. 1991, *Ap. J.*, **368**, 28.
Storchi-Bergmann, T., Eracleous, M., Ruiz, M. T. *et al.* 1997, *Ap. J.*, **489**, 87.
Sunyaev, R. A., Titarchuck, L. G. 1980, *A & A*, **86**, 121.
Taam, R. E., Lin, D. N. C. 1984, *Ap. J.*, **287**, 761
Turner, M. J. L., Courvoisier, T., Staubert, R. *et al.* 1995, *Sp. Sci. Rev.*, **40**, 623.
Ulrich, M. H., Courvoisier, T. J. L., Warnsteber, W. 1988, *A & A*, **204**, 21
Unwin, S., Wehrle, A., Lobonov, A. P. *et al.* 1997, *Ap. J.*, **480**, 1997
von Montigny, C. *et al.* 1993, *A& A Suppl Ser.*, **97**, 101.
Warrell, D. M., Mushotzky, R. F., Boldt, E. A. *et al.* 1979, *Ap. J.*, **232**, 683.
Wilkes, B. J., Elvis, M. 1987, *Ap. J.*, **323**, 243,
Williams, O. R., Turner, M. J. L., Stewart, G. C. *et al.* 1992, *A & A*. **285**, 119.
Yu, Q., Lu, Y. 2001, *A & A*, **377**, 17.